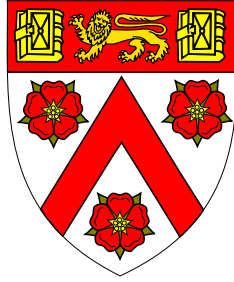


Experimental Platform for a Box-Trapped Dipolar Quantum Gas



Milan Krstajić

Trinity College

This dissertation is submitted for the degree of
Doctor of Philosophy

Supervisor: **Dr Robert Smith**

June 2021

Cavendish Laboratory
Department of Physics



**UNIVERSITY OF
CAMBRIDGE**

*To my dearest sister Katarina,
parents Tamara and Dragutin,
grandma Milica
and in the loving memory of my grandparents
Slobodanka, Milorad and Danilo...*

Declaration

This thesis is the result of my own work and includes nothing which is the outcome of work done in collaboration except as declared in the Preface and specified in the text. I further state that no substantial part of my thesis has already been submitted, or, is being concurrently submitted for any such degree, diploma or other qualification at the University of Cambridge or any other University or similar institution except as declared in the Preface and specified in the text. It does not exceed the prescribed word limit for the relevant Degree Committee.

Milan Krstajić

June 2021

Abstract

Title: Experimental Platform for a Box-Trapped Dipolar Quantum Gas

Author: Milan Krstajić

This thesis describes the design and building of an experimental platform for investigating many-body physics in homogeneous dipolar quantum gases of erbium. The interest in such systems lies in a multitude of quantum phenomena that stem from dipole-dipole interactions, particularly their long-range and anisotropic nature. Consequentially, dipolar quantum gases make up an increasingly popular branch within an already thriving field of ultracold quantum gases. The thesis details the design, construction and testing of the experimental setup, including the vacuum chamber, optical and laser systems, magnetic fields and supporting control and data acquisition systems. I present results describing both the progress towards reaching the goal of an erbium Bose-Einstein condensate in an optical box potential as well as the difficulties encountered along the way. At present, the experiment is capable of producing clouds with 100 million atoms at the temperature of 15 microkelvin in the magneto-optical trap, which translates into about 15 million atoms at 50 microkelvin following transfer into an optical dipole trap. I detail the remaining steps to complete the intended goal and present an overview of some of the research topics our platform will make accessible, including roton physics, out-of-equilibrium many-body phenomena and dynamics of phase transitions in systems with long-range interactions. I also briefly touch upon the subject of expanding the apparatus to a dual species experiment with potassium, which will enable investigating systems with impurities. Finally, these discussions are augmented with results from numerical simulations on the stability of a dipolar quantum gas in a general power-law trap (of which the optical box is an example), that are likely to help with planning future experiments.

Acknowledgements

While writing the acknowledgements section might come across as a mere formality to an uninformed observer - every thesis has one and most share the same format - it is everything but that. Here I am, rewinding the previous four years, and, even though I am mostly staying within the domain of the PhD course and associated student life, I am overwhelmed by the realisation of both the number of people I am grateful to, and the myriad of reasons behind that gratitude. I was fortunate enough to live and work both in Cambridge and in Oxford over the course of my PhD¹, and besides all the inspiring scenery and enchanting architecture, it was the army of amazing people with whom I had the opportunity to work or spend time and from whom I got to learn, that made it such an enjoyable experience. And, at the forefront of that 'army' is, naturally, the leader...

... of our research group and my supervisor, Dr Robert Smith, to whom I am immeasurably grateful for entrusting me with the opportunity to work on the erbium project. He maintained a motivating and supportive atmosphere for everyone in the group and always ensured that his extraordinary intuition and experience in experimental physics were at our disposal, both for us to learn and to advance the experiment.

Dr Anna Marchant is one of the friendliest people I have ever encountered and I enjoyed every day of collaborative work with her. She had a major influence on me as a physicist and I take the opportunity here to promise that all the good practices that I learned from her are here to stay.

My colleagues Peter and Lucas have joined me in the lab ever since moving to Oxford and brought a lot of wit and humour to the typical work day. Our newest colleague Jirka only added to the good vibes in the team when he arrived and I very much look forward to continuing to work with the three of them.

Nathaniel Vilas accompanied me during the most dynamic and exciting times in this project, when tasks involved in designing and building the experiment from scratch greatly outnumbered the students. I couldn't have asked for a better and more committed 'partner in crime' back in those days.

¹And unfortunate enough to be asked a thousand times the unanswerable question - "Which one do you like more?"

Many more people left a mark within the group during my PhD, both in terms of research and a nice and friendly atmosphere. Therefore, I thank Gloria Clausen, Daniel Ruttley, David Strachan, Edward Gandar, Tanish Satoor, Tobias Schaich and Alexander Norden for their company and invested work.

I am grateful to Prof Zoran Hadžibabić for all the advice and knowledge he conveyed to me. I have always admired him for his scientific talent, quick thinking and far reaching interests. Being a part of his group before the move was a truly amazing experience.

I thank all the fantastic colleagues from Zoran's group, including but not limited to Julian Schmitt, Christoph Eigen, Panagiotis Christodoulou, Maciej Galka, Raphael Lopes, Jake Glidden, Lena Dogra, Nishant Dogra, Jay Man, Jinyi Zhang and Timon Hilker who made sure that no day in the Cambridge lab passed without an interesting discussion, good humour or some fun activity². Furthermore, such a large concentration of knowledge and experience in ultracold atoms, just one casual question away, was unimaginably helpful when building a new experiment without much prior experience. On the same note, my gratitude extends across AMOP, and specially to Konrad Viebahn and Matteo Sbroscia who offered advice or lent us equipment on countless occasions.

The help we received from the Cavendish Laboratory student workshop supervisor, Kevin Mott, was priceless, especially considering the occasion when he saved us from months of delays by devising a way to repair a faulty vacuum chamber part.

Following the move to Oxford, the colleagues at ALP were equally helpful whenever we needed anything, and here I especially thank Elliot Bentine for the time and enthusiasm invested in helping our group and the interesting discussions that were an integral part of that.

I am also most grateful to Trinity College, both for the financial support during the course of my studies and for admitting me into a welcoming, supportive and inspiring community that left me with only the best and happiest memories of Cambridge.

The last four years wouldn't have been nearly as fun if it wasn't for my dearest friends Saša, Luka, Lazar, Jovan, Ivan and many others. Thanks to them I am left with countless fond memories and friendships to last a lifetime.

A special place in my life is always reserved for my sister Katarina, my parents Tamara and Dragutin and grandma Milica. There are no words to describe the love and support I keep receiving from them every day.

²Although, I can't guarantee that everyone listed looks back at some activities, e.g. following the 2018 FIFA World Cup, as 'fun'.

Last, and in no way least, my heart belongs to Petra for all the love, caring and magical moments in my life she is responsible for, and especially for keeping me happy and smiling during the hectic time that the years of 2020-21 have brought.

Table of contents

1	Introduction	1
1.1	Overview of Ultracold Atom Systems	1
1.2	Properties of Erbium	4
1.2.1	Electronic Configuration and Transitions	5
1.2.2	Magnetic Properties	7
1.2.3	Scattering Properties	8
1.3	Bose Gas with Dipolar Interactions	11
1.3.1	Gross-Pitaevskii Equation	11
1.3.2	Excitations and Roton Minimum	12
1.4	Project Goals	15
1.5	Overview of the Experiment	15
1.6	Contributions and Thesis Outline	19
2	Vacuum Chamber Design and Construction	20
2.1	Design Considerations	21
2.1.1	Modelling Pumping and Pressures	22
2.1.2	Effusion Cell and the Atomic Beam	25
2.2	Magnetic Field Control	30
2.3	Optical Access	33
2.3.1	HV Section	33
2.3.2	UHV Section	34
2.4	Vacuum Chamber Assembly	36
2.5	Reaching the UHV Regime	38
3	Laser Cooling on the Atomic Beam	41
3.1	401 nm Laser System	41
3.2	Spectroscopy and Laser Stabilisation	44
3.2.1	Modulation Transfer Spectroscopy	45

3.2.2	Modulated Fluorescence Spectroscopy	51
3.3	Transversal Cooling	53
3.4	Zeeman Slower	56
3.4.1	Idealised Zeeman Slower	57
3.4.2	Realistic Zeeman Slower	58
3.4.3	Implementation	62
3.4.4	Optimisation and Results	64
4	Narrow-Line Magneto-Optical Trap	69
4.1	Principle of Operation	69
4.2	583 nm Laser	74
4.3	Spectroscopy and Laser Stabilisation	76
4.3.1	Modulation Transfer Spectroscopy	77
4.3.2	Shelving Spectroscopy	79
4.4	Implementation of the MOT	81
4.4.1	Experimental Control	81
4.4.2	Experimental Sequence	82
4.4.3	Optimisation and Performance	85
5	Optical Trapping, Transport and Dynamical Potentials	92
5.1	Light Shift Potentials	92
5.1.1	Polarizability of Erbium	93
5.1.2	Harmonic Trapping in Focused Gaussian Beams	94
5.2	1030 nm Laser System and the Transport Setup	95
5.2.1	Optical System Design and Realisation	96
5.2.2	Performance and Observed Issues	99
5.2.3	Outlook and Proposed Alterations	101
5.3	Optical Access to the Science Cell	102
5.4	Optical Box Potential	104
5.5	Arbitrary Optical Potentials and Bragg Spectroscopy	107
5.5.1	Generation of Arbitrary Intensity Patterns	107
5.5.2	Design of the Projection Objective	108
5.5.3	Bragg Spectroscopy	110
6	Ground State Stability in a Box Trap - Numerical Simulations	113
6.1	Numerical Simulation	114
6.1.1	Defining the System	115

6.1.2	Calculation of the Dipolar Energy/Hamiltonian Term	117
6.1.3	Spatial Discretisation	118
6.1.4	Imaginary Time Propagation	119
6.1.5	Preconditioned Conjugate Gradient Method	120
6.1.6	Angular Roton Instability	122
6.2	Results Analysis	123
6.2.1	Stability Against Collapse	124
6.2.2	Measure of Homogeneity	126
7	Conclusion and Outlook	131
7.1	Conclusion	131
7.2	Completing the Experimental Platform	132
7.3	Future Projects	133
7.3.1	Probing the Roton Physics	133
7.3.2	Phase Transition Dynamics with Long Range Interactions	133
7.3.3	Dual-Species Experiments with Potassium	136
	Appendix A Pumping System Design	138
A.1	Molecular Flow Regime	138
A.2	Gas Sources	140
A.3	Calculations for Our Experiment	141
A.4	Bakeout Process	144
	Appendix B Computer Simulation of the Atomic Beam	145
B.1	Effusion Cell	145
B.2	Transversal Cooling	147
B.3	Zeeman Slower	148
	Appendix C Atomic Beam Fluorescence Measurements	150
C.1	Transversal Probing	151
C.1.1	Calibration	151
C.1.2	Flux Measurements	152
C.2	Angled Probing	153
	Appendix D Vacuum Cleaning, Assembly and Bakeout Procedures	154
D.1	Preparation	154
D.2	Cleaning	156
D.3	Assembly	157

D.4	Bakeout	158
Appendix E Computer Control and Data Acquisition		160
E.1	Control System Architecture	160
E.2	Imaging	160
E.2.1	Absorption Imaging	161
E.2.2	Fluorescence Imaging	162
E.3	Publication : Atom Cloud Detection and Segmentation Using a Deep NN .	162
Appendix F Laser Cooling		179
Appendix G Integral and Discrete Transforms for the Numerical Simulation		182
G.1	Continuous Fourier and Hankel Transforms	182
G.2	Discrete Transforms	183
G.2.1	Discrete Fourier Transform	183
G.2.2	Discrete Cosine Transform	184
G.2.3	Discrete Hankel Transform	184
References		187

Chapter 1

Introduction

In this thesis, I am offering a detailed overview of the experimental effort I have undertaken together with my supervisor and colleagues, in designing and setting up a platform for investigating many-body quantum physics in systems with dipolar interactions. The full duration of my PhD course is covered, starting from October 2017 until June 2021, and I address the motivation for building the experiment, all the design considerations and theoretical calculations that were factored in and report on the progress in building and commissioning the system. Finally, the thesis also describes the research projects that are planned for the near future, once the experiment is fully operational.

1.1 Overview of Ultracold Atom Systems

In the past three decades, ultracold atom experiments have become known as very capable testbeds for theoretical models from condensed matter physics and many-body quantum mechanics. Following breakthrough research in laser cooling and the development of the Magneto-Optical Trap (MOT) [1], a degenerate quantum gas of bosons, the Bose-Einstein Condensate (BEC), was created in 1995 at JILA [2] with ^{87}Rb and MIT [3] with ^{23}Na in quick succession, and shortly after that, with ^7Li at Rice University [4]. Reaching quantum degeneracy in a fermionic system followed in 1999 [5]. With these achievements enabling the creation of macroscopic quantum-correlated systems, the ground was laid for experiments that can probe fundamental aspects of many-body quantum physics. The research that ensued has brought about an arsenal of tools and techniques that keep the field of ultracold atoms at the forefront of the wider scientific topic of quantum simulation. As a result, scientists now have at hand different trapping geometries ranging from various types of bulk traps to optical lattices, as well as the ability to tune the strength [6, 7] and nature of the interactions and address the atomic internal states with electro-magnetic fields and radiation. Some of

the most prominent achievements in the early days of the field include the demonstration of matter-wave interference of two BEC's [8] directly showing the spatial coherence of the state [9], the realisation of the BEC-BCS crossover [10–12], observation of quantised vortices and lattice ordering of vortices [13–15] and the observation of the Mott insulator transition in optical lattices [16]. Nowadays, the interests in the field are turned towards numerous topics - systems out of equilibrium [17], condensed matter lattice models [18], dynamics of phase transitions [19], precision metrology [20] and quantum information [21] - to list a few out of many. What is common to most of the approaches is the concept of tuning the Hamiltonian of the system to match a desired model, bringing the system into a specific initial state and then looking at the subsequent evolution. That is in essence the definition of a quantum simulator and the extensive ability of parameter tuning in cold atom systems makes them ideal for this purpose.

Confinement of atoms is realised either with magnetic fields or non-resonant light fields via the AC Stark effect. In both cases, the imposed fields create a potential well, or in the case of optical lattices - a periodic array of wells, trapping the atoms. Most of the common methods, e.g. an optical dipole trap made out of focused Gaussian beams or a magnetic TOP trap, result in (approximately) harmonic trapping potentials. This suffices for many applications, still offering a decent degree of tuning freedom in terms of the aspect ratio, anharmonicity or tightness of the trap, but falls short in simulating models that require homogeneous density. Fortunately, techniques for sculpting light intensity patterns have enabled the development of the optical box potential [22], opening the door for numerous experiments that called for uniform systems, such as exploring the dynamics of the phase transition to BEC [23] or turbulent flow [24].

In addition to the ability to tune the geometry of the trap, the available trapping methods allow for the creation of systems of reduced dimensionality. By imposing sufficiently tight trapping along one or two directions, the system can be forced into motional ground states along these axes, effectively freezing out these dimensions. This was realised in various ways, leading to the observation of inherently one-dimensional [25, 26] or two-dimensional effects [27].

The discovery of Feshbach resonances in ultracold atom [6, 7] systems was probably one of the most deciding moments for the future of the field. The situation was already favourable as, due to low thermal energies involved, the interactions in most cold gases could be well described by a hard-sphere model involving only two-body collisions - a model with only one parameter, the scattering length - and the Feshbach resonances can now be used to tune this parameter. The possibilities range from changing the nature of the interactions between

1 H 1998																	2 He 2001
3 Li 1995	4 Be											5 B	6 C	7 N	8 O	9 F	10 Ne
11 Na 1995	12 Mg											13 Al	14 Si	15 P	16 S	17 Cl	18 Ar
19 K 2001	20 Ca 2009	21 Sc	22 Ti	23 V	24 Cr 2004	25 Mn	26 Fe	27 Co	28 Ni	29 Cu	30 Zn	31 Ga	32 Ge	33 As	34 Se	35 Br	36 Kr
37 Rb 1995	38 Sr 2009	39 Y	40 Zr	41 Nb	42 Mo	43 Tc	44 Ru	45 Rh	46 Pd	47 Ag	48 Cd	49 In	50 Sn	51 Sb	52 Te	53 I	54 Xe
55 Cs 2002	56 Ba	71 Lu	72 Hf	73 Ta	74 W	75 Re	76 Os	77 Ir	78 Pt	79 Au	80 Hg	81 Tl	82 Pb	83 Bi	84 Po	85 At	86 Rn
87 Fr	88 Ra	103 Lr	104 Rf	105 Db	106 Sg	107 Bh	108 Hs	109 Mt	110 Ds	111 Rg	112 Cn	113 Nh	114 Fl	115 Mc	116 Lv	117 Ts	118 Og
lanthanides	57 La	58 Ce	59 Pr	60 Nd	61 Pm	62 Sm	63 Eu	64 Gd	65 Tb	66 Dy 2011	67 Ho	68 Er 2012	69 Tm	70 Yb 2003			
actinides	89 Ac	90 Th	91 Pa	92 U	93 Np	94 Pu	95 Am	96 Cm	97 Bk	98 Cf	99 Es	100 Fm	101 Md	102 No			

Fig. 1.1 **Bose-Einstein Condensation of Different Atomic Species** - The periodic system of chemical elements with the chemical elements that have been successfully condensed into a BEC highlighted. The fields also state the year when the condensate was first reported.

repulsive and attractive to turning them off completely or making them as strong as quantum mechanics allows - the so called, unitarity limit.

More recently, the development of the specific laser cooling techniques required for more exotic species expanded the spectrum of elements that can be cooled to quantum degeneracy (Figure 1.1). This includes a few elements with very high magnetic moments (chromium [28], erbium [29], dysprosium [30]) adding a new dimension to experiments that can be realised, introducing long-range and anisotropic, dipole-dipole interactions (DDI) on top of the aforementioned contact interactions, that are inherently short range and isotropic.

First results obtained with chromium demonstrated the anisotropic nature of the dipolar force and how it is reflected in the aspect ratio of a trapped cloud [31] or density patterns emerging after collapse of a cloud brought to instability [32] and the examination of the impact of the dipole-dipole interactions on the stability of a BEC [33]. Further advances came with condensates of dysprosium and erbium, as their higher magnetic moments combined with larger atomic masses make dipolar interactions even more pronounced relative to contact interactions. Furthermore, in these two elements, the contact interactions can be tuned more readily, due to the abundance of accessible Feshbach resonances [29, 34]. This eventually

Isotope	^{162}Er	^{164}Er	^{166}Er	^{167}Er	^{168}Er	^{170}Er
Abundance	0.14%	1.61%	33.6%	23.0%	26.8%	15.0%
Statistics	boson	boson	boson	fermion	boson	boson

Table 1.1 **Erbium Isotopes** - Abundances and spin statistics of different erbium isotopes.

allowed for the detection of the roton-minimum in the excitation spectrum of a strongly dipolar gas [35, 36], signalling similarities with strongly correlated systems like liquid helium [37], with the additional ability to tune the roton minimum depth via the contact interactions. The earlier observation of dipolar quantum droplets, emerging from a cloud collapsing due to strong dipolar interactions [38, 39], was also linked to the roton instability, eventually leading to the creation of an exotic and interesting supersolid state of matter [40–42], combining both spatial order and the phase coherence of a superfluid.

At this moment, there is a number of experiments with magnetic ultracold atoms (Er or Dy) around the world, including the ones in Innsbruck [29], in Stuttgart [43], at Stanford [30], at Harvard [44], at MIT [45], in Bonn [46], in Paris [47], in Pisa [48], in Hong Kong [49] etc.

Finally, it would be a mistake not to mention that the fields of ultracold molecules [50, 51], Rydberg atoms [52] and trapped ions [53] have been developing at an equally fast pace side-by-side with the systems with ultracold neutral atoms, sharing many of the experimental techniques and striving towards similar objectives. Relevant for this topic, ultracold polar molecules and Rydberg atoms are also promising platforms for researching many-body physics with dipole-dipole interactions. Both types of systems offer dipole moments larger by up to two orders of magnitude and can achieve significantly stronger dipolar interactions, but come at the cost of short lifetime of samples (as experiments are performed on metastable states) and typically require more complex apparatus.

1.2 Properties of Erbium

Erbium is a metallic element from the lanthanides section of the periodic table, and is also classified as a rare-earth element. It was discovered in a sample of gadolinite ore by Carl Gustav Mosander in 1843 [54]. Its name (along with the names of terbium, ytterbium and yttrium) is derived from the mine where the ore originated - Ytterby. By appearance, erbium is a pale, silvery metallic substance, that easily oxidises and hence usually covers itself with a layer of oxide when exposed to air. It has the atomic number of $Z = 68$, and the average

atomic mass of $A = 167.26$ amu. It naturally occurs in six stable isotopes, five of them bosonic, as shown in the Table 1.1. Its uses range from being a dopant element in solid state and optical-fibre laser active media, to manufacturing coloured glasses and high heat capacity alloys for usage in cryo-technology.

In the scope of the ultracold atomic physics, erbium is interesting for its large magnetic dipole moment and electronic level structure favourable for laser cooling and accessibility of both bosonic and fermionic isotopes. This makes it handy for implementing standard cooling and trapping methods for reaching low temperatures and quantum degeneracy, and then exploring the phenomena in many-body quantum mechanics with dipole-dipole interactions.

1.2.1 Electronic Configuration and Transitions

The electronic configuration of erbium is $[Xe] 6s^2 4f^{12}$, exemplifying the case of a submerged shell configuration, where the valence electrons populate a filled $6s$ orbital while a $4f$ sub-shell remains partially filled. This configuration is the primary reason for the high magnetic moment of erbium, where the two holes in the $4f$ sub-shell contribute to the total angular momentum of $J = 6$ in the ground state.

Transition	Blue	Yellow
Wavelength	400.97 nm	582.84 nm
Natural Linewidth	29.7 MHz	190 kHz
Doppler Temperature	714 μ K	4.6 μ K
Recoil velocity	6.0 $\frac{\text{mm}}{\text{s}}$	4.1 $\frac{\text{mm}}{\text{s}}$
Saturation Intensity	60.3 $\frac{\text{mW}}{\text{cm}^2}$	0.13 $\frac{\text{mW}}{\text{cm}^2}$

Table 1.2 Laser Cooling Atomic Transitions

The complicated electronic structure is also reflected in the very rich spectrum of electronic excited states (Figure 1.2). Looking at the electronic-dipole-allowed transitions from the ground state, several transitions of interest for laser cooling may be identified [57], covering a range of line widths, from wide (30 MHz) to ultra-narrow (2 Hz). An important criterion for a level to be directly suitable for laser cooling is a small branching ratio, enabling the cooling scheme to be set up on a two-level subsystem. Two transitions of particular interest for our experiment are the ones at 401 nm and 583 nm with linewidths of 29.7 MHz and 190 kHz respectively. These two transitions are highlighted in Figure 1.2 and their properties are shown in Table 1.2. The 401 nm transition is the most prominent transition in erbium, making it very convenient for initial stages of laser cooling as it provides a large photon

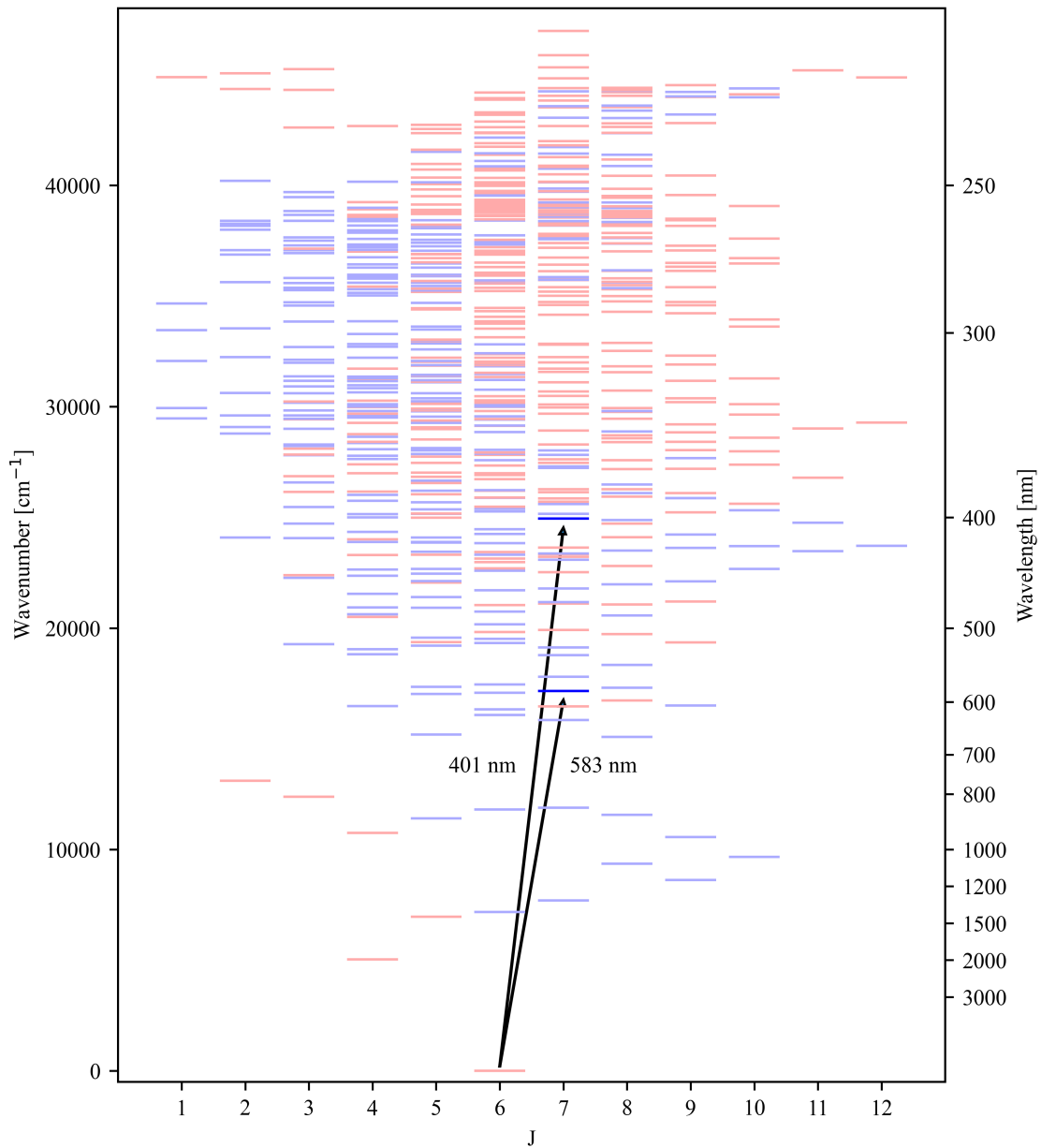


Fig. 1.2 **Electronic Orbitals of Erbium** - Energy levels of erbium arranged by orbital quantum number J . Even (odd) parity levels are indicated in (red) blue. The two transitions that we employ for laser cooling, at 401 nm and 583 nm are highlighted. Spectroscopic data obtained from [55, 56].

scattering rate. In parallel, it has the leading order influence on the atomic polarizability, which is relevant for optical trapping (as discussed in Chapter 5). The yellow transition, at 583 nm, being reasonably narrow, is well suited for the magneto-optical trap, giving a very low Doppler temperature of approximately five microkelvin.

1.2.2 Magnetic Properties

Elements with the largest magnetic moments can be found among the lanthanides. Dysprosium and terbium lead the charts with $\mu = 10\mu_B$, followed by holmium, europium and erbium with $8\mu_B$, $7\mu_B$ and $7\mu_B$ respectively ($\mu_B = \frac{e\hbar}{2m_e}$ is the Bohr magneton). As mentioned in the previous subsection, erbium owes its magnetic moment to the two holes in the $4f$ sub-shell. The appropriate spin-orbit coupling scheme for this submerged shell configuration is a special type of jj -coupling, called J_1J_2 -coupling. In this picture, LS -coupling is assumed to separately couple the angular momenta of the submerged $4f$ shell holes and the angular momenta of the outer valence electrons, yielding J_1 and J_2 , that are subsequently coupled together. In the ground state, the two valence $6s$ electrons are in the $L = 0$ and $S = 0$ state, and the $4f$ electrons give an overall 3H_6 state with $L = 5$, $S = 1$ and $J = 6$, which also corresponds to the final coupled state. The Landé g -factor for this state can be theoretically calculated as:

$$g_J = 1 + (g_S - 1) \frac{J(J+1) - L(L+1) + S(S+1)}{2J(J+1)} = 1.1670533 \quad (1.1)$$

where $g_S \approx 2.00232$ is the gyromagnetic ratio of the electron [58]. This formula does not include several known corrections, that would otherwise yield a value much closer to the actual, experimentally measured value of $g_J = 1.163801(1)$ [55, 56]. Knowing the Landé g -factor it is possible to calculate the magnetic moment of the given fine structure state, given by the value of m_J :

$$\mu = m_J g_J \mu_B . \quad (1.2)$$

From here, we see that the total magnetic moment of an erbium atom in its ground state is $\mu(m_J = 6) = 6.982806(6)\mu_B$.

The two excited states corresponding to the optical transitions used in the experiment, both having $J = 7$, are:

- 401 nm excited state: $[Xe]4f^{12}({}^3H_6)6s6p({}^1P_1)(6,1)_7$
- 583 nm excited state: $[Xe]4f^{12}({}^3H_6)6s6p({}^3P_1)(6,1)_7$

with the Landé g -factors of $g_J = 1.160$ and $g_J = 1.195$ respectively [55, 56]. These values are important as the Zeeman shift of a given transition $|J_g, m_g\rangle \rightarrow |J_e, m_e\rangle$ induced by the magnetic field B is calculated according to:

$$\Delta E_{\text{Zeeman}} = (m_e g_e - m_g g_g) \mu_B B . \quad (1.3)$$

1.2.3 Scattering Properties

Typical densities encountered in ultracold atomic clouds are on the order of $n \sim 10^{20} \text{ m}^{-3}$, corresponding to an average inter-particle distance of $d \sim n^{-\frac{1}{3}} \sim 200 \text{ nm}$ [59, 60]. As it will be justified below, the representative length scales associated with the scattering processes are on the order of $10^2 \times a_0 \approx 5 \text{ nm} \ll d$, a_0 being the Bohr radius, placing the system in the regime where scattering can be described accurately by only considering two-body encounters. Furthermore, at ultracold temperatures and for a gas spin polarised in the $|6, -6\rangle$ ground state, 2-body inelastic collision processes are generally frozen-out¹.

Interactions and scattering processes in a dipolar gas are governed both by the dipolar and the van der Waals potential:

$$U(\mathbf{r}) = U_{\text{vdW}}(\mathbf{r}) + U_{\text{dd}}(\mathbf{r}). \quad (1.4)$$

The potential energy originating from dipole-dipole interactions (DDI), directed along unit vectors \mathbf{e}_1 and \mathbf{e}_2 , and separated in space by \mathbf{r} is given by:

$$U_{\text{dd}}(\mathbf{r}) = \frac{C_{\text{dd}}}{4\pi} \frac{(\mathbf{e}_1 \cdot \mathbf{e}_2) r^2 - 3(\mathbf{e}_1 \cdot \mathbf{r})(\mathbf{e}_2 \cdot \mathbf{r})}{r^5} \quad (1.5)$$

where for magnetic dipoles, $C_{\text{dd}} = \mu_0 \mu^2$. In the case of a polarised gas, with dipoles aligned with the z -axis, this simplifies to:

$$U_{\text{dd}}(\mathbf{r}) = \frac{C_{\text{dd}}}{4\pi} \frac{1 - 3 \cos^2 \theta}{r^3} \quad (1.6)$$

with θ being the angle between \mathbf{r} and the polarisation axis. The anisotropy of the DDI force is shown graphically in Figure 1.3, demonstrating how the interactions can be either repulsive or attractive depending on the positioning of the atoms.

The situation with the dispersion potential describing the van der Waals interactions is a bit more involved, due to the complicated electronic structure of erbium. Since the ground state electronic configuration includes two holes in the f subshell, the dispersion potential is anisotropic, reflecting the lack of spherical symmetry of the electronic density distribution, and cannot be represented with in the simple form $U_{\text{vdW}}(r) = -\frac{C_6}{r^6}$. Consequentially, the dispersion potential is described by a spread of C_6 coefficients, representing couplings between different pairs of total angular momentum eigenstates, quantified by ΔC_6 , which for erbium take the values of $C_6 = 1723 \text{ a.u.}$ and $\Delta C_6 \sim 350 \text{ a.u.}$ [61]. While this anisotropy has profound consequences on the spectrum of Feshbach resonances, due to the rotational barrier

¹The Zeeman splitting in a $B = 1 \text{ G}$ bias field corresponds to a temperature of $T = \frac{gJ\mu_B B}{k_B} \approx 80 \mu\text{K}$

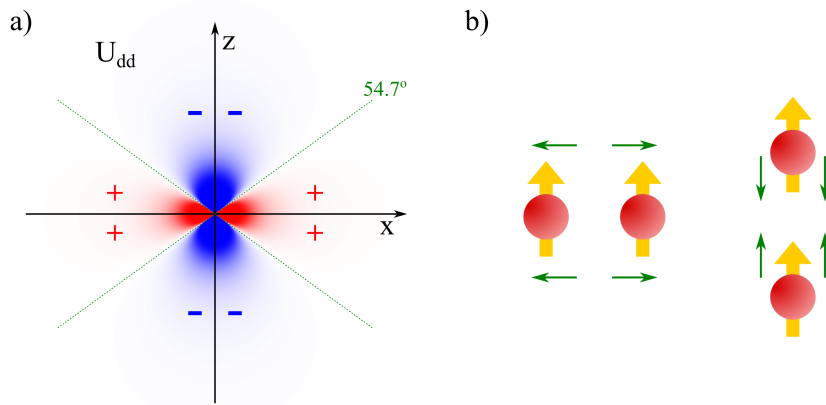


Fig. 1.3 **Dipole-Dipole Interaction** - a) The anisotropic profile of the interaction potential for a pair of parallel dipoles. The potential changes sign at the angle of 54.7° , between being attractive for ‘head-to-tail’ dipoles and repulsive for ‘side-by-side’ dipoles - also shown in b).

for ultracold collisions, it still only amounts to s -wave scattering, and can be represented by a hard-core pseudo potential and a unique scattering length [57, 62].

Even with the dipolar force taken into account, the pseudo potential formalism can still be employed, but with two modifications. The first is the obvious addition of the anisotropic term from Equation 1.6, and the second is a modification to the s -wave scattering length by a hard-sphere contribution of the DDI:

$$a_s^{\text{eff}} = \sqrt{a_s^2 - \frac{4}{5}a_D^2} \quad (1.7)$$

where $a_D = \frac{m_r \mu_0 \mu^2}{12\pi \hbar^2}$ and m_r is the reduced mass of two colliding dipoles [57]. Therefore, in a gas of polarized dipolar atoms, the full pseudo potential with dipolar interactions included can be written as:

$$V_{\text{int}}(\mathbf{r}) = \frac{4\pi \hbar^2}{m} \left(a_s^{\text{eff}} \delta(\mathbf{r}) + \frac{3}{4\pi} a_{\text{dd}} \frac{1 - 3 \cos^2 \theta}{r^3} \right) \quad (1.8)$$

with the introduction of DDI length scale, $a_{\text{dd}} = \frac{m \mu_0 \mu^2}{12\pi \hbar^2}$ [33]. This length scale is used to compare the relative importance of the contact interactions and dipole-dipole interactions, through the definition of the dipolar character²:

$$\epsilon_{\text{dd}} = \frac{a_{\text{dd}}}{a_s}. \quad (1.9)$$

²From here on we drop the ‘eff’ superscript from a_s^{eff} .

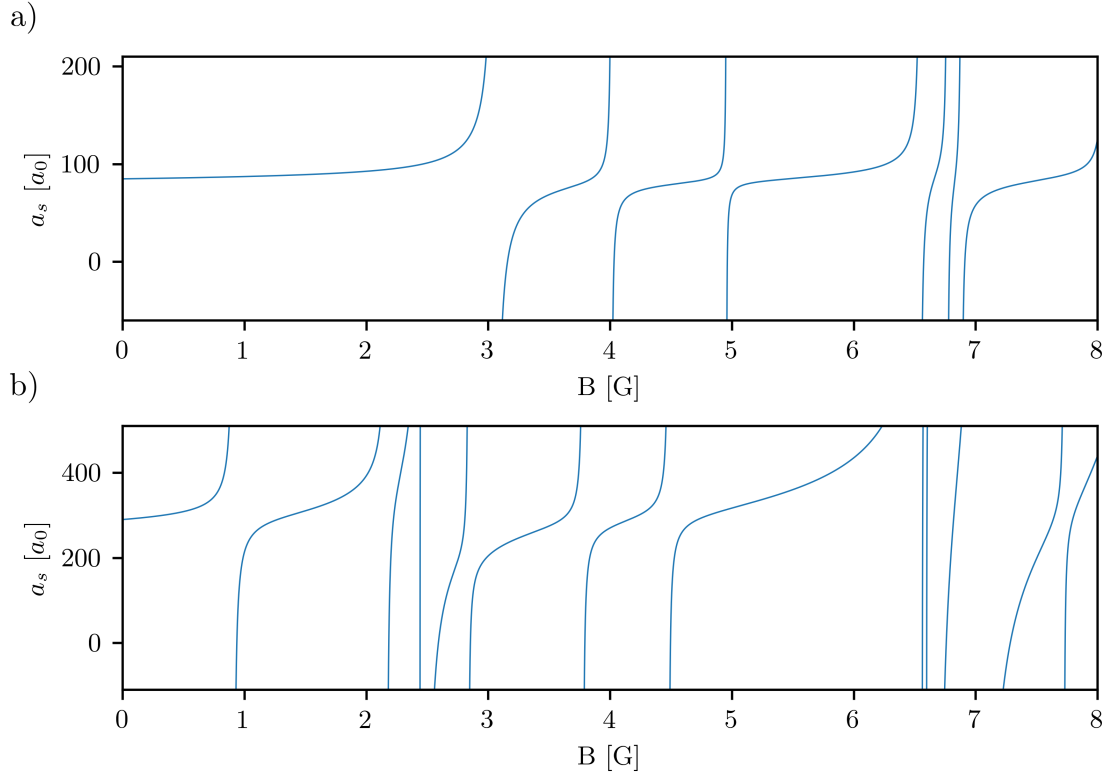


Fig. 1.4 **Feshbach Resonances in ^{166}Er and ^{168}Er** - Evaluated using data on positions and widths of resonances and estimates on the background scattering length (assumed constant across the interval of fields) from [57, 29] for the two most abundant isotopes - ^{166}Er (a) and ^{168}Er (b) and fields up to 8 G. Due to a large uncertainty in the background scattering length, these plots offer only approximate values of scattering length, but describe the general structure of the Feshbach spectrum.

The effective s -wave scattering length can be controlled via the Feshbach resonances, by tuning the background magnetic field. The variation in the vicinity of a resonance of width ΔB located at the field value B_0 can be represented by [6]:

$$a_s = a_{\text{bg}} \left(1 - \frac{\Delta B}{B - B_0} \right). \quad (1.10)$$

The anisotropic nature of the van der Waals potential, that has the ability to couple the electronic degrees of freedom of the two colliding atoms, with the molecular rotation of the bound states. This enables a large number of coupling channels that contribute to Feshbach resonances resulting in a dense spectrum. Figure 1.4 shows the resonances for ^{166}Er and ^{168}Er , up to the field of 8 G. Unlike most of the species used in ultracold atom experiments, the Feshbach spectrum of erbium is very rich even in such a narrow field interval. Experimental measurements have been performed up to much higher fields, and the density of ~ 3 resonances per gauss was observed for both mentioned isotopes [57, 29].

1.3 Bose Gas with Dipolar Interactions

Our planned experimental effort focuses on work with the bosonic isotopes of erbium. A Bose gas, cooled down sufficiently (typically to several 10s or few 100s of nK), will undergo a phase transition to the BEC. This state is characterised by the macroscopic population of the ground state. Under such conditions, a simple picture that describes the gas can be constructed using the notion of the condensate wave function and small excitations on top of the ground state. This provides a basis for theoretically exploring the influence of interactions and trapping geometry onto the behaviour of the system.

1.3.1 Gross-Pitaevskii Equation

Assuming a dilute bosonic gas with two-body elastic collisions only and a population of N atoms, the evolution of the system is described by the Heisenberg equation applied to the field operator $\hat{\Psi}(\mathbf{r}, t)$ in the scope of second-quantisation [63]:

$$i\hbar \frac{\partial}{\partial t} \hat{\Psi}(\mathbf{r}, t) = [\hat{\Psi}(\mathbf{r}, t), \hat{H}] = \left[-\frac{\hbar^2 \nabla^2}{2m} + V_{\text{trap}}(\mathbf{r}) + N \int \hat{\Psi}^\dagger(\mathbf{r}', t) V_{\text{int}}(\mathbf{r}' - \mathbf{r}) \hat{\Psi}(\mathbf{r}', t) d\mathbf{r}' \right] \hat{\Psi}(\mathbf{r}, t). \quad (1.11)$$

The field operator can be represented in terms of a collection of single particle states and the associated ladder operators:

$$\hat{\Psi}(\mathbf{r}) = \Psi_0(\mathbf{r}, t) \hat{a}_0 + \sum_{n \neq 0} \psi_n(\mathbf{r}, t) \hat{a}_n. \quad (1.12)$$

When the gas is condensed, the majority of the atomic population resides in the lowest lying state Ψ_0 , so the non-commutativity of operators \hat{a}_0 and \hat{a}_0^\dagger can be neglected³ and both \hat{a}_0 and \hat{a}_0^\dagger can be safely substituted by a c-number $\sqrt{N_0}$. If additionally the occupations of the excited states ψ_n are altogether neglected, this yields the Gross-Pitaevskii equation (GPE)

³The commutation relation for the bosonic ladder operators specifies $[\hat{a}_0, \hat{a}_0^\dagger] = \hat{a}_0 \hat{a}_0^\dagger - \hat{a}_0^\dagger \hat{a}_0 = 1$, while both $\hat{a}_0 \hat{a}_0^\dagger$ and $\hat{a}_0^\dagger \hat{a}_0$ are of order $N_0 \gg 1$

for the condensate wave function in the mean field approximation:

$$i\hbar \frac{\partial}{\partial t} \Psi_0(\mathbf{r}, t) = \left[-\frac{\hbar^2 \nabla^2}{2m} + V_{\text{trap}}(\mathbf{r}) + \int \Psi_0^\dagger(\mathbf{r}', t) V_{\text{int}}(\mathbf{r}' - \mathbf{r}) \Psi_0(\mathbf{r}', t) d\mathbf{r}' \right] \Psi_0(\mathbf{r}, t) \quad (1.13)$$

where a factor of \sqrt{N} is now absorbed into the condensate wave function ($\Psi_0^{\text{new}} = \sqrt{N} \Psi_0^{\text{old}}$) for it to account for $N \approx N_0$ particles. In the case of a time-independent Hamiltonian, a stationary state can be found in the form $\Psi_0(\mathbf{r}, t) = \exp(-i\mu t) \Psi_0(\mathbf{r})$, where μ is the chemical potential of the gas. Similarly, given the condensate wave function, the energy of the system is calculated as:

$$E[\Psi_0] = \int \left[\frac{\hbar^2}{2m} |\nabla \Psi_0(\mathbf{r})|^2 + V_{\text{trap}}(\mathbf{r}) |\Psi_0(\mathbf{r})|^2 + \frac{1}{2} \int V_{\text{int}}(\mathbf{r} - \mathbf{r}') |\Psi_0(\mathbf{r}')|^2 |\Psi_0(\mathbf{r})|^2 d\mathbf{r}' \right] d\mathbf{r} . \quad (1.14)$$

1.3.2 Excitations and Roton Minimum

The GPE only describes the static properties of the condensate. Staying within the mean field picture, but allowing for small occupation probability of the excited states, i.e. writing the equation 1.12 as:

$$\hat{\Psi}(\mathbf{r}) = \sqrt{N_0} \Psi_0(\mathbf{r}) + \eta \delta\psi(\mathbf{r}, t) \quad (1.15)$$

for $\eta \ll 1$ constitutes the Bogoliubov approximation [63, 64]. This approach is used to predict excitation modes at low temperatures and it proceeds by defining a trial perturbation wave function in the form:

$$\delta\psi(\mathbf{r}, t) = u(\mathbf{r}) e^{-i\omega t} + v^*(\mathbf{r}) e^{i\omega t} \quad (1.16)$$

with an accompanying normalisation rule:

$$\int (|u(\mathbf{r})|^2 - |v(\mathbf{r})|^2) d\mathbf{r} = 1 . \quad (1.17)$$

If the ansatz from Equation 1.15 together with Equation 1.16 is plugged into the Heisenberg equation for the evolution of the system, keeping only terms up to $\mathcal{O}(\eta)$, a set of coupled

equations for the excitation modes is obtained:

$$\begin{pmatrix} H_{\text{GP}}[\Psi_0] + \hat{X} & \hat{X} \\ -\hat{X} & -H_{\text{GP}}[\Psi_0] - \hat{X} \end{pmatrix} \begin{pmatrix} u \\ v \end{pmatrix} = \hbar\omega \begin{pmatrix} u \\ v \end{pmatrix} \quad (1.18)$$

with \hat{X} being the exchange energy operator, which takes the form:

$$\hat{X}\chi(\mathbf{r}) = \int \Psi_0(\mathbf{r}') V_{\text{int}}(\mathbf{r}' - \mathbf{r}) \chi(\mathbf{r}') d\mathbf{r}' \Psi_0^*(\mathbf{r}). \quad (1.19)$$

In the case of the dipolar gas, the simplest, but still very informative result, that can be obtained using this approach, is the excitation spectrum of the homogeneous dipolar gas. If the condensate wavefunction is uniform and fills up all of space, it can be simply written as $\Psi_0 = \sqrt{n_0}$. The solution to the Bogoliubov equations gives the excitation spectrum [63]:

$$\omega(\mathbf{k}) = \sqrt{\frac{\hbar^2 k^2}{4m^2} \left(k^2 + \frac{4mn_0g}{\hbar^2} (1 + \epsilon_{\text{dd}} (\cos^2 \theta_{\mathbf{k}} - 1)) \right)} \quad (1.20)$$

with $\cos \theta_{\mathbf{k}} = \frac{k_z}{k}$ and $g = \frac{4\pi\hbar^2 a_s}{m}$. This equation leads to an interesting observation that the bulk dipolar gas will be unstable for $\epsilon_{\text{dd}} \leq 1$.

In a slightly more complicated setting of a planar-infinite system with harmonic trapping along the z -axis, applying the Bogoliubov theory reveals the roton feature in the excitation spectrum [65]. In this case the gas is assumed to be confined by the trapping potential $V_{\text{trap}} = \frac{m\omega_z^2 z^2}{2}$ and that the cloud density is sufficiently high such that the Thomas-Fermi (TF) approximation applies ($\mu \gg \hbar\omega_z$), where μ is the chemical potential. In this case, the condensate ground state is described by the TF profile in the z -direction and is otherwise uniform in the xy -plane, i.e. $\Psi_0(z) = n_0(1 - \frac{z^2}{L^2})$ with $L = \sqrt{\frac{2\mu}{m\omega_z^2}}$. The spectrum that is obtained after solving the Bogoliubov equations for $kL \gg 1$ takes the form:

$$\omega = \omega_z \sqrt{\frac{k^4 l_z^4}{4} + \frac{2(1 - \epsilon_{\text{dd}})(5\epsilon_{\text{dd}} + 1)}{3(2\epsilon_{\text{dd}} + 1)(4\epsilon_{\text{dd}} + 1)} \frac{\mu}{\hbar\omega_z} \frac{k^2 l_z^2}{2} + 1} \quad (1.21)$$

where $l_z = \sqrt{\frac{\hbar}{m\omega_z}}$. The dispersion relation for $kL \ll 1$ can be similarly calculated to be:

$$\omega = \omega_z \sqrt{\frac{2\mu}{3\hbar\omega_z} k l_z}. \quad (1.22)$$

Figure 1.5a shows an example spectrum obtained from this model, demonstrating the emergence of the roton feature for $\epsilon_{\text{dd}} > 1$. The softening of the excitation spectrum at

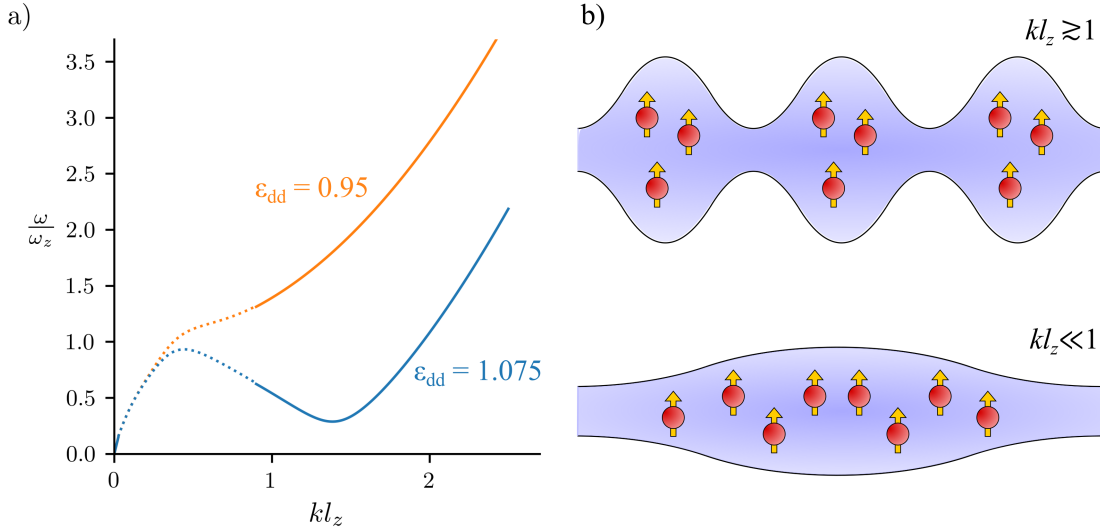


Fig. 1.5 **Roton Minimum** - a) The excitation spectrum of dipolar gas harmonically trapped in an infinite plane, modelled by the Equations 1.21 and 1.22 in the short and long wavelength limits for $\mu = 50 \times \hbar\omega_z$. The dotted lines serve as guides to the eye connecting the spectra across the interval where the models do not apply. The spectrum for $\epsilon_{dd} = 1.075$ contains the roton minimum whereas the $\epsilon_{dd} = 0.95$ line is monotonically increasing. b) A cartoon showing the effect of the short and long wavelength excitations on the density distribution (exaggerated) rationalising the reduction of the DDI energy at intermediate wave numbers due to the increased contribution of the attractive component of the force from the dipoles aligned roughly ‘head-to-tail’.

intermediate wave numbers can be rationalised by looking at the geometry of the density perturbations (see the cartoon in Figure 1.5b). The medium wavelength excitations ($kl_z \gtrsim 1$) lead to perturbations that make the atoms more likely to be aligned ‘head-to-tail’, involving excursions into the attractive domain of the DDI force. This is not the case for long wavelength oscillations ($kl_z \ll 1$) where the atoms mostly feel the repulsive part of the dipole force. Finally, at very short wavelengths ($kl_z \gg 1$) the kinetic term eventually overshadows the other components making the dispersion relation to tend towards the free particle dispersion ($\omega \propto k^2$). Therefore, the negative contribution from the DDI potential at intermediate wave numbers causes the overall energy to drop, creating the roton minimum.

1.4 Project Goals

One of the key messages the opening section aims to relate is the significance of ultracold atomic systems for the subject of quantum simulation and the key role of their versatility for such a qualification. Our vision is to combine the novel techniques of trapping atoms in uniform potentials with the long range and anisotropic nature of the dipole-dipole interactions provided by magnetic atoms to create a platform for exploring various aspects of many body physics. The design we are going for will enable us to tune the geometry of the optical box trap, as well as the strength and nature of the interactions.

A flattened BEC with sufficiently strong dipolar interactions exhibits a roton-like excitation spectrum [35, 36, 65] and will allow us to investigate the implications of these excitations on the behaviour of the gas, including its superfluid properties. Crucially, in such a system, both angular roton modes and vortices can be excited, enriching the accessible physics. A further consequence of the roton feature in the excitation spectrum is the dynamical instability it can induce and the supersolid phase [40–42], stabilised by quantum fluctuations, that can form as a result. We also plan to look closely at the properties and dynamics of this phase transition as well as the impact of the dipole-dipole interactions on the conventional phase transition to BEC. This is intended as an extension of the application of the Kibble-Zurek theory on ultracold atomic systems [23, 24]. As both the BEC phase transition and the formation of the supersolid are processes sensitive to atomic density, we consider the uniform trapping potential to be an important requirement for studying these processes in depth.

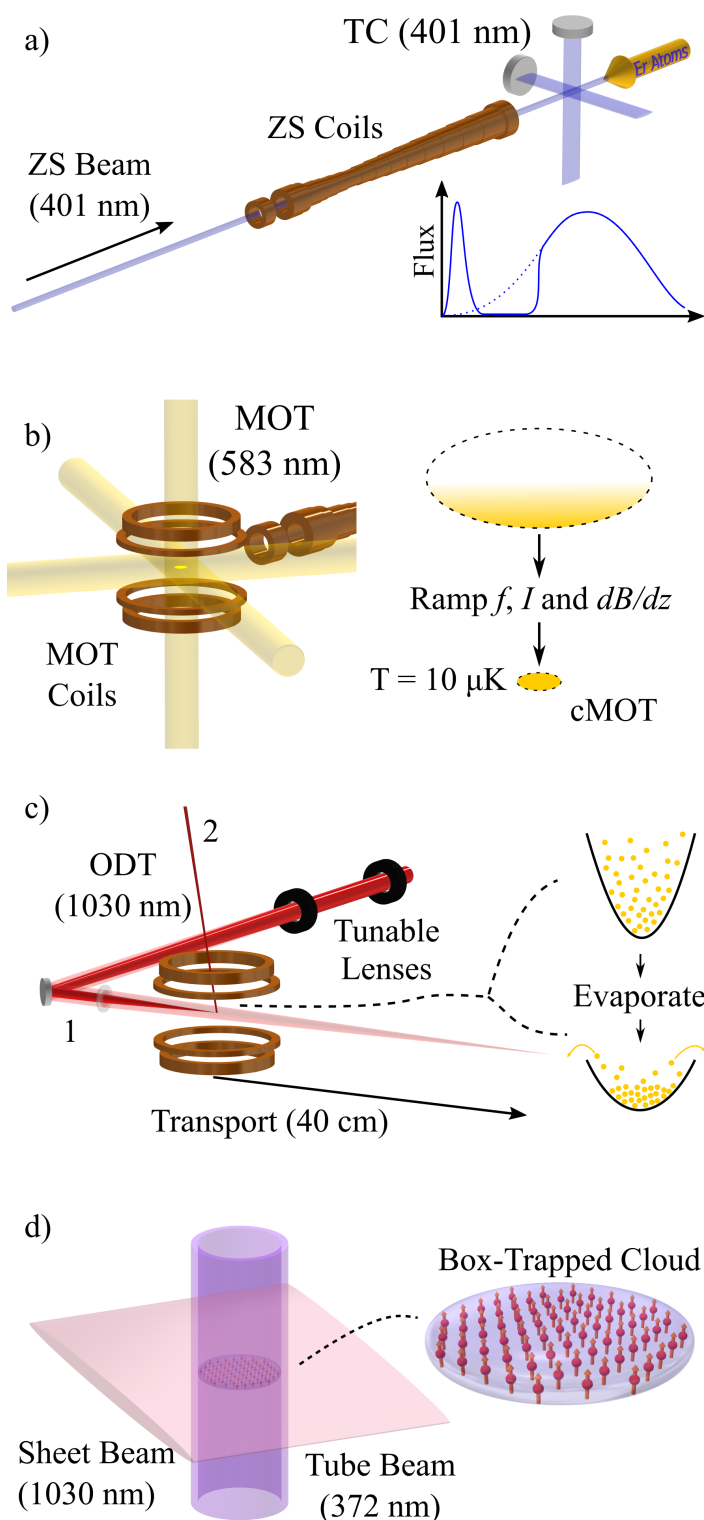
Following the addition of potassium as the second atomic species to the experiment, introducing impurities to the system will be another possibility for setting up experiments. Currently, we aim to investigate Bose polaron physics [66] and qubit decoherence in non-Markovian systems [67, 68].

Further details about the project plans are provided in Chapter 7.

1.5 Overview of the Experiment

There are several steps in the experimental sequence required to produce a quantum-degenerate gas of atomic erbium in the box trap. A brief summary of these steps, which have been the basis of our experimental design, is presented here with the aid of Figure 1.6. Due to high temperatures needed to achieve significant vapour pressure levels of erbium, atoms are sourced from an effusion cell oven typically operating at 1100 °C. It produces a collimated beam of hot atoms that are first subjected to 2D molasses cooling in the transversal directions (Transversal Cooling - TC), and then slowed down using a Zeeman Slower (ZS).

Fig. 1.6 Achieving Box-Trapped BEC - Outline of the cooling and trapping methods leading towards an erbium BEC trapped in an optical Box Trap: a) Zeeman Slower (ZS) slows the atoms emerging from the oven with velocities below a certain capture velocity. Total flux of slow atoms is enhanced with a 2D transversal Doppler cooling (TC); b) Narrow line Magneto Optical Trap (MOT) is loaded from the atomic beam with atoms slowed by the ZS. Low temperatures ($\sim 10\mu\text{K}$) are obtained by ramping the trap into the compressed MOT trap (cMOT), which also creates better overlap with the optical trap during subsequent transfer into the Optical Dipole Trap (ODT); c). The ODT is formed using a high power 1030 nm laser that is projected onto the atoms using an optical system incorporating a pair of focus-tunable lenses, and creates an attractive potential for the atoms. The focus of the trap can be translated across the length of 40 cm between the two experimental chambers. Also, prior to transport, evaporative cooling can be performed in a crossed optical dipole trap, created with an additional beam; d) Upon transport, the atoms will be transferred into the box trap that is made up from a hollow, tubular repulsive beam (372 nm) and a highly flattened elliptical sheet beam (1030 nm). This creates a trap with a high aspect ratio and a homogeneous in-plane trapping potential.



This technique targets atoms up to the capture velocity that typically lies at $\sim 350 \frac{\text{m}}{\text{s}}$ in the case of our setup, and slows them down to $< 10 \frac{\text{m}}{\text{s}}$. These initial stages of cooling employ the broad 401 nm atomic transition.

The slow atoms are loaded into the narrow-line Magneto-Optical Trap (MOT), operating on the 583 nm transition, where further Doppler cooling reduces the temperature to $\sim 10 \mu\text{K}$ and the atomic cloud is simultaneously compressed, preparing it for transfer into the Optical Dipole Trap (ODT). We use a high power 1030 nm laser to form an attractive, non-resonant optical trap. The main ODT beam (ODT 1) is projected using a setup incorporating focus tunable lenses, allowing the trapping potential well, that is formed in the focus of the beam, to be translated along the propagation direction. This technique is to be used to transport the atoms from the MOT chamber into the glass science cell where the box trap will be implemented. Prior to transport, an additional trapping beam (ODT 2) is overlaid with the main beam, to enhance the axial confinement of the trap in order to perform evaporative cooling. Finally, upon transport, the atoms will be transferred into the box trap, that is formed by a combination of a repulsive, hollow cylindrical beam trapping the atoms in the horizontal direction, and an attractive sheet beam for vertical confinement. The repulsive potential is provided by a 372 nm laser, that is blue-detuned w.r.t. the dominant atomic transition.

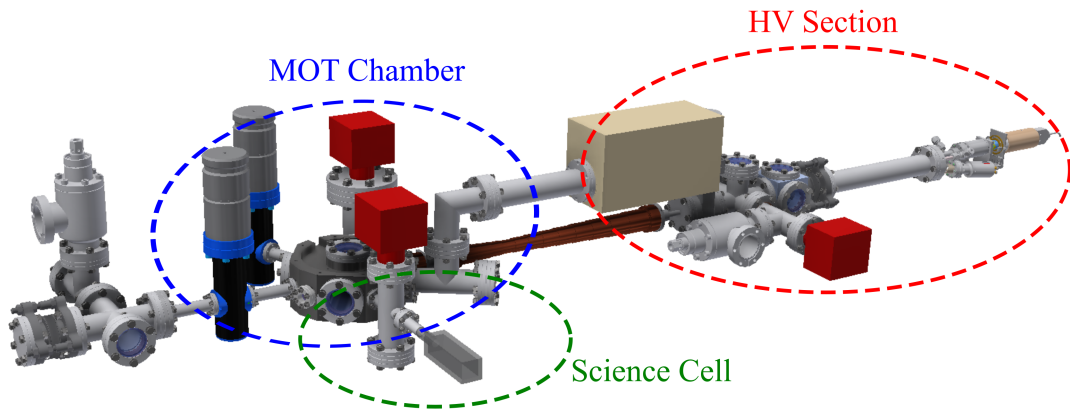


Fig. 1.7 Vacuum System Design - The vacuum chamber geometry we opted for consists of three distinct parts. The HV Section houses the erbium oven and viewports for transversal cooling and probing of the atomic beam. It is separated from the remainder of the system with a low conductance section to prevent the potentially high outgassing rate originating from the oven section having an impact to the pressure in regions where the atom clouds will be created and cooled. The MOT chamber is the central merging point of all the sections of the experiment, and the place where the main cooling steps will take place (MOT and evaporative cooling). As it consequentially lacks optical access for the box trap and measurement apparatus, we transport the atoms into an all glass chamber, referred to as the ‘science cell’. There, the box trap will be implemented, along with high-resolution imaging and probing and manipulation optical beams.

We have opted for a ‘three chamber’ layout in the design of our vacuum system that will accommodate all of the above (Figure 1.7). The reasoning for such a decision mainly revolves around separating the erbium oven section from the rest of the system using a low-conductance tube that can support a large pressure differential and would protect the ‘science’ section from potentially high outgassing rate originating from the heated parts of the oven. The second factor was the issue of optical access for probing and manipulation of the atoms, which led us to incorporate a transparent glass cell that will be the location of the box trap and all the experiments involving the gas trapped in it. In this configuration, after the initial stages of cooling are performed in the MOT chamber, the gas will be optically transported to the glass cell.

1.6 Contributions and Thesis Outline

The structure of the remainder of the thesis is outlined here, highlighting any collaborative work and contributions from colleagues from subject to subject:

- **Chapter 2** describes the vacuum system in the core of the experiment, from the design process to reaching the desired vacuum levels. A significant contribution to the work outlined there is the design of the magnetic field coils by Nathaniel Vilas.
- **Chapters 3 & 4** focus on the laser cooling methods applied to the oven generated atomic beam - transversal cooling and the Zeeman slower, and the subsequent narrow-linewidth magneto-optical trap, respectively. The setting up of the apparatus and a large fraction of performed measurements were done in collaboration with Dr Anna Marchant, with contributions from Nathaniel Vilas in the early stages of designing the laser systems. The data acquisition, storage and analysis software was written and maintained by Lucas Hofer, also resulting in a technical publication presented with this thesis in Appendix E.
- **Chapter 5** deals with optical trapping, transport and probing of the atoms. The design of the optical systems responsible for evaporative cooling and transport of the cloud into the ‘science’ chamber of the system, its confinement into the optical-box trap and the Bragg spectroscopy technique for recording the excitation spectrum are laid out there. The design of the trapping and transport setup was done by Péter Juhász, prototyping of the Bragg spectroscopy setup was a collaborative effort with Gloria Clausen, while the planning and prototyping of the optical box potential setup was done together with Lucas Hofer, Dr Anna Marchant and Daniel Ruttley.
- **Chapter 6** offers a look into a numerical simulation that explores the dependence of the stability and ground state properties of a trapped dipolar BEC on the confining geometry and strength of interactions. This was a joint effort with Péter Juhász, with contributions from David Strachan and Edward Gandar.
- **Chapter 7** discusses the progress achieved so far and covers the future projects planned on the experimental platform, including exploring roton physics, dynamics of phase transitions and dual species experiments with potassium atoms.

Chapter 2

Vacuum Chamber Design and Construction

This chapter discusses the design considerations for our vacuum chamber and presents an overview of its assembly and commissioning. The main design goals that guided this process are:

- Ultra-High Vacuum (UHV) conditions in the ‘science’ section of the experiment, with pressures below 10^{-11} mbar to ensure long atomic cloud lifetimes.
- High degree of optical access for the laser cooling and trapping methods to go from the atomic beam exiting the oven to an ultracold atomic cloud in the box potential, and to accommodate probing and measurement beams for future experiments.
- High stability and controllability of magnetic fields in and around the chamber. This includes the fields required for the Zeeman slower and the magneto-optical trap, bias fields for maintaining spin polarisation and tuning the interactions, and the ability to compensate any background fields and actively stabilise the field in the critical regions to milligauss levels.
- Sufficient flux in the atomic beam emerging from the erbium oven, leading to quick and efficient loading of the MOT to atom numbers of $\sim 10^8$ within several seconds.

In addition, we plan to add potassium as a second atomic species to the experiment, so space was designated to make that possible.

2.1 Design Considerations

The final design solution we converged to is a ‘three-chamber’ system consisting of the High Vacuum (HV) section mounting the erbium oven as the source of atoms, the MOT chamber, housing the majority of the laser cooling methods, and the glass science cell that, given the degree of optical access it offers, provides the versatility required for the multitude of future projects on this platform. The latter two regions need to be maintained at ultra-high vacuum conditions in order to achieve long atomic cloud lifetimes required for performing measurements. Hence, we often refer to these two sections together as the Ultra-High Vacuum (UHV) section. The HV and UHV sections are separated by a low conductance tube that simultaneously carries the Zeeman Slower (ZS) coils. The diagram showing details of this design is shown in Figure 2.1.

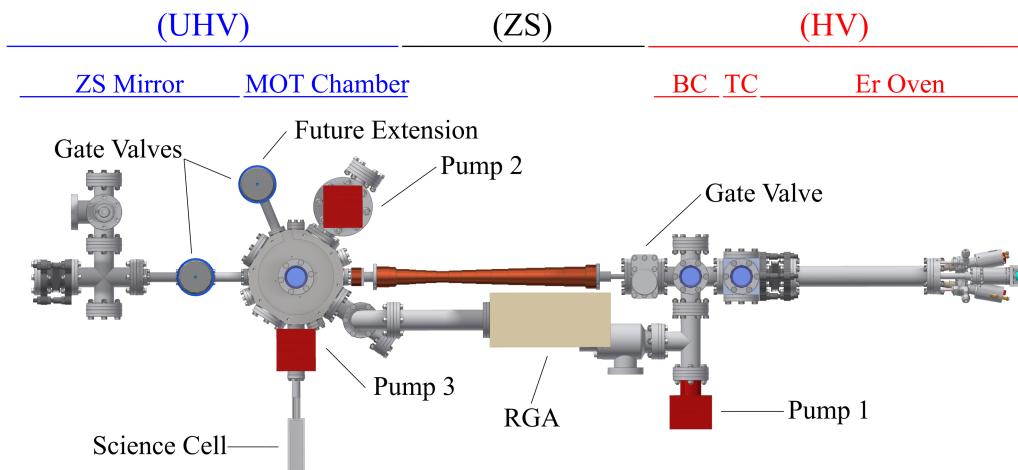


Fig. 2.1 **Vacuum Chamber Layout** - Top view of the vacuum system. The High Vacuum section (HV) consists of the effusion cell erbium oven, the cube with transversal cooling viewports (TC), the cross with optical access for atomic beam characterisation (BC) and connecting the vacuum pump. The Zeeman slower tube carries the magnetic field coils for the simultaneous laser cooling application and also maintains the pressure differential towards the Ultra-High Vacuum (UHV) section of the chamber. The latter consists of the MOT chamber, glass science cell for performing experiments, and connections for the ZS beam delivery system, the residual gas analyser (RGA) and the port for the future extension of the chamber (potassium 2D MOT).

The design process called for a series of calculations and simulations to aid and support decisions. Firstly, the atomic beam emerging from the effusion cell oven was modelled in a Monte Carlo simulation to gain better understanding of its propagation and the implications towards the chamber geometry and laser cooling methods. In parallel with that, we investigated the performance of different candidate solutions for the system of vacuum pumps, in terms of type, number and placement within the chamber. The model we used assumes the

molecular flow regime, and estimates ultimate pressure levels in different locations in the system taking into account the pumping speeds of vacuum pumps, background gas sources and chamber section conductances. Armed with experience gained from the results of these calculations, we created a blueprint of the chamber, also drawing inspiration from existing experiments of similar type [57, 62].

2.1.1 Modelling Pumping and Pressures

We decided to use the combined NEG¹-Ion pump elements in our system to reach the desired vacuum levels. This was motivated by the fact that this technology has the ability to pump all types of gases typically present in vacuum chambers, and is especially efficient in pumping molecular hydrogen gas, that is the dominant background component in stainless steel chambers. Although this significantly narrows down the options for pumps, the decision on the number of pumps and their pumping speeds and positioning still had to be made. Additionally, as our system incorporates an effusion cell oven² that requires very high temperatures³, above 1000°C, to generate an atomic beam with sufficient flux, we were concerned about the potentially high outgassing rates it would produce. Consequently, a low conductance section between the oven and the ‘science’ region of the experiment, that can support a pressure differential of at least two orders of magnitude, was set as one of the design goals.

The molecular flow model that we used in the calculations is presented in Appendix A, together with the justification of the assumptions made and the parameters used. As shown in Figure 2.2, the chamber is divided into 10 regions, and the molecular conductances, C_{ij} are estimated between all connected regions. Vacuum pumps are represented by their pumping speeds, S_i , whereas the background gas source terms, Q_i , are estimated based on assumptions about outgassing, permeation and leaks. As demonstrated in Appendix A, this allows us to draw an equivalent electrical circuit, where pressure levels correspond to voltages, and by solving it, obtain estimates for the equilibrium pressure values in different sections.

The design we ultimately converged to incorporates three vacuum pumps⁴ - one $100 \frac{\text{L}}{\text{s}}$ pump is mounted on the HV side, next to the start of the ZS tube, whereas on the UHV side, a $300 \frac{\text{L}}{\text{s}}$ pump is mounted on a large, DN63CF reducer cross adjacent to the MOT chamber, and another $100 \frac{\text{L}}{\text{s}}$ pump sits on the cross between the MOT chamber and the glass cell⁵. The locations of the pumps correspond to regions labelled 2, 6 and 9 in the drawing,

¹Non-Evaporable Getter

²See Section 2.1.2 for technical details about the effusion cell oven.

³For reference, the melting point of erbium is 1529°C

⁴The quoted pumping speeds are for H₂. Specifications for other relevant species are given in Appendix A.

⁵2 × Nextorr D 100-5 and Nextorr D 300-5 from SAES Getters

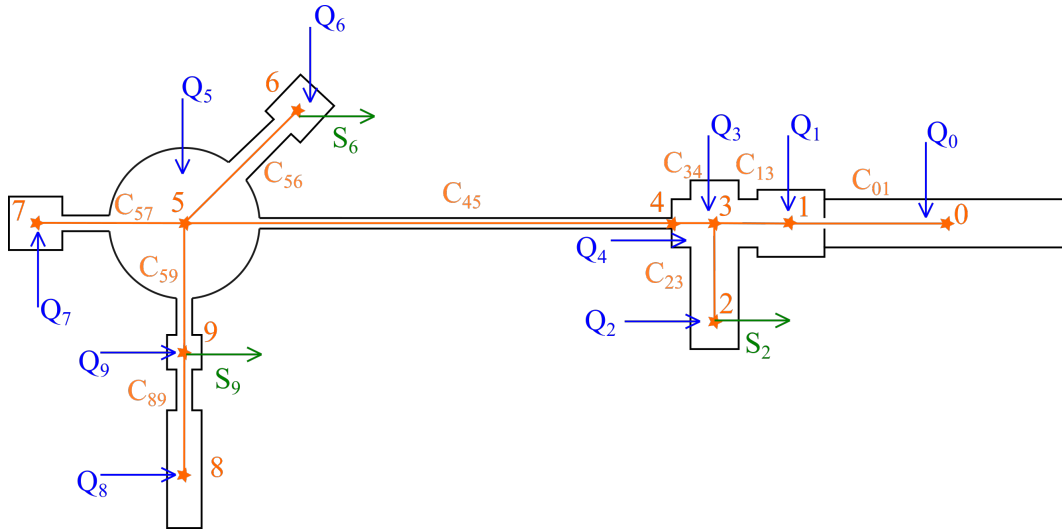


Fig. 2.2 **Molecular Flow Model** - A simplified representation of the vacuum system used to estimate pressures in different regions as a result of pumping. The model covers several gaseous components, and accounts for leaks, outgassing of hydrogen from chamber walls and permeation of helium through glass. The source input rates, Q_i , are calculated for each section based on geometry, number of connections and materials involved. The molecular conductances of different sections, C_{ij} , are also deduced from the geometry and the appropriate pumping speeds S_2 , S_6 and S_9 are assigned to the nodes housing the vacuum pumps.

respectively. The inner diameter of the ZS tube, that is used to maintain a pressure differential, is 8 mm, yielding a conductance of $0.41 \frac{\text{L}}{\text{s}}$ for molecular hydrogen at room temperature. The pressure estimates obtained for this configuration are $P_3 = 3 \times 10^{-11}$ mbar in the HV section, $P_5 = 3 \times 10^{-11}$ mbar in the MOT chamber and $P_8 = 1 \times 10^{-11}$ mbar in the science cell.

The above model does not account for any extra outgassing from the oven section, save for the usual contribution from the flange connection leaks and hydrogen gas desorption from the exposed stainless steel tubing⁶ around the oven. This is due to an uncertainty of how to model different outgassing sources present in that case. The oven is made of a number of materials, including tantalum, ceramics and steel, and it also goes through regular temperature changes between the stand-by temperature of 700°C and the working temperature of $\geq 1100^\circ\text{C}$. Instead, we approached the problem by querying the model for the equilibrium pressures in cases when the oven outgassing rate for hydrogen is set to progressively higher values (Figure 2.3). This test shows that going to narrower tube diameters than 8 mm does not bring much immediate advantage except in the case of extreme outgassing in the oven region, whereas larger diameters would visibly reduce the degree of protection provided by the differential pumping tube. As the chamber pressures are only

⁶The chamber encompassing the oven only heats up mildly, by several tens of degrees, when the oven is at the working temperature

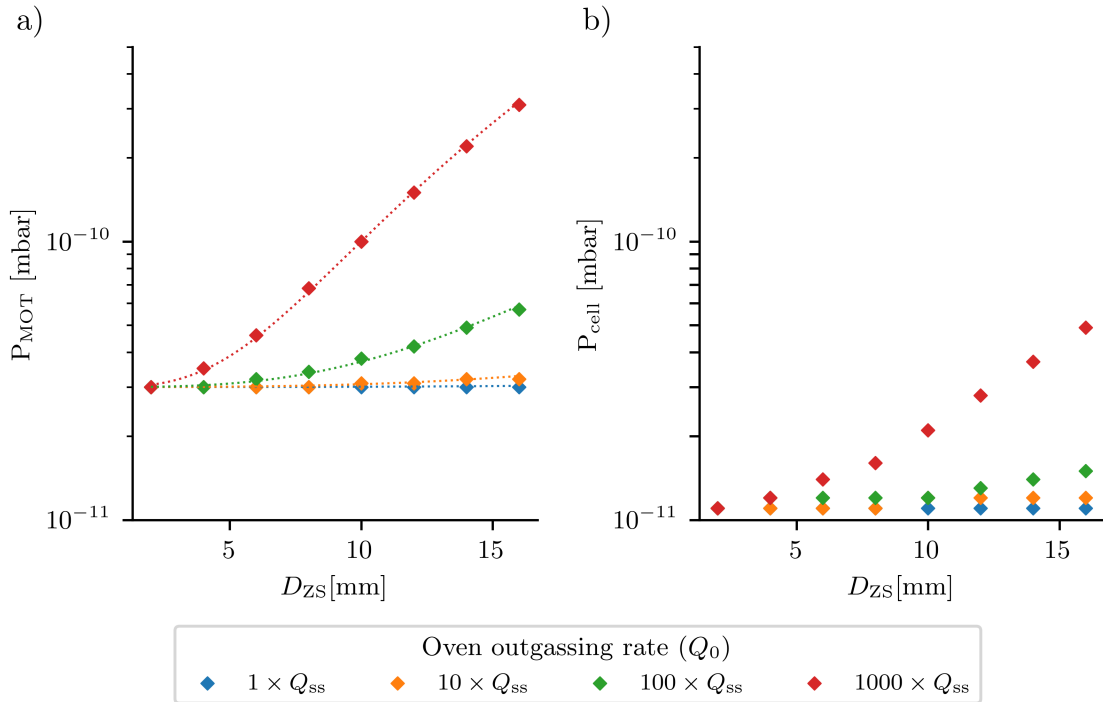


Fig. 2.3 **Differential Pumping** - Pressure estimate in the MOT chamber (a) and the science cell (b) for different outgassing rates in the oven section (set to multiples of $Q_{ss} = 5 \times 10^{-10} \text{ mbar L s}^{-1}$, which represents the outgassing rate stainless steel at room temperature). The dotted lines in a) represent fits of the function $P_{MOT} = P_{MOT}^{(0)} + A Q_0 D_{ZS}^3$ (with a unique value of $A = 1.4 \times 10^{-4} \text{ s}$), demonstrating the simple inverse scaling of the maximum achievable pressure differential with the tube conductance.

one of the factors relevant for this decision, it will be revisited in the next subsection from the perspective of the atomic beam flux. It is also worth noting that it is not only the oven outgassing that we will be protected against, but also the potential ramifications of the fact that this section of the chamber will have to be opened for maintenance (primarily for oven refilling). This will inevitably lead to a decrease in the NEG pump efficiency upon the exposure of an activated element to air and moisture, as well as increased surface desorption should the full bakeout of this section turn out to be impossible, e.g. due to equipment that is now in place nearby.

Two other major decisions that were aided by the molecular flow calculations concern the vacuum pumps in the UHV section. As the atoms should eventually be transported between the MOT chamber and the science cell, installing a cross with an additional pump along this path renders this task more difficult. On the other hand, the science cell is the region of the chamber where we wish for the lowest possible pressure. As the simulation estimates a fourfold increase in pressure in the science cell in the case without the pump, we deemed that installing it is worthwhile, even at the cost of more challenging optical

transport. Related to that, it was debated whether the pump in the cross next to the MOT chamber (position 6) should be the same as the other two, or a stronger model. Given that the molecular conductance between the cross and the MOT chamber is $C_{56} = 100 \frac{\text{L}}{\text{s}}$ ($30 \frac{\text{L}}{\text{s}}$) for H_2 (N_2), a pump with pumping speeds of $300 \frac{\text{L}}{\text{s}}$ ($100 \frac{\text{L}}{\text{s}}$) would perform significantly better than the weaker $100 \frac{\text{L}}{\text{s}}$ model. This is corroborated by the estimates obtained from the calculation that predict that the MOT chamber pressure would equilibrate at a 40% higher value if the latter pump option was used.

The ultimate measure of success of this feat would be a BEC lifetime sufficiently longer than the period of one experimental cycle (~ 10 s). Although we have not been able to check this directly yet, there are positive indications that make us believe that we are on track to achieve this goal. Ever since the chamber was pumped down to vacuum and heat-treated in the bakeout process, the ion pump pressure gauges on all three pumps maintained a reading below their detection level of 1×10^{-10} mbar. Additionally, a more convincing and direct confirmation was the lifetime of the atomic cloud in the MOT that was measured to be in the range of 30 – 50 s with strong indications it is limited by light-assisted molecule-forming collisions rather than the background gas pressure (see Subsection 4.4.3).

2.1.2 Effusion Cell and the Atomic Beam

The effusion cell oven⁷ consists of a tantalum crucible⁸, housing the solid erbium material, that is heated to high temperatures to increase the vapour pressure, and has a system of two heated apertures that produce a collimated atomic beam. The geometry of the oven assembly with detailed dimensions is given in Figure 2.4. The region of the crucible with the second aperture, the ‘hot lip’, can have its temperature independently controlled by a separate heater filament, and primarily serves the purpose of limiting the flux of divergent atoms and preventing material build-up on the second aperture. The third aperture, in the form of a bored copper gasket, is installed at the first flange connection after the oven to block the most divergent atoms. This oven and aperture geometry was also used in [57]. A shutter, operated via a mechanical feed-through, can be used to block the atomic beam in front of the exit aperture of the oven. In our design, the oven is mounted to a port aligner, that would allow any tilt of the oven to be corrected, followed by a cubic chamber with viewports for transversal cooling (TC). It is further followed by a 6-way cross, connecting the vacuum pump⁹ and the rough pumping port, and also carrying three auxiliary viewports

⁷Dual Filament Cell, model DFC-40-10-WK-2B-SHE, from *Createc*

⁸Melting point of tantalum is 3017 °C

⁹Nextorr D 100-5

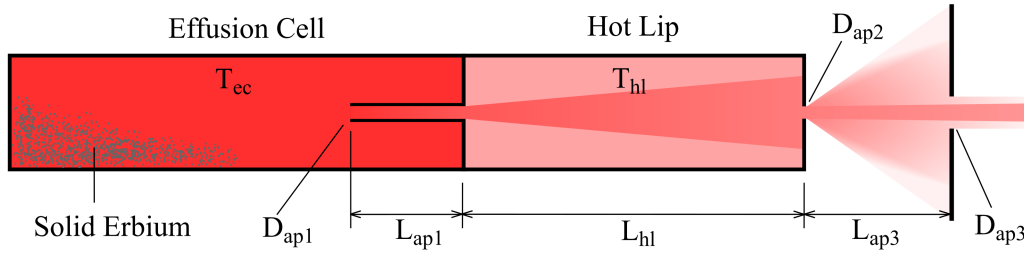


Fig. 2.4 **Effusion Cell Oven Geometry** - A set of three apertures, two of them integrated into the oven and thereby heated, are used to produce a collimated atomic beam. The first aperture, leading from the effusion cell where the solid erbium is evaporated, has tubular geometry with $D_{ap1} = 3$ mm and $L_{ap1} = 30$ mm. The hot lip section of length $L_{hl} = 50$ mm mounts the second aperture, with $D_{ap2} = 3$ mm, that collects the highly divergent atoms, and is kept at a further elevated temperature to prevent material accumulation. Finally, a third aperture, in the form of a copper gasket with a $D_{ap3} = 8$ mm bored hole, is mounted in front of the oven, $L_{ap3} = 33$ mm from the exit aperture of the hot lip. This aperture stops the atoms with no chance of reaching the MOT chamber, that make up about 96% of the total flux.

for spectroscopy and measurements on the atomic beam. Finally, the path of the atomic beam proceeds through the ZS tube into the MOT chamber.

The oven requires water cooling to prevent excessive heating of the surrounding chamber and enhance the responsiveness of the temperature control loop. The cooling water is supplied via a closed loop system built around a commercial central heating water pump and also incorporates a secondary loop with an additional pump activated via an interlock circuit as a fail-safe.

I wrote a numeric simulation that models the atomic beam emerging from the oven and propagating towards the MOT chamber. The assumptions and physical considerations that feed into this simulation are presented in Appendix B. This program was used to gain a better understanding of the flux profile of the atomic beam and its implications towards the design of the laser cooling methods and chamber geometry. The centrepiece of the simulation is a molecular flow model of the effusion cell oven that creates a Monte Carlo sample of the emerging atoms and calculates the associated flux. In the work presented here, we use a set of five samples containing 2×10^6 atoms each, generated at effusion cell temperatures in the $T_{cc} = 1000 - 1200$ °C range. The model assumes that the vapour pressure in the cell is given by the Antoine equation¹⁰ [57, 69]:

$$p_{\text{vap}}(T_{cc}) = 10^{A - \frac{B}{C + T_{cc}}} \text{ mbar} \quad (2.1)$$

which is then used to seed the sample atoms and normalise the calculated fluxes.

¹⁰The empirical coefficients for erbium are $A_{Er} = 7.103(4)$, $B_{Er} = 12170(20)$ K and $C_{Er} = -173(2)$ K.

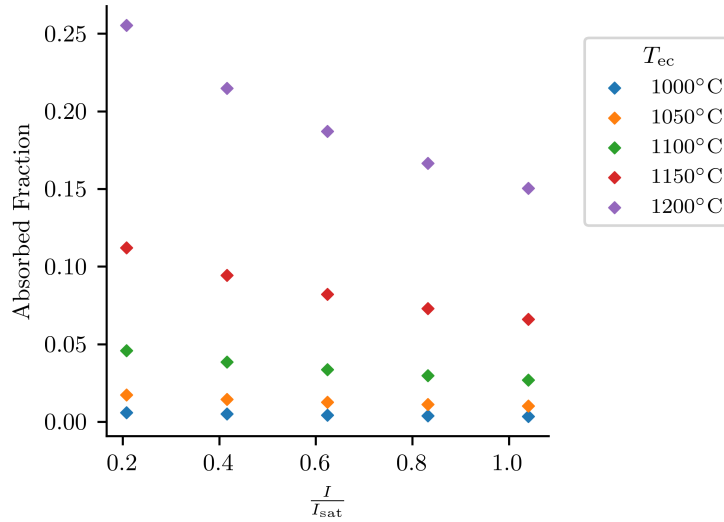


Fig. 2.6 **Light Absorption in TC** - The atomic beam numerical simulation was used to estimate the fraction of photons from the TC beams absorbed by the passing atoms. The figure presents the results for a range of beam powers used and temperatures between 1000 °C and 1200 °C. At temperatures above 1100 °C the attenuation of the beams becomes significant which renders the use of retro-reflected beams impractical. Also, this corroborates the initial reasoning for using the third aperture after the oven to prevent the useless divergent atoms from entering the TC region and thereby increasing absorption of cooling light. Here, the isotope abundance of ^{166}Er was used to normalise the atomic flux.

damage within the oven assembly caused by thermal stresses during temperature ramps¹¹. This is due to be addressed in maintenance planned for the near future. In Figure 2.5b, the estimated lifetime of the 8.0g sample of erbium metal loaded into the oven is shown. At the working temperature of $T = 1100$ °C, this should allow for at least 2.5 years of active running¹². The figure also contrasts the oven aperture design we use (from Figure 2.4) with a simpler design that does not employ the tubular aperture in the effusion cell. It clearly shows how the latter oven design leads to a weakly collimated beam with a larger total flux, but smaller number of usable atoms, which would require yet larger temperatures to reach sufficient MOT loading rates, leading to impractically short material lifetimes.

To demonstrate the importance of stopping the divergent atoms by employing the gasket aperture, we estimate the fraction of absorbed photons from the TC beams. The scattering

¹¹Ideally, we would only bring the oven down to room temperature in exceptional circumstances. Unfortunately, a series of long power cuts, need to replace faulty touch-screens in the oven controller and the Covid-19 lockdown forced us to do this several times, likely causing the decrease in flux. One power cut incident stands out as we were left unnotified about it for hours, which led to the draining of our emergency power supplies and a brief period of uncontrolled cooling of the oven. We have since installed additional protection in the form of an interlock system that initiates a controlled rampdown in the case of a prolonged power outage.

¹²The oven is kept at a standby temperature of $T = 700$ °C while the experiment is not in use.

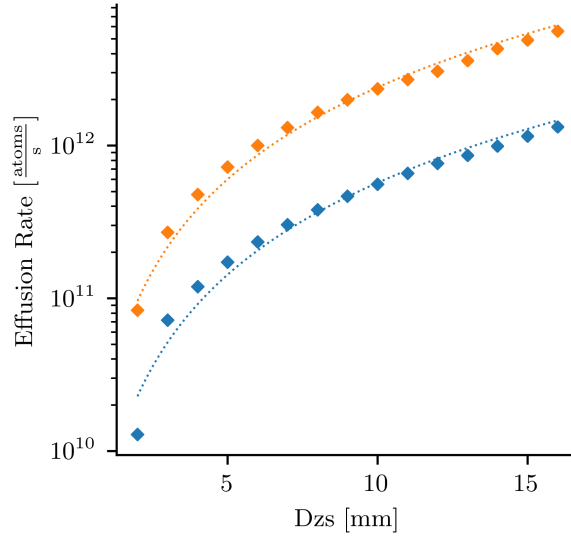


Fig. 2.7 **MOT Chamber Atomic Flux** - To aid the decision for the ZS tube diameter, we use the numerical simulation to estimate the atomic flux in the MOT chamber over a range of sizes. The data is shown for a simulation involving TC (40 mW per beam, corresponding to $\frac{I}{I_{\text{sat}}} \approx 0.8$, orange markers) and without it (blue markers). The flux shows the expected scaling proportional to the solid angle at which the end of the ZS tube is seen from the oven (fits corresponding to this scaling are shown as dotted lines). Note that the cited fluxes are for the full set of isotopes.

events are counted up for a sample of atoms, scaled appropriately to the flux represented by the sample and then compared to the total available rate of incoming photons, $R_{\text{tot}} = \frac{P_{\text{tot}} \lambda}{hc}$. The results presented in Figure 2.6 suggest that at the working temperature of $T = 1100$ °C, the absorption level is at 3 – 5% depending on the beam power, which is non-negligible, but still sufficiently low to permit the usage of retro-reflected beams in TC. At higher temperatures, the atomic flux would be sufficient to significantly reduce the intensity of the reflected beam, rendering the TC stage imbalanced and leading to a transversal velocity bias. Similarly, if the gasket-aperture had not been installed, the larger flux resulting from the excess divergent atoms would have led to a much greater beam attenuation. The negative effects of such a situation are well illustrated in Section 3.3 where the same symptoms result from faulty viewport coatings. In that case, the beam power was reduced by 25% – 40% in the retro-reflected branch, and the resulting velocity bias completely annuls the positive effects of the TC.

Another important consideration, that is also related to the pressure management and differential pumping discussions from Section 2.1.1, concerns the impact of the ZS tube diameter, D_{zs} , on the atomic flux that can reach the MOT chamber. As Figure 2.7 suggests, the flux of potentially loadable atoms scales approximately as D_{zs}^2 , i.e. the solid angle corresponding to the end of the tube from the point of view of the oven. This poses a clear

trade-off where wider tube diameters allow for a greater number of atoms to pass to the MOT region, but offer a weaker differential pressure margin. The combined results from Figures 2.7 and 2.3 convinced us that $D_{zs} = 8\text{ mm}$ is a good compromise. A lesser, but not insignificant factor was also the architecture of the ZS magnetic coil, that would require more windings or higher currents, in order to produce the required field profile if the tube was made thicker.

2.2 Magnetic Field Control

Magnetic fields are employed for a wide set of purposes in our experiment. Laser cooling techniques - the MOT and the ZS - require particular field profiles to create a spatially variable detuning for the respective atomic transitions. Homogeneous offset fields are also required for maintaining the spin polarisation of the atoms, tuning interactions and controlling the position of the MOT cloud. Finally, as erbium is a strongly magnetic atomic species with closely spaced Feshbach resonances (see Figure 1.4, and also [29]), any spurious noise and offsets in the magnetic field need to be cancelled out, ideally down to milligauss level ¹³, to fully isolate the atoms from the surroundings.

For this set of purposes, we implement a range of magnetic field coils around the vacuum chamber. The coils installed so far [70], surrounding the MOT chamber, are shown in Figure 2.8a, and the design of the science cell coils will follow in the near future. As the field stability is particularly important in the region around the science cell and the MOT chamber, the majority of stainless steel chamber components in the immediate vicinity are manufactured out of 316LN stainless steel, that has a particularly low magnetic permeability (typically $\mu_r - 1 \sim 10^{-3}$) and these components are highlighted in Figure 2.8b. Furthermore, both the breadboard on which the experiment was assembled, and the optical table on which it is now mounted are made of non-magnetic materials (aluminium and 316L stainless steel).

The Zeeman slower system consists of six coils, three of which comprise the characteristically shaped Profile (and Bias) field coil in the ‘spin-flip’ configuration. An additional coil is used to adjust the field at the end of the slowing trajectory and a pair of compensation coils is used to cancel any residual field offsets and gradients originating from the remainder of the ZS system. All details about the design and implementation of the Zeeman slower are laid out separately in Section 3.4.

The MOT chamber is equipped with four sets of coils. The gradient coils, that are in near-anti-Helmholtz configuration and the bias coils, in near-Helmholtz configuration, are

¹³Which will be achieved through active feedback using the set compensation coils and employing a high resolution 3-axes magnetometer probe (Honeywell HMC2003).

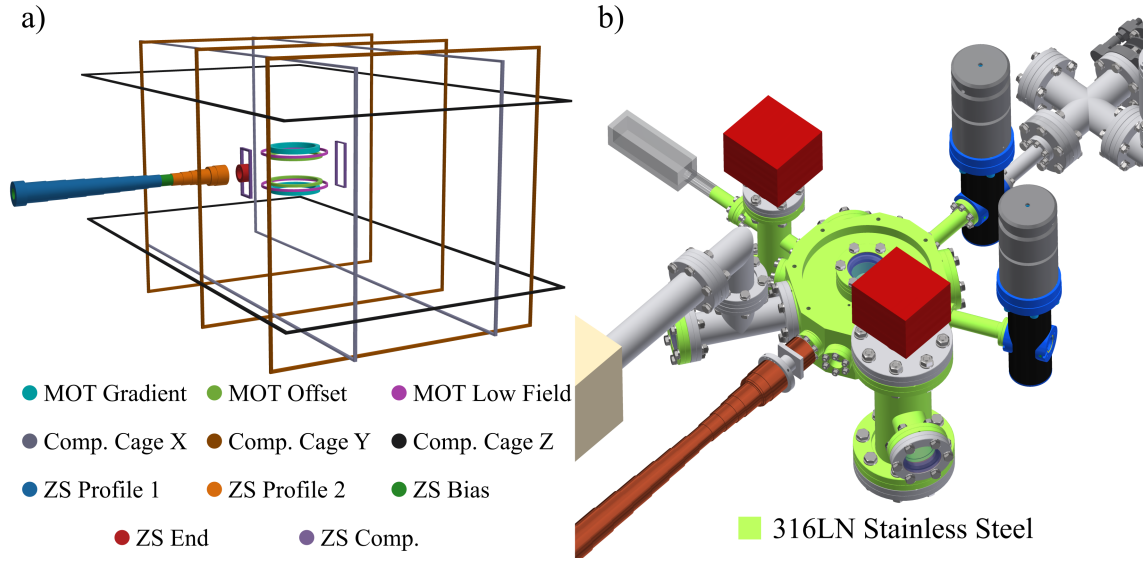


Fig. 2.8 **Magnetic Fields** - a) The collection of magnetic field coils surrounding the MOT chamber. This includes the Zeeman slower coil system including a pair of small compensation coils that mitigate for any residual field at the MOT position originating from the ZS. The MOT chamber itself is fitted with a gradient coil required for cooling, and two offset coils for fine and coarse adjustments. Finally, a large compensation cage surrounds the chamber and can be used to apply uniform fields along all three directions. b) In order to have a full control over the fields, we designed the majority of steel parts in the critical regions around the MOT chamber and the science cell to be made from 316LN stainless steel, that has a very low magnetic permeability. These components are shown in light-green.

Coil	Quadrupole	Offset	Low Field
Windings	6×4	6×2	2×2
Radius (Inner)	44.0 mm	49.3 mm	65.8 mm
Distance (Inner)	36.6 mm	24.0 mm	31.0 mm
Thickness (R)	8.1 mm	8.1 mm	2.7 mm
Thickness (H)	10.4 mm	5.2 mm	5.2 mm
Field	$833 (-416) \frac{\text{mG}}{\text{cm}} \frac{\text{cm}}{\text{A}}$	$2.0 \frac{\text{G}}{\text{A}}$	$535 \frac{\text{mG}}{\text{A}}$
Resistance	78 m Ω	46 m Ω	18 m Ω
Inductance	150 μH	50 μH	10 μH

Table 2.1 MOT Chamber Coil Specifications

intended for controlling vertical field gradient and offset. The gradient field is essential for the operation of the MOT, whereas the offset field can be used to control the vertical position of the MOT, and in the future, the scattering properties of atoms via Feshbach resonances. In

addition to these, there is also a pair of lower-current ‘fine’ offset coils, and a single loop RF antenna (coaxial with the remaining coils, not pictured in Figure 2.8a). The geometry and field characteristics of these three pairs of coils, stemming from the design done by a colleague [70], are given on Table 2.1.

Coils	X	Y	Z
Windings	6×4	6×4	6×4
Width	482 mm	515 mm	560 mm
Length	977 mm	540 mm	1 010 mm
Distance	288 mm	286 mm	336 mm
Field	$664 \frac{\text{mG}}{\text{A}}$	$744 \frac{\text{mG}}{\text{A}}$	$583 \frac{\text{mG}}{\text{A}}$
Resistance	3.3Ω	2.4Ω	3.6Ω
Inductance	3.5 mH	2.3 mH	3.8 mH

Table 2.2 Compensation Cage Coil Specifications

The entire UHV section of the vacuum chamber is encapsulated inside the compensation cage - a set of seven¹⁴ large rectangular coils, 24 windings each. It is designed to be used for active compensation of magnetic field noise, as well as for applying bias fields, primarily during optical transport to maintain the polarisation of the atomic cloud. The geometry was optimised for field uniformity, which had a direct impact on the size, and therefore on the frequency response specifications of this system. Therefore, we are considering the introduction of a more compact set of local compensation coils in the science cell region that would enable field control at higher frequencies (> 1 kHz). Dimensions and field parameters of the compensation cage are presented in Table 2.2.

The coils designed and built so far allow for the implementation of the laser cooling techniques, background field compensation, and implementation of bias fields in the MOT chamber and during transport. The entire coil system for the science cell remains to be added.

¹⁴The direction along the transport path (Y) is addressed by three coils, as a pair of coils cannot provide sufficiently uniform field along the full length between the MOT chamber and the science cell.

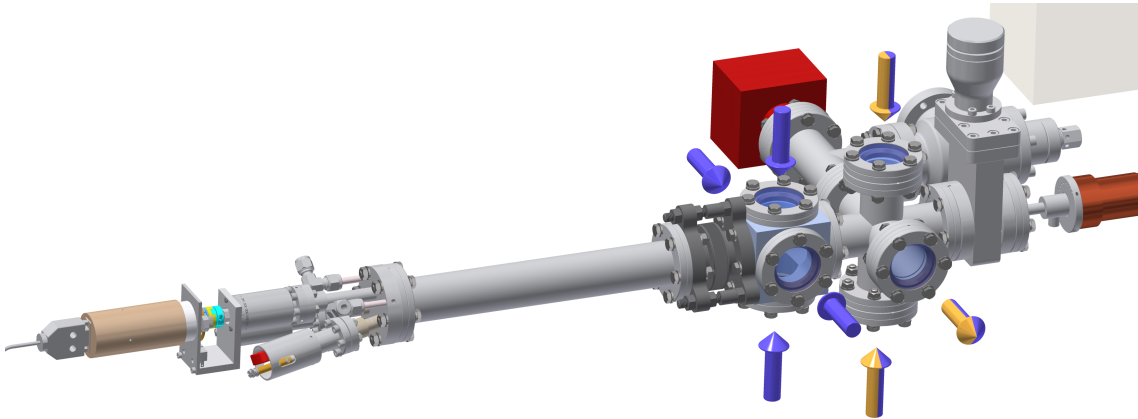


Fig. 2.9 **Optical access for Transversal Cooling and Fluorescence measurements** - A set of four viewports mounted on the cube immediately after the oven provides the optical access for transversal cooling. The available clear aperture is 35 mm. The cross mounted adjacent to the TC cube gives opportunity for fluorescence or absorption measurements on the atomic beam.

2.3 Optical Access

The range of techniques for manipulation and imaging of atoms in our experiment calls for lavish optical access to the chamber. This has greatly influenced the final shape of the chamber, especially the design of the 14-port MOT chamber and implementation of a separate glass science cell, as well as the large number of different anti-reflection coatings used on chamber viewports¹⁵.

2.3.1 HV Section

In the HV section of the chamber shown in Figure 2.9, straight after the erbium oven, we perform transversal cooling of the atomic beam, by crossing orthogonally two retro-reflected elliptical laser beams, addressing the 401 nm transition in erbium. Following that, a 6-way cross is fitted, carrying three auxiliary viewports for spectroscopy and measurements on the atomic beam. The details about implemented optical coatings are given in Table 2.3. After repeated usage of these viewports for fluorescence measurements, we realised that leaving space for a viewport on the rear side of the cross would have been useful, as it would allow for a mirror to be placed behind it to collect twice the amount of the fluorescence light.

¹⁵All viewports are manufactured by Torr Scientific, excluding the ones designated for ‘Atom Beam Probing’ in the HV section (see following footnote)

Designation	Qty.	Position	Fig.	Size	AR Coating
Transversal Cooling	4	HV Section	2.9	34 mm	401 nm
Atomic Beam Probing	3	HV Section	2.9	34 mm	Unknown ¹⁶

Table 2.3 HV Section Anti-Reflection Coatings

2.3.2 UHV Section

The MOT chamber is the central part of the experimental apparatus where the other sections merge and it also provides optical access for the MOT beams, optical transport, imaging and the Zeeman Slower beam (Figure 2.10, also see Table 2.4 for information about AR coatings). We opted for a solid block chamber design with 12 flange connections (4x DN40CF & 8x DN16CF) in the horizontal plane and two DN40CF in the vertical plane. On its top and bottom side it has 20 mm deep grooves machined around the flanges to house the magnetic field coils. Also, it has eight holes on either side, symmetrically arranged around the collar, to act as support points for the chamber itself, as well as the optics and coils mounted around the chamber.

Designation	Qty.	Position	Fig.	Size	AR Coating
MOT - Vertical	2	MOT Chamber	2.10	34 mm	583 nm, 767 nm, 1030 nm
MOT - Horizontal	4	MOT Chamber	2.10	34 mm	583 nm, 767 nm
ZS Beam Input	1	UHV Section	2.10	34 mm	401 nm
Imaging	2	MOT Chamber	2.10	15 mm	401 nm, 767 nm
ODT and Transport	1	MOT Chamber	2.10	15 mm	1030 nm, 1570 nm
Auxiliary	1	MOT Chamber	2.10	15 mm	Uncoated

Table 2.4 UHV Section Anti-Reflection Coatings

A rectangular glass cell¹⁷ is fitted on one side of the MOT chamber to provide good optical access for performing the experiments. An all-glass chamber means that we have access from almost all directions, which leaves great freedom in the design of the optical systems around it, and also a good degree of flexibility for any future alterations. On the other hand, we decided against AR coating the science cell as optical access will be required

¹⁶These viewports have been recycled from a vacuum chamber no longer in use and hence the coatings are unknown. We measured the transmission for a single viewport to be $\sim 94\%$ at the wavelength of 401 nm

¹⁷30 mm \times 30 mm \times 100 mm cell with 2.5 mm thick walls, made from Boroflat glass by Precision Glass-blowing

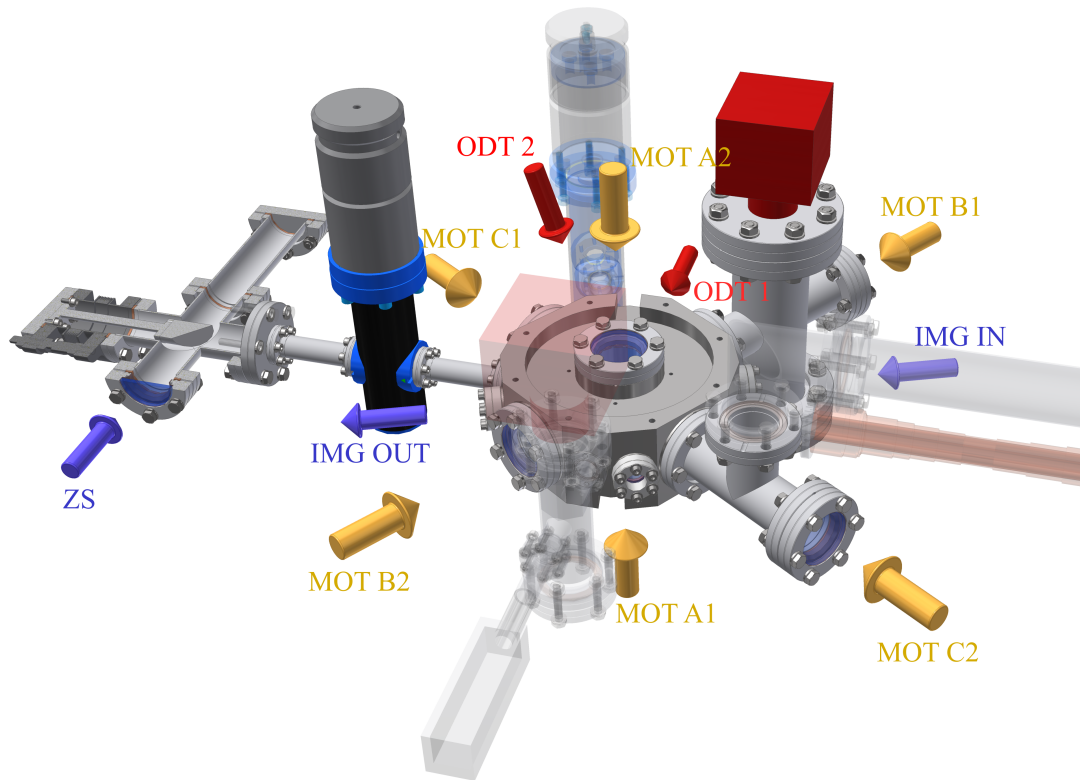


Fig. 2.10 **Optical access to the MOT chamber** - The chamber houses 14 ports in total. The six DN40CF viewports with a 34 mm clear aperture diameter provide access for the MOT beams. The A1-2 MOT viewports are also used for a crossed optical dipole trap beam (ODT2). The chamber additionally has four DN16CF viewports: (15 mm clear aperture diameter) for the optical dipole trap and transport beam access (ODT1), absorption imaging (IMG IN/OUT) and an auxiliary viewport (sometimes used for fluorescence imaging). Finally the chamber extension shown in half-section view is the entry point of the Zeeman Slower beam (ZS) that is subsequently reflected off a in-vacuum mirror. The information about the anti-reflection coatings implemented in this chamber section is presented in Table 2.4.

from various angles of incidence and over a very wide interval of wavelengths. In that case, coating the cell which improves performance for certain beams will necessarily impair the reflection properties for some other beams. In order to achieve a good atomic cloud lifetime in final trap, we decided to include a reducer cross with a vacuum pump between the MOT Chamber and the science cell. This sets the total distance over which the atoms need to be transported at approximately 40 cm.

The ZS laser beam needs to be directed into the path of the atoms off a mirror, as the incoming atoms are being deposited on the first surface they encounter, precluding the usage of a viewport for this purpose (according to quick estimates, a mono-layer of erbium atoms would form on a viewport after a day of operating the experiment). On the other hand, the deposition of erbium on the mirror does not affect its performance significantly, as observed

on similar experiments [57, 62] and also confirmed in our case after extended usage. For this purpose we use a solid aluminium mirror with a UV-enhanced, polished and coated surface¹⁸. It is fixed on a post resting on a flange mounted on a port aligner, giving an additional degree of freedom for coarse alignment (see Figure 2.10). The base of the post that is flush with the blank flange has a pattern of grooves etched into it to prevent any air pockets from getting trapped, causing virtual leaks. This section is also valved off in case mirror maintenance is required at some point over the lifetime of the experiment.

2.4 Vacuum Chamber Assembly

Putting together a complex vacuum chamber while ensuring structural integrity, and avoiding contamination is a delicate task. Fortunately, plentiful written material and unwritten procedural experience has accumulated among experimental physicists, which we chose to follow. Naturally, this all was seasoned with a pinch of improvisation where necessary. This section, along with Appendix D, aims to give insight into this daunting but interesting process, and hopefully leave some useful advice for colleagues in the field.

The first part of the system that was put together was the HV section, save for the effusion cell oven and the vacuum pumps to avoid exposing them to moisture for prolonged periods (they all arrived with flanged covers keeping them under vacuum), and viewports to protect the AR coatings from mechanical damage. The ZS mirror branch of the chamber was completed next, and after the compensation cage was positioned into place, the MOT chamber was connected to it. The remaining branches around the MOT chamber followed, with the ZS tube being the last part to be added, aligning the direction of the atomic beam in the process. When tightening the flange connection between the ZS tube and the MOT chamber, care was taken not to introduce stress by stretching the tube between the two supported parts, by carefully lifting the HV section allowing any tension to relax. Only after the passive chamber components were all assembled, the viewports, pumps and the oven were installed.

The oven was filled with 8.0 grams of erbium following the instructions from the manual and also the detailed description of the procedure given in [57]. The erbium metal¹⁹ was cut into small pieces, less than 3 mm in size, using clean wire cutters. The tantalum crucible of the oven was filled with erbium and assembled by fixing the apertures and the hot lip section in place. The crucible was then carefully inserted into the body of the oven, watching out

¹⁸Custom mirror by Thorlabs, mirror surface and coating equivalent to F01 UV Enhanced Aluminium mirrors.

¹⁹Distilled dendritic erbium from Alfa Aesar

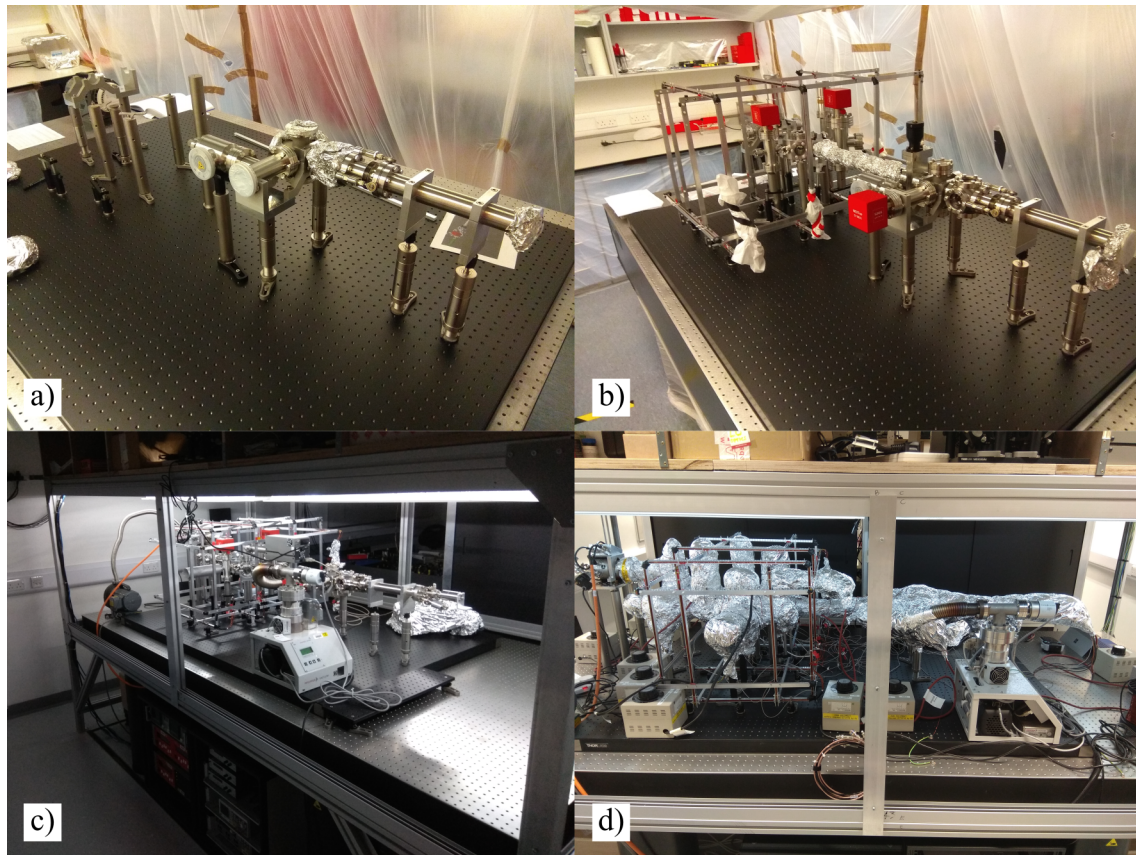


Fig. 2.11 **Chamber Construction and Pumpdown** - a) Initial steps in assembly; b) Mostly assembled chamber; c) Fully assembled chamber with turbo pumps attached; d) Chamber wrapped in heaters and insulation during the bakeout.

for the brittle ceramic discs holding the oven heaters, and then fixed in place using tantalum wire.

During assembly, at the stage when the viewports on the MOT chamber²⁰ were being installed, it was observed that some of the bolts holding the flanges were slipping inside the tapped holes. This prevented us from establishing leak-proof connections as the screws could not be tightened sufficiently. After the examination of the affected tapped holes, it was observed the threads were too shallow in the radial direction. The internal diameter of the threads was measured to be between 5.5 mm and 5.7 mm, instead of 5.0 mm as prescribed for standard M6 tapped holes, in all 24 holes on the DN40CF flanges in the horizontal plane of the MOT chamber²¹. With the help and advice of the student workshop supervisor at

²⁰Custom 316LN stainless steel chamber made by Scanwel.

²¹We have not been able to determine the exact cause of this defect, even after speaking to the manufacturer, but we suspect it might have been due to either the usage of a wrong drill bit, or due to drill malfunction causing it to wobble.

the Cavendish Laboratory, the threads were refurbished using *Helicoil* spirals. This process consists of boring a wider, 6.3 mm diameter hole in place of the damaged thread, followed by tapping a larger gauge thread with a tool included in the refurbishment kit, and then inserting a spiral that functions as an adaptor between the larger thread and M6. The spirals are made from a non-magnetic type of stainless steel (most probably 304L)²² and should not compromise the magnetic specifications of the chamber. Following this repair procedure, the chamber was thoroughly cleaned with acetone, including a treatment in the ultrasonic bath, to remove machine oil. Following this repair procedure, all connections to the vacuum chamber were successfully tightened with no detectable leaks.

Anticipating the relocation of the experiment from Cambridge to Oxford, the entire vacuum system was built on an aluminium breadboard²³ that is sufficiently light to allow easy transport, but also rigid at the same time.

2.5 Reaching the UHV Regime

Once the vacuum chamber was fully assembled and closed, we attempted pumping out the air with the rough pumps to check for serious leaks. While this was successful, we still had to open the vacuum chamber on two occasions. First, the anti-reflection coatings on the MOT viewports²⁴ failed after being exposed to vacuum conditions, and then the gate valve between the HV and UHV sections malfunctioned so it had to be replaced. During the period of waiting for replacements, we decided to acquire and install the RGA²⁵, that would later become useful for leak checking.

To check for leaks, we used a helium cylinder with a tube mounted with a medical needle as a dispenser, along with a mass spectrometer attached to the chamber. Initially, a borrowed external leak checking station served this role²⁶, while later we switched to using the RGA. The flange connections were then tested by spraying helium around them and monitoring the leak rate on the detector. Wherever a leak was detected, additional tightening was tried first. If there was no result, the gasket was replaced and the pumpdown process was repeated.

²²With the help of a permanent magnet, it was deduced that these are not made out of a ferromagnetic material.

²³Thorlabs PBG52521, 1800 mm × 1250 mm × 55 mm honeycomb aluminium breadboard

²⁴The coated surfaces on the interior side developed smudge marks upon first contact with vacuum. The viewports were shipped back to manufacturer for examination and recoating. No explanation was given about the source of this issue, but we suspect (based on the experiences of colleagues) that the coating was damaged by the cleaning agent leftover under the coating which started evaporating when the pressure was reduced.

²⁵Stanford Research Systems RGA100

²⁶Leybold Cerlikon UL 200 Helium Leak Detector

Rough pumping during the initial pump-down was performed with a turbo pump²⁷ backed with a scroll pump²⁸. The backing is necessary as the turbo can only function at output pressures below 10 mbar. Once we approached the final pumpdown, another pumping station was employed on the HV side, to provide sufficient pumping capacity for the bakeout.

A detailed insight into the implemented bakeout procedure is shown in Figure 2.12. As the ion pump magnets were not rated for use above 150°C, we decided to perform the bakeout in two rounds, first for about two weeks at 180°C without employing the ion/NEG pumps, following a pause during which the magnets could be reinstalled, and then again for about two weeks at 140°C, activating the NEG elements along the way (Temperature and pressure spikes in Figures 2.12b and d). Since a filament gauge was available to track the pressure during the bakeout, we could observe that a leak has opened during the first round of baking (Day 16 in Figure 2.12c). This was addressed before the second bakeout by tightening the flange bolts on the respective connection. During both rounds of baking and the break in between, temperature and pressure readings were monitored and logged on a PC via a serial connection to the pump controllers and the thermocouple reader.

Drawing from Figure 2.12c it is clear that the first bakeout is responsible for almost all of the outgassing reduction, which can be deduced from the behaviour of pressure during intervals with constant temperature. Over the course of this bakeout, we observed a drop in pressure by $\sim 10^4$ (see pairs of points labelled 1-4 in Figure 2.12c marking the ends of the four relevant intervals). This agrees very well with the predictions from literature, that quote a drop in outgassing of similar magnitude for stainless steel chambers following typical bakeout procedures [71].

With the end of the bakeout, the heating and insulation equipment was dismantled and the chamber was again exposed. We then proceeded to a final round of leak checking, using the RGA as the mass spectrometer. This has revealed a number of smaller leaks, that were promptly closed by tightening bolts. Nevertheless, a leak sealant liquid had to be employed on two connections involving viewports, as further tightening was not possible, due to the softness of the fully annealed copper gaskets that, as it would risk contacting the flange faces. After a lavish amount of the sealant²⁹ was applied, both of the leaks were eventually closed. The chamber was left with no leaks detectable with the RGA.

²⁷Leybold Öerlikon Turbovac TW70H

²⁸Leybold Öerlikon Scrollvac SC 5D

²⁹KL-5 Vacuum Leak Sealant from Kurt J Lesker

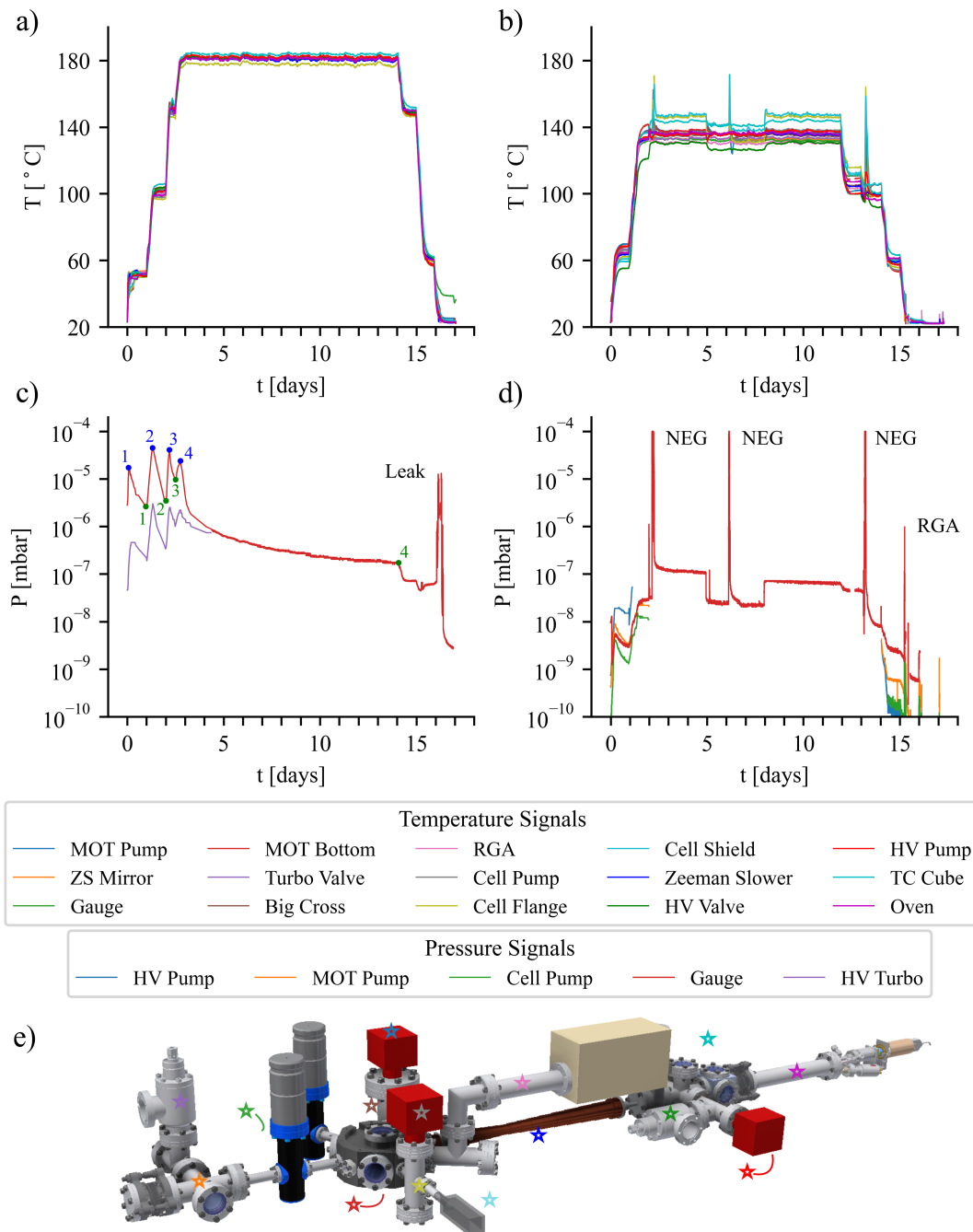


Fig. 2.12 **Bakeout procedure** - Temperature readings during the first (a) and second (b) round of baking. The three temperature spikes in b) correspond to the activation and conditioning of the NEG elements of the vacuum pumps. c) Pressure readings during the first round of baking, showing a leak opened on day 16. Note that the ion pumps were inactive as magnets were removed. Points numbered 1-4 label the intervals of constant elevated temperature showing a total drop in pressure by a factor of $\sim 10^4$. d) Pressure readings during the second round of baking. The ion pumps were only active during the ramping of the temperature to track the evolution of the pressure. The pressure spikes are caused by excess outgassing during activation of the NEG elements and the RGA (immediately after the bakeout) e) The diagram of the vacuum chamber showing the locations of the temperature sensors.

Chapter 3

Laser Cooling on the Atomic Beam

Laser cooling is the key ingredient in reaching the ultra low temperatures required for quantum degeneracy in atomic gases. The method relies on manipulating the light scattering force to slow down individual atoms, resulting in a reduction in temperature. Our experiment implements a sequence of laser cooling stages slowing and capturing hot atoms from the beam emerging from the oven that is maintained at 1100 °C, eventually producing a cloud of cold atoms at a temperature as low as 10 μ K in the MOT. This step is a prerequisite for the cooling to proceed further via evaporation methods. The current and the following chapter cover the foundations of the methods we use and show the progress in their implementation.

3.1 401 nm Laser System

The blue laser (401 nm) is used for the initial laser cooling steps, the Transversal Cooling (TC) and the Zeeman Slower (ZS), and for absorption imaging. The choice of this particular wavelength comes from the broad linewidth of the corresponding atomic transition, which makes it ideal for the job due to large achievable scattering rate. As the accompanying Doppler limit on the temperature that can be reached with this methods is high, more than 700 μ K, further cooling will be performed on a narrower transition. Additionally, a probe beam at this wavelength is required in the shelving spectroscopy setup that we temporarily use for locking the 583 nm laser (Details in Subsection 4.3.2). The light is generated by a frequency doubled¹ Ti-Sapphire² laser pumped from a solid state laser operating at 532 nm³. This system is capable of outputting up to 2.0 W of optical power at 401 nm from the frequency doubler stage, while the available power of pre-doubled, 802 nm light is 4.2 W.

¹MSquared ECD-X module

²MSquared SOLSTiS system

³15W Lighthouse Photonics Sprout G

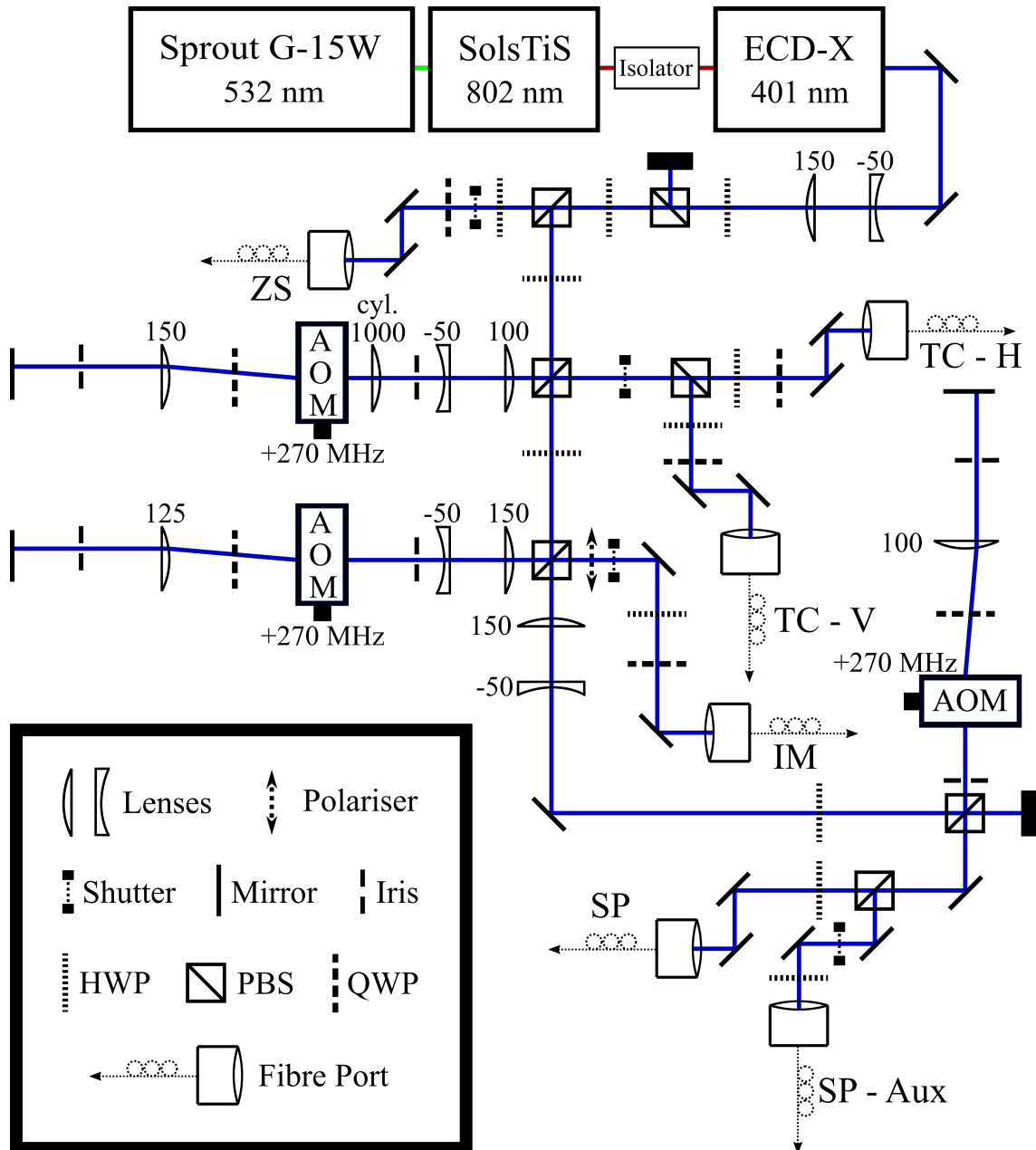


Fig. 3.1 **401 nm Laser Distribution Optics** - Zeeman slower light is drawn straight from the laser whereas all remaining beams are frequency-shifted by AOMs. We use 3:1 (and 2:1) telescopes to keep the light intensity on certain optical elements below the damage threshold, since these can be comparatively low for near-UV light. All focal lengths are in millimetres. Fibre ports legend: ZS = Zeeman Slower; SP (- Aux) = Spectroscopy (auxiliary port); TC - H(V) = Transversal Cooling - Horizontal (Vertical); IM = Absorption Imaging.

The light distribution setup is shown in detail in Figure 3.1. We employ three double pass AOMs⁴ to implement frequency offsets and control the light intensity of the spectroscopy,

⁴Gooch & Housego AOMO 3270-125 Acousto-Optical Modulator at 270MHz

imaging and TC light, while the ZS light is picked off directly from the laser output. With this configuration, the imaging and TC light can be tuned in the vicinity of the atomic transition, while the ZS light stays red detuned by approximately 540 MHz.

As described in Sections 3.2 and 4.3, we failed to replace a broken hollow cathode lamp (HCL), that had been discontinued by the manufacturer, with a new one that would match performance in terms of optical density. As a result, we have been forced to switch between using two different laser locking methods to stabilise the frequency of this laser system. Consequentially, there are two fibre ports designated for spectroscopy - the main one leading to the modulation transfer spectroscopy (MTS) setup, using a HCL as an atomic reference, and the auxiliary one leading to the vacuum chamber, used for modulated fluorescence spectroscopy on the atomic beam from the effusion cell oven.

Due to a relatively high optical power present in the system, we have opted for using a 1:3 telescope after the laser output, to increase the beam waist radius to about 1 mm. Short wavelength laser light is known for its detrimental effects to optical elements, particularly PBS cubes⁵. With the addition of the telescope system, we assured that the intensity levels are an order of magnitude below damage thresholds of the elements used, enabling long-term functioning of the system. Otherwise, we have not experienced issues with other polarisation optics⁶ at this wavelength. Another issue caused by high optical power is the distortion of the optical beam on the AOM in the TC branch. This issue was identified by projecting the resulting beam onto a camera and then mitigated for by installing a long focal length cylindrical lens in front of the AOM. The cause was narrowed down to thermal effects originating from the absorbed laser light after investigating transient behaviour caused by switching the light or the RF power on and off. Finally, care had to be taken to find appropriate optical fibres⁷ for the ZS and TC light as these require up to 200 mW at the fibre input.

Finally, there are several issues with the laser itself that are worth pointing out:

- After one year of regular use and another year of light use, the Sprout G pump laser was no longer able to maintain the specified 15 W of power and had to be operated at lower set points. In parallel with that, it would frequently experience episodes of intermittent mode-hopping, resulting in unlocking of the Ti-Sapphire system. The laser was shipped to the manufacturer for repair and as of June 2021 (one year after repair) it functions without issues.

⁵We use high power PBS cubes from lens optics - PBC0,5"-370/420 HP - at places where the highest light intensities are present

⁶We use a number of half-wave and quarter-wave plates from Thorlabs and Day Optics

⁷Schäfter+Kirchhoff PMC-E-400Si-2.8-NA011-3-APC.EC-700-P

- An issue where a back-reflection originating from somewhere within the frequency-doubler cavity corrupts the Ti-Sapphire wavelength lock kept appearing during usage. This was mitigated by installing an optical isolator⁸ between the two components. We suspect that the issue might have been present from the start, but as it was only explicitly discovered⁹ after lengthy usage and it is not discernible from the previous issue unless the right monitor signals are tracked, we cannot say with certainty when it originated. Before this issue was fully solved, the remedy was to slightly change the input alignment into the doubler cavity and then reoptimise the intra-cavity alignment. This would usually solve the problem temporarily, but due to a very sensitive dependence on the system alignment, it would reappear again as a result of thermal drifts.
- Finally, the frequency-doubler is very sensitive to vibrations, apparently due to a relatively low-frequency piezo resonance (~ 2 kHz) present in its cavity locking loop. With the right cavity lock loop logic settings applied in the control software¹⁰, the impact of this issue was minimised, as it would often spontaneously jump back into lock after vibration-causing incidents of lesser extent.

3.2 Spectroscopy and Laser Stabilisation

The lasers employed for laser cooling in our experiment need to be locked to the respective atomic transitions. The available options are either using an atomic reference, i.e. a sample of erbium, and doing spectroscopy on the actual transition of interest, or providing a stable frequency reference such as an optical cavity or a stabilised secondary laser source. In our case, there are two possibilities for the atomic reference - the beam emerging from the erbium oven or an erbium spectroscopic lamp¹¹. The former is readily accessible and has a relatively narrow distribution of transversal velocities, but other laser beams interfere with it over the course of the experimental sequence and the relatively low atomic (flux) density that is available makes locking to the narrower, 583 nm line quite challenging. The other option consists of using a Hollow Cathode Lamp as a reference. This technology involves a pair

⁸IO-5-780-HP

⁹The 'smoking gun' was the observation that jumping would only occur on condition that there was 401 nm light being generated by the doubler. If the light was blocked before or within the doubler cavity, the Ti-Sapphire would remain locked indefinitely. The issue with the pump laser had similar apparent symptoms, but was obviously not correlated with the presence of the doubled light in any way.

¹⁰Disabling the immediate re-lock scan search upon losing lock.

¹¹Erbium vapour cells do not exist as, due to the high melting point of erbium (1 529°C), impractically high temperatures are required for any significant vapour to be formed.

of electrodes in an enclosure filled with buffer gas, typically neon or argon. The cathode is shaped as a hollow cylinder and coated with erbium on the internal surface. Additionally, for this type of spectroscopy, a special see through geometry is required, where a laser beam can be directed through the cylindrical cathode. Finally, when a high voltage (about 120 V DC, for a typically used current of 10 mA) is applied across the electrodes, a stream of ionised buffer gas atoms flows from the anode towards the cathode, sputtering erbium atoms off the coated surface into the region inside the cylinder. This provides a stable and independent source of atoms, albeit with a larger velocity spread. Unfortunately, we only purchased one lamp initially¹², with the aim to test the method and prototype the optical system. Shortly after, that lamp model was discontinued by the manufacturer and it turned out that the performance of other lamps available on the market varies greatly. We then purchased a different model of the HCL¹³, initially as a spare option¹⁴, but it has proved to be inferior to the former model in terms of atomic density that it produces. The chronological summary of the spectroscopy techniques used for locking our cooling lasers is shown in Table 3.1.

Usage period	401 nm Lock	583 nm Lock	Reason for changing
02/19 - 02/20	MTS (Heraeus HCL)	MTS (Heraeus HCL)	MOT unstable
02/20 - 01/21	Mod. Flu (oven beam)	MTS (Heraeus HCL)	HCL broken
02/21 - 06/21	MTS (Photron HCL)	Shelving (oven beam)	MOT unstable
06/21 -	MTS (Photron HCL)	PDH (ULE Cavity)	NA

Table 3.1 **Laser stabilisation techniques employed on the experiment -**

3.2.1 Modulation Transfer Spectroscopy

The laser locking technique most widely used in our setup so far is Modulation Transfer Spectroscopy (MTS) [72, 73]. This method is relatively simple to implement and provides a Doppler-free, zero-offset signal, that is also insensitive to background magnetic fields. It employs a phase-modulated pump beam that overlaps with a counter-propagating probe beam within the region containing the sample of atoms. The combined action of the two beams induces three-wave-mixing processes that ultimately result in photons offset by the

¹²Erbium Single-Element See-Through Hollow Cathode Lamp from Heraeus

¹³Supplied by Photron

¹⁴At this point in time we were using the a single lamp to lock both lasers, which later proved to be insufficiently stable for the MOT laser.

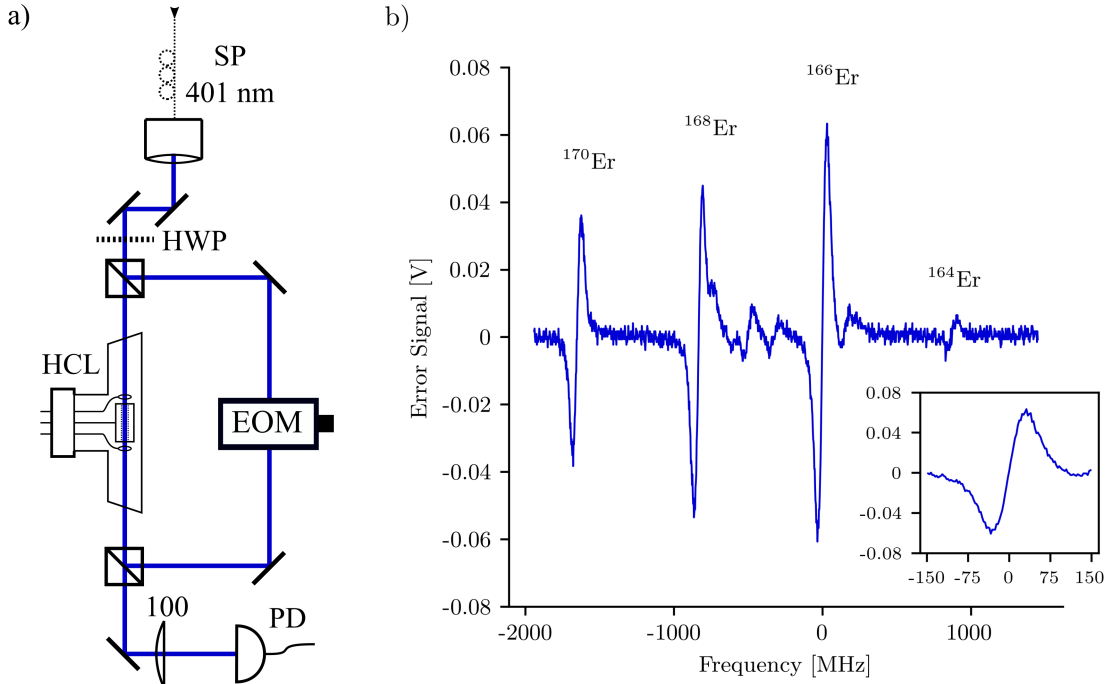


Fig. 3.2 **Modulation Transfer Spectroscopy Setup (basic version)** - a) The setup now used for locking the 401 nm laser to the atomic transition in our experiment. Spectroscopy light is supplied through single fibre input where the probe and the pump beam are simply split on a polarising beam splitter. b) The error signal from the 401 nm transition generated using the Heraeus HCL and a 19 MHz modulation frequency on the EOM. The inset offers a closer look onto the ^{166}Er peak.

modulation frequency being emitted into the path of the probe beam. This induces a beating note in the intensity of the probe beam that can be measured on a photodiode and extracted using a phase sensitive detection technique. The basic version of the setup is shown in Figure 3.2a, along with an example of the error signal in Figure 3.2b.

To gain further understanding of the technique and the underlying processes, one can set up a simple model based on a two-level system (Figure 3.3) - an atom with levels $|a\rangle$ and $|b\rangle$ with energies $\hbar\omega_a$ and $\hbar\omega_b$ - with transition frequency $\omega_0 = \omega_b - \omega_a$ and rate of spontaneous decay Γ . A probe beam at frequency ω is incident onto the atoms from one direction, and a modulated pump beam with an offset carrier frequency $\omega + \Delta$ and sidebands $\omega + \Delta \pm \delta$ is counter-propagated to it.

The Hamiltonian governing the evolution of this system can be written as $\hat{H} = \hat{H}_0 + \hat{H}_1$ where \hat{H}_0 is the unperturbed part:

$$\hat{H}_0 = \hbar\omega_a |a\rangle \langle a| + \hbar\omega_b |b\rangle \langle b| \quad (3.1)$$

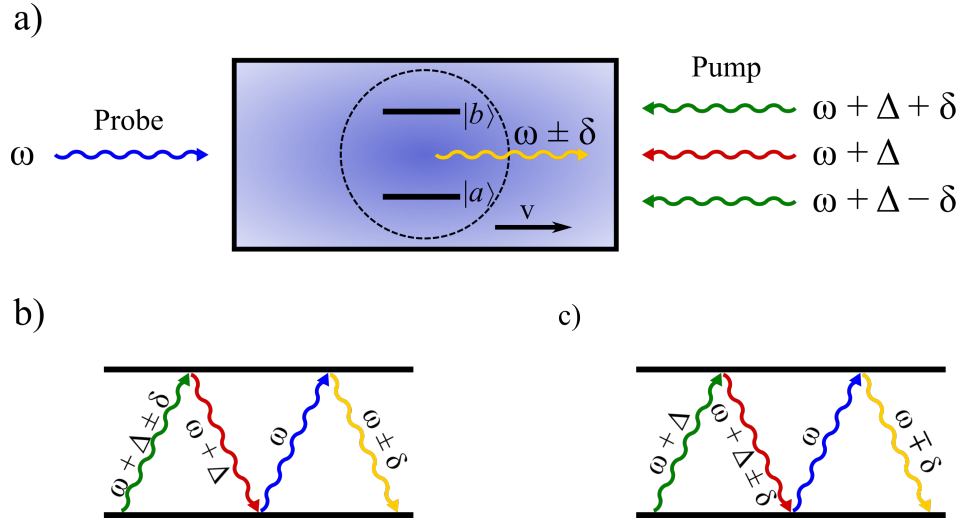


Fig. 3.3 **Modulation Transfer Spectroscopy - Simple Model** - a) The layout of the simple model showing the two-level structure of the atoms in the interaction region, along with the incoming light-fields of different frequencies corresponding to the pump ($\omega + \Delta$, $\omega + \Delta \pm \delta$) and probe (ω) beams, and the emitted ‘modulation’ photons at frequency $\omega \pm \delta$. b-c) The three-wave-mixing processes that result in the ‘modulation’ photons.

and the perturbation due to the light electric field (assuming linear polarisation along the z -axis) is [74]:

$$\hat{H}_1 = E(t)\mu_{ab}(|a\rangle\langle b| + |b\rangle\langle a|) \quad (3.2)$$

where $\mu_{ab} = e\langle a|z|b\rangle$ is the dipole transition matrix element. The electric field that corresponds to the probe and the pump beam is:

$$E(t) = \frac{1}{2} \sum_{\alpha} \left(\mathcal{E}_{\alpha} e^{i(\omega_{\alpha}t - k_{\alpha}x)} + \text{c.c.} \right) \quad (3.3)$$

where the sum over α iterates over the four field components present in the beams, and the associated parameters ω_{α} and k_{α} take the values listed in Table 3.2. \mathcal{E}_{α} are complex electric field amplitudes, reflecting the absolute phase of the field.

The evolution of the density matrix $\rho = |\psi\rangle\langle\psi|$, with $\psi = c_a|a\rangle + c_b|b\rangle$ representing the wave function of the system, describing the populations and coherences in the rest frame of the atom is governed by the Lindblad master equation [75, 76]:

$$\dot{\rho} = -\frac{i}{\hbar} [\hat{H}, \rho] - \frac{\Gamma}{2} (|b\rangle\langle b|\rho + \rho|b\rangle\langle b| - 2|a\rangle\langle b|\rho|b\rangle\langle a|) . \quad (3.4)$$

Following the approach from [77, 78], given an atom with velocity v , we can substitute $x = x_0 + vt$ into Equation 3.3 and implement the Hamiltonian from above, yielding the

Component	α	ω_α	k_α
Probe	p	ω	k_0
Pump carrier	c	$\omega + \Delta$	$-k_0$
Pump + sideband	$+$	$\omega + \Delta + \delta$	$-k_0$
Pump - sideband	$-$	$\omega + \Delta + \delta$	$-k_0$

Table 3.2 **Definitions of ω_α and k_α from Equation 3.3** - $k_0 = \frac{2\pi}{\lambda}$ is the wave number of the laser light used.

following set of differential equations:

$$\dot{\rho}_{bb} = -\dot{\rho}_{aa} = -\Gamma\rho_{bb} + \frac{i\mu_{ab}E(t)}{\hbar}(\rho_{ab} - \rho_{ba}), \quad (3.5)$$

and

$$\dot{\rho}_{ab} = \dot{\rho}_{ba}^* = \left(-\frac{\Gamma}{2} + i\omega_0\right)\rho_{ab} - \frac{i\mu_{ab}E(t)}{\hbar}(2\rho_{bb} - 1). \quad (3.6)$$

As long as the transition is not strongly saturated, these equations can be solved by treating the electric field as a perturbation and expanding the density matrix into a series in terms of the powers of the electric field:

$$\rho_{ij} = \sum_n \rho_{ij}^{(n)} \quad (3.7)$$

for $i, j \in \{a, b\}$. The unperturbed solutions are obtained from the simple equations:

$$\dot{\rho}_{bb}^{(0)} = -\Gamma\rho_{bb}^{(0)}, \quad (3.8)$$

and

$$\dot{\rho}_{ab}^{(0)} = \left(-\frac{\Gamma}{2} + i\omega_0\right)\rho_{ab}^{(0)} \quad (3.9)$$

and the perturbations are then obtained iteratively from:

$$\dot{\rho}_{bb}^{(n)} = -\Gamma\rho_{bb}^{(n)} + \frac{i\mu_{ab}E(t)}{\hbar}(\rho_{ab}^{(n-1)} - \rho_{ba}^{(n-1)}), \quad (3.10)$$

and

$$\dot{\rho}_{ab}^{(n)} = \left(-\frac{\Gamma}{2} + i\omega_0\right)\rho_{ab}^{(n)} - \frac{i\mu_{ab}E(t)}{\hbar}(2\rho_{bb}^{(n-1)} - \delta_{n,1}) \quad (3.11)$$

that are integrable for sinusoidal driving. The group of terms containing the modulation transfer signal is contained in $\rho_{ab}^{(3)}$ and can be obtained by first applying the rotating wave-

approximation and discarding the transient terms (any terms that are decaying exponentially in time):

$$\rho_{ab}^{(3)MTS} = \frac{i}{4} \sum_{q,r,s} \left[\frac{1}{\left[\frac{\Gamma'}{2} - i(\omega_s - \omega_0 - k_s v) \right]} + \frac{1}{\left[\frac{\Gamma'}{2} + i(\omega_r - \omega_0 - k_r v) \right]} \right] \times \frac{\Omega_q \Omega_r \Omega_s^* e^{i(\omega_q + \omega_r - \omega_s)t - i(k_q + k_r - k_s)x}}{\left[\frac{\Gamma'}{2} + i(\omega_q + \omega_r - \omega_s - \omega_0 - (k_q + k_r - k_s)v) \right] [\Gamma + i(\omega_r - \omega_s - (k_r - k_s)v)]} \quad (3.12)$$

where $\Omega_\alpha = \frac{\mu_{ab} \mathcal{E}_\alpha}{\hbar}$ is the complex Rabi frequency associated with the light component α and Γ and Γ' represent the natural linewidth of the optical transition, and the decoherence rate (If there is no pressure broadening, then $\Gamma = \Gamma'$). Each term in the series corresponds to an light field with frequency $\omega_t = \omega_q + \omega_r - \omega_s$ and wavevector $k_t = k_q + k_r - k_s$. These can be interpreted as three-wave mixing processes [79], and the ones that create modulation carrying photons, with $\omega_t = \omega \pm \delta$ and $k_t = k_0$ are shown in Figure 3.3(b-c). The overall resonance condition for these processes is that both the one-photon and three-photon detunings should be zero. For the first process (Figure 3.3b), assuming that the interacting atom has velocity v , this implies:

- One-photon resonance: $\omega + \Delta \pm \delta + kv = \omega_0$,
- Three-photon resonance: $(\omega + \Delta \pm \delta + kv) - (\omega + \Delta + kv) + (\omega - kv) = \omega_0$.

From these conditions it is deducible that the process is resonant for laser detuning $\Delta_0 = \omega - \omega_0 = -\frac{\Delta}{2} \mp \delta$ for the velocity group $v = -\frac{\Delta}{2k}$. Similarly, for the second process (Figure 3.3c):

- One-photon resonance: $\omega + \Delta + kv = \omega_0$
- Three-photon resonance: $(\omega + \Delta + kv) - (\omega + \Delta \pm \delta + kv) + (\omega - kv) = \omega_0$

where the resonance occurs for $\Delta_0 = -\frac{\Delta \mp \delta}{2}$ and the velocity group $v = -\frac{\Delta \pm \delta}{2k}$.

If a thermal velocity distribution, with Doppler width much wider than Γ is assumed, the expression from Equation 3.12 can be integrated over velocities [77, 78] and the resulting signal (i.e. the modulation component in the electric field) takes the form:

$$S(\Delta_0) \propto \frac{1}{\Gamma' + i\delta} \left[\frac{1}{\Gamma + i(\Delta_0 + \frac{\Delta}{2} + \delta)} + \frac{1}{\Gamma - i(\Delta_0 + \frac{\Delta}{2} - \frac{\delta}{2})} - \frac{1}{\Gamma + i(\Delta_0 + \frac{\Delta}{2} + \frac{\delta}{2})} - \frac{1}{\Gamma - i(\Delta_0 + \frac{\Delta}{2} - \delta)} \right] \quad (3.13)$$

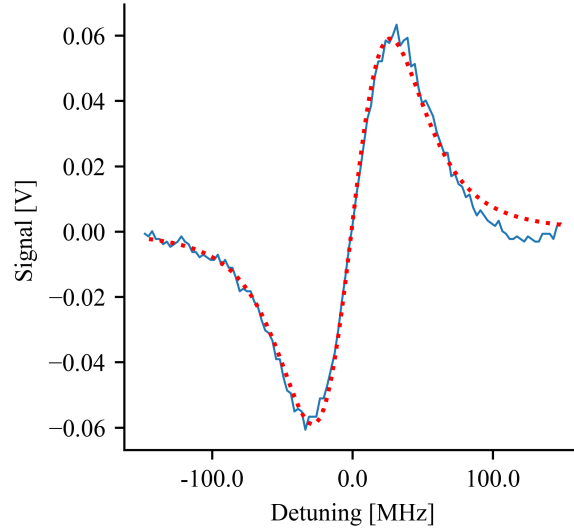


Fig. 3.4 **Fitted MTS Signal** - The expression from Equation 3.13 fitted on top of an MTS signal obtained on the 401 nm transition using the ^{166}Er isotope and the HCL current of 5 mA. The optical powers in the pump and the probe beams were 1.2 mW and 1.4 mW, with both beams having a waist diameter of approximately 2 mm.

where Γ (Γ') represents the transition linewidth (adjusted for pressure broadening).

We can employ this result to attempt to give an estimate of the pressure broadening in the HCL, Γ_p . Taking the ^{166}Er peak from Figure 3.2b, we can fit the phase-demodulated version of Equation 3.13, taking $\Gamma = \Gamma_0\sqrt{1+s}$ and $\Gamma' = \sqrt{\Gamma^2 + \Gamma_p^2}$, and then using the amplitude, phase and Γ_p as free parameters. The saturation parameter corresponding to the total optical power in the setup used to obtain this data¹⁵ is $s = 1.5 \pm 0.5$. The fit is shown together with the data in Figure 3.4 yields $\Gamma_p = 2\pi \times (4.1 \pm 0.1)$ MHz, giving a similar estimate to the one in [57]. Given that $s \sim 1$, so the above perturbative approach is not strictly valid, this should only be taken as a rough estimate.

As shown in [80], assuming $\Gamma' = \Gamma$, the in-phase¹⁶ and quadrature components of the signal from Equation 3.13 reach maximum peak-to-peak values for $\delta = 1.20 \times \Gamma$ and $\delta = 1.50 \times \Gamma$, respectively. Also, more importantly for locking, the slopes of the two components are maximised for $\delta = 0.35 \times \Gamma$ and $\delta = 0.67 \times \Gamma$. As the lock-in amplifier offers the possibility of using an arbitrary demodulation phase, an interesting result is that the signal slope is maximised for $\phi = 0.52 \times \pi$ and $\delta = 0.74 \times \Gamma$

¹⁵The uncertainty margin originates from the value of beam diameter at the time of the measurement that is not known exactly.

¹⁶The convention in the literature is to leave out the term $\frac{1}{\Gamma' + i\delta}$ when defining the zero-phase, such that the in-phase component represents a combination of four absorption-like features and the quadrature component is a combination of four dispersion-like signals.

3.2.2 Modulated Fluorescence Spectroscopy

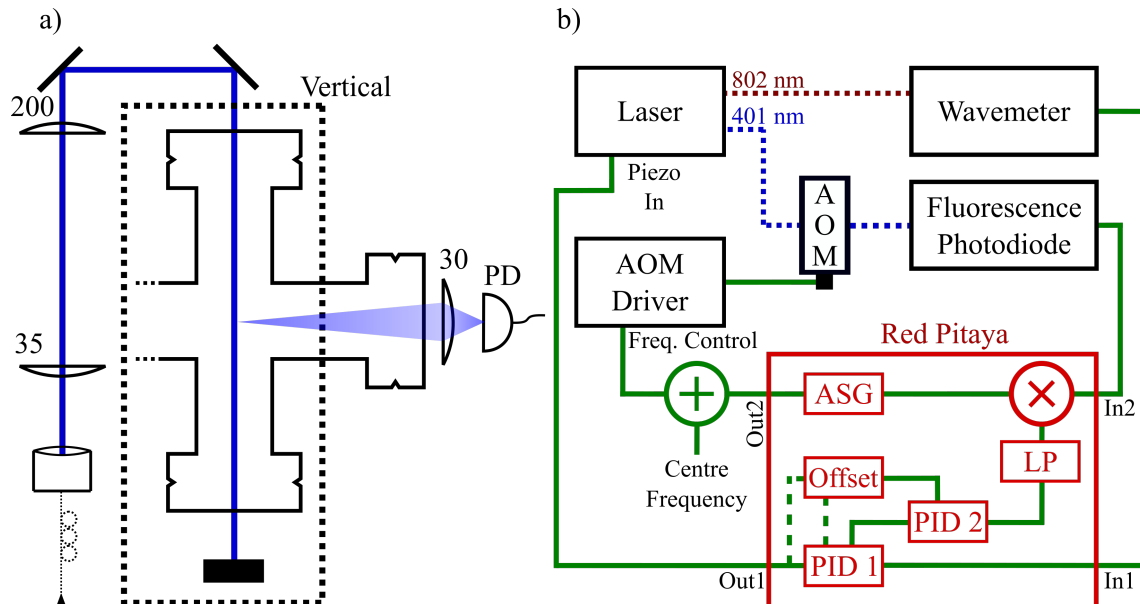


Fig. 3.5 **Modulation Fluorescence Spectroscopy** - a) The simple optical setup used to obtain a locking signal for the blue laser. An 8 mm diameter beam was orthogonally intersected with the atoms propagating from the oven at the cross in the HV section. The laser frequency is frequency-modulated at 30 kHz and the resulting fluorescence signal is picked up on the large area photodiode; b) Double feedback loop, implementing a Red Pitaya controller board, used for laser stabilisation where the atomic spectroscopy provides lock point offset correction to the main loop based on a wavemeter. The PID 1 in the Red Pitaya is responsible for the main feedback loop, while its offset is periodically updated by enabling the loop incorporating PID 2 that takes the spectroscopy error signal as the input. When the experiment is active, the output of PID 2 is kept frozen at its last updated value. The board is also used to generate the modulation harmonic sent to the AOM driver and subsequent lock-in detection on the photodiode signal.

After having to delegate the single properly functioning HCL in our possession for locking the 583 nm laser, because of the poor performance of the locking setup with the lamp shared by the two lasers (also see Section 4.3), an alternative method for locking the 401 nm was needed, so we commissioned the wavemeter¹⁷ for this purpose. While its short timescale stability of 2 MHz is more than sufficient to keep the laser on resonance with the broad atomic transition, the drift of its frequency reference due to temperature fluctuations would significantly detune the laser over a few hours. The solution we implemented to mitigate for thermal drifts consists of relying on the wavemeter to keep the laser locked while running measurements, with periodic updating of the lock-point based on the fluorescence signal on the atomic beam between experimental sequence cycles.

¹⁷High Finesse WS7-60

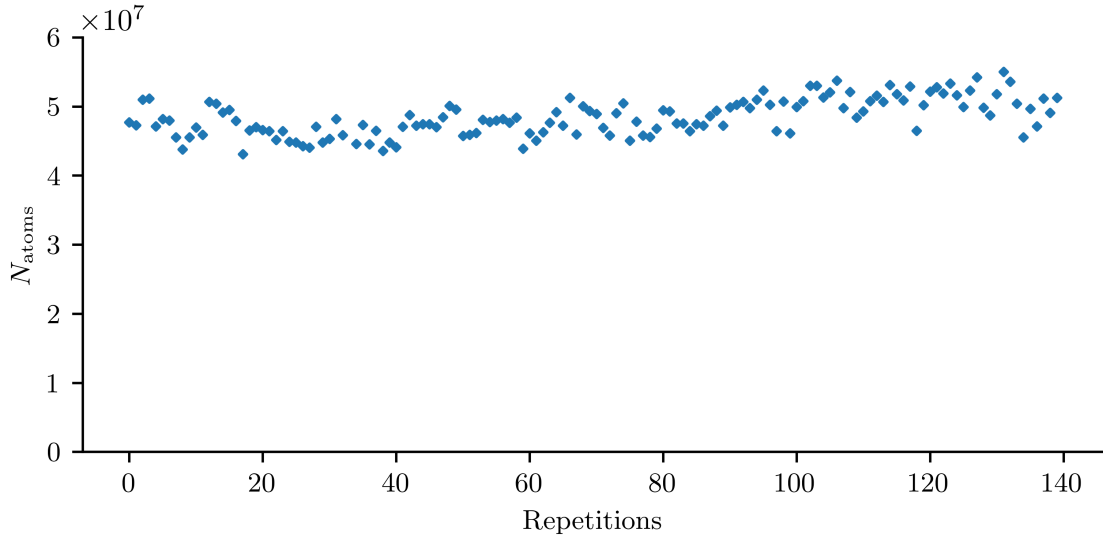


Fig. 3.6 **MOT Loading Stability** - Variation of the number of atoms loaded into the MOT with $t_{\text{load}} = 15$ s over 140 repetitions of the sequence. The mean and standard deviation of the atom number in this sample are $(4.84 \pm 0.26) \times 10^7$.

Since we have taken the opportunity to mount extra viewports on the oven side of the chamber, this point of access was now used to set up the fluorescence measurement on the atomic beam, shown in Figure 3.5a. A 4 mm waist radius beam, frequency modulated at 30 kHz was sent through the chamber, crossing the atomic beam perpendicularly to its propagation direction. The fluorescence from the atoms was collected using a set of 2 inch lenses through a third viewport, and directed onto a large surface area photodiode¹⁸. The locking signal is then generated by demodulating the intensity signal using a lock-in detection loop (Figure 3.5b). The feedback was then done using a double loop configuration, where the main loop was feeding back the error signal from the wavemeter to the laser, with its locking offset being determined by the secondary loop, that fed back the spectroscopy signal from the atomic beam. When the experiment is running, the output of the secondary loop could be frozen, allowing for the TC and ZS light to act onto the atoms without interfering with the lock position. The full locking loop, including the lock-in amplifier, the two PID circuits and the logic controls is implemented using a Red Pitaya controller board¹⁹ running the PyRPL software package [81]. Using this technique, we successfully compensated the thermal drift of the wavemeter, bringing the MOT loading number fluctuations to 5% RMS (Figure 3.6).

¹⁸Thorlabs PDA100A2, 75.4 mm² amplified Si photodiode

¹⁹Red Pitaya STEMLab 125-14

3.3 Transversal Cooling

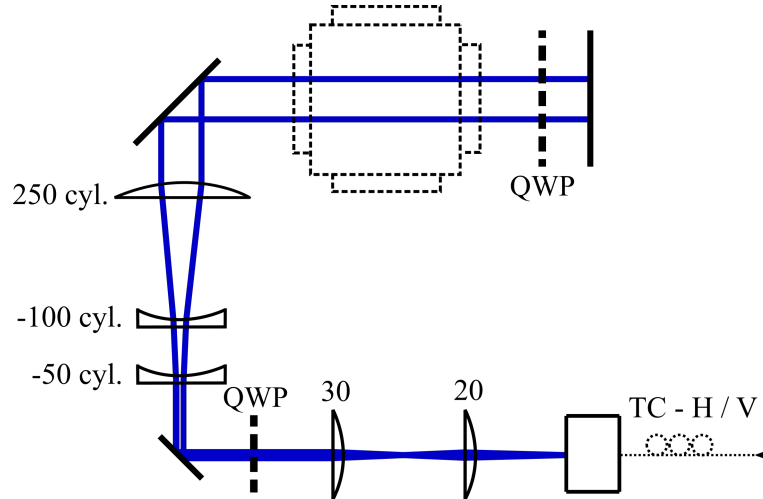


Fig. 3.7 **Transversal Cooling Optics** - The delivery optics system layout used in both of the transversal cooling beams. A set of two spherical and three cylindrical lenses is used to provide a tuning range for beam waists along both directions. Initially, a 17 mm by 3 mm collimated elliptical beam was used, but after the AR coatings on the viewports deteriorated, we proceeded to make the beams slightly converging to mitigate for the attenuation. Upon passing through the chamber, the beam is retro-reflected, and a quarter-wave plate is used to prevent interference of the beam with itself.

In order to increase the atomic flux available for the Zeeman slower as well as to mitigate for the transversal spreading of atoms upon slowing, a 2D Doppler molasses cooling stage is implemented after the oven. It consists of two orthogonal pairs of elliptical, retro-reflected laser beams addressing the 401 nm transition. The optical setup for shaping the beams is depicted in Figure 3.7 and incorporates two spherical lenses to set the minor waist of the beam, followed by a triplet of cylindrical lenses adjusting the aspect ratio to achieve the desired major waist. This five-lens configuration allows for both waist radii to be adjusted independently within a narrow range around the design goal of 17 mm by 3 mm (see below). Two quarter-wave plates, one on either side of the chamber set the polarisation such that the direct and the back-propagating beam have circular polarisations of opposite handedness, to prevent fringing within the cooling region, that can be detrimental to the performance.

We again employed the atomic beam numerical simulation to get a better grasp of the parameters that we should use and the expected gains from this technique. The results outlining the effects of varying the laser power and detuning are presented in Figure 3.8, while the analysis into optimising the beam size is shown in Figure 3.9. With the help of these results, we decided on the beam size of 17 mm by 3 mm, which also matches well with the expected size of the atomic beam in the TC chamber. Not surprisingly, the simulation also

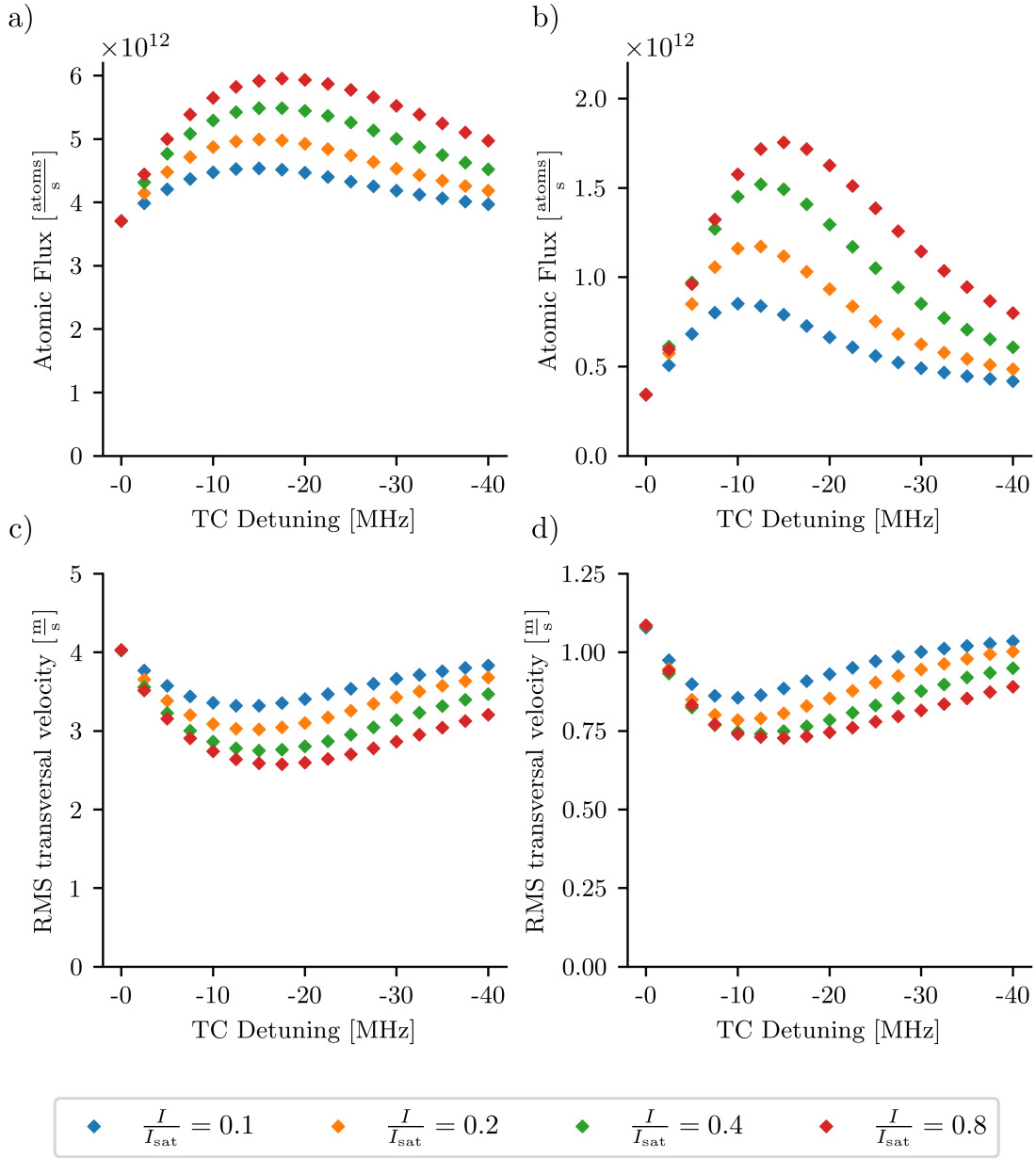


Fig. 3.8 Transversal Cooling Power and Detuning - Predictions for the flux (a-b) and RMS transversal velocity (c-d) at the start and the end of the ZS tube, respectively, obtained from the atomic beam numerical simulation. The results show a large gain in flux of slow atoms that can be attained by using transversal cooling and also a decrease in the transversal velocity that mitigates for the splaying effect at the end of the ZS. Note that the cited fluxes do not account for the natural abundance of any given Er isotope.

predicts that the cooling is optimised for a detuning in the vicinity of $-\frac{\Gamma_{401}}{2} = -2\pi \times 15$ MHz. As demonstrated by the blue markers on Figure 3.10a, the effect of TC on MOT loading was

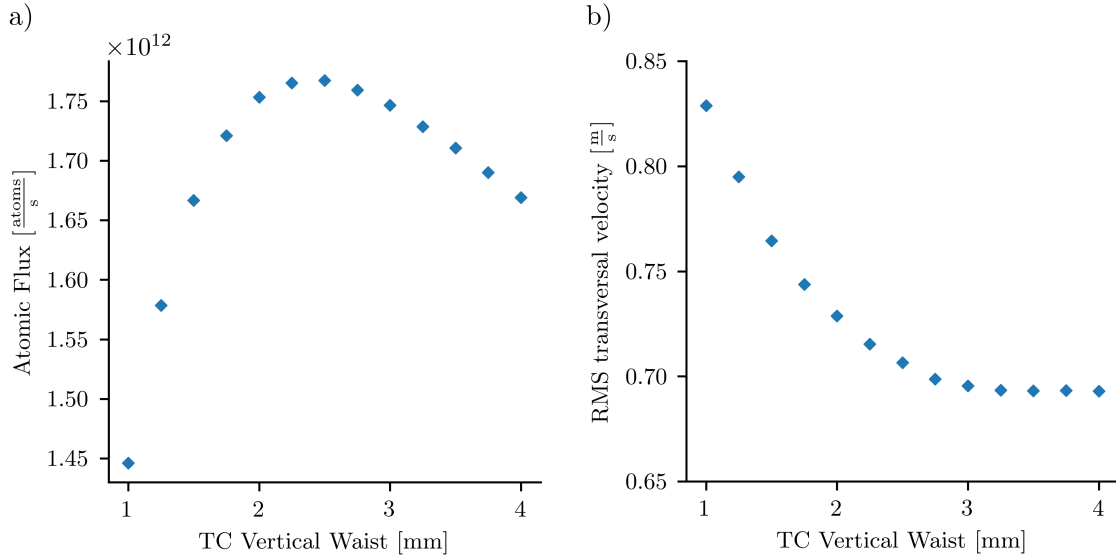


Fig. 3.9 **Transversal Cooling Beam Waists** - Numerical simulation results for the flux (a) and the RMS transversal velocity (b) at the end of the ZS tube with the TC power and detuning kept fixed at $P = 40$ mW ($\frac{I}{I_{\text{sat}}} = 0.8$) and $\delta = -2\pi \times 12.5$ MHz. The results show that the flux is optimised in the range of minor radii 2.0 – 3.0 mm whereas the cooling along the transversal direction favours slightly higher waists. Both quantities seem to be insensitive to the major waist radius over the range from 10 mm to 17 mm. Note that the cited fluxes do not account for the natural abundance of any given Er isotope.

shown to be an enhancement of the loaded number by up to three times, which is in decent accordance with the idealised prediction from the simulation predicting approximately a fourfold gain. Furthermore, the optimal value for the detuning was experimentally determined to be $\delta_{\text{TC}} = -2\pi \times 12.5$ MHz.

After experiencing a problem with the AR coatings on the entire set of viewports (Figure 3.10b), leading to significant loss of light intensity upon the passage through the chamber²⁰, we took advantage of the tunability of the optical system, to make the beams slightly converging along the minor axis direction. This re-established the balance of forces in the TC setup and avoided imprinting a transversal velocity bias to the atomic beam. The replacement viewports have been sourced and will be installed during the first oven maintenance procedure that will inevitably happen in the near future.

²⁰The single-pass loss of 25% – 40% was measured.

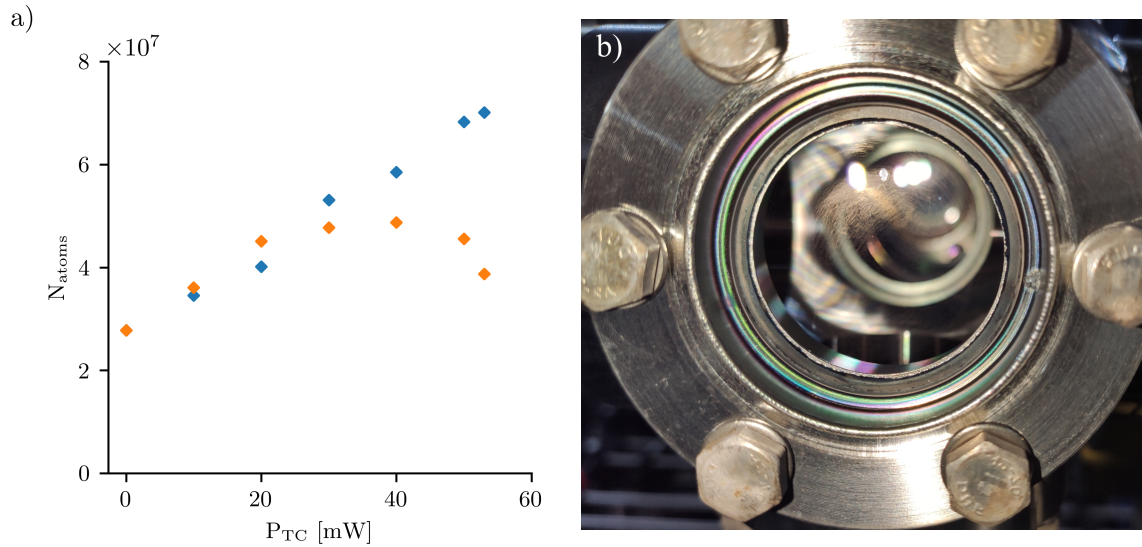


Fig. 3.10 **Enhancement of MOT loading by TC** - a) Measured dependence of the MOT loading number as a function of the single-beam optical power in the transversal cooling. The figure also shows how the failed optical coating (pictured on (b)) caused an imbalance between the counter-propagating beams, leading to TC imprinting a transversal velocity bias to the atoms and eventually poor loading at high TC powers (orange markers). This was mitigated by making the beams slightly converging, leading to an improvement in performance (blue markers). The laser detuning we use in the TC setup for best performance is $\delta_{\text{TC}} = -2\pi \times 12.5$ MHz.

3.4 Zeeman Slower

In many cold atom experiments, including ours, the atoms are sourced from a high temperature oven that emits a collimated beam. At typical oven temperatures, the emerging atoms have velocities of several hundreds of meters per second on average. Therefore, it is necessary to slow the beam down considerably before loading the atoms into a trap, e.g. a MOT, where capture velocities range between several and few tens of meters per second²¹. Since most optical transitions used for cooling are in the (near-) visible wavelength range and have line widths in the range of 0.1 – 30 MHz, the Doppler shift would span many transition line widths during slowing. In order to employ the light scattering force, it is necessary to keep the atoms near the resonant frequency, and the commonly used tool is the Zeeman Slower (ZS). Its functioning principle is that the atoms are subjected to the scattering force of a counter-propagating laser beam and specifically shaped electromagnetic coils provide the field that offsets the atomic resonance via the Zeeman effect, compensating for the Doppler shift change resulting from slowing.

²¹The MOT capture velocity is approximately $10 \frac{\text{m}}{\text{s}}$ in our case, see Section 4.1

3.4.1 Idealised Zeeman Slower

The basic, first order, approach in designing a Zeeman slower is aiming for constant deceleration of atoms, which allows for straightforward determination of the velocity along the length of the slower. As the scattering force (equation F.1) will stay constant for constant detuning δ , the magnetic field profile should be such that it exactly counteracts the change in the Doppler shift.

Assuming that the saturation factor of the optical transition as $s = \frac{I}{I_{sat}}$ is constant along the slower for simplicity (uniform profile, collimated beam; negligible absorption), the equation of motion can be written as:

$$v_0^2 - v(x)^2 = \frac{2xF_{scatt}}{m} = \frac{\hbar k \Gamma x}{m} \frac{s}{1 + s + \frac{4\delta^2}{\Gamma^2}} \quad (3.14)$$

leading to the expression for velocity:

$$v(x) = v_0 \sqrt{1 - \frac{x}{x_0}} \quad (3.15)$$

where x_0 is the length of the slowing region and it is then related to the capture velocity as:

$$x_0 = \frac{mv_0^2}{\hbar k \Gamma s} \left(1 + s + \frac{4\delta^2}{\Gamma^2} \right). \quad (3.16)$$

The total detuning, that we aim to keep constant along the length of the slower, depends on the laser detuning w.r.t. to the optical transition, δ_0 , the Doppler shift, kv , and the Zeeman shift, $\mu'B$, is given by the formula $\delta = \delta_0 + kv + \frac{\mu'B}{\hbar}$. Here $\mu' = \mu_B(m_e g_e - m_g g_g)$ denotes the Zeeman factor of the optical transition used for cooling, as defined in Equation 1.3. From this relation, we see that the ideal Zeeman slower magnetic field profile is calculated as:

$$B(x) = -\hbar \frac{\delta_0 - \delta + kv(x)}{\mu'} \quad (3.17)$$

leading to the explicit solution:

$$B(x) = B_{bias} + B_{prof} \sqrt{1 - \frac{x}{x_0}}, \quad (3.18)$$

$$B_{bias} = \hbar \frac{\delta_0 - \delta}{\mu'}, \quad (3.19)$$

$$B_{prof} = \frac{\hbar kv_0}{\mu'}. \quad (3.20)$$

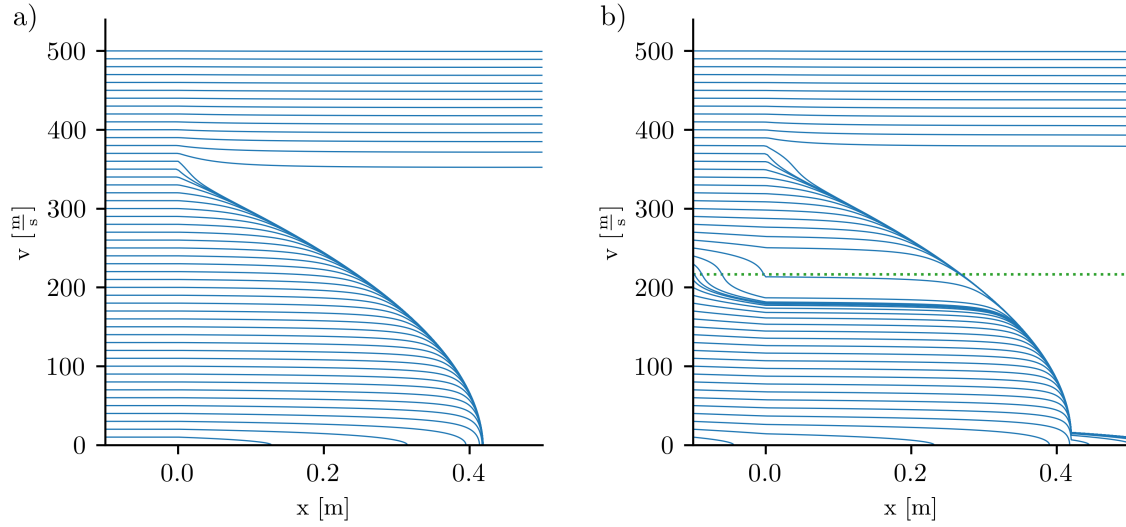


Fig. 3.11 **Ideal Zeeman Slower** - Atom trajectories for an ideal ZS designed with the parameters $v_0 = 350 \frac{\text{m}}{\text{s}}$, $x_0 = 0.42 \text{ m}$, $\delta = -2\pi \times 10 \text{ MHz}$ and $s = 2$: a) assuming no interaction with the light outside the field region; b) implementing an offset to the field profile to achieve a finite final velocity and accounting for the interactions with the light beam before and after the slower. The green dotted line marks the velocity group that is resonant with the ZS light at zero field. These residual interactions cause some atoms to slow down before entering the slower, as well as the atoms at the end of the slower to experience some residual slowing.

These fields are designed to slow down atoms entering the slower at or below the capture velocity, v_0 , down to rest at the end of the slowing region. Figure 3.11a shows the trajectories of atoms with different initial velocities encountering an ideal Zeeman slower.

While this ideal picture gives a sufficient basis for the design of the slower, there are multiple additional points that need to be considered to make a robust and efficient system. From the imperfections in the magnetic field profile and the slowing laser beam to the forces acting on atoms outside of the slower design region, these all need to be accounted for to gain full understanding of the Zeeman slower operation.

3.4.2 Realistic Zeeman Slower

In order to make the slowing action robust to field imperfections and scattering force fluctuations, the total detuning, δ , should be negative. This assures that the atoms travelling slower compared to the ideal velocity trajectory $v(x)$ at any point, experience reduced slowing, and the atoms travelling (slightly) faster than the ideal velocity experience enhanced slowing. Therefore, all the atoms that enter the Zeeman slower at $v \leq v_0$ will eventually approach the ideal slowing trajectory described by Equation 3.15.

In order to select an appropriate value for δ , we can define the ZS efficiency factor as the ratio of the actual and the maximum attainable ZS deceleration, $a_{ZS}^{(\max)} = \frac{\hbar k \Gamma}{2m} \frac{s}{1+s}$:

$$\eta = \frac{a_{ZS}}{a_{ZS}^{(\max)}} = \frac{1+s}{1+s + \frac{4\delta^2}{\Gamma^2}}. \quad (3.21)$$

Designing the slower with a lower η value enhances robustness, as it leaves a larger velocity headroom at any point along the trajectory. A good way to show this explicitly is to look for the maximum value of the excess velocity $\Delta v(x) = v - v_{\text{ideal}}(x)$ for which the ratio $\frac{v}{v_{\text{ideal}}(x)}$ will decrease. Here $v_{\text{ideal}}(x)$ represents the ideal velocity trajectory from Equation 3.15. This condition can be written down as $\frac{d}{dx} \left(\frac{\Delta v(x)}{v_{\text{ideal}}(x)} \right) < 0$, or equivalently:

$$-\frac{1}{mv_{\text{ideal}}^2} F_{\text{scatt}}(x,v) + \frac{v}{2v_{\text{ideal}}(x_0 - x)} < 0. \quad (3.22)$$

This will eventually yield a quadratic inequality, leading to the maximum locally-stable excess velocity:

$$\Delta v_{\text{max}}(x) = v_{\Gamma} \sqrt{\frac{1-\eta}{\eta}} + \sqrt{\frac{v_{\text{ideal}}^2}{2} - v_{\Gamma}^2} - \frac{v_{\text{ideal}}}{2} \quad (3.23)$$

where $v_{\Gamma} = \frac{\Gamma \sqrt{1+s}}{2k}$. While the fulfilment of this condition does not strictly guarantee stability along the full trajectory²², it clearly demonstrates how the η parameter affects robustness.

In contrast, drawing from Equation 3.16, the design length of the ZS can be expressed as:

$$x_0 = \sqrt{\frac{mv_0^2}{\hbar k \Gamma \eta} \frac{1+s}{s}} \quad (3.24)$$

showing that increasing the robustness of the Zeeman slower by decreasing the η parameter directly calls for a longer slowing trajectory, if the capture velocity v_0 is to be kept unaltered. A typical compromise between these two lines of reasoning is using $\frac{1}{2} \leq \eta \leq \frac{2}{3}$ [57].

As suggested by Equations 3.18, the maximal magnitude of the fields required for the slower is $|B|_{\text{max}} = \max(|B_{\text{bias}}|, |B_{\text{bias}} + B_{\text{prof}}|)$. In order to minimise the required volume of the coils and the electrical power required to drive them, slower are often designed in the so called ‘spin-flip’ configuration, with a negative B_{bias} . Such slower are characterised by the existence of a point along the trajectory with zero net magnetic field. Given that multiple Zeeman levels are a prerequisite for this technique to be used, this inevitably renders the levels degenerate in the vicinity of the zero-field region, leading to the population of the

²²It functions well as a global condition in regions where $v_{\text{ideal}} \gg v_{\Gamma}$

ground state envelope to be redistributed away from the state useful for slowing. It is then essential for the operation of the ZS that the population is optically pumped back to the correct state, before transitions from the remaining m_g levels become off resonant. With a simple heuristic investigation, this condition can be tested for a given set of design parameters. Assuming that the Zeeman slower operates on the $m_g = -J \rightarrow m_e = -(J+1)$ transition, the differential Zeeman coefficient between this transition and the outermost transition of the same type, $m_g = J \rightarrow m_e = J-1$ will be:

$$\Delta\mu' = |\mu'(-J \rightarrow -(J+1)) - \mu'(J \rightarrow J-1)| = 2J\mu_B|g_g - g_e|. \quad (3.25)$$

This means that the detunings of all the transitions lie within the range of $\delta_{\text{diff}} = \frac{\Delta\mu'}{\hbar} \left| \frac{dB}{dx} \right| \Delta x$, where Δx is the distance from the zero crossing. For this purpose, the magnetic field slope at the zero field point can be reasonably estimated as $\left| \frac{dB}{dx} \right| = \frac{B_{\text{prof}}}{x_0}$. Assuming that the velocity at this point is $v \approx v_0$, the time it takes an atom to reach the point where $\delta_{\text{diff}} = \Gamma$, is:

$$\tau = \frac{\hbar\Gamma x_0}{2Jv_0\mu_B|g_g - g_e|B_{\text{prof}}} \quad (3.26)$$

which would mark the point where different transitions are no longer simultaneously resonant. Finally, the number of scattering events during this period can be estimated as:

$$N_{\text{scatt}} = \frac{\eta\Gamma s\tau}{2(1+s)} = \frac{\hbar\eta\Gamma^2 x_0}{4Jv_0\mu_B|g_g - g_e|B_{\text{prof}}} \frac{s}{1+s}. \quad (3.27)$$

The atoms will be optically pumped back into the correct state following the passage through the spin-flip point as long as $N_{\text{scatt}} \gg 2J$, as each scattering process moves the atom one Zeeman state closer to the desired stretched state, on average. If we substitute a set of parameters representative of our experiment²³, we obtain $\frac{N_{\text{scatt}}}{J} \sim 10^3$, proving that the field zero-crossing will not lead to loss of atoms from the trajectory.

As the MOT position cannot coincide with the end of the ZS field profile, it is not practical to configure the slower to bring the atoms to rest. What is normally done, is to slightly offset the bias field from the ideal configuration, such that the atoms are slowed down to a finite final velocity, typically on the order of $10 \frac{\text{m}}{\text{s}}$. In the first order approximation, for shifts that are much smaller than the capture velocity, we can assume that the atoms still trace a trajectory of constant detuning set by the field profile, which leads to the following

²³Parameter values used in this calculations are: $\Gamma = 2\pi \times 29.7 \text{ MHz}$; $x_0 = 0.42 \text{ m}$; $v_0 = 300 \frac{\text{m}}{\text{s}}$; $s = 1$; $J = 6$; $|g_e - g_g| = |1.195 - 1.1638| = 0.0312$ and $B_{\text{prof}} = 300 \text{ G}$, all being representative of the realistic conditions in our experiment.

expression for the final velocity:

$$v_{\text{fin}} = \frac{\mu' B_{\text{bias}} - \hbar(\delta_0 - \delta)}{\hbar k}. \quad (3.28)$$

In the scope of the same approximation, the capture velocity would increase by the same amount. Nevertheless, one should bear in mind that shifting the ‘square root’ field profile compromises the constant force assumption, and increasing the final velocity is done at the expense of robustness.

Another reason which calls for the design with a finite final velocity is the inevitable residual force from the ZS light after the passage through the intended slowing region. Despite being far-red detuned for the slow atoms, the light may still exert enough force to significantly change the velocity and possibly turn the atoms back. In our setup, the beam detuning is $\delta_0 = -540 \text{ MHz} \approx -18 \times \Gamma$ and the distance from the field profile end to the MOT position is $L_{\text{end}} \approx 0.1 \text{ m}$, based on the value of the quantity (also taking $s \approx 1$):

$$\frac{2L_{\text{end}}F_{\text{scatt}}}{m} = \frac{\hbar k \Gamma x}{m} \frac{s}{1 + s + \frac{4\delta_0^2}{\Gamma^2}} \approx 90 \frac{\text{m}^2}{\text{s}^2} \quad (3.29)$$

we can see that this residual force can turn back atoms that exit the ZS field with velocities of $\sim 10 \frac{\text{m}}{\text{s}}$ or less (This effect is also visible in Figure 3.11b).

Final design consideration that is useful to address is the light absorption in the beam. Assuming an ideal slower profile, the scattering rate for an atom following the path would be $R_{\text{scatt}} = \frac{\eta \Gamma}{2} \frac{s}{1+s}$ and the time of flight through the slower is:

$$t_{\text{scatt}} = \sqrt{\frac{2mL}{F_{\text{scatt}}}} = \sqrt{\frac{4mL}{\hbar k \eta \Gamma} \frac{1+s}{s}}. \quad (3.30)$$

If we assume that the flux of atoms interacting with the Zeeman slower is $F = 10^{11} \frac{\text{atoms}}{\text{s}}$ (e.g. from Figure 2.7), then the total rate of scattering of photons is:

$$R_{\text{ph}} = FR_{\text{scatt}}t_{\text{scatt}} = 6 \times 10^{15} \quad (3.31)$$

while the photon flux available in the slowing beam with $P_{\text{ZS}} = 100 \text{ mW}$ is:

$$R_{\text{av}} = \frac{P_{\text{ZS}} \lambda}{hc} = 2 \times 10^{17} \quad (3.32)$$

which still estimates the absorbed fraction at only $\sim 3\%$ despite the flux value used in this calculation being a very safe overestimate.

3.4.3 Implementation

The Zeeman slower coil system consists of a set of six independent parts. Firstly, the bias coil and a pair of profile coils create the main profile of the slower field. The profile coil is divided into two sections as our implementation assumes a ‘spin-flip’ configuration, characterised by the presence of a zero-field point along the length of the slower. This coil layout requires only about a half of the maximum magnitude of the magnetic field compared to an equivalent non-‘spin-flip’ slower. Furthermore, as the field goes back to zero after the end of the slower, this assures that the slow atoms are kept off-resonant after the slower, avoiding excessive slowing in the region between the ZS and the MOT.

The main coils are augmented with a compact end coil at the entrance to the MOT chamber, that was added to translate the end of the slowing region closer to the MOT position after issues with loading were observed (described in detail in Subsection 3.4.4). Finally, a pair of rectangular compensation coils on either side of the MOT chamber provides the possibility of cancelling the field offset and gradient that originates from the Zeeman slower at the centre of the MOT. The details about the geometry of the main coils are given in Table 3.3. All these coils are made up from 1 mm coated copper wire²⁴. The bias/profile coil system was wound directly onto the vacuum tube, that also accommodates water cooling for the coils. This was done on a lathe in the machine workshop, and the winding layers were glued with heat resistant epoxy resin²⁵. The compensation coils are wound on 50 mm by 120 mm rectangular brackets, with 24 (12) windings in front of (behind) the MOT chamber. The full drawing of the coils along with the calculated field profiles that they create is shown in Figure 3.12.

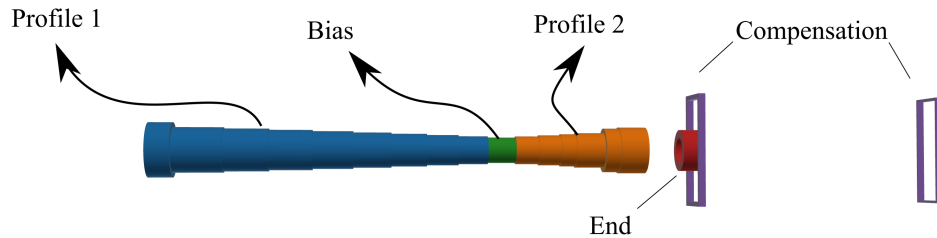
	Layer / Length [mm]											
	1	2	3	4	5	6	7	8	9	10	11	12
Bias	420											
Profile 1 (neg.)	282	257	230	200	168	134	98	61	20	20	20	20
Profile 2 (pos.)	114	94	75	62	37	37	37	37	24			
End (pos.)	19	19	19	19	19	19						

Table 3.3 **Zeeman Slower Coil Geometry** - The design originates from [70]

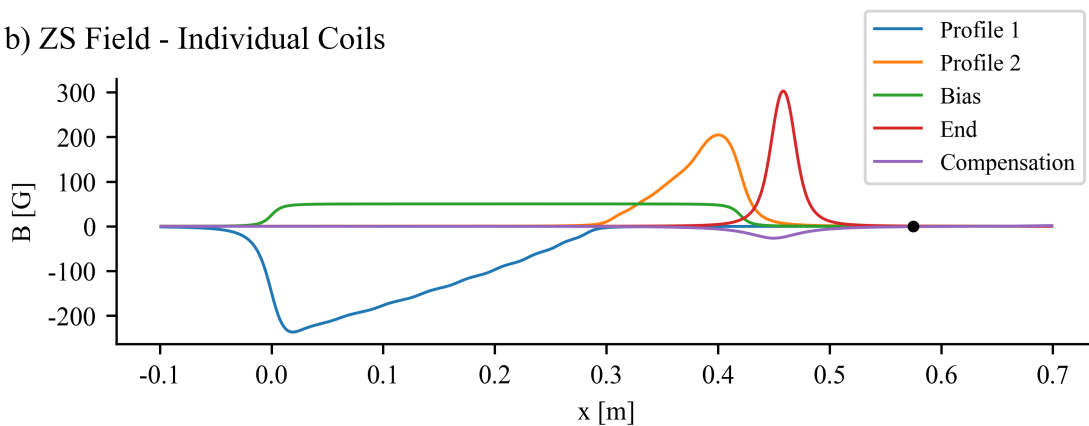
²⁴Insulation coating is Polyester 200/polyamide-imide rated up to 212 °C

²⁵Electrolube ER2223, rated up to 180 °C

a) ZS Coils - Geometry



b) ZS Field - Individual Coils



c) ZS Field - Total

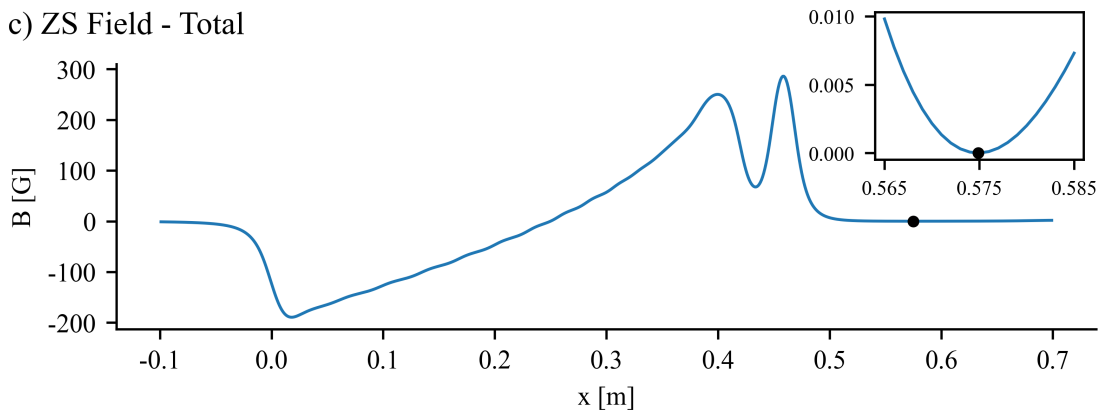


Fig. 3.12 **Zeeman Slower Coils and Fields** - a) The spatial layout of the Zeeman slower coil system showing the profile coils (1 - blue, 2 - orange), the bias coil (green), the end coil (red) and the pair of compensation coils (violet). b) The calculated longitudinal magnetic field components created by individual coils from the system. c) The total calculated Zeeman slower magnetic field with the inset focusing on the region around the MOT position (black dot). For reference the coil currents corresponding to the example field profile given in b) and c) are $I_{\text{bias}} = 4.0$ A, $I_{\text{prof1}} = -2.2$ A, $I_{\text{prof2}} = 2.3$ A, $I_{\text{end}} = 7.4$ A, $I_{\text{comp1}} = -6.9$ A, $I_{\text{comp2}} = 0.9$ A.

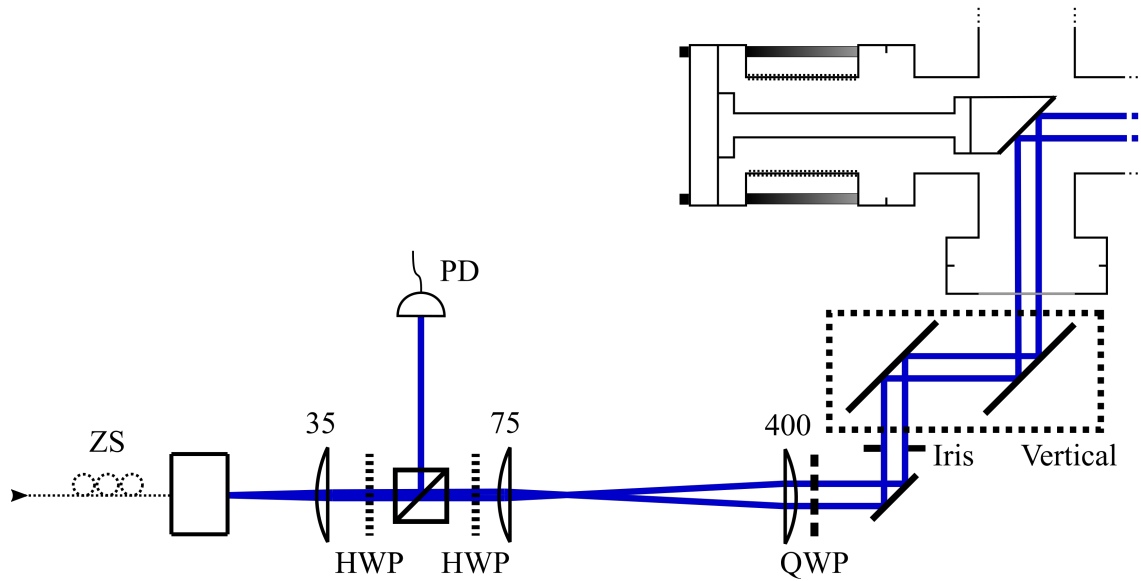


Fig. 3.13 **Zeeman Slower Optics** - The Zeeman slower beam is created using a three-lens system that provides the tunability of the beam radius between 2 mm and 8 mm while keeping the beam approximately collimated along the length of the chamber. The polarisation is set to be circular after the final mirror using the PBS cube and a pair of wave plates.

If we fit an ideal ZS field profile to the predicted field profile of the coils installed in our system, the profile and bias fields would take the values $B_{\text{bias}} = 12.5 \frac{\text{G}}{\text{A}} \times I_{\text{bias}} + 95 \frac{\text{G}}{\text{A}} \times I_{\text{prof}}$ and $B_{\text{prof}} = 230 \frac{\text{G}}{\text{A}} \times I_{\text{prof}}$.

The slowing light beam is delivered to the experiment through an optical fibre, and the delivery optics that sets the size and polarisation of the beam is shown in Figure 3.13. The system is designed such that it can produce nearly collimated beams with waist radii ranging from 4 mm to 6 mm that can be easily tuned. The maximum optical power that can be directed into the chamber is 100 mW.

3.4.4 Optimisation and Results

The first step in setting up the Zeeman slower is aligning the beam through the vacuum chamber. The beam size was adjusted using the three-lens system after the fibre, and the waist radius was measured to be within 5% of the desired 4.0 mm at positions corresponding to the start and the end of the ZS region. The polarisation was then set to be circular using the pair of wave-plates mounted in the path of the beam. As the mirrors alter the polarisation that is not purely S or P oriented, and the goal is for the polarisation to be circular after the last reflection, a metal mirror was inserted before the chamber to mimic the effect of the in-vacuum mirror during this operation. The alignment was performed using the two

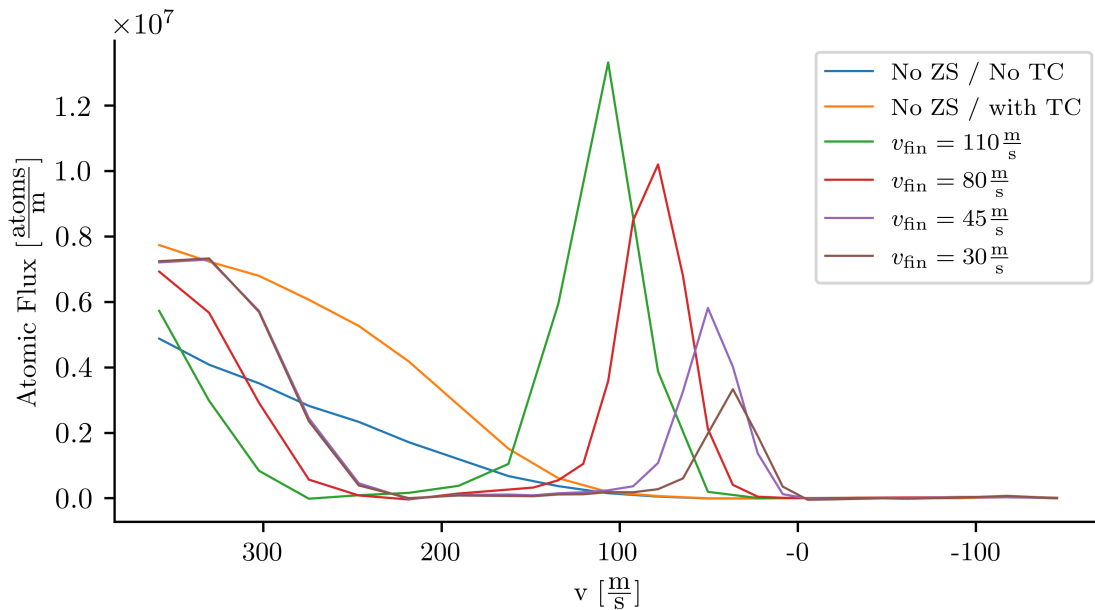


Fig. 3.14 **Zeeman Slower Velocity Distribution** - Fluorescence measurements taken using a probe beam tilted 2.5° into the atomic beam in the MOT chamber. The Zeeman slower causes the atoms to form a peak in the velocity distribution, that is then translated to slower velocities by tuning the field profile. The total flux contained in the peak drops as the progressively slower atoms splay out further, hitting the walls of the chamber. This was subsequently improved by installing the End coil

periscope mirrors, mounted immediately prior to the chamber. In order to aid the alignment process, a camera was directed into the cross with viewports in the HV section of the chamber, providing a view of the fluorescence induced by the ZS light incident on the atoms in the beam. Given the very long path length of this beam (> 1 m from the second periscope mirror to the oven-side of the ZS tube), a high degree of accuracy is required when performing this alignment²⁶.

We used fluorescence imaging with a tilted 583 nm beam to measure the velocity distribution after the Zeeman Slower. The details about this technique are provided in Appendix C, and here we use both the ‘Top’ and ‘Side’ beams described in the appendix. Figure 3.14 shows an example of the ‘Top’ beam measurements where the final velocity of the slow peak in the distribution is tuned using the currents in the coils (Bias and Profile 2, the End coil current is zero):

As Figure 3.14 clearly shows, the flux contained in the slowed peak clearly starts dropping as the atoms are slowed further. The reason for this is the splaying out of the atomic beam caused by the increasing relative contribution of the transversal velocity as the longitudinal velocity is decreased. The end of the Profile 2 coil is positioned 65 mm from the end of the

²⁶The effects of poor alignment are visible in Figure 3.16.

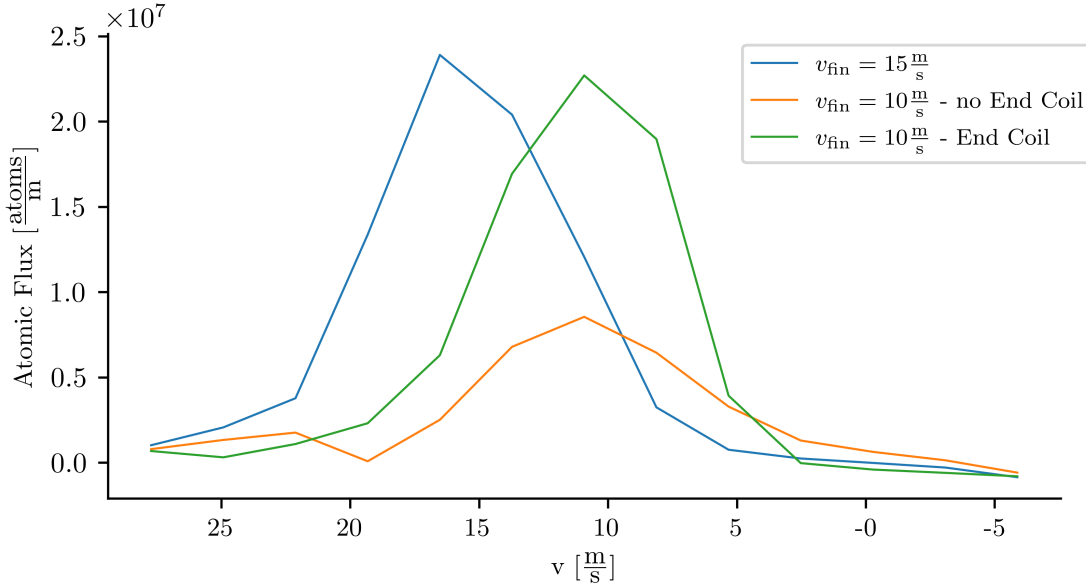


Fig. 3.15 **Zeeman Slower Side Beam Measurements** - A higher resolution measurement using a beam that is tilted 57° into the atomic beam. The blue signal represents a Zeeman slowed flux distribution obtained without resorting to the End coil, having a final velocity of $15 \frac{\text{m}}{\text{s}}$. The effect of the End coil is demonstrated here by comparing the two peaks for which the velocity was further reduced either using only the bias field (orange signal) or by turning on the End coil (green signal). The losses are reduced by postponing the final slowing until the End coil, hence reducing the transversal spreading of the beam. Additionally, by integrating the area under the curves, we can estimate the flux of the slow ($v < v_c^{\text{MOT}} \approx 8 \frac{\text{m}}{\text{s}}$) atoms at $\sim 5 \times 10^7 \frac{\text{atoms}}{\text{s}}$ for the case with the End coil. The actual MOT loading rate we measure (see Figure 4.13b) is approximately five times lower, but the flux estimate done here should be taken with caution, due to calibration errors.

ZS tube²⁷, so atoms with average transversal velocity of $\sim 1 \frac{\text{m}}{\text{s}}$ slowed down to $\sim 10 \frac{\text{m}}{\text{s}}$ longitudinally would see their rms waist increase by 6.5 mm, leading to a large portion of the atoms hitting the walls of the ZS tube (ID = 8 mm). Additionally, as the atoms have to cover another 100 mm from the end of the ZS tube to the MOT capture region, even some of the atoms that make it through the ZS tube will eventually evade the MOT. This was reflected in comparatively poor loading of the MOT, only reaching the atom numbers in the low 10^7 range.

In order to mitigate for this problem, we wound an extra coil (otherwise referred to as the ‘End’ coil) at the end of the ZS tube, within the narrow region between the water cooling connection and the MOT chamber. As the centre of this coil is only 20 mm away from the end of the tube, this allowed us to use the main set of ZS coils (Profile 1/2 and Bias) to slow the flux peak to a higher velocity, and then introduce a final kick towards the very low

²⁷In order to allow space for the water cooling tube connection and the vacuum chamber flange bolts

velocities in the region of the End coil, shortening the distance over which the atomic beam would expand. The atomic flux measurements directly demonstrating this effect are shown in Figure 3.15.

As the final measure of quality of the slowing process is the MOT loading rate, we can directly compare the scenarios with and without the end coil. The comparison is shown in Figure 3.16, with the MOT number after 15 s of loading. While this figure demonstrates the effect of the end coil on MOT loading, the velocity profiles are not the representative of the best configuration that we have achieved. The ZS laser beam seems to be misaligned resulting in a portion of the atoms being unaddressed. This will be treated at the next opportunity for doing maintenance which consists of a tedious alignment process.

Another possibility for solving the issue of the transversal expansion of the beam, that has been implemented by some research groups, includes a pair of slowing beams that would implement a final decelerating kick just prior to the MOT [45, 82]. Analogously to the end coil approach, the ZS is then used to slow the atoms to a finite velocity at which the splaying is not extreme, and these beams would then be used to lower it further, below the capture velocity of the MOT.

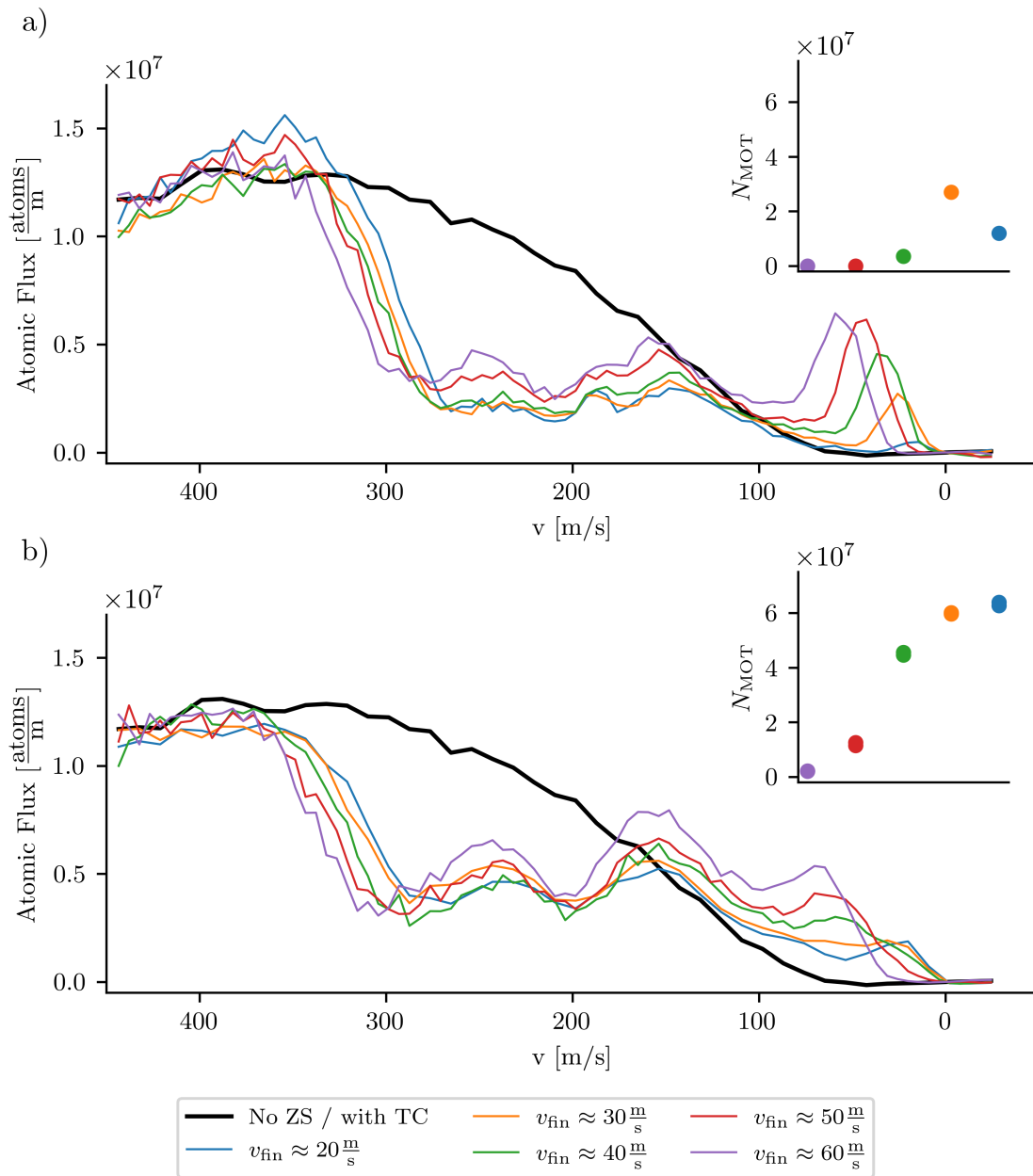


Fig. 3.16 **Zeeman Slower velocity distribution and MOT loading** - Flux in the atomic beam after emerging from the Zeeman slower resolved over longitudinal velocities for a ZS configuration without (a) and with (b) the end coil. The coloured correspond to five different bias currents resulting in progressively slower atoms in the MOT region (solid black line shows the distribution without the Zeeman Slower). The insets show atom numbers present in the MOT after 15 s of loading, directly reflecting the loading rate. The configuration without the end coil suffers from a significant drop-off in the atom number due to lateral spreading at the end of the slower. Note that the performance of the Zeeman slower was also plagued by poor alignment at the time of the measurement, resulting in a significant portion of the atoms not experiencing slowing.

Chapter 4

Narrow-Line Magneto-Optical Trap

With the slowing on the atomic beam implemented, the stage in the cooling sequence that follows next is the magneto optical trap (MOT). From this point onwards, it is beneficial to use the narrow, yellow transition for laser cooling, for its low Doppler temperature of $T_D = 4.6\mu\text{K}$. By implementing the MOT on this transition, we managed to cool down the atomic cloud to as low as $10\mu\text{K}$. Apart from the low temperatures, sufficiently tight confinement and stable and consistent spatial manipulation of the cloud are also required to optimise the atomic cloud for subsequent loading into the optical dipole trap.

4.1 Principle of Operation

The magneto-optical trap combines the Doppler and the Zeeman effect to harness the light scattering force for trapping and cooling simultaneously. It is implemented by superimposing counter-propagating near-resonant laser beams with a magnetic field gradient. In the most common configuration, also used in our experiment, one pair of beams is vertical (z -axis), and the remaining two pairs are in the horizontal plane - all being mutually orthogonal. The magnetic field gradient is generated using a pair of coils in the quasi anti-Helmholtz configuration and takes the form of a quadrupole field:

$$\mathbf{B}(x, y, z) = G \left(-\frac{1}{2}\mathbf{x} - \frac{1}{2}\mathbf{y} + \mathbf{z} \right) \quad (4.1)$$

where $G = \left| \frac{\partial B}{\partial z} \right|$ is the magnitude of the quadrupole field gradient. The primary function of the quadrupole field is to introduce a spatially varying Zeeman shift to transitions between atomic states. For a pair of levels $|g\rangle$ and $|e\rangle$, with orbital angular momentum projection

quantum numbers m_g and m_e , this shift is equal to:

$$\delta_B = \frac{\mu_B B}{\hbar} (g_g m_g - g_e m_e) \quad (4.2)$$

where g_g and g_e are the Landé projection factors for the two states. Note that a positive sign of δ_B corresponds to the laser being blue-shifted w.r.t. the transition. We use the 583 nm narrow-line transition for the MOT, where the ground state has $J_g = 6$ and the excited state has $J_e = 7$. As listed in Chapter 1, the Landé factors for these two states are $g_g = 1.163801$ and $g_e = 1.195$. For a MOT operating on the lowest lying Zeeman state in the ground state manifold ($m_g = -6$), the Zeeman shift factors for the three types of transitions can be calculated from Equation 4.2 and are provided in the Table 4.1.

$m_g \rightarrow m_e$	$-6 \rightarrow -7$	$-6 \rightarrow -6$	$-6 \rightarrow -5$
Designation	σ^-	π	σ^+
$\frac{\delta_B}{2\pi B} \left[\frac{\text{MHz}}{\text{G}} \right]$	1.93	0.26	-1.41

Table 4.1 **Transition Zeeman Factors** - for the three different types of transitions from the ground state via the 583 nm transition.

Another manifestation of the atom-field interaction is the position-dependent magnetic force onto the atoms. As each atom carries a magnetic dipole moment $\mu = \mu_B g_g m_g$ and is subjected to a field gradient, there is a net force of

$$\mathbf{F} = -\mu \nabla |\mathbf{B}| \quad (4.3)$$

acting on the atom, accounting for the fact that the dipole direction is always aligned with the B -field vector. Since the atoms are in a high-field seeking state, this effect contributes with some anti-trapping. Along the vertical direction in the region below the centre of the MOT, this leads to an effective gravity field strength of:

$$g' = g + G \frac{\mu}{m} . \quad (4.4)$$

One peculiarity of narrow-line MOTs is the vertical sagging and the accompanying bowl-like appearance. The understanding of the vertical position dependence on MOT parameters can be drawn from a simple model where the atom interacts only with the bottom MOT beam [47]. Assuming this, the balance of gravity and the light scattering force onto an atom (at

rest) along the vertical direction can be written as (using Eq F.1):

$$\frac{\hbar k \Gamma}{2} \frac{s}{1 + s' + \frac{4\delta_{\text{loc}}^2}{\Gamma^2}} = mg' \quad (4.5)$$

where δ_{loc} represents the local detuning of the atom, given by:

$$\delta_{\text{loc}} = \delta_0 + \delta_B = \delta_0 + Gz\beta_{\sigma^-} . \quad (4.6)$$

From the force balance equation, one can then obtain the local detuning required for an atom to satisfy it:

$$\delta_{\text{loc}} = -\frac{\Gamma}{2} \sqrt{\eta s - s' - 1} \quad (4.7)$$

where we define $\eta = \frac{\hbar k \Gamma}{2mg'}$. Combining the above equations, one obtains the expression for the equilibrium position:

$$z_{\text{eq}} = -\frac{\delta_{\text{loc}} - \delta_0}{\beta_{\sigma^-} G} . \quad (4.8)$$

While in this regime, most of the cooling originates from the bottom beam (from here on, we also assume $s = s'$ for the same reason), and the velocity damping coefficient can be readily extracted [83]:

$$\alpha_z = -\frac{1}{m} \frac{\partial F_{\text{scatt}}^{(z)}}{\partial v_z} = \frac{2\hbar k^2 \sqrt{(\eta - 1)s - 1}}{ms\eta^2} \quad (4.9)$$

along with the effective trapping frequency:

$$\omega_z = \sqrt{-\frac{1}{m} \frac{\partial F_{\text{scatt}}^{(z)}}{\partial z}} = \sqrt{\frac{2\hbar k G \beta_{\sigma^-} \sqrt{(\eta - 1)s - 1}}{ms\eta^2}} . \quad (4.10)$$

Further to this, the diffusion coefficient in the MOT is shown to be (see Appendix F, also [57, 83]):

$$D_z = \frac{\hbar^2 k^2 \Gamma}{2\eta} \quad (4.11)$$

leading to the equilibrium temperature of :

$$T_{\text{eq}} = \frac{D_z}{k_B m \alpha} = \frac{\hbar \Gamma \eta s}{4k_B} \sqrt{\frac{1}{(\eta - 1)s - 1}} . \quad (4.12)$$

The regime where the atoms only interact with the bottom beam is only valid for sufficiently large detunings. If both vertical beams are included, we can see that the sagging only sets in when the detuning is significantly larger than the linewidth of the transition. As

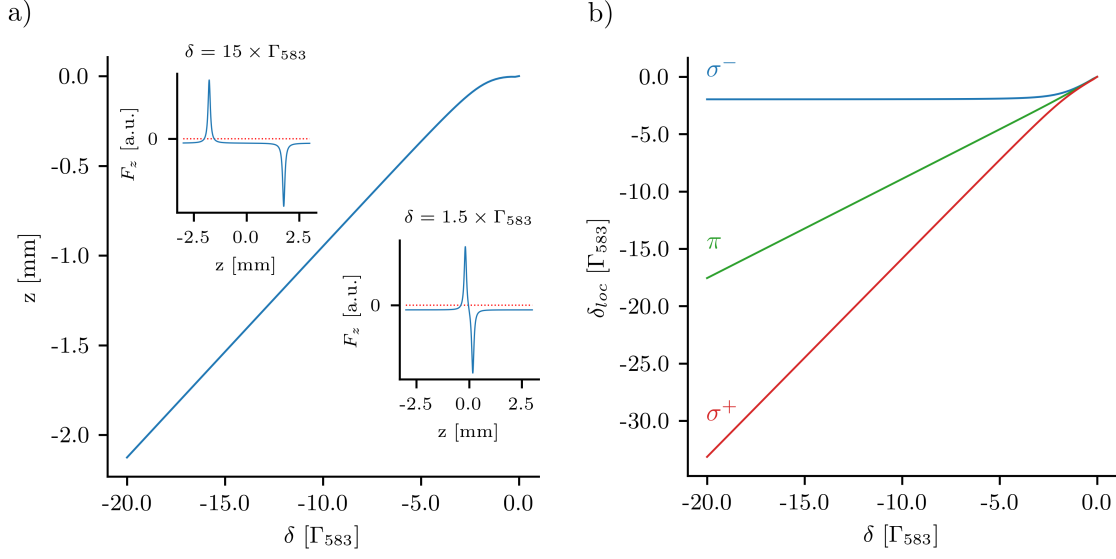


Fig. 4.1 **cMOT Position and Local Detuning** - Calculated for $s = 2$ and the field gradient of $8 \frac{\text{G}}{\text{cm}}$. a) Equilibrium vertical position of the MOT cloud as a function of the laser detuning. For detunings that are comparable to the transition linewidth, the light force is able to support the MOT close to the origin. Once the force profiles of the top and the bottom beam separate in frequency space, the cloud position will trail the bottom beam force profile as it moves in the $-z$ direction (depicted on the two insets) b) Local detuning of the atoms in the cloud as a function of the laser detuning. For small detunings the three types of transitions (σ^- , π and σ^+) are not mutually detuned as the atoms are located in the vicinity of the field zero. Once vertical sagging sets in, the three transitions drift apart, opening the possibility for a spin-polarised MOT, given that the atoms will preferentially interact with the σ^- bottom beam.

figure 4.1b shows, sagging is required for the three transitions to become detuned, making it a prerequisite for spin polarisation.

For a MOT in the sagging regime it is also possible to estimate the volume occupied by the cloud using a simple set of approximations. The boundary within which the atoms are constrained by the light force is approximately defined by the resonance condition applied to stationary atoms:

$$\delta_0 = |B|\beta_{\sigma^-} \quad (4.13)$$

which, assuming the quadrupole field profile from Equation 4.1, represents an ellipsoidal surface:

$$x^2 + y^2 + 4z^2 = \frac{4\delta_0^2}{G^2\beta_{\sigma^-}^2} = R_0^2. \quad (4.14)$$

Due to the gravitational pull, the atoms will occupy the bottom portion of this region and the characteristic height of the cloud can be estimated from equating the gravitational and thermal energy scales, i.e. $h = \frac{k_B T}{mg}$. The approximate volume of the cloud then takes the

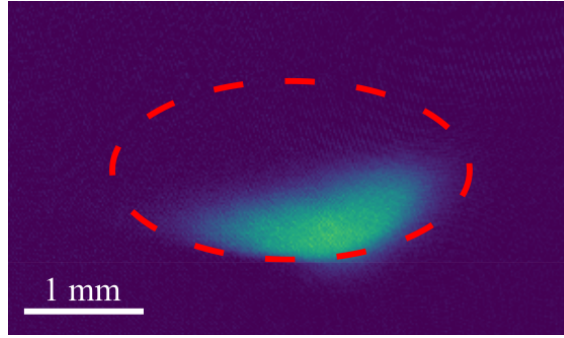


Fig. 4.2 **Compressed MOT Cloud in the Trap** - The figure shows a compressed MOT cloud with the theoretical ellipsoidal surface of constant force drawn from Equation 4.14 (The size of the ellipse is calculated from the light and field parameters while the position is adjusted freely to align it with the cloud).

form:

$$V = \frac{2\pi}{3} h^2 (3R_0 - 2h) . \quad (4.15)$$

This formula predicts $V_{\text{MOT}} = 6 \times 10^{-9} \text{m}^3$ and $V_{\text{cMOT}} = 6 \times 10^{-12} \text{m}^3$ if parameters typically used in our experimental sequence are used ¹. The latter prediction seems to underestimate the realistic size, as it can be deduced by comparing it to Figure 4.2, which shows the compressed MOT cloud along with the predicted force profile based on the parameters.

Another useful estimation that can be drawn from a similar simplified model is that of the MOT capture velocity. Assuming that the atom approaches along the x -axis with velocity v , and interacts only with the $\pm x$ MOT beams. In order to emulate the situation from our experiment, where the incoming atoms do not enter the chamber along one of the MOT beam directions, but rather interact with components from both horizontal pairs, each incident at a different angle to the atomic beam, the interaction is limited to a 3 cm wide region around the origin, and the light intensity obeys a Gaussian distribution with a waist radius of $w_x = 1.5$ cm. The equation of motion takes the form:

$$m \frac{d^2x}{dt^2} = \frac{\hbar k \Gamma}{2} \left(-\frac{s}{1 + s + \frac{4\delta_{x,v}^2}{\Gamma^2}} + \frac{s}{1 + s + \frac{4\delta_{-x,-v}^2}{\Gamma^2}} \right) \quad (4.16)$$

where the detuning $\delta_{x,v}$ now encapsulates both the Zeeman and Doppler shifts:

$$\delta_{x,v} = \delta_0 + \delta_B + \delta_D = \delta_0 + \frac{G}{2} x \beta_{\sigma^-} + kv \quad (4.17)$$

¹ $G = 8.3 \frac{\text{G}}{\text{cm}}$; $s_{\text{MOT}} = 50$; $s_{\text{cMOT}} = 0.2$; $\delta_{\text{MOT}} = -12$ MHz and $\delta_{\text{cMOT}} = -3$ MHz.

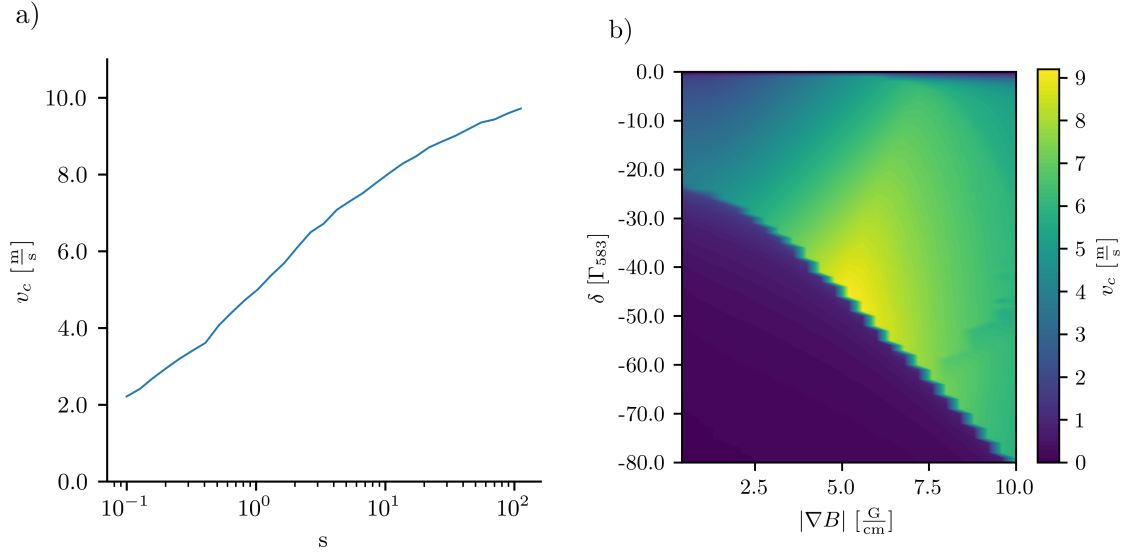


Fig. 4.3 **Capture Velocity Estimation** - a) Dependence of the capture velocity on the light intensity, expressed through s , maximised over the other parameters (detuning and field gradient). b) The capture velocity for $s = 55$ over different field gradients and detunings. The dark region in the lower left corner is caused by the sharp cut-off of the MOT intensity at the edges of the cooling region.

and the saturation parameter reflects the Gaussian intensity distribution $s = s_0 \exp\left(-2\frac{x^2}{w_x^2}\right)$. This equation can be integrated numerically to obtain an estimate of the capture velocity. The free parameters that can be accessed experimentally are the bare laser detuning, δ_0 , the gradient G and the light intensity, here represented through s . The results of the numerical simulation are shown in Figure 4.3. In the presented results, the detuning and the field gradient are constrained to ranges that are experimentally accessible, while the light intensity is varied over a wider range, for demonstrative purposes. We see that in the ideal scenario, assuming the largest experimentally achievable value of $s = 55$, we can expect the capture velocity of the MOT to be about $9 \frac{\text{m}}{\text{s}}$.

4.2 583 nm Laser

The yellow laser system is primarily designated for the MOT, with the plan to also employ it in the Bragg diffraction setup in the future, as described in Section 5.5. A diode laser with a tapered amplifier and a frequency doubling cavity² provides up to 700 mW of light, which is more than sufficient for the operation of the MOT, given the low saturation intensity of

²Toptica DL-TA-SHG-Pro

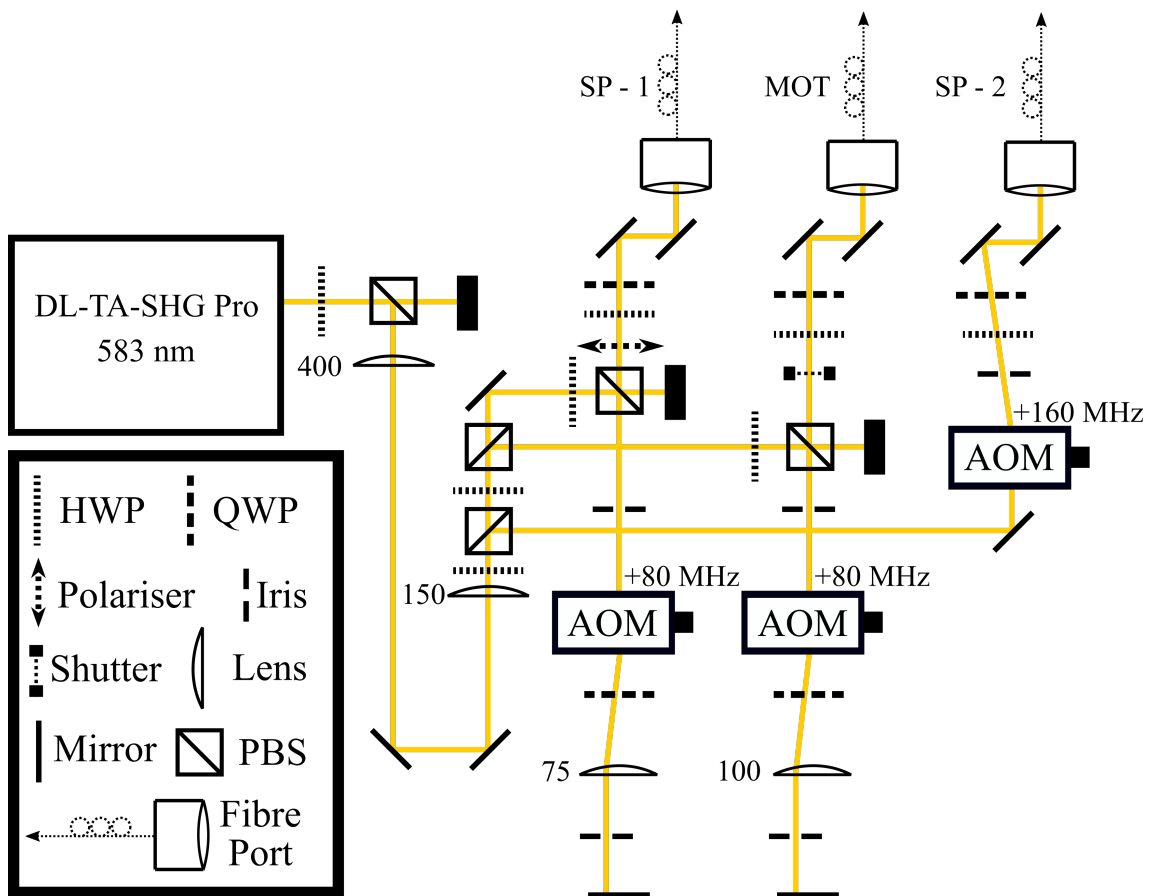


Fig. 4.4 **583 nm Laser Distribution Optics** - All focal lengths are in millimetres. Fibre Ports: SP (1 & 2) = Spectroscopy; MOT = Magneto-Optical Trap.

the 583 nm transition of $0.13 \frac{\text{mW}}{\text{cm}^2}$. The layout of the optical system is depicted in Figure 4.4. This setup employs three AOMs³ to independently control the frequency offsets of the MOT light and the two beams used for Modulation Transfer Spectroscopy. In an alternative locking setup employing shelving spectroscopy, we only use the light from the SP-1 fibre.

The arrangement of the polarizing beam splitters in the setup is made such that any spurious reflections from either of the AOM systems or fibres cannot find a direct path to any of the other fibres. This was done after the observation that these back reflections, either from the MOT branch or the other spectroscopy branch can cause noise in the MTS locking setup that decreases the quality of the lock, sometimes destroying it altogether. Similarly, reflections in the opposite direction from spectroscopy branches into the MOT system can have detrimental effect onto the lifetime of the atoms in the trap.

³2 × Gooch & Housego AOMO 3080-125 Acousto-Optical Modulator at 80MHz; Gooch & Housego AOMO 3200-125 Acousto-Optical Modulator at 200MHz

4.3 Spectroscopy and Laser Stabilisation

As the main purpose of this laser system is cooling in the magneto optical trap operating on a narrow atomic transition ($\Gamma = 2\pi \times 190$ kHz), it is essential to tightly stabilise its frequency. Depending on its spectral characteristics, any laser frequency noise would lead to either heating or positional jitter in the trap. Our main locking scheme in this laser system so far used to be modulation transfer spectroscopy, but due to the lack of an adequate replacement for the hollow cathode lamp that reached the end of its lifespan, alternatives had to be found. We attempted switching to an alternative locking technique - shelving spectroscopy [84] - but the frequency stability turned out to be inferior to the MTS locking setup. A permanent solution was found in an Ultra Low Expansion (ULE) optical cavity, which will be implemented in the weeks following the submission of this thesis.

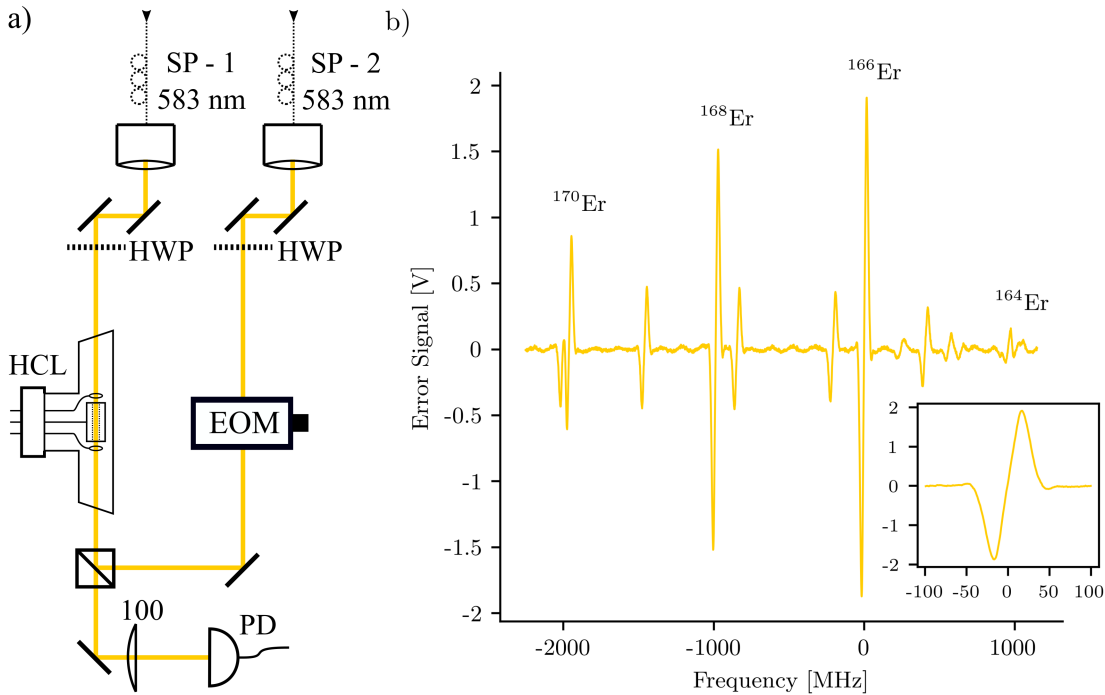


Fig. 4.5 **Modulation Transfer Spectroscopy Setup (with probe-pump offset)** - a) The setup used for locking the 583 nm laser to the atomic transition. The probe and the pump beams are supplied from different AOMs via two fibres introducing the possibility of a frequency offset between them to reduce the contribution of spurious reflections to interference noise. b) An example spectroscopy signal from the 583 nm transition. The inset presents a zoom in on the ^{166}Er error signal, in this case having the slope of $132 \frac{\text{mV}}{\text{MHz}}$.

4.3.1 Modulation Transfer Spectroscopy

The simplest version of the setup, such as the one described in Section 3.2 that is used for locking the 401 nm laser, is sensitive to noise that originates from spurious reflections along the path of the pump beam interfering with the probe light. Given the strict requirements for the quality of the lock that are imposed on this laser system, the locking system needs to be optimised on all fronts. This issue can be mitigated by introducing a frequency offset between the two beams, which shifts the interference noise in the frequency spectrum, while leaving the useful signal at the modulation frequency [72]. This is implemented by drawing the pump and the probe beam from two different AOMs, allowing for their frequencies to be tuned independently. The setup with this tweak implemented is shown in Figure 4.5a, along with an example of a recorded spectroscopy signal in Figure 4.5b.

Due to Heraeus discontinuing their model of the see-through HCL⁴, and the inability of the other HCL that we sourced to match the desired performance (and initially, failure to provide a measurable signal), we were prompted to try locking both lasers to a single spectroscopy cell. The setup used is essentially an overlay of the two previously shown MTS systems (Figures 3.2 and 4.5), and it is shown in Figure 4.6. We use a set of filters and dichroic mirrors to overlap the two wavelengths in the HCL and through the EOM, and then to split them again for detection. This approach worked in principle, but was problematic for a number of reasons. Firstly, the exact shape and slope of the yellow (narrow-line) locking signal was dependent on the intensity of the blue laser beams, leading to increased noise in the yellow signal. Additionally, the optimal density of sample atoms differed greatly for the two transitions, with the blue signal favouring lower densities due to strong absorption, while the yellow signal favoured higher densities. Since the setup from Figure 4.5 remained as the only viable option for locking the yellow laser based on the available frequency references, the blue laser locking was migrated to the modulated fluorescence spectroscopy method described in Subsection 3.2.2. Ultimately, with the Heraeus HCL reaching the end of its lifetime, we briefly attempted the shelving spectroscopy method outlined below, and then decided to switch to an ultra-low expansion (ULE) cavity⁵ as the long term solution for this locking setup. This will also lead to a tighter lock, enhancing the MOT positional stability and lowering the ultimate achievable temperature.

⁴See Section 3.2 for details.

⁵From Stable Laser Systems

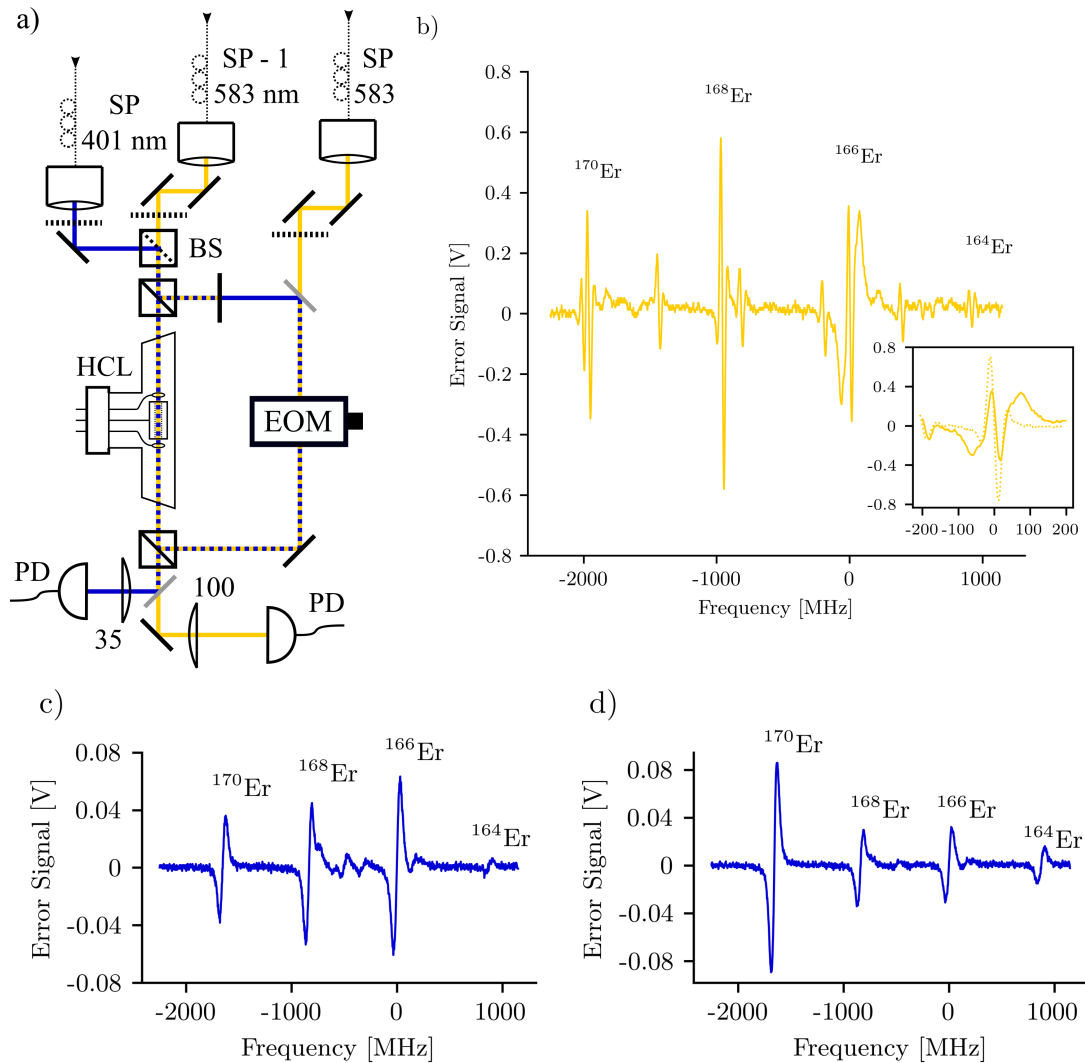


Fig. 4.6 Modulation Transfer Spectroscopy Setup (dichroic version) - a) Setup trialled for locking both the 401 nm and the 583 nm lasers to the respective atomic transitions using a single Hollow cathode lamp. The yellow light is supplied via a pair of fibres with a frequency offset between the pump and the probe, while the blue light enters at a single frequency. The two wavelengths are merged and separated using a 50:50 beam splitter and dichroic mirrors. b) An example spectroscopy trace on the yellow transition with the blue locked to the respective transition of the ^{166}Er isotope. The inset contrasts the error signal distorted by resonant blue light (solid line) with the bare signal obtained when the blue light is absent or non-resonant (dotted line). The distortion results in a considerably smaller slope, $45 \frac{\text{mV}}{\text{MHz}}$ as opposed to $87 \frac{\text{mV}}{\text{MHz}}$ in this example, that cannot be restored by changing the phase. c) Blue error signal for a low HCL current setting (5 A). d) Blue error signal for a high HCL current setting (10 A), at which the dichroic setup needs to be operated, showing the damping of peaks corresponding to abundant isotopes (^{166}Er , ^{167}Er , ^{168}Er) due to absorption.

4.3.2 Shelving Spectroscopy

Owing to its narrow linewidth, spectroscopy methods on the 583 nm transition are substantially more difficult to implement than the ones on the broad 401 nm transition. This was reflected in the overall difficulty even to observe a spectroscopy signal on the narrow transition using the atomic beam as the spectroscopic medium. Taking into account that the scattering rate would be smaller by a factor $\frac{\Gamma_{583}}{\Gamma_{401}}$ and also that the light would simultaneously resonantly address fewer atoms, as few as another factor of $\frac{\Gamma_{583}}{\Gamma_{401}}$, the overall signal can be up to $\left(\frac{\Gamma_{401}}{\Gamma_{583}}\right)^2 = 2.4 \times 10^4$ times weaker. Inspired by the approach of [84], we have set up a system where the atoms are excited by the yellow light, but the resulting populations are 'read out' using blue light, leading to a stronger signal. Unlike the setup in reference paper, the pump and the probe beam cannot be spatially separated in our scheme, because the lifetime of the narrow-line excited state, $\tau_{583} = 5.4 \mu\text{s}$ is too short for the atoms to cover the distance between the two beams. Instead, we completely overlap the beams, which still induces a dependence between the intensity of the fluorescence signal from the 401 nm probe beam on the frequency of the 583 nm pump beam. Similarly to Subsection 3.2.2, the pump light is modulated at 20 kHz and a lock-in detection technique⁶ is used to extract the signal from the probe beam fluorescence (Figure 4.8). While the obtained locking slope is comparable to the one produced by the best iteration of the MTS setup (Figure 4.5), we suspect that the issue with this method lies in the narrower locking bandwidth originating from the constraints of the lock-in detection method⁷.

⁶Implemented using the Zurich Instruments HF2 lock-in amplifier

⁷The modulation frequency is limited by the response of the AOM driver, which in turn sets an upper limit on the filter bandwidth that can be used after the demodulator.

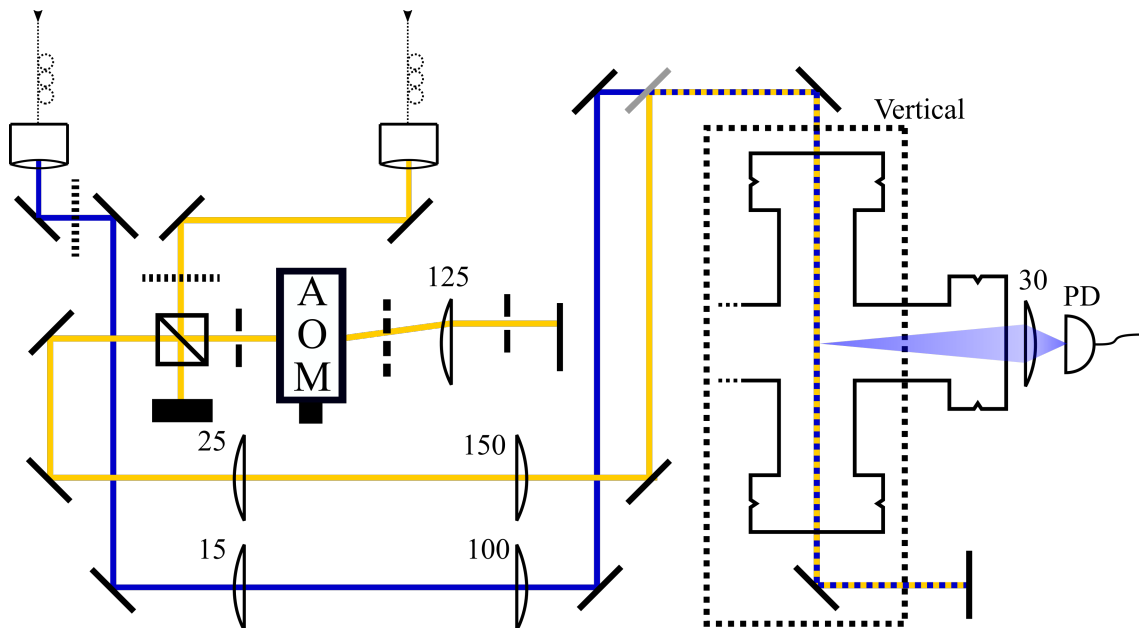


Fig. 4.7 **Shelving Spectroscopy** - The fluorescence spectroscopy method that addresses the atoms with the light at the wavelength corresponding to the narrow transition (yellow) and then probes the populations using the broad transition (blue laser). Since the yellow laser light is frequency modulated, the modulation is transferred to the atomic level populations, and consequentially into the blue fluorescence signal. This is then detected using a lock-in amplifier, leading to a signal exemplified in Figure 4.8.

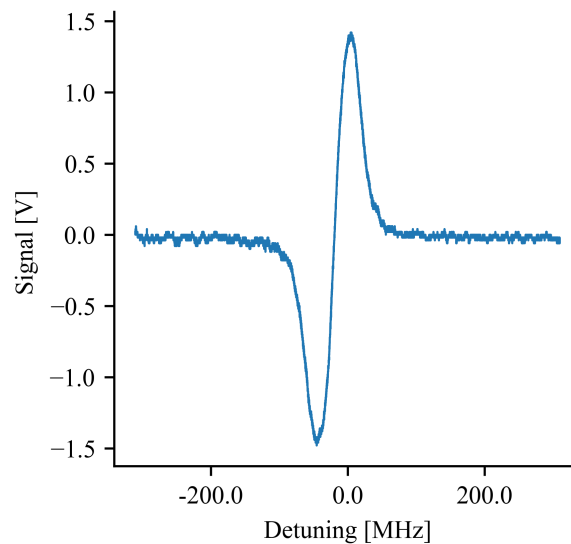


Fig. 4.8 **Shelving Spectroscopy** - The signal from the shelving spectroscopy used for locking the yellow laser. The steepest locking slope that we managed to obtain from this system while keeping the signal to noise ratio as low as possible is $96 \frac{\text{mV}}{\text{MHz}}$.

4.4 Implementation of the MOT

Being an intermediate stage in the cooling sequence, the main role of the MOT is to prepare the atoms for transfer into the optical dipole trap (ODT). Ideally, we wish for a maximum number of atoms at the lowest temperature possible, with good positional stability, to eventually assure high and consistent phase-space density in the ODT. The number of atoms loaded is a result of interplay of the MOT capture velocity, and the Zeeman slower efficiency. Upon compression of the MOT, the temperature is primarily set by the light intensity and the stability of the laser frequency. Finally, the positional stability, which is crucial for repeatable loading into the dipole trap, is linked to laser frequency stability and light intensity and polarisation fluctuations in the MOT beams. As it will be laid out below, this latter condition proved to be crucial for consistent transfer.

4.4.1 Experimental Control

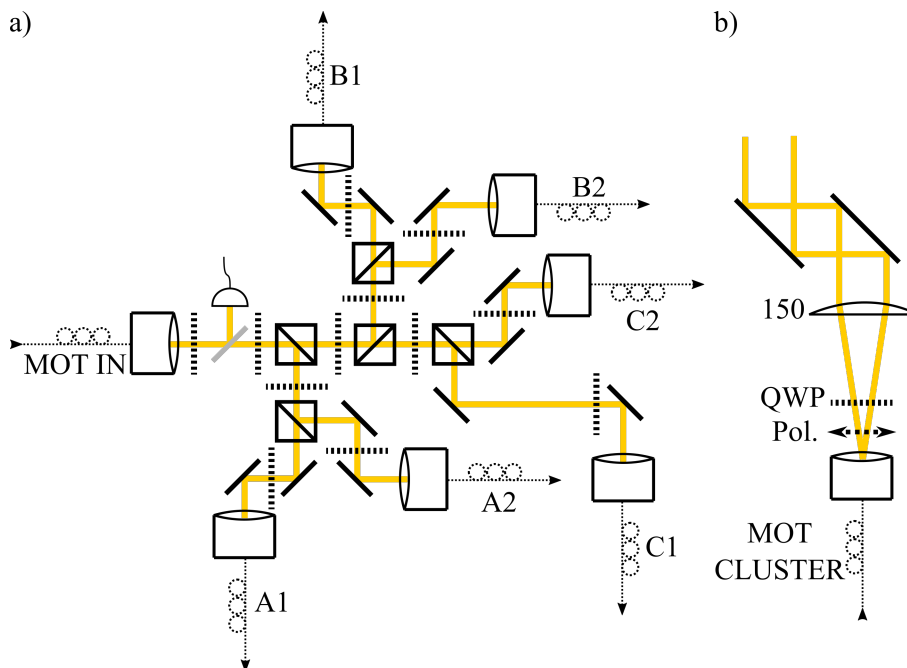


Fig. 4.9 **Fibre Cluster and MOT Beam Delivery** - a) The input light is brought from the experiment via a long optical fibre and then split 6-ways using an array of PBS cubes and half-wave plates. The fibre cluster also includes a monitor photodiode at the input. b) Each of the MOT beams is launched from the optical fibre into a single plano-convex lens, resulting in a 33 mm waist diameter beam. The polarisation is set using a polariser, mounted such that it can be rotated together with the fibre, and a quarter-wave plate, ultimately yielding a circular polarisation after the pair of steering mirrors.

Apart from the Zeeman slower parameters that control the flux in the atomic beam, the performance of the MOT is also governed by the magnetic fields (quadrupole gradient field and offset field), the laser detuning and optical powers in the different MOT beams. The magnetic fields are created by the set of coils mounted on the MOT chamber, for which the technical details were laid out in Section 2.2, and powered by supplies that can be controlled. The laser light for the MOT is processed using a double-pass AOM setup which has the ability to control both the frequency offset and the light intensity.

On the experiment table, the light for the MOT is split 6 ways into individual beams using a home made fibre cluster (Figure 4.9a). Each fibre is then routed towards a MOT beam launching stage that consists of a polariser and a quarter-wave plate, followed by a 150 mm focal length lens, collimating the beam to the diameter of 33 mm and simultaneously cutting off the light outside this diameter with an iris, blocking the light that would hit the viewport edges.

We have up to 180 mW of laser power available at the input to the fibre cluster, and that translates to the peak intensity of $5.6 \frac{\text{mW}}{\text{cm}^2}$ (or, alternatively $s = \frac{I}{I_{\text{sat}}} = 45$) averaged over the six beams. All experimental sequence parameters relevant to the MOT are controllable through the computer control software, except for the power balance between the beams that can only be tuned manually within the fibre cluster.

4.4.2 Experimental Sequence

Every experimental run starts with turning on the TC, ZS and MOT laser light, and ramping of the magnetic field coils. The Zeeman slower is kept on for t_{Load} , typically set to 15 s. Following loading, the Zeeman slower light and coils are turned off, and a hold time of up to 1 s is implemented for the sloshing in the cloud caused by the changing magnetic field to dampen out. The MOT parameters are then ramped in order to simultaneously compress and cool the cloud, which makes it more appropriate for transfer into the ODT. An example sequence, with realistic parameters is shown in Figure 4.10.

During loading, it is beneficial to keep the light intensity at the practical maximum, as it assures the maximum capture velocity possible, and also, the laser detuning should be set to a sufficiently red-shifted value, such that the cloud sags significantly below the trap centre (Figure 4.11a), ideally just below the ZS laser beam. This keeps the atoms away from the blue light that reduces the lifetime of the cloud, and also, keeps them resonant only with the σ^- transition and dominantly with the bottom MOT beam, resulting in the spin polarisation of the cloud without the need for additional optical pumping.

In order to approach the theoretical cooling limit set by the Doppler temperature, the light intensity needs to be ramped down (see Equation 4.12). As this also affects the vertical

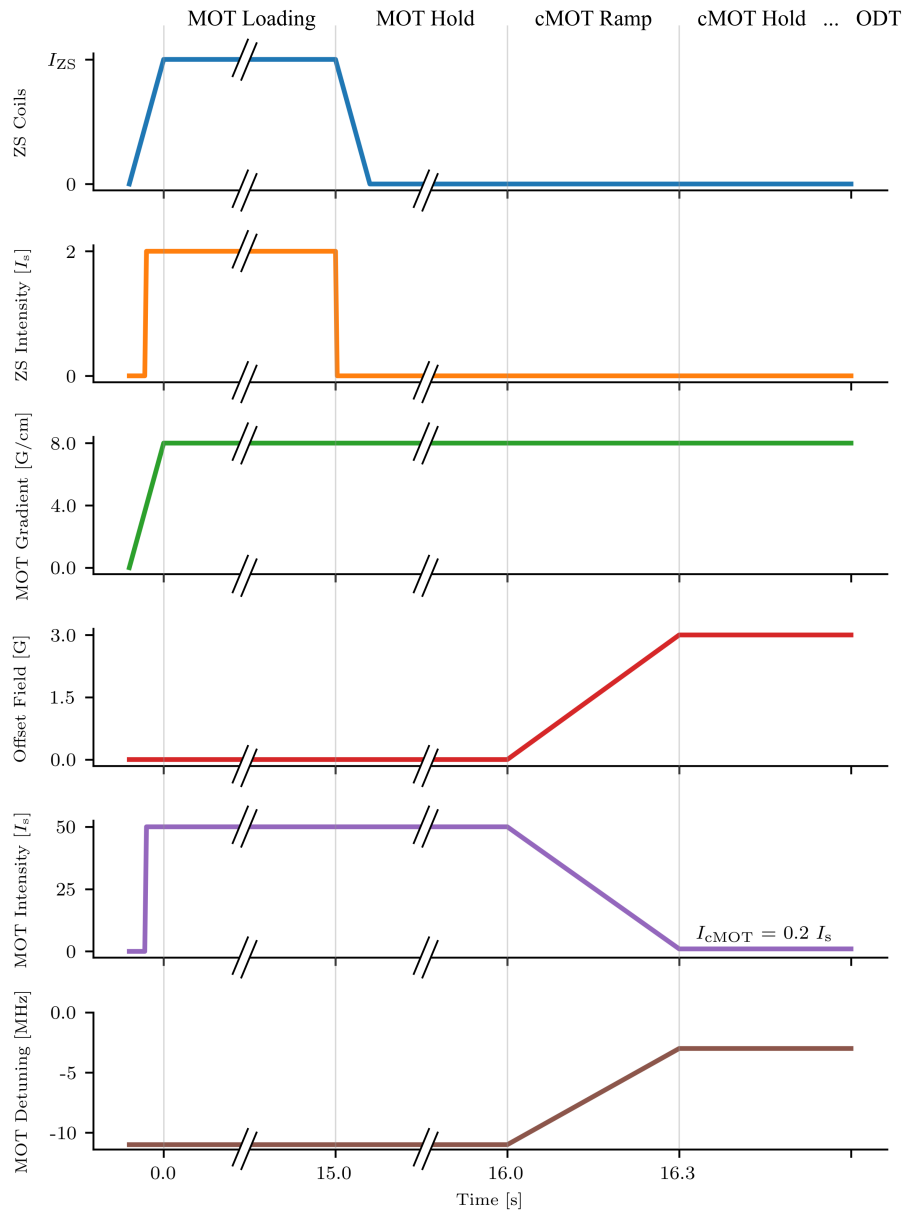


Fig. 4.10 **MOT Loading Sequence** - The MOT loading process is started by ramping up the currents in the ZS and MOT quadrupole coils while simultaneously turning on the laser light in the MOT and ZS. We typically load for $t_{load} = 15$ s at the maximum available intensity of MOT light, $I \approx 50I_s$ and a detuning of $\delta_{MOT} = -11$ MHz, roughly corresponding to $-70 \times \Gamma_{583}$. Once the loading is completed, the ZS light and coils are turned off, and after a 1 s long hold time (the cloud typically receives a small ‘kick’ from the varying magnetic fields upon the turn-off of the ZS coils), the MOT light frequency and intensity are ramped in parallel to cool and compress the MOT. The intensity is reduced to $0.2I_s$ while the detuning is brought to $\delta_{cMOT} = -3$ MHz ($\approx -15 \times \Gamma_{583}$) as any further ramping of either parameter leads to atom loss (Figures 4.15 and 4.14). At the same time, we introduce an offset magnetic field vertically, to raise the cloud to the height of the optical dipole trap beam.

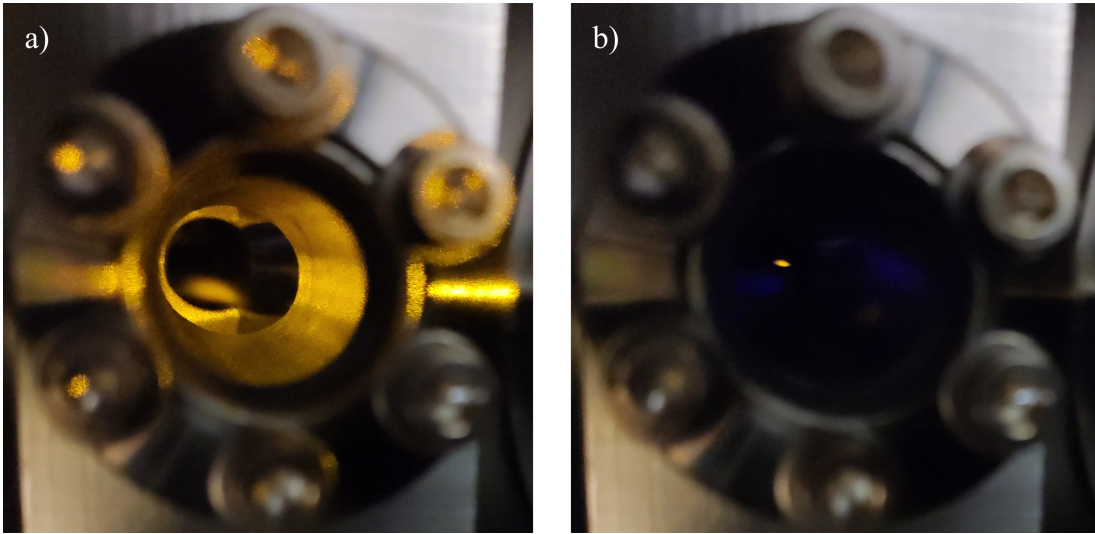


Fig. 4.11 **MOT and cMOT** - a) A photograph showing the MOT cloud during loading, taking up a characteristic oblate and diffuse shape and sagging below the centre of the trap due to gravitational sagging; b) The cloud in the late stage of the compression towards cMOT, making it more compact and closer to the centre of the chamber. The fluorescence is still visible, but the total power in the beams is considerably reduced by this point.

position of the cloud, causing it to shift downwards if no other parameters are changed, a ramp of the laser detuning to the blue is required to counter this. In parallel, the frequency ramp serves to compress the cloud through bringing the force profiles from opposing beams closer in frequency. The range through which the frequency can be changed is constrained by the requirement to keep the π and σ^+ transitions far detuned, maintaining the spin polarisation in the MOT. Any further raising of the cloud, required for levelling the compressed MOT with the ODT should be done with a magnetic field offset, shifting the centre of the quadrupole field upwards. This stage in the MOT sequence bears the name compressed MOT (cMOT), and a representative example is shown in Figure 4.11.

Beam	A1 (Bottom)	A2 (Top)	B1	B2	C1	C2
Peak I/I_{sat}	30	20	55	55	55	55

Table 4.2 **Table of MOT Beam Powers** - Peak saturation intensities in the six MOT beams. The Bottom beam (A1) has a reduced power as a consequence of the optimisation. The Top Beam was then also tuned down for the balance along the vertical direction to be roughly restored (although this is of limited importance as the vertical axis is inherently asymmetric due to gravitational sagging).

4.4.3 Optimisation and Performance

MOT Loading - Maximising N

Optimisation for the maximum loading number consists of finding a good combination of the MOT beam power balances and the loading laser detuning. During this process, we constrained the powers in the four horizontal beams to be equal and only varied the power balance in the vertical branch. In general, the system seemed to favour a weaker bottom MOT beam, which can be explained by the fact that the loading favours clouds that sag below the ZS laser beam, known to reduce the lifetime of the cloud. If this was to be accommodated with solely the laser detuning, then the burden of capturing the atoms from the incoming beam is shifted towards the outer regions of the horizontal beams, where the intensity is lower, which yields fewer atoms overall. By reducing the intensity in the bottom beam, the vertical equilibrium position is lowered without compromising the capture velocity.

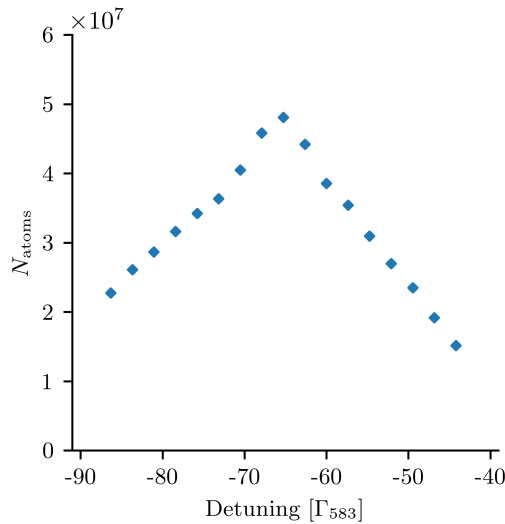


Fig. 4.12 **MOT Loading Frequency** - showing a clear maximum in the number of atoms loaded reached for a detuning of $\delta_{\text{MOT}} \approx -65 \times \Gamma_{583}$, corresponding to about 12 MHz. These results are in good accordance with the simple loading model outlined in Figure 4.3. The parameters used in this run were $\left| \frac{dB}{dz} \right| = 8 \frac{\text{G}}{\text{cm}}$ and beam powers listed in Table 4.2

Figure 4.12 shows number of atoms loaded into the MOT over t_{load} against the loading frequency. Results are in good accordance with the simple loading model outlined in Figure 4.3 predicting that there will be a well defined maximum in the dependence. The sharp roll-off at large negative detunings predicted by the calculation is not observed, as the geometry of the model is oversimplified. On the other hand, it correctly predicts that the loading maximum (stemming from maximised v_c) is achieved at $\approx -60 \times \Gamma_{583}$ for the field gradient of $8 \frac{\text{G}}{\text{cm}}$.

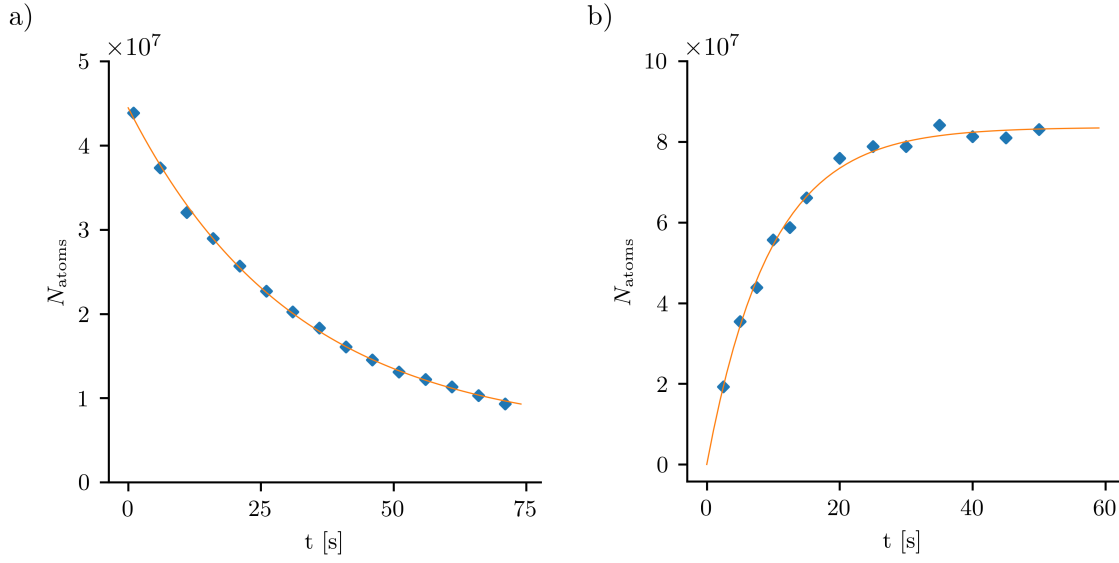


Fig. 4.13 **MOT lifetime and loading rate**-a) Lifetime measurement where the MOT was loaded for 15 s followed by a variable hold time. The orange line represents the exponential decay fit to the data yielding a lifetime of $\tau_{\text{MOT}} = 31$ s (orange line). b) The number of atoms in the MOT was measured after different loading times and the data was fitted with the solution of the appropriate rate equation (see text), leading to the loading rate value of $R = 8.8 \cdot 10^6 \text{ s}^{-1}$ (orange line).

Once the loading was optimised, the MOT loading rate and lifetime were measured. To extract the lifetime of the MOT cloud the number of atoms remaining in the trap after different holding times was recorded (Figure 4.13a). Fitting the exponential decay function $N = N_0 e^{-\frac{t}{\tau_{\text{MOT}}}}$ to the data yields the lifetime of $\tau_{\text{MOT}} = 31$ s. Similarly, by fitting the loading rate equation $N = R\tau_{\text{load}}(1 - e^{-\frac{t}{\tau_{\text{load}}}})$ to the dependence of the number of atoms in the trap following different loading durations (Figure 4.13b) we obtain the loading rate of $R = 8.8 \cdot 10^6 \text{ s}^{-1}$ and the loading time constant $\tau_{\text{load}} = 9.5$ s, ultimately yielding the limit for the loaded number of atoms of $N_0 = R\tau_{\text{load}} = 8.4 \cdot 10^7$.

The losses are caused by the collisions with the background gas and through light-assisted molecule formation between Er atoms themselves. In our trap, we reach⁸ peak densities of up to $5 \cdot 10^9 \text{ cm}^{-3}$ in the MOT during loading, and $5 \cdot 10^{12} \text{ cm}^{-3}$ upon compression. The two-body loss rate constant for erbium can be expected⁹ to be of the order of $\beta \sim 10^{-11} \text{ cm}^3 \text{ s}^{-1}$, yielding the expected loss timescales of $\tau_{\text{MOT},2b} (\beta n_{\text{MOT}})^{-1} = 20$ s and $\tau_{\text{cMOT},2b} (\beta n_{\text{cMOT}})^{-1} = 20$ ms. While these estimates give shorter lifetimes compared to what has been measured, they suggest that light-induced two-body collisions must be factored

⁸Assuming $N_{\text{MOT}} = 5 \cdot 10^7$ and using the volume estimates based on Equation 4.15 and numbers quoted there.

⁹Based on the equivalent values available for dysprosium [47, 85], which has similar values for all relevant parameters.

in, especially in the case of the cMOT, where it they are expected to be the dominant loss mechanism. Regarding the collisions with the background gas, a classical scattering theory approach [86, 87] predicts the loss rate to pressure scaling for a given component (labelled i) of the background gas to be:

$$\Gamma_{\text{MOT},i} = 6.8 \frac{p_i}{(k_B T)^{\frac{2}{3}}} \left(\frac{C_i}{m_i} \right)^{\frac{1}{3}} (Dm)^{-\frac{1}{6}} \quad (4.18)$$

where, p_i and m_i are the partial pressure and the atomic or molecular mass of the background gas component and C_i is the van der Waals coefficient for the collisions between the background gas particles and the cloud atoms; $T \approx 300$ K is the background temperature and D is the trap depth. Expecting H_2 to be the dominant contributor in the background gas, and taking $D = k_B \cdot 2$ K and $C_i = 150$ a.u. (1 a.u. = $e^2 a_0^5$)¹⁰ this equation would require $p_{\text{H}_2} = 8.5 \cdot 10^{-10}$ mbar to explain the lifetime cited in Figure 4.13. This value is considerably larger than both our pressure estimate from Appendix A and the readings on our ion pumps. While there are uncertainties in the input parameters to the above model, and this can change the answer by a factor of up to two, this can only be taken as another confirmation of the role of the light-assisted two-body molecule formation. The only remaining possible contributor to loss of atoms could be the leak light in the MOT beams or from the surroundings of the chamber, but we rank that as highly unlikely. All in all, the real quality factor is the lifetime itself, and it is certainly long enough for the purpose of conducting experiments with quantum gases.

Compressed MOT (cMOT) - Minimising T

The function of the cMOT is to simultaneously cool and compress the atomic cloud. Compression is primarily governed by the detuning ramp, which was rationalised in Section 4.1, showing that the volume of the cloud is decreased by tuning the laser closer to resonance. The limit of how far the ramp can go is ultimately determined by the local detunings of the π and σ^+ transitions that will compromise the spin purity of the cloud and also lead to losses. Figure 4.14 shows how the spin purity and the population of the cMOT are affected by the final frequency of the cMOT ramp. The trap maintains the atom number and unique spin polarisation for detunings up to $-15 \times \Gamma_{583}$. The Figure 4.14a shows the density distributions after the cloud is let to fall with a magnetic field gradient applied, in a measurement that corresponds to a Stern-Gerlach experiment. For frequencies that are too close to the

¹⁰The dependence of the pressure estimate on these parameters is very weak so only rough estimates were taken. In the case of C_i a number, only values for alkali metals were available from [87], so a value similar to the one for Rb and Cs was used

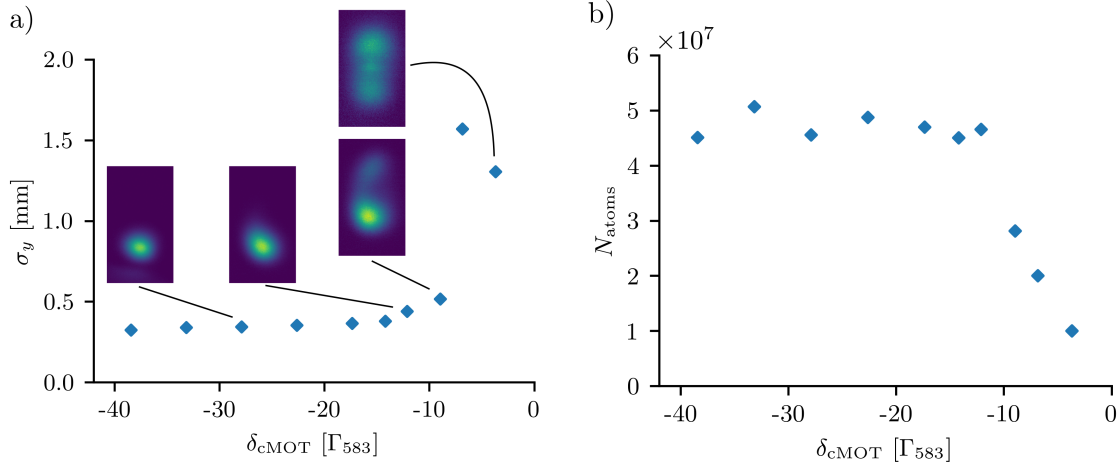


Fig. 4.14 **cMOT Frequency** - The measurement of purity of the spin polarisation of the cMOT cloud depending on the final frequency in the ramp showing the second moment of the density distribution along the vertical as a result of a Stern-Gerlach measurement of spin purity (a), and the remaining atom number in the MOT following the ramp (b). As the trends on both plots, along with the snippets showing the density profiles suggest, extending the ramp too close to the resonance mixes in other spin states, leading to inelastic scattering and atom loss.

resonance, different spin states become spatially resolved by this measurement which is also reflected in the vertical extent of the cloud. Figure 4.14b also shows losses that are brought about by scattering between atoms in different states.

The cooling that happens in parallel with compression is a consequence of the reduction in intensity. Figure 4.15a shows that the measured temperatures are in good accordance with the model given by Equation 4.12. We do not reach the theoretical minimum of the model as the laser intensity and frequency noise lead to heating and atom losses. At the same time, lowering the laser intensity decreases the depth of the trap, causing losses once it becomes commensurate with the thermal energy scale of the cloud (Figure 4.15b). The temperature of the cloud is measured using the Time-of-Flight (ToF) method, whereby the atoms are released from the trap and imaged after a varying time interval. The clouds are then fitted with a Gaussian function and the temperature is extracted from the temporal evolution of the cloud widths. Assuming the cloud initially also has a Gaussian distribution, the Gaussian width (here defined as $e^{-\frac{1}{2}}$ radius) should obey:

$$\sigma^2(t) = \sigma_0^2 + \frac{k_B T}{m} t^2 \quad (4.19)$$

hence the temperature can be extracted from the slope of $\sigma^2(t^2)$.

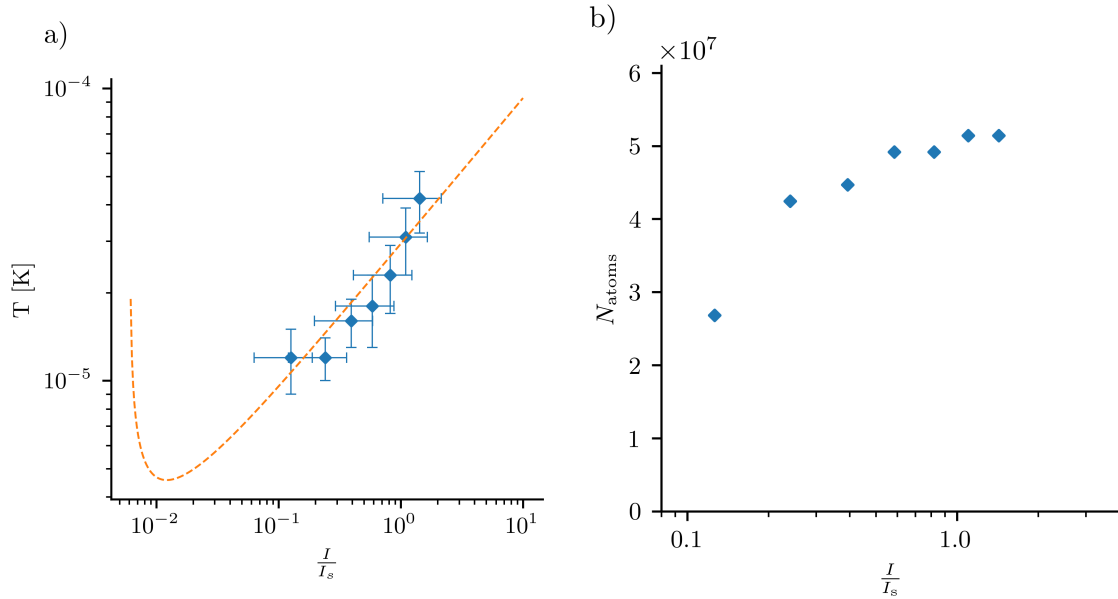


Fig. 4.15 **cMOT Temperature** - a) A comparison of the MOT temperature measurements at different final light intensities (blue markers) with the theoretical prediction given in Equation 4.12 (dashed orange line). The temperature values used are averages of the two estimates from the ToF method using the horizontal and the vertical cloud size. b) Shows the remaining atom number in the MOT following the ramp, showing that once we reach $I/I_{\text{sat}} = 0.2$ further ramping leads to atom loss. This still allows us to approach the temperatures of $\sim 10\mu\text{K}$.

In order to measure the lifetime in the cMOT, we implement a hold time interval after the compression ramp, after which the atoms are released and imaged. Figure 4.16 shows different lifetimes measured for cMOT clouds of different densities. We generally require tightly trapped clouds in order to better match the spatial profiles of the cMOT and the ODT cloud, but this comes at the cost of the lifetime.

MOT Stability - Reaching Consistent Transfer into ODT

In order to load into the ODT that has the cross section of $30\mu\text{m}$ (V) by $100\mu\text{m}$ (H) it is necessary to maintain good spatial overlap during transfer. Given that the vertical extent of the cMOT is about $100\mu\text{m}$, we need to keep any positional jitter below that length scale. Generally, this jitter originates from the laser frequency and intensity noise, where the frequency noise should only significantly contribute to vertical motion due to symmetry. Unexpectedly, we observed pronounced jitter in both directions, being particularly severe horizontally (Figure 4.17), which could not be correlated with powers in individual MOT beams that we consequentially started monitoring. The problem was diagnosed after an observation that the amount of jitter is strongly dependent on the vertical position of the cloud,

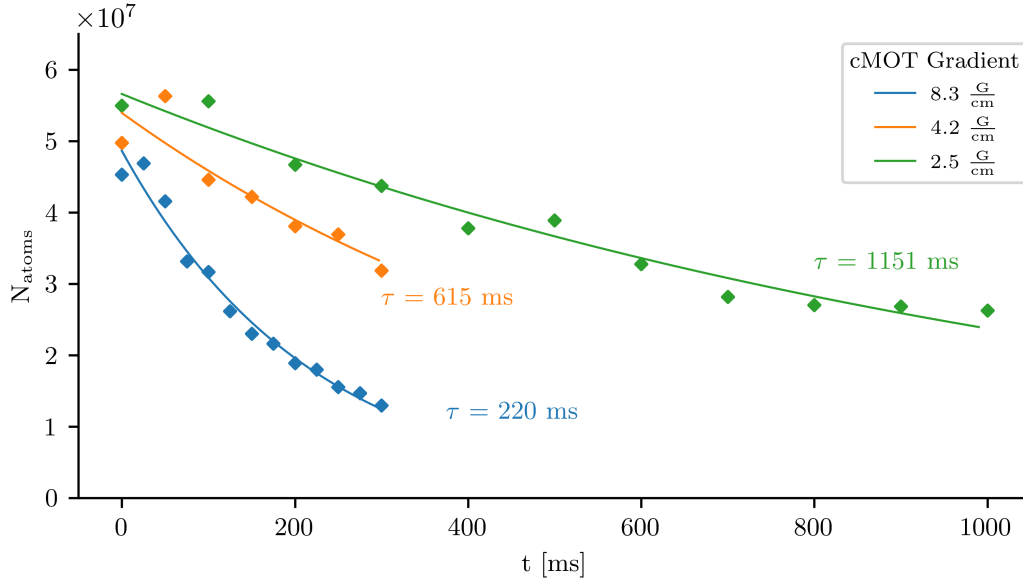


Fig. 4.16 **cMOT Lifetime** - Lifetime of the atoms in the cMOT, measured by varying the hold time in the trap following compression. The three data sets were taken for three different values of the magnetic field gradient, resulting in clouds of different size. The runs with higher gradient values yield denser clouds, which enhances the light-assisted 2-body loss rate, shortening the lifetime.

being different from region to region. This prompted us to check the purity and uniformity of polarisation in the beams, and it was observed that certain beams have regions where the polarisation strays from circular and any time-dependent fluctuations originating from the optical fibres are more pronounced there. The root of this behaviour was found in the mirrors¹¹ that were used to steer the beams into the chamber, with some of them being faulty, making the light polarisation non-uniform across the beam¹². Once these have been swapped, the stability improved significantly. This resulted in the vertical direction showing more pronounced position jitter, which is probably due to laser frequency stability, and should be mitigated by the imminent introduction of the ULE cavity as the locking method for the MOT laser.

Performance under typical use

In daily running of the experiment, we typically load the MOT for 15 s, leading to $N_{\text{MOT}} = 6 \cdot 10^7$ atoms being loaded. The cMOT ramp is performed as described in Section 4.4.2, with the final light intensity being ramped from $\frac{I}{I_{\text{sat}}} = 45$ to $\frac{I}{I_{\text{sat}}} = 0.2$, yielding $N_{\text{cMOT}} = 6 \cdot 10^7$ atoms at the temperature of $T = 13 \mu\text{K}$.

¹¹Thorlabs BB2-E02 2" dielectric mirrors

¹²A stripe-like region of different polarisation was measured across the middle of the beam.

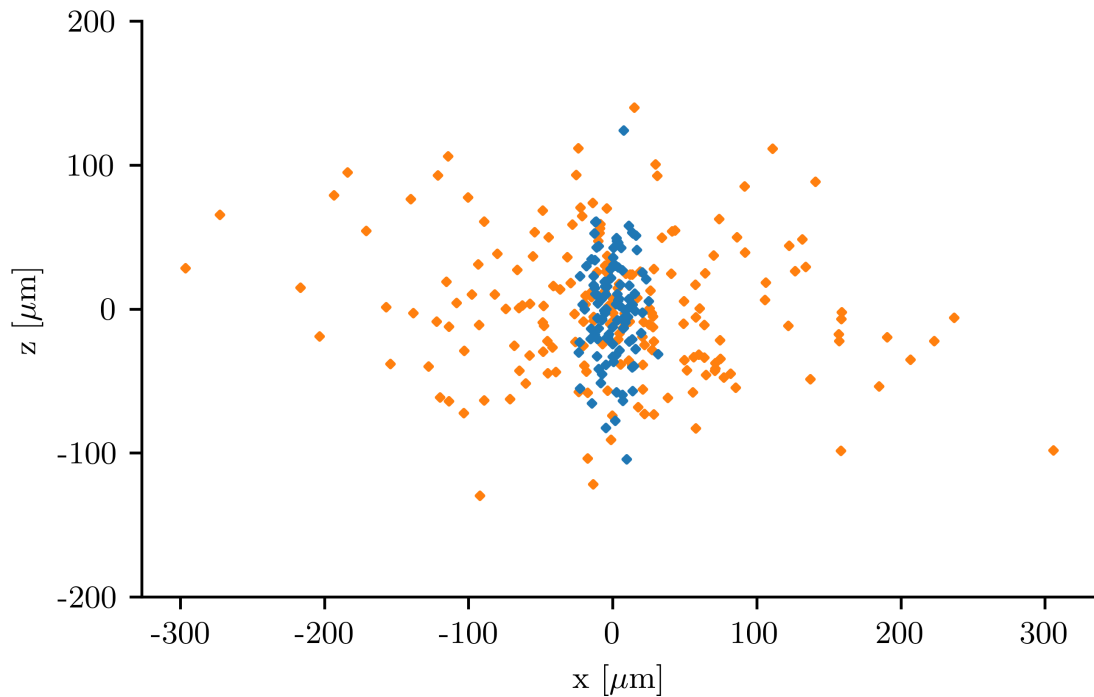


Fig. 4.17 **MOT position variation** - measurement of the centre position of the compressed MOT cloud after a short time of flight, before (orange markers) and after (blue markers) replacing the set of mirrors in the horizontal MOT beams. Standard deviations of the two data sets are $\sigma_x^{\text{OLD}} = 88 \mu\text{m}$ and $\sigma_z^{\text{OLD}} = 47 \mu\text{m}$ before the mirror replacement and $\sigma_x^{\text{NEW}} = 12 \mu\text{m}$ and $\sigma_z^{\text{NEW}} = 35 \mu\text{m}$ after the replacement. The residual vertical jitter is either coming from the laser frequency stability, or some remaining polarisation issues.

Chapter 5

Optical Trapping, Transport and Dynamical Potentials

The electric polarisation induced by non-resonant light fields incident on atoms and the accompanying shift in energy provides for a powerful tool for manipulating atomic clouds and the motional states of constituent atoms. In our experiment, several techniques are used based on this phenomenon. Firstly, the system of optical dipole trap beams creates attractive potentials for trapping and transporting the atoms. Then, the hollow, cylindrical beam will make up a repulsive wall that creates the optical box trap in conjunction with an attractive light sheet. Finally, we also plan to implement a Bragg spectroscopy setup that employs a dynamical light shift potential¹. These techniques become particularly valuable for trapping species in magnetically non-trappable (high-field seeking) states, such as erbium atoms polarised in the $J = 6$, $m_j = -6$ state following the MOT. In this chapter, I describe the methods we use, and lay out their foundations. Additionally, I rationalise the choices made for the particular wavelengths selected for these applications.

5.1 Light Shift Potentials

When atoms are subjected to a non-resonant light field, their potential energy changes through the AC-Stark effect. That effect can be simply explained through the ‘dressed states’ picture, where the eigenstates of the atom in the light field are original eigenstates mixed with small proportions of other states. All the states corresponding to transitions for which the laser is blue (red) detuned increase (decrease) the energy of the atom. For a two level system, with

¹Instead of the usual pair of counter-propagating beams

the far detuned light field, the energy shift is given as:

$$\Delta E = \frac{\hbar\Omega^2}{4\Delta} = -\frac{1}{2\epsilon_0 c} I \alpha . \quad (5.1)$$

Where Ω is the Rabi frequency of the light field for this transition and Δ is the detuning. However, most often, the magnitude of the shift of a given atom species is stated in terms of the light intensity, I , and polarizability, α . Additionally, as the goal is to keep the light non-resonant and prevent it from exciting the transition, which leads to heating and losses, with the scattering rate given by:

$$\Gamma_{\text{loss}} = \frac{\Omega^2 \Gamma}{4\Delta^2} \quad (5.2)$$

where Γ is the transition line width, needs to be maintained at a negligible level. Fortunately, the scattering rate falls off faster with detuning, compared to the light shift potential, so this becomes just a matter of selecting a sufficiently large detuning.

5.1.1 Polarizability of Erbium

In general, the polarizability accounts for the effect from all transitions and has a tensorial character, due to the anisotropy of the electronic orbitals and transitions being polarisation dependent. Therefore, three components - scalar, vector and tensor - are required to fully describe the dependence of polarizability on geometry [88, 89]:

$$\alpha_{\text{tot}}(\omega) = \alpha_{\text{scal}}(\omega) + \mathcal{E} \cos \theta_k \frac{m_J}{2J} \alpha_{\text{vect}}(\omega) + \frac{3m_J^2 - J(J+1)}{J(2J-1)} \frac{3 \cos^2 \theta_p - 1}{2} \alpha_{\text{tens}}(\omega) \quad (5.3)$$

where (J, m_J) are the quantum numbers of the electronic state the atom is in (6 and -6 for the absolute ground state of erbium in magnetic field), and \mathcal{E} is the ellipticity parameter of the light polarisation. The polarizability also depends on the angle between the quantisation axis and the polarisation of the light field, θ_p and the angle between the quantisation axis and the propagation direction of the light beam, θ_k . For erbium, in the case when both of these angles are 90° , the polarizability is shown in the Figure 5.1. From this graph, it is clear that an attractive optical dipole trap (ODT) can be successfully created using wavelengths in the 1030 nm region, and a repulsive optical box potential may be set up using light close to 372 nm.

²a.u. here represents the atomic units of polarizability 1 a.u. = $4\pi\epsilon_0 a_0^3 = 1.65 \times 10^{-41} \text{ C}^2 \text{ m}^2 \text{ J}^{-1}$

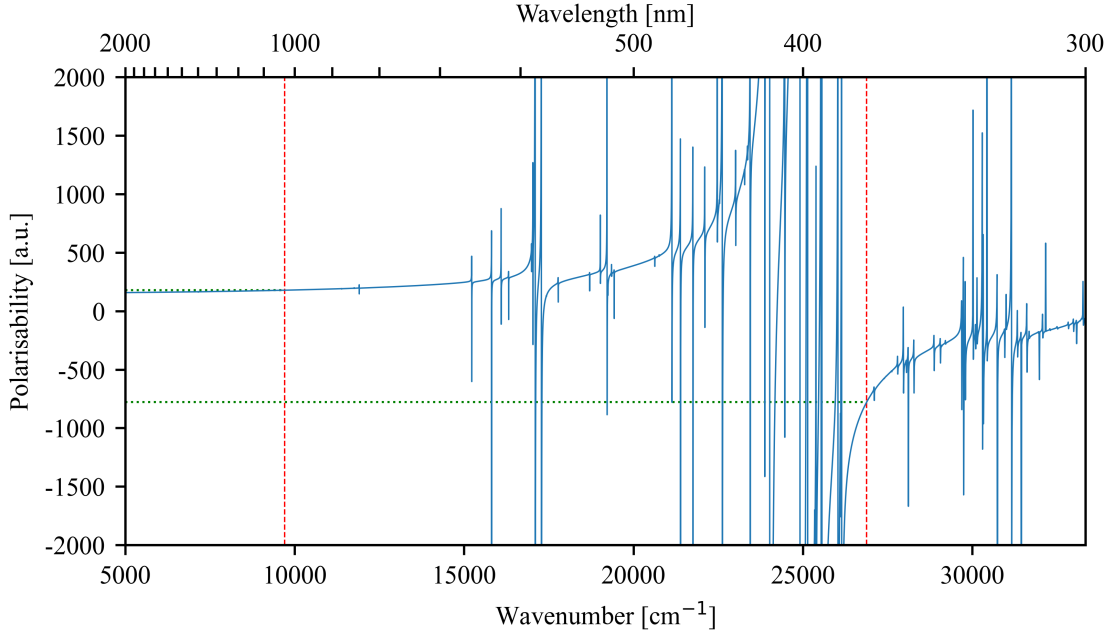


Fig. 5.1 **Total atomic polarizability of erbium** - here shown for $\theta_k = \theta_p = 90^\circ$, which is the configuration we will use in the ODT1 trap. We highlight the two wavelengths we plan to use for trapping - 1030nm for the optical evaporation, transport and planar confinement in the box trap, and 372nm for radial confinement in the box trap. The polarizability values extracted from the above model at these wavelengths are 178 a.u. and -779 a.u. respectively². This figure is reconstructed using the data from [89]

5.1.2 Harmonic Trapping in Focused Gaussian Beams

For an elliptical Gaussian beam, the intensity takes the form:

$$I(x, y, z) = \frac{2P}{\pi w_x(z) w_y(z)} \exp \left[-2 \left(\frac{x^2}{w_x^2(z)} + \frac{y^2}{w_y^2(z)} \right) \right] \quad (5.4)$$

where the beam waists along the two axes vary according to $w_{x,y}(z) = w_{0x,y} \sqrt{1 + \frac{z^2}{z_{Rx,y}^2}}$ and $z_{Rx,y} = \frac{\pi w_{0x,y}^2}{\lambda}$ are the Rayleigh ranges along the principal directions. The effective Rayleigh range of the beam, i.e. the distance from the focus along the propagation axis over which the peak intensity reaches half of the maximum value, is:

$$z_{\text{Reff}} = \sqrt{\frac{2}{w_{0x}^4 + w_{0y}^4}} \frac{\pi w_{0x}^2 w_{0y}^2}{\lambda}. \quad (5.5)$$

The trapping potential in the vicinity of the focus can be expanded using a Taylor series to obtain the harmonic approximation:

$$U(x, y, z) = -\frac{1}{2\epsilon_0 c} \text{Re}(\alpha) \frac{2P}{\pi w_{0x} w_{0y}} \left[1 - \frac{2x^2}{w_{0x}^2} - \frac{2y^2}{w_{0y}^2} - \frac{z^2}{z_{\text{Reff}}^2} \right] \quad (5.6)$$

From here, the associated trap frequencies can be extracted, showing their relation to the beam geometry:

$$\omega_x = \sqrt{\frac{4\alpha P}{m\epsilon_0 c \pi w_{0x}^3 w_{0y}}}, \quad (5.7)$$

$$\omega_y = \sqrt{\frac{4\alpha P}{m\epsilon_0 c \pi w_{0x} w_{0y}^3}}, \quad (5.8)$$

$$\omega_z = \sqrt{\frac{\alpha P \lambda^2 (w_{0x}^4 + w_{0y}^4)}{m\epsilon_0 c \pi^3 w_{0x}^5 w_{0y}^5}} \quad (5.9)$$

and full trap depth is given by:

$$U_0 = \frac{1}{2\epsilon_0 c} \text{Re}(\alpha) \frac{2P}{\pi w_{0x} w_{0y}}. \quad (5.10)$$

5.2 1030 nm Laser System and the Transport Setup

Upon reaching temperatures of about 10 μK in the MOT, we need to resort to evaporative cooling to finally reach quantum degeneracy. Concurrently, we require a mobile trap to perform the transport of the atomic cloud into the glass science cell. For both of these tasks, we opted for a red-detuned optical dipole trap, employing a 1030 nm laser. The choice of the wavelength was primarily motivated by the availability of single frequency lasers with sufficiently high power in the vicinity of 1064 nm, and we decided to use a wavelength somewhat lower than that as it was reported that 1064 nm traps have shorter lifetimes when the fermionic isotope ^{167}Er is used³.

³We do not plan to use ^{167}Er at this point, but as this design constraint was simple to implement and it keeps the door open for introducing the fermionic isotope in the future, we avoided the lasers in range between 1050 nm and 1070 nm.

5.2.1 Optical System Design and Realisation

The light for the optical dipole trap is sourced from a 45 W, single-frequency doped-fibre laser⁴. The power is currently split into two beams, as shown in Figure 5.3 The main trapping beam (ODT1) and the auxiliary beam to form a crossed trap in the MOT chamber (ODT2). The intended function of ODT2 is to provide stronger longitudinal confinement after the atom transfer from the MOT and during the first stages of pre-transport evaporation. The optical system delivering the ODT1 beam incorporates a pair of focus-tunable lenses⁵ that allow independent tuning of the trapping beam's focal position and waist [90]. The design goal for this system was to provide focal point translation over a distance of 40 cm and waists between 25 μm and 45 μm along this trajectory [91]. In addition, we have the ability to further increase the horizontal waist of the trapping beam, up to three times, by dithering the modulation frequency of the appropriate AOM in the setup. We aim for a 30 μm \times 30 μm waist beam for the ODT1 (extending to about 100 μm in the horizontal direction when dithering is applied). Assuming that 35 W of optical power reaches the focus, we predict the trapping frequencies of $(\omega_x, \omega_y, \omega_z) = 2\pi \times (1.8 \text{ kHz}, 1.8 \text{ kHz}, 18 \text{ Hz})$ and a trap depth of $k_B \times 700 \mu\text{K}$. When dithering is applied, the trap frequencies change to $(\omega_x, \omega_y, \omega_z) = 2\pi \times (1.1 \text{ kHz}, 350 \text{ Hz}, 5.3 \text{ Hz})$, while the trap depth reduces to $k_B \times 230 \mu\text{K}$. The second beam, ODT2, approaches in the plane perpendicular to the propagation of OD1, at an angle of 7° to the vertical. It has a 150 μm waist along the transport direction, a 50 μm waist orthogonally and a maximum power of 5 W (limited by the optical fibre). With these parameters, it can provide up to 400 Hz of additional trapping across the long direction of the ODT1 (i.e. transport direction).

The transport system is designed such that the pair of tunable lenses can shift the focus of the beam along the trajectory between the MOT chamber and the science cell. The functional part of it is shown in Figure 5.2 and consists of two tunable lenses at separation l_1 and a fixed lens with focal length $f = 400 \text{ mm}$ next to the chamber at the distance l_2 from the second tunable lens. The focal lengths of the two tunable lenses, f_1 and f_2 can be freely tuned over a range from -500 mm through infinity to 333 mm. In the special configuration with the distance between the second tunable lens and the last, fixed lens is set to the focal length of the fixed lens (i.e. $l_2 = f$), the focus position and the beam waist vary as (for more details, see [90, 91]):

$$w_f = \frac{f|f_1|w_0\lambda}{\sqrt{(f_1 - l_1)^2 \pi^2 w_0^4 + f_1^2 \lambda^2 l_1^2}}, \quad (5.11)$$

⁴Azur Light Systems ALS-IR-1030-50-I-SF

⁵EL-16-40-TC-NIR-5D from OptoTune

$$x_f = f - f^2 \left(\frac{1}{f_2} + \frac{(f_1 - l_1) \pi^2 w_0^4 + f_1^2 \lambda^2 l_1}{(f_1 - l_1)^2 \pi^2 w_0^4 + f_1^2 \lambda^2 l_1^2} \right) \quad (5.12)$$

where w_f is measured w.r.t. to the last lens. Resulting from the above constraint imposed on l_2 , the waist radius at the focus does not depend on f_2 , implying that transport at fixed waist can be performed by solely tuning the focal length of the second tunable lens. Given the design parameters, this system satisfies the desired goals (transport over 40cm at waists between $25\mu\text{m}$ and $45\mu\text{m}$), even when the finite apertures of the tunable lenses and the chamber viewport are counted in.

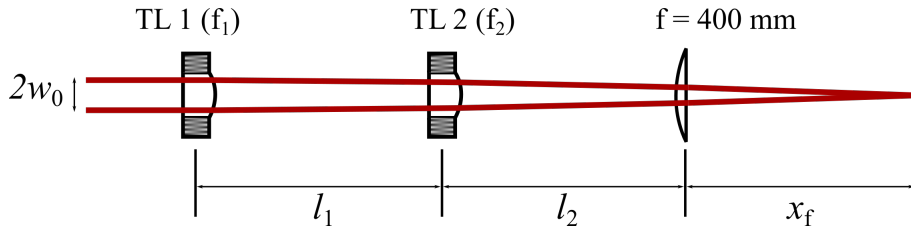


Fig. 5.2 **Optical Transport Scheme** - We implement the optical system design proposed in [90] which incorporates a pair of focus tunable lenses ('TL 1' and 'TL 2') to produce a trapping beam with adjustable waist and focus position. The design also specifies the constraint $l_2 = f$, under which the operation of the system is described by Equations 5.11 and 5.12. As a result, the beam waist is only tuned with TL 1, enabling simple implementation of transport at constant waist.

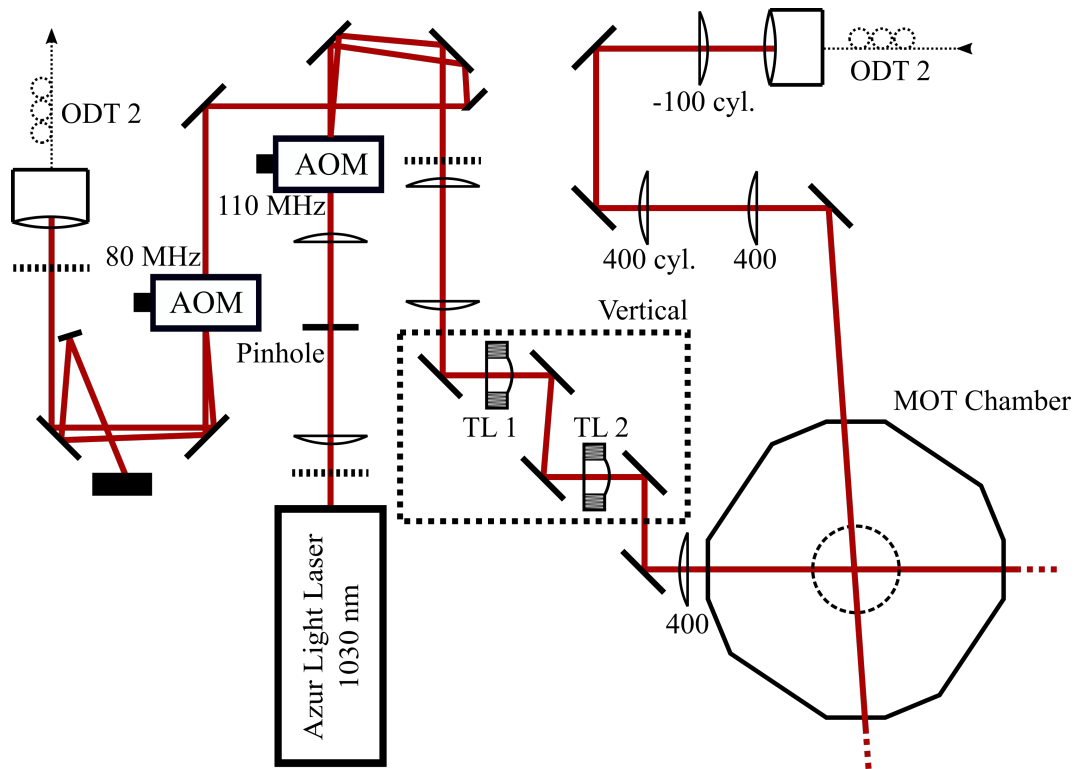


Fig. 5.3 **1030 nm Laser System** - The light is supplied by a 45 W single-frequency laser, and after passing through a telescope/spatial filtering stage, it is directed through an AOM. The AOM is set up in a single-pass configuration where it serves a double purpose - to switch and control the intensity of the light and to deflect the position of the ODT1 beam focus in the horizontal, transversal direction. This dithering functionality is employed to modulate the trap position at a high frequency (~ 30 kHz), creating an effective potential for the atoms with a broader waist in one direction. The tunable lenses, used to control the focal position waist of the ODT1 beam, are mounted on the vertical breadboard to minimise aberrations caused by the effect of gravity onto the liquid and the lens membrane. Additionally, a second trapping beam is created from the undeflected component of the beam after the first AOM. This beam (ODT2) is sent through a second AOM and an optical fibre to enter the chamber at 7° to the vertical, and provide additional confinement for the atoms in the MOT chamber. The system also incorporates a set of photodiodes for laser power control and stabilisation, picking off the signal from specular reflections off half-wave plates in the system (not pictured as major improvements are planned for this subsystem to mitigate for polarisation drift effects).

5.2.2 Performance and Observed Issues

Following the enhancements to the positional stability of the MOT cloud (end of Subsection 4.4.3), we have achieved relatively steady transfer efficiency into the ODT1 trap, of approximately 20%, as shown in Figure 5.4a. The improvement in consistency indeed seems correlated with the enhanced stability of the MOT, based on the evidence offered in Figure 5.4b.

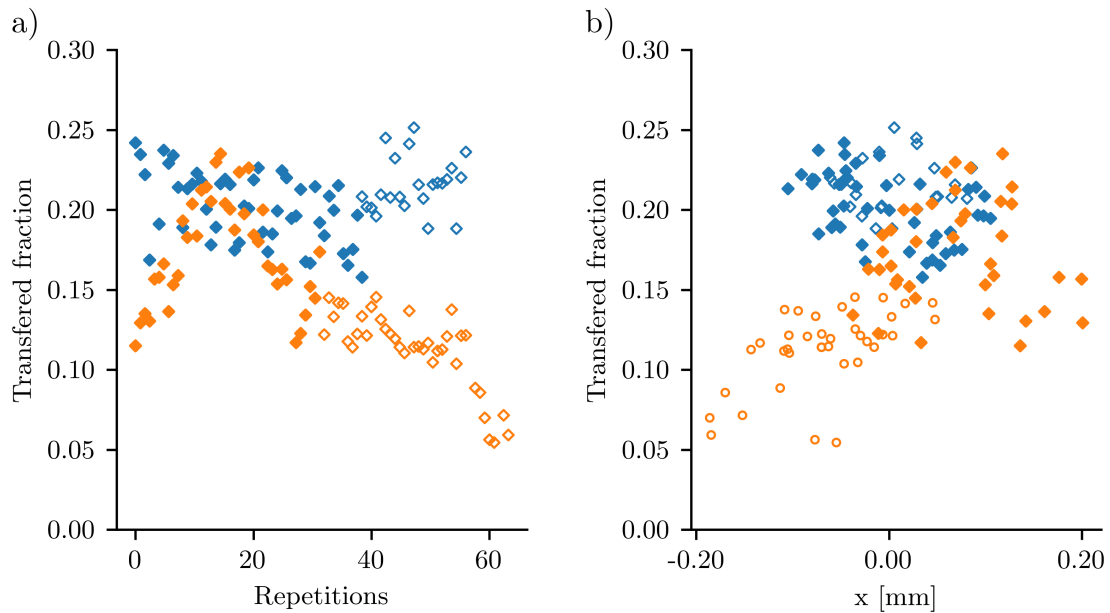


Fig. 5.4 **Transfer Consistency** - a) shows measured transfer efficiency from the MOT into the ODT, both before the MOT mirrors were changed (orange markers) and after that (blue markers) depicting the improvements brought about by better stability and uniformity of MOT light polarisation. Data was taken in two different runs for each of the two sets, discriminated by marker filling. In b), we demonstrate the correlation between the transfer efficiency and the measured horizontal position of the MOT cloud (labelled x , measured by looking at the atoms remaining in the falling MOT cloud after not being transferred).

As achieving good transfer efficiency relies on good spatial overlap between the ODT and the cloud, we make use of the spatial dithering to temporarily broaden the beam along the horizontal direction. The transfer efficiency with and without dithering applied, as a function of the focal point position is shown in Figure 5.5. The effect of dithering is an improvement of transfer by about 40%, and it can also be seen that the undithered beam reaches maximum transfer efficiency away from the focus, indicating that the waist is too narrow at the focus itself.

By performing time-of-flight measurements on the ODT cloud itself, we measured the temperatures after transfer, and the lowest achieved value in the trap with the dithering off

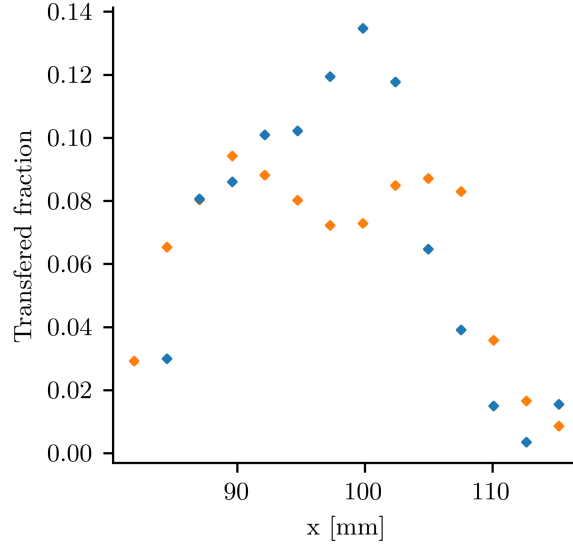


Fig. 5.5 **Transfer to ODT at Different Positions** - The figure shows the transfer efficiency dependence on the focal point position in cases with (blue markers) and without dithering (red markers). When dithering is applied, the trend shows a single peak in the centre of the region, whereas, without dithering, the transfer peaks when the MOT cloud is located at either side of the ODT focus.

was $50\mu\text{K}$. Assuming the ideal trap frequencies of $2\pi \times (1.8 \text{ kHz}, 1.8 \text{ kHz}, 18 \text{ Hz})$ and $N = 10^7$, we estimate that we reach typical phase-space densities of up to:

$$PSD_{\text{ODT}} = N \left(\frac{\hbar}{k_B T} \right)^3 \omega_x \omega_y \omega_z = 5 \times 10^{-4}. \quad (5.13)$$

If the ODT is loaded slightly off-centre, the atom density will exhibit damped centre-of-mass oscillations. These can be used to estimate the trapping frequency of the ODT (Figure 5.6a), yielding $\omega_x = 2\pi \times 2.8 \text{ Hz}$. In this dataset with dithering enabled, the expected longitudinal trapping frequency, inferred from measured beam waists, is $\omega_x^{\text{ideal}} = 2\pi \times 5.3 \text{ Hz}$. Additionally, as the cloud adjusts to the shape of the ODT, being loaded from the cMOT cloud that is significantly narrower longitudinally, a sloshing mode is excited, which can also be observed in the evolution of the cloud width (Figure 5.6b).

Apart for the discrepancy between the expected and measured trapping frequency, another issue that was noticed was the drifting of the focal point position due to thermal effects in the lenses caused by the high optical power that is incident on them. We observed this behaviour both by directly imaging the evolution of the beam profile at different positions along the beam [91] and also in the behaviour of the atomic cloud (Figure 5.7).

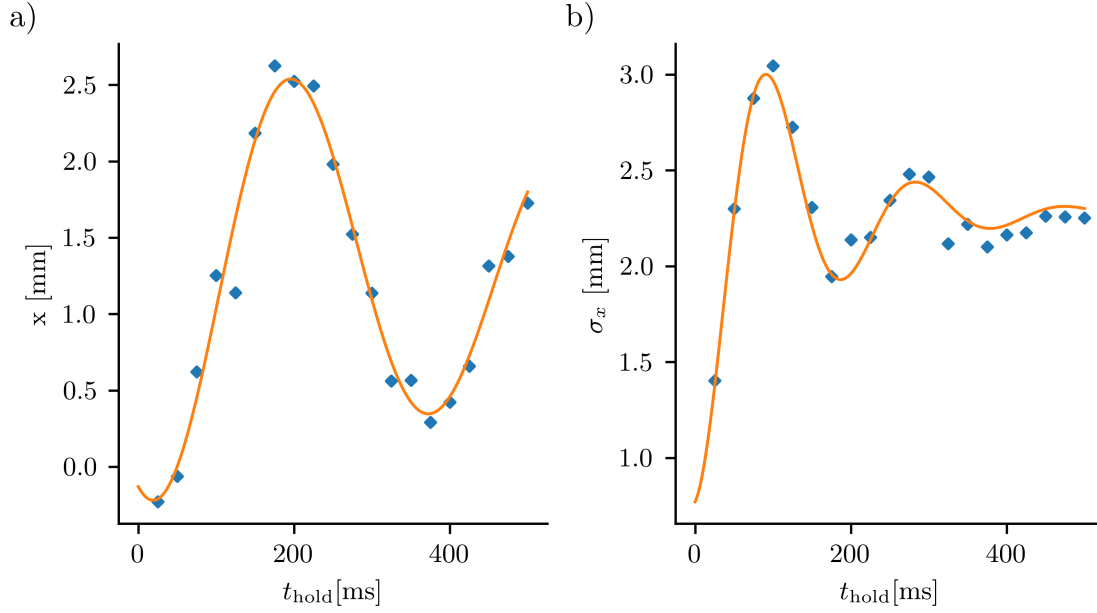


Fig. 5.6 **ODT Dynamics Following Transfer** - a) The evolution of the centre position of the cloud after transfer into the ODT from the MOT. The focus of the ODT beam is offset from the MOT, leading to a centre-of-mass oscillation, that is fitted with a damped harmonic oscillation with a frequency of $\omega_x = 2\pi \times 2.8$ Hz and a decay time constant of $\tau_x = 770$ ms; b) The evolution of the Gaussian width of the cloud, also showing damped harmonic evolution with a frequency of $\omega_\sigma = 2\pi \times 5.1$ Hz and a decay time constant of $\tau_\sigma = 130$ ms obtained from fitting.

5.2.3 Outlook and Proposed Alterations

The performance of our ODT trap seems to be plagued primarily by the poor axial confinement provided by the ODT1 Beam. This results in clouds that are severely elongated along the beam propagation axis, reaching waists of up to 2 mm, rendering them unsuitable for evaporation and transport.

We plan for further testing of the capabilities and improvements of the current setup, including re-designing the tunable lens setup to gain on the axial confinement front at the expense of the tuning range for the beam waist or attempting the implementation of better heat management in the tunable lenses [92]. In parallel with this, alternatives for the liquid tunable lenses are being considered. Currently available options are opting for the conventional method based on a low-vibration translation stage [93], or switching to a Moiré lenses⁶ [94], a different type of tunable lenses, which are reportedly significantly more immune to aberrations and thermal lensing effects.

⁶Produced by Diffratec

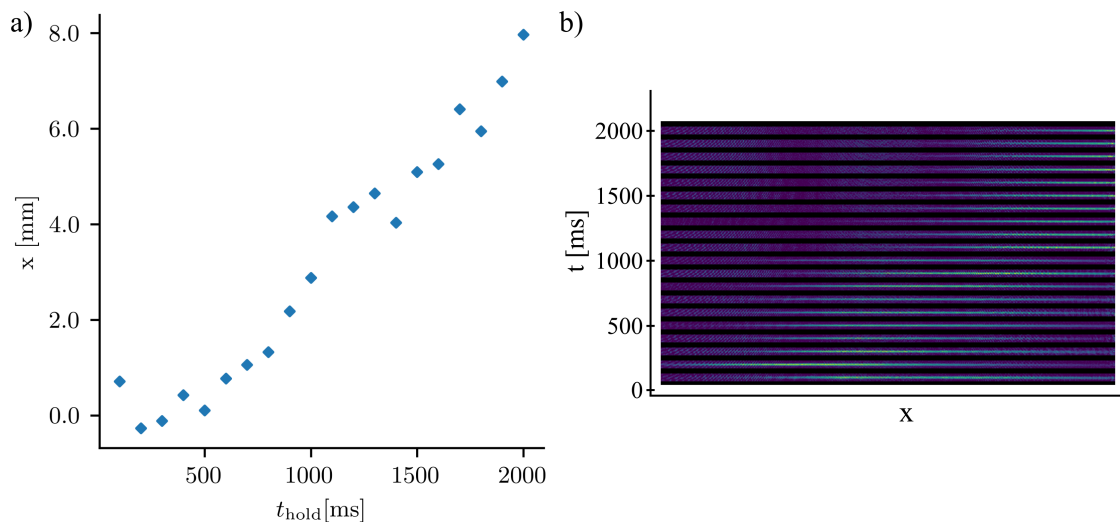


Fig. 5.7 **Drift of the ODT Cloud** - Due to thermal effects in the tunable lenses, originating from the high optical power in the ODT1 beam, the focal point of the trapping beam starts drifting after ~ 500 ms. This is reflected in the measurements of the centre position of the cloud shown in a) which yield an approximate drift rate of $5 \frac{\text{mm}}{\text{s}}$. Absorption images corresponding to these measurements are also shown in b), giving a pictorial demonstration of the drift.

5.3 Optical Access to the Science Cell

The region around the science cell will be the place a number of optical systems will have to be combined - just the bare experimental platform calls for the two beams comprising the optical box trap, access for imaging and picking up and disposing the transport laser beam. On top of that, we will continue to install various optical systems for probing and manipulation of the atoms for the purpose of scientific experiments, with the Bragg spectroscopy being the first example of such. Therefore, space management and optical access need to be organised well. Figure 5.8 shows the planned layout for the optical box, imaging for both atomic species and Bragg spectroscopy. In order to combine and separate the beams at different wavelengths where required, we are implementing two long pass filters⁷ and one notch filter⁸.

As this design assumes that the tube beam for the optical box will share the projection objective with the Bragg spectroscopy setup, the final design of the objective will have to be adjusted such that it provides satisfactory performance at both 583 nm and 372 nm.

⁷BrightLine FF389-DI01-25X36X1.5 and BrightLine FF506-DI03-25X36 from Semrock

⁸LAS-042742 from Semrock

Imaging of the atomic cloud will be performed using the Hamamatsu ORCA-Fusion camera⁹ that has the capability of taking pairs of images in quick succession with a global shutter, which is necessary for some dual-species experiments we have in planning.

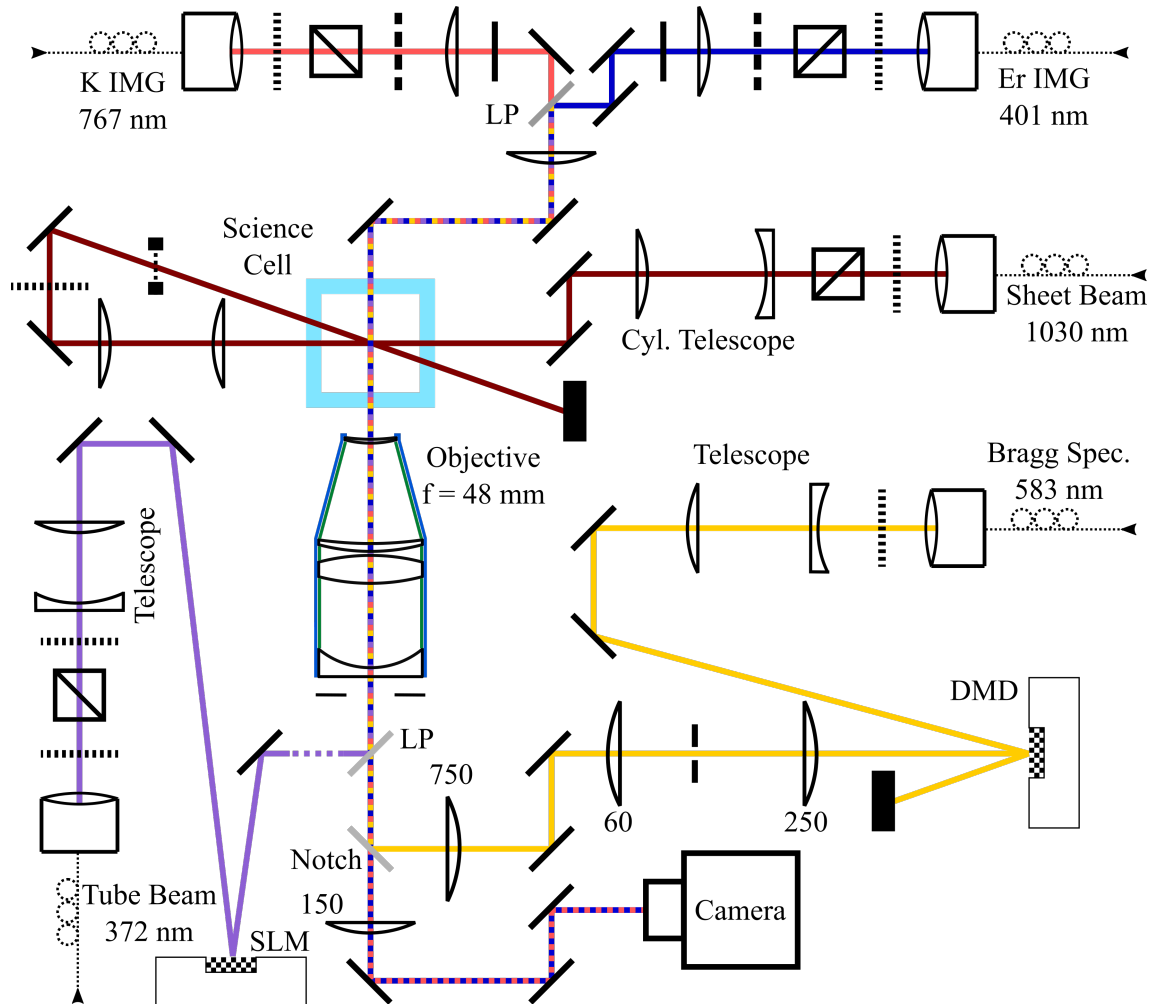


Fig. 5.8 Science Cell Optical Setup - The preliminary blueprint of all optical systems around the science cell, including the optical box potential (the 372 nm tube beam and the 1030 nm sheet beam; see Section 5.4), the Bragg spectroscopy setup (see Section 5.5) and absorption imaging for both Er and K. The imaging beams, Bragg spectroscopy and the box tubular beam all share a common optical axis and the custom projection objective that corrects for optical aberrations originating from passage through the 2.5 mm thick glass cell wall.

⁹2304 × 2304 CMOS array

5.4 Optical Box Potential

The optical system for generating a uniform trapping potential in the science cell will be a combination of an elliptical Gaussian beam for vertical confinement, along with a hollow repulsive cylindrical beam for in-plane trapping. The latter will be generated using 372 nm light projected off a phase-only Spatial Light Modulator¹⁰. The approximate layout of this optical system is shown in Figure 5.8 as a part of the full setup around the science cell.

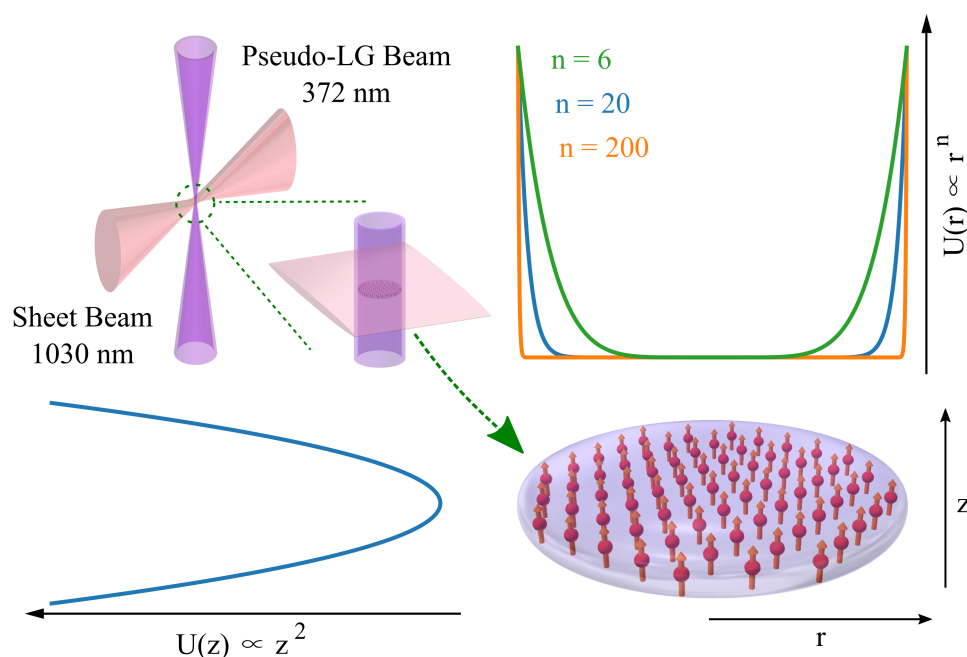


Fig. 5.9 **Optical Box Potential** - A trap created by superimposing the attractive, hollow pseudo-Laguerre-Gauss beam with a repulsive, high-aspect ratio elliptical sheet beam. Such a configuration would produce a trap that can be modelled by a general power-law potential $U(r, z) \propto r^n + \gamma^2 z^2$. The plots in the lower left and upper right sections of the figure show the trapping potential profiles along the two directions - simple harmonic trapping implemented vertically with the radial trapping potential shown for three different cases of power-law exponents, leading to different wall steepness. Practically achievable traps will have the steepness between $n \sim 10 - 20$.

The device that we utilise is a reflective, phase-only SLM, consisting of a reflective pixelated screen, where a phase shift can be implemented independently across all pixels. A Gaussian laser beam is directed at the SLM and the reflection is projected into a Fourier plane using a system of lenses [22]. There are multiple options for SLM phase patterns resulting in cylindrical beams [95], with the most common one being the simple phase winding¹¹,

¹⁰Hamamatsu LCOS-SLM Model X13267-05

¹¹Here, θ is the radial angle coordinate with respect to the centre of the screen

$\Delta\phi = l\theta$, resulting in a pseudo-Laguerre-Gauss (pLG) beam with the intensity profile in the Fourier-plane of:

$$I_{LG}(r) = \frac{r^2}{w_0^2} e^{-\frac{r^2}{w_0^2}} \left[\mathcal{J}_{\frac{l-1}{2}} \left(\frac{r^2}{2w_0^2} \right) - \mathcal{J}_{\frac{l+1}{2}} \left(\frac{r^2}{2w_0^2} \right) \right]^2 \quad (5.14)$$

where $\mathcal{J}_n(x)$ is the modified Bessel function of the first kind¹² and w_0 is the Gaussian waist that the beam would have in the focal plane if there was no phase modification by the SLM. Other options outlined in [95] include the axicon and spiral axicon beams, that can produce steeper traps with larger depth at the same power, but have a profile that is asymmetric around the focus point, and additionally, the normal axicon beam is not fully dark in the centre of the tube.

The trap steepness can be extracted by fitting a power law dependence r^n to the radial intensity profile of the beam. As the realistic profile is not a simple power-law, the exponent that fits it best varies with the cut-off radius for fitting. The approach taken in [95] is to define the fitting cut-off at the radius where the potential reaches $1/\eta$ of the peak value, and it is shown that for $\eta > 10$ the fits will give a relatively well defined exponent. In the referenced work, $n \sim 10$ is obtained for $l = 12$. This method is appropriate as the atomic cloud will typically have a temperature by an order of magnitude smaller than the trap depth, so the fitting is then performed only across the region of the potential which the atoms explore.

For trap depth and size estimation purposes, the radius of the pLG beam for $l \gg 1$ can be taken to be $r_l = \frac{l}{2}w_0$ and its thickness is of the order $\Delta r_l \approx \frac{l}{3}w_0$. Therefore, we can roughly estimate the trap depth for a given radius and optical power as¹³:

$$U_0 = -\frac{1}{2\epsilon_0 c} \text{Re}(\alpha) \frac{4P}{\pi \Delta r_l (2r_l + \Delta r_l)}. \quad (5.15)$$

In order to create a $k_B \times 1 \mu\text{K}$ deep trap of radius $R = 30 \mu\text{m}$, we would require $P \approx 7 \text{ mW}$ to be delivered to the focus, taking the value of polarizability of $\text{Re}(\alpha) = -779 \text{ a.u.}$ from Figure 5.1 (originally from [89]).

The sheet beam at 1030 nm will be generated from the same laser as the ODT/Transport beam, and will be projected into the science cell using a set of cylindrical lenses. The intention is to have an elliptical Gaussian beam, with a large aspect ratio, and horizontal waist much larger than the radius of the tubular beam. An example configuration we currently have as a working version in the design would result in a beam with waists of $w_x = 500 \mu\text{m}$

¹²Caligraphic font used here to avoid naming confusion due to intensity also having the symbol I

¹³Assuming that all the power is distributed across a ring of inner (outer) radius of r_l ($r_l + \Delta r_l$), and that the peak intensity is equal to twice the mean intensity.

and $w_y = 11 \mu\text{m}$ using a set of three cylindrical lenses and a input beam. Using equations 5.7 - 5.9 and erbium polarizability of 178 a.u. at 1030 nm from [89], we conclude that such trap would have a depth of $\sim k_B \times 2 \mu\text{K}$ and vertical trapping frequency of $\sim 2\pi \times 300\text{Hz}$ for 0.4 W of optical power. The residual trapping frequencies in the horizontal plane in this come out as $\sim 2\pi \times 5\text{Hz}$, and if we conclude that we need to reduce that for the trap to be flat, we can increase the aspect ratio of the beam.

This all assumes that the atomic cloud is simultaneously levitated, as otherwise, gravitational potential would greatly reduce the depth of the trap. Given the magnetic moment of erbium in its magnetic ground state of $\mu = 6.98\mu_B$, a field with a gradient of:

$$G = \frac{mg}{\mu} = 4.2 \frac{\text{G}}{\text{cm}} \quad (5.16)$$

would fully compensate for gravity.

5.5 Arbitrary Optical Potentials and Bragg Spectroscopy

We plan to install an optical setup for projecting arbitrary intensity patterns onto the atoms trapped in the box trap. The intended applications range from Bragg spectroscopy to stirring and dynamic trapping potentials. This will be implemented using a Digital Micro-mirror Device (DMD), an array of mirror-pixels that can be independently tilted into two different positions and thereby reflecting an arbitrary pattern into either of the two directions.

5.5.1 Generation of Arbitrary Intensity Patterns

Our setup is designed around a DMD device with a 1920×1080 pixel array¹⁴. As shown in Figure 5.10a, the incident light onto the DMD is provided in the form of a wide Gaussian Beam, that fills the DMD screen. Since the tilting axis of the mirrors is at 45° with respect to the vertical, and the two states are tilted at $\pm 12^\circ$ to the either side of the screen plane (Figure 5.10b-c), the input beam needs to approach from a direction that is out of the horizontal plane. It is essential to have the DMD screen orthogonal to the optical axis, in order to have the entirety of the screen in focus at once, when the pattern is projected onto the atoms. When correctly set up, the light reflected from the pixels in the ‘ON’ state will be reflected along the optical axis, whereas the ‘OFF’ pixels will send the excess light into a different direction such that it can be disposed off (Figure 5.10d).

The pattern is projected onto the atoms through a series of lenses, constituting two consecutive telescope stages with a total demagnification of approximately $\sim 1/80$ and diffraction limited spatial resolution of $2\mu\text{m}$ [96]. The first telescope also serves as a spatial filtering stage, blocking the higher diffraction orders originating from the DMD screen due to pixel grid periodicity. The second telescope consists of a long focal length lens and a specially designed objective that serves to correct for any optical aberrations caused by the passage of the converging beam through the glass wall of the science cell. This is done by using a pair of meniscus lenses that cancel the resulting optical path differences between different rays. Details about the design of the objective are laid out in Subsection 5.5.2.

Despite that the DMD can only project binary images, it is still possible to exploit the finite resolution of the system and create grayscale patterns. In our system, the combination of the pixel size of $7.6\mu\text{m}$ and the demagnification results in approximately $N_{\text{gs}} = 20$ pixels being imaged across one resolution length scale. Consequentially, images from $\sim N_{\text{gs}}^2$ pixels will partially overlap, leading to spatial averaging. The final step in creating such grayscale patterns is generating the binarised image for the DMD. The primary objective for any such procedure is to keep the local average of the intensity (calculated over an area of $N_{\text{gs}} \times N_{\text{gs}}$

¹⁴Model V6501 from Vialux

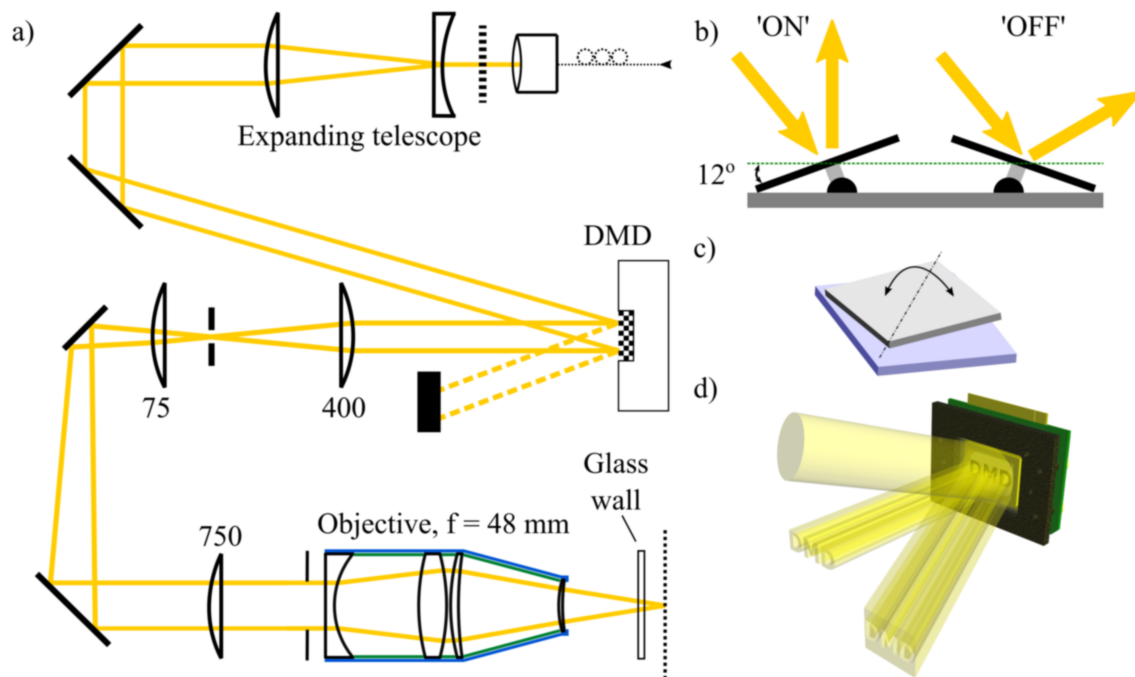


Fig. 5.10 **DMD Optical System** - a) The projection optical system that produces the real-space image of the illuminated DMD in the plane where the atoms are trapped. A large, ~ 15 mm waist radius, laser beam is reflected off the DMD screen, launching the modulated intensity pattern through the optical system. The demagnification optics consists of two telescope stages in series, yielding net demagnification of $\sim 1/80$. The first telescope has a spatial filtering stage, to eliminate higher diffraction orders resulting from the screen pixelation, and the final constituent lens in the system is a composite, aberration correcting objective, described in Section 5.5.2; b) Depiction of the 'ON' and 'OFF' states of individual DMD pixels, sitting at 12° in either direction to the plane of the screen. Note that the mirrors can also occupy the flat, 'PARK', position when not in use, or during the pixel updating procedure. c) Geometry of a single pixel, showing the rotation axis being across the pixel diagonal; d) Rendering showing a DMD in operation, projecting a word pattern "DMD" down the optical axis, and dumping the excess light.

pixels) as close as possible to the desired pattern. Further to that it is desirable to maintain maximum brightness and contrast of the pattern and to avoid regular patterns, such as parallel lines or extended checkerboard patterns, emerging from the binarisation algorithm, as these will lead to interference artefacts in the resulting image. The most widely used method for binarisation, that fulfils the above requirements, is the Floyd-Steinberg algorithm [97] depicted in Figure 5.11.

5.5.2 Design of the Projection Objective

In order to approach the diffraction limited regime, we need to compensate for the optical aberrations caused by the passage of the light through the 2.0 mm thick glass-cell wall. For

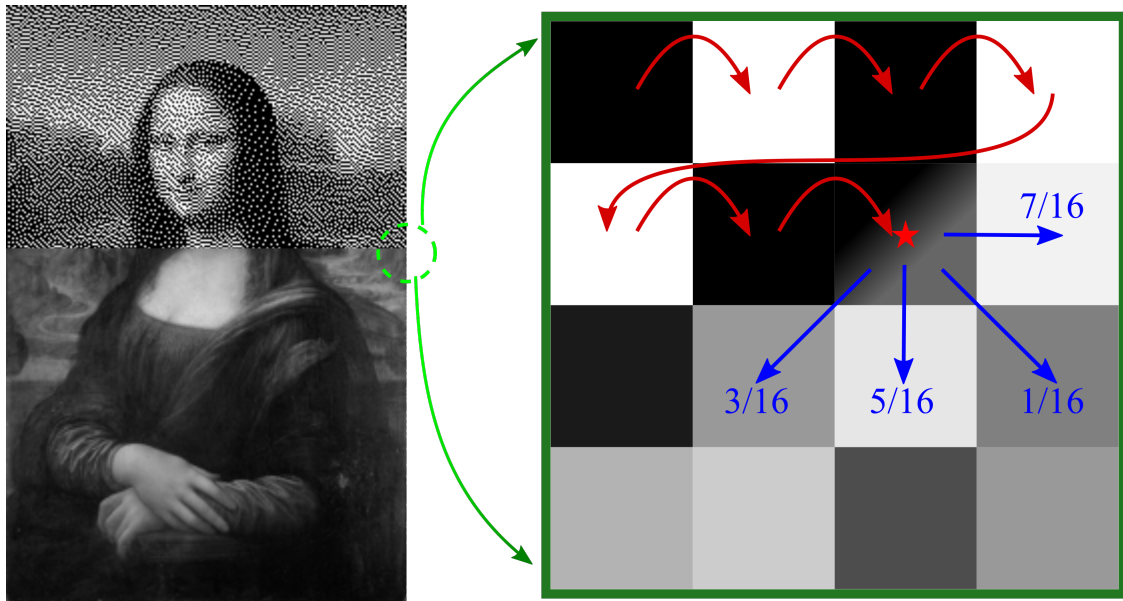


Fig. 5.11 **Floyd-Steinberg Algorithm** - Method for binarisation of greyscale images through error diffusion [97]. The algorithm traverses the image sequentially, applying simple thresholding to each individual pixel, setting it to 1 if its greyscale intensity was in the upper half of the scale, and otherwise to 0. The residual error resulting from this operation is then distributed across still unprocessed pixels in the vicinity. The exact fractions for this error diffusion step vary between implementations, and we opted for the simple option that distributes the residual over four nearest neighbour pixels, as indicated above.

this purpose, we have opted for a composite objective constructed using four commercially available lenses¹⁵, two of which are meniscus lenses, following the basic design idea from [98]. A ray-tracing program [99] was used to assess the performance of different lens combinations and to optimise the positioning of the optical components within the objective [96, 100]. The resulting design, that was prototyped and tested in the cited master theses of my colleagues, is shown in Figure 5.12. Theoretically, this configuration yields a diffraction limited resolution of $2.0\mu\text{m}$, with the geometric aberrations accounting for an additional $0.2\mu\text{m}$ towards the total point-spread-function RMS width.

As the aberration cancelling ability of the objective may be significantly reduced away from the design wavelength, the final design will have to be adjusted such that the 372nm optical box beam, that shares the same projection axis, is also focused without excessive aberrations at the position of the atoms within the cell.

¹⁵From Thorlabs, part numbers and focal lengths shown in Figure 5.12

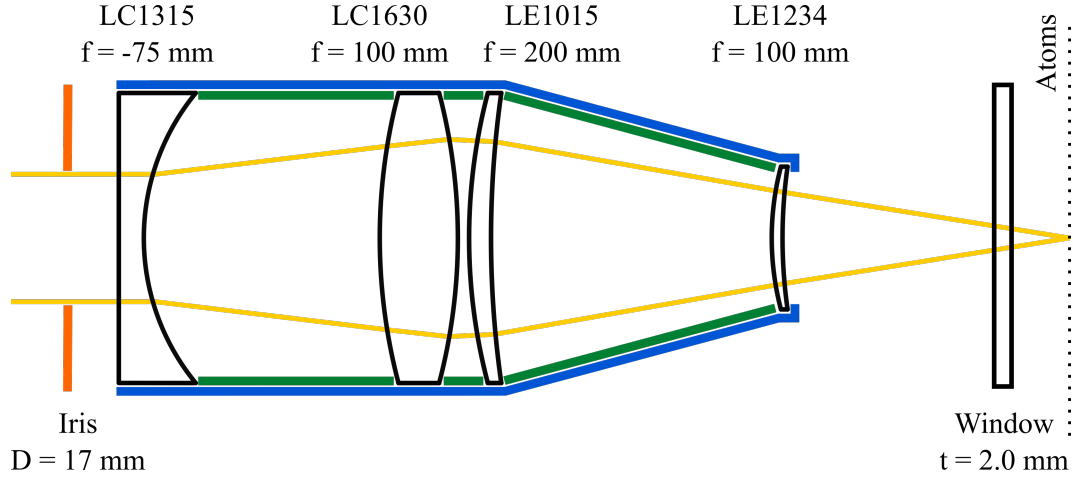


Fig. 5.12 **Projection Lens Objective** - The prototype design for the objective, optimised using a ray-tracing program. For 583 nm light, the focal length of the objective is 48.3 mm with a working distance of 46.9 mm. Best performance was achieved for an input iris diameter of 17.0 mm (resulting in $NA = 0.18$).

5.5.3 Bragg Spectroscopy

The Bragg spectroscopy method in this context represents a technique of probing the energy-momentum excitation spectrum of a given system through two-photon, Raman-type processes, that leave the constituent atoms in the same electronic ground state $|g\rangle$, while imparting a momentum \mathbf{q} to it. An excited state $|e\rangle$ is used as a mediator for this Raman process. The conventional method for Bragg Spectroscopy involves a pair of counter-propagating or crossed laser beams, with a frequency offset $\omega_1 - \omega_2 = \omega$ between them [101–104]. Since the laser beams typically have significant detunings w.r.t to the excited state in order to avoid exciting a significant atomic population, the effects of the atom-photon scattering processes can be equivalently described by the action of a light shift potential from the resulting intensity:

$$I(\mathbf{r}) \propto \cos^2 \left(\frac{\mathbf{k}_1 - \mathbf{k}_2}{2} \mathbf{r} - \frac{\omega_1 - \omega_2}{2} t \right) \quad (5.17)$$

which represents a sinusoidal intensity pattern with wavelength $\lambda = \frac{2\pi}{|\mathbf{k}_1 - \mathbf{k}_2|}$ with translational velocity $v = \frac{\omega_1 - \omega_2}{|\mathbf{k}_1 - \mathbf{k}_2|}$. An alternative configuration to this would be to directly create such an intensity pattern by modulating a single laser beam using the DMD [36, 105]. In essence, the electric field of such a pattern would be identical to that of a pair of beams at frequencies ω_0 and $\omega_0 + \omega$ crossing at an angle $\theta = \arcsin \frac{q}{2k_0}$. The system state evolution can then

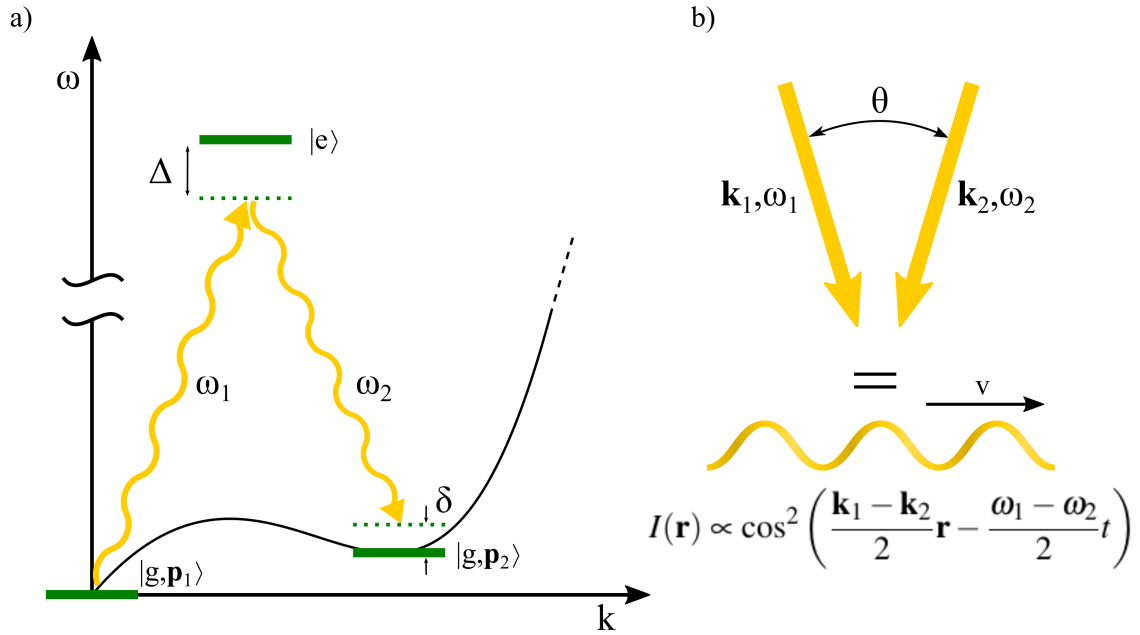


Fig. 5.13 **Bragg Spectroscopy Mechanism** - a) The two-photon Raman-type transition that is employed for Bragg spectroscopy. The atoms at rest in the ground state, $|g, \mathbf{p}_1 = 0\rangle$, can be imparted with a momentum and transferred to state $|g, \mathbf{p}_2 = \mathbf{q}\rangle$ via this process, without populating the excited state $|e\rangle$ significantly. While this is conventionally done with two crossed and frequency-offset laser beams, it can be shown that the same process can be induced using a dynamic light shift potential in the form of a moving sinusoidal intensity pattern (b).

be described equivalently using a three-level picture¹⁶ and a Raman process with a large one-photon detuning Δ , as depicted in Figure 5.13. The sinusoidal pattern can be projected onto the atoms either by directly imaging the pattern off the DMD [105] or by Fourier plane holography [106, 36]. We opted for the direct projection method as the dynamic translation of the pattern is simpler to implement in that scenario.

Provided that the one-photon detuning is much larger than the other energy scales that govern the dynamics of the system, namely $\Delta \gg |E_{\mathbf{p}_2} - E_{\mathbf{p}_1}|$, $\Delta \gg |\delta|$ and $\Delta \gg \Omega_{1,2}$, the evolution of the system can be well described through an effective two-level system with a driving Rabi frequency of:

$$\Omega_{\text{eff}} = \frac{\Omega_1 \Omega_2}{2\Delta}. \quad (5.18)$$

In the translated pattern scheme, both Ω_1 and Ω_2 are established from the mean pattern intensity I_0 as $\Omega_{1,2} = \Gamma \sqrt{\frac{I}{2I_{\text{sat}}}}$. Therefore, the effective Rabi frequency is set by the beam

¹⁶Full description would require introducing the effect of all energy levels via the atomic polarizability. Since we plan to implement the scheme in the immediate vicinity ($\Delta \sim 1000 \times \Gamma$) of the 583 nm transition, considering only that level is a valid approximation.

light intensity and the one-photon detuning:

$$\Omega_{\text{eff}} = \frac{\Gamma^2 I}{4\Delta I_{\text{sat}}} . \quad (5.19)$$

In practice, measurements will be performed by implementing a π -pulse of Bragg spectroscopy light, that would coherently pump the atoms from $|g, \mathbf{p}_1\rangle$ to $|g, \mathbf{p}_2\rangle$ imparting a momentum to them, followed by a time-of-flight interval that should lead to spatial separation of the excited atoms from the remaining cloud. In order to decide on the magnitude of Ω_{eff} , there are two considerations that need to be taken into account. The pulse duration $\tau_\pi = \frac{\pi}{\Omega_{\text{eff}}}$ should be sufficiently short in order for the atom loss from the trap to be negligible during the measurement. On the other hand, in order for the intensity pattern motion to be well defined during the course of the pulse, the projection frame rate of the pattern needs to be at least an order of magnitude higher than Ω_{eff} . The DMD that is a part of our system has a maximum frame rate of 10.3 kHz, therefore aiming for $\Omega_{\text{eff}} = 2\pi \times 1$ kHz as a design goal satisfies both conditions. Assuming we select a one-photon detuning of $\Delta = 2\pi \times 200$ MHz, and that the projection area¹⁷ is a circle of radius $R = 100 \mu\text{m}$, the required optical power for attaining this effective Rabi frequency would be $0.9 \mu\text{W}$.

In a similar consideration, the target range for the wave vector \mathbf{q} needs to be accommodated in the design. The accessible range of wave vectors needs to be sufficiently broad such that it includes the roton feature. Drawing from Subsection 1.3.2 (and originally from [65]), we expect the roton wave vector to be at $k_r \approx l_z^{-1}$, where l_z is the harmonic oscillator length associated with the vertical confinement of the trap. In our experiment (see Section 5.4), the trap frequency will be set to $\omega_z \approx 2\pi \times 300$ Hz, implying $l_z \approx 1 \mu\text{m}$. Consequentially, we should aim for a system that is able to create a pattern with a wavelength as short as $\lambda_{\text{min}} = \frac{2\pi}{k_r} \approx 6 \mu\text{m}$. The ultimate limit on the pattern wavelength is set by the imaging resolution, and since our projection objective provides the resolution of $2 \mu\text{m}$, we should be able to reach up to approximately $3 \times k_r$ when probing the spectrum.

¹⁷Such that it extends wider than the box trapping potential with $R_{\text{box}} \lesssim 50 \mu\text{m}$

Chapter 6

Ground State Stability in a Box Trap - Numerical Simulations

A consequence of the anisotropic nature of the dipolar force is the strong dependence of the stability of trapped condensates on the trapping geometry. As each atom in the cloud attracts a portion of the remaining atomic density that is within the conical domain around the dipole axis, in some arrangements this can render atomic clouds unstable. This is the case when the attractive component of the force is too strong for the repulsive interactions, the confining potential and quantum pressure to counter this effect. A well known result is that a bulk¹, strongly dipolar gas ($\epsilon_{dd} \geq 1$) is unstable [63]. Furthermore, in the case of a trapped gas, clouds that are more oblate w.r.t. to the axis of magnetic polarisation tend to be more stable [33]. The subject of stability in harmonic traps in general has been extensively investigated [33, 65, 107, 108]. Finally, another interesting observation for dipolar gases trapped in box-like potentials is that, due to the long-range nature of the interactions, peaks of atomic density tend to develop near sharp trap walls [109], affecting the homogeneity of the cloud. This is in stark contrast with the behaviour of gases with contact interactions only, where a perfect box potential is desired when pursuing a uniform density distribution. As our experimental research goals² call for a uniform quantum gas system with strongly dipolar interactions (i.e. with pronounced roton-like nature of excitations - near the stability boundary), the interest behind this numerical study lies in better understanding how to realise such a system and potential implications towards experimental implementation of the optical box trap.

¹infinite, filling all of space

²e.g investigating phase transition dynamics in the context of Kibble-Zurek theory [110, 111] requires uniform atomic density. See Section 7.3.2

In this chapter, I report on the ongoing effort directed at investigating the effect of the trap geometry on the stability against collapse and uniformity of the atomic cloud. Our intended approach revolves around numerically finding ground states of the Gross-Pitaevskii equation with dipolar interactions (dGPE) and testing them for dynamical stability using the Bogoliubov-de Gennes formalism (BdG). The latter step is necessary, as we do the energy minimisation assuming cylindrical symmetry, which does not take into the account any angular density perturbations. We also constrain our effort to a particular class of power-law traps, broadly mimicking the capabilities of our experimental setup design and, for now, to the case of a purely dipolar gas with no contact interactions.

The presented results are preliminary, as we currently only have a working implementation of the dGPE ground state solver, while the application of the BdG method for testing the states for angular roton instability is under development. Nevertheless, this first insight into the simulation results hints some interesting trends that are potentially relevant for the implementation of future experiments with the optical box. We particularly find interesting the effect that the box wall steepness has on the homogeneity of the atomic density, and the implications for creating uniform clouds.

6.1 Numerical Simulation

The entirety of the simulation code is written in Python and it consists of scripts for finding the ground state of systems described by the dGPE and for their subsequent testing for dynamical stability. In the quest of finding the ground states of dGPE, we have implemented both the imaginary time propagation method [112, 113, 95] and the conjugate gradient method [114–117] for the ground state search. Here, I mostly focus on the conjugate gradient method, and all the presented data is obtained with it. However, it should be noted that, as a part of the testing process, we have thoroughly compared the results obtained from both methods and found complete agreement. As the implemented calculations rely heavily on the Fourier and Hankel transforms, conventions and definitions that we use, along with some useful identities, are provided in Appendix G.

The implementation of the BdG formalism is still under way, but I will briefly touch upon the key steps in using it for stability testing, pointing towards the relevant literature. The procedure comes down to solving an eigenvalue problem for the linearised system of equations representing the evolution of different BdG excitation modes. Whenever the process yields imaginary eigenvalues for the excitation frequency, this indicates the existence of a mode softened sufficiently to cause the instability. In this process, we employ the

ARPACK package [118] available through the `linalg.eigs` functionality of the SciPy library in Python.

6.1.1 Defining the System

The centrepiece of the simulation is the dipolar Gross-Pitaevskii equation (from Equation 1.13) that governs the dynamics of the system and determines its ground state properties:

$$i\hbar \frac{\partial \psi(\mathbf{r}, t)}{\partial t} = \left[-\frac{\hbar^2}{2m} \nabla^2 + V_{\text{ext}}(\mathbf{r}) + \frac{4\pi\hbar^2 a_s N}{m} |\psi(\mathbf{r}, t)|^2 + N \int U_{\text{dd}}(\mathbf{r} - \mathbf{r}') |\psi(\mathbf{r}, t)|^2 d^3 \mathbf{r}' \right] \psi(\mathbf{r}, t) \quad (6.1)$$

with the wavefunction being normalised to unity: $\int_V d^3 \mathbf{r} |\psi(\mathbf{r}, t)|^2 = 1$.

The dipolar interaction, for magnetic dipoles, is described by the equation:

$$U_{\text{dd}}(\mathbf{r} - \mathbf{r}') = \frac{\mu_0 \bar{\mu}^2}{4\pi} \frac{1 - 3 \cos^2(\theta)}{|\mathbf{r} - \mathbf{r}'|^3}. \quad (6.2)$$

The dGPE can be made dimensionless by introducing the length and time units of measure, x_s and t_s and then further simplified by the appropriate choice of these units. The transformation into the dimensionless form is performed by the substitutions:

$$\mathbf{r} \rightarrow \frac{\mathbf{r}}{x_s}, \quad t \rightarrow \frac{t}{t_s}, \quad \psi \rightarrow \frac{\Psi}{x_s^{\frac{3}{2}}}. \quad (6.3)$$

Applying these substitutions to the dGPE leads to:

$$i \frac{\partial \psi(\mathbf{r}, t)}{\partial t} = \left[-\frac{\hbar t_s}{2m x_s^2} \nabla^2 + \frac{t_s}{\hbar} V_{\text{ext}}(\mathbf{r}) + \frac{4\pi\hbar a_s N t_s}{m x_s^3} |\psi(\mathbf{r}, t)|^2 + \frac{N \mu_0 \bar{\mu}^2 t_s}{4\pi\hbar x_s^3} \int \frac{1 - 3 \cos^2(\theta)}{|\mathbf{r} - \mathbf{r}'|^3} |\psi(\mathbf{r}, t)|^2 d^3 \mathbf{r}' \right] \psi(\mathbf{r}, t). \quad (6.4)$$

The first convenient selection of units is to fix $t_s = \frac{m x_s^2}{\hbar}$ which directly leads to:

$$i \frac{\partial \psi(\mathbf{r}, t)}{\partial t} = \left[-\frac{1}{2} \nabla^2 + \frac{m x_s^2}{\hbar^2} V_{\text{ext}}(\mathbf{r}) + \frac{4\pi\hbar a_s N}{x_s} |\psi(\mathbf{r}, t)|^2 + \frac{N \mu_0 \bar{\mu}^2 m}{4\pi\hbar^2 x_s} \int \frac{1 - 3 \cos^2(\theta)}{|\mathbf{r} - \mathbf{r}'|^3} |\psi(\mathbf{r}, t)|^2 d^3 \mathbf{r}' \right] \psi(\mathbf{r}, t) \quad (6.5)$$

which now allows us to define the dimensionless contact and dipolar interaction strengths:

$$g_s = \frac{4\pi\hbar a_s N}{x_s}, \quad D = \frac{N\mu_0\bar{\mu}^2 m}{4\pi\hbar^2 x_s}. \quad (6.6)$$

Finally, by absorbing the numerical coefficients into a dimensionless trapping potential $V(\mathbf{r}) = \frac{m x_s^2}{\hbar^2} V_{\text{ext}}(\mathbf{r})$, and by defining $V_{\text{dd}} = \frac{1-3\cos^2(\theta)}{|\mathbf{r}-\mathbf{r}'|^3}$ we reach the final compact form of the dGPE:

$$i\frac{\partial\psi(\mathbf{r},t)}{\partial t} = \left[-\frac{1}{2}\nabla^2 + V(\mathbf{r}) + g_s|\psi(\mathbf{r},t)|^2 + D \int_V V_{\text{dd}}(\mathbf{r}-\mathbf{r}')|\psi(\mathbf{r}',t)|^2 d^3\mathbf{r}' \right] \psi(\mathbf{r},t). \quad (6.7)$$

Finally, the energy functional in the dimensional units is:

$$E[\psi] = \int \left[\frac{1}{2}|\nabla\psi(\mathbf{r})|^2 + V(\mathbf{r})|\psi(\mathbf{r})|^2 + \frac{g_s}{2}|\psi(\mathbf{r})|^4 + \frac{D}{2} \int V_{\text{dd}}(\mathbf{r}-\mathbf{r}')|\psi(\mathbf{r}')|^2|\psi(\mathbf{r})|^2 d^3\mathbf{r}' \right] d^3\mathbf{r} \quad (6.8)$$

An axially symmetric power-law trap, which is the type of the trapping potential that is of interest to us, can be defined as (in dimensionless units):

$$V(r,z) = \frac{1}{2}(r^p + \gamma^2 z^2) \quad (6.9)$$

which implicitly assumes $x_s = R_p$, where R_p is the characteristic radius of the power law trap, determined by the condition:

$$V_{\text{ext}}(R_p, 0) = V_{\text{ext}}(0, l_z) \quad (6.10)$$

and $l_z = \sqrt{\frac{\hbar}{m\omega_z}}$ is the oscillator length of the vertical harmonic trap. The box radius can be expressed in terms of the oscillator length along the z (harmonic) direction as:

$$R_p = \sqrt{\gamma} l_z \quad (6.11)$$

For the purposes of visualising and presenting data, we also recall the dimensionless quantity ν that is inspired by the definition in [108]. Here we define it using the inverse relation - transforming ν to D :

$$D = \frac{3\pi^{\frac{1}{2}}\Gamma\left(1 + \frac{2}{p}\right)}{16\Gamma\left(\frac{5}{2} + \frac{2}{p}\right)} \left(\frac{3}{2} \nu \gamma^{\frac{6+\frac{3}{2}p}{3p+4}} \right)^{\frac{3p+4}{3p}} \quad (6.12)$$

which is constructed by using the peak density in the Thomas-Fermi approximation in place of the area density in the definition of v in [108].

6.1.2 Calculation of the Dipolar Energy/Hamiltonian Term

By employing the convolution theorem the dipolar term in the Hamiltonian, given in the Equation 6.2, can be rewritten in a more convenient form:

$$\hat{H}_{\text{dip}}[\psi] = DV_{\text{dd}} * |\psi|^2 = D\mathcal{F}^{-1}\{\mathcal{F}\{V_{\text{dd}}\} \cdot \mathcal{F}\{|\psi|^2\}\}. \quad (6.13)$$

Recall that the dipolar potential in the dimensionless units takes the form:

$$V_{\text{dd}}(\mathbf{r}) = \frac{1 - 3 \cos^2 \theta}{|\mathbf{r}|^3} \quad (6.14)$$

which can then be efficiently calculated using a Discrete Fourier Transform (DFT) The Fourier transform of the dipolar potential can be written analytically, and takes the form:

$$\tilde{V}_{\text{dd}}(\mathbf{k}) = 4\pi \left(\cos^2 \theta_k - \frac{1}{3} \right) \quad (6.15)$$

where $\cos \theta_k = \frac{k_z}{|\mathbf{k}|}$.

While this result allows for a faster calculation of the dipolar term, it introduces a new issue - as the DFT assumes the transformed function to be periodic, there will be a contribution to the overall dipolar interaction from the aliased images of the cloud outside the grid domain. To mitigate for this, one can limit the range of the dipolar force by introducing a cut-off, and make sure that a sufficiently large grid is used in the simulation [119, 113, 120]. The options for the cut-off, in terms of geometry are the spherical cut-off:

$$V_{\text{dd}}^S(\mathbf{r}) = \begin{cases} \frac{1-3\cos^2\theta}{|\mathbf{r}|^3} & \text{if } |\mathbf{r}| < R_c \\ 0 & \text{otherwise} \end{cases} \quad (6.16)$$

with its Fourier transform given by:

$$\tilde{V}_{\text{dd}}^S(\mathbf{k}) = 4\pi \left(\cos^2 \theta_k - \frac{1}{3} \right) \left[1 + 3 \frac{\cos(R_c k)}{R_c^2 k^2} - 3 \frac{\sin(R_c k)}{R_c^3 k^3} \right]. \quad (6.17)$$

This is a simple option, but can be inefficient in cases when the cloud has a large aspect ratio, which would lead to the cut-off sphere encompassing a lot of empty space, and consequentially the grid would be unnecessarily large along the vertical direction. The

possible solution for this is using a cylindrically shaped cut-off region instead:

$$V_{\text{dd}}^C(\mathbf{r}) = \begin{cases} \frac{1-3\cos^2\theta}{|\mathbf{r}|^3} & \text{if } \rho < \rho_c \text{ and } z < Z_c \\ 0 & \text{otherwise} \end{cases}. \quad (6.18)$$

The Fourier transform of the cylindrically cut-off potential takes the form:

$$\begin{aligned} \tilde{V}_{\text{dd}}^C(\mathbf{k}) = & 4\pi \left(\cos^2\theta_k - \frac{1}{3} \right) \\ & + 4\pi e^{-Z_c k_\rho} \left[\sin^2\theta_k \cos(Z_c k_z) - \sin\theta_k \cos\theta_k \sin(Z_c k_z) \right] \\ & - 4\pi \int_{\rho_c}^{\infty} \rho d\rho \int_0^{Z_c} dz \cos(k_z z) \frac{\rho^2 - 2z^2}{(\rho^2 + z^2)^{\frac{5}{2}}} J_0(k_\rho \rho) \end{aligned} \quad (6.19)$$

which is a semi-analytic expression and requires a costly numerical evaluation every time a grid is defined. This can be avoided in cases when the discrete Fourier-Hankel transform is used, as it does not suffer from aliasing. In that case it is sufficient to implement the cut-off along the vertical direction only, given by:

$$V_{\text{dd}}^V(\mathbf{r}) = \begin{cases} \frac{1-3\cos^2\theta}{|\mathbf{r}|^3} & \text{if } z < Z_c \\ 0 & \text{otherwise} \end{cases} \quad (6.20)$$

and its Fourier transform:

$$\begin{aligned} \tilde{V}_{\text{dd}}^V(\mathbf{k}) = & 4\pi \left(\cos^2\theta_k - \frac{1}{3} \right) \\ & + 4\pi e^{-Z_c k_\rho} \left[\sin^2\theta_k \cos(Z_c k_z) - \sin\theta_k \cos\theta_k \sin(Z_c k_z) \right]. \end{aligned} \quad (6.21)$$

6.1.3 Spatial Discretisation

Exploiting the cylindrical symmetry of the system, enforced by the shape of the trapping potential (Equation 6.9), we reduce the problem to a two-dimensional one when looking for the ground state. Furthermore, we know that the ground state will be even around the $z = 0$ plane, therefore all system quantities can be sampled only on one side of the plane, and additionally, this allows for a discrete cosine transform (DCT) to be used in place of the full DFT. The wave function $\Psi(r, z)$ is then represented on a $N_r \times N_z$ grid, spanning the region of $[0, L_r] \times [-L_z, 0]$. The grid is evenly spaced in the z -direction, whereas the spacings along the radial direction generally take different values along the axis, as the sampling is

governed by the discrete Hankel transform (DHT), that is the equivalent of the DFT for this grid geometry. Following the definitions from Appendix G, the grid point coordinates are defined as $\mathbf{r}_{mn} = (r_m, z_n)$, where:

$$r_m = \frac{\alpha_m L_r}{S} \quad \text{for } m \in \{0, \dots, N_r - 1\}, \quad (6.22)$$

$$z_n = -L_z + \frac{n L_z}{N_z - 1} \quad \text{for } n \in \{0, \dots, N_z - 1\} \quad (6.23)$$

where α_m represents the m -th zero of J'_0 , the first derivative of the zeroth order Bessel function of the first kind - J'_0 , and S is a constant parameter originating from the implementation of the DHT [121], and it takes the form:

$$S = 2|J_0^{-1}(\alpha_\kappa)| \sqrt{1 + \sum_{n=1}^{N_r-1} J_0^{-2}(\alpha_n) J_0^2\left(\frac{\alpha_\kappa \alpha_n}{J_{N_r}}\right)} \quad (6.24)$$

where J_{N_r} is the N_r -th zero of $J_0(r)$ and $\kappa = \text{Int}\left(\frac{N_r+1}{4}\right)$. The grid spacings along the radial direction are only significantly non-uniform across the several points closest to the origin, while the outer portion of the grid has approximately evenly distributed points. Appendix G provides further details about the grid geometry, including the definition of the inverse space grid $\mathbf{k}^{mn} = (k_r^m, k_z^n)$ and mentions the interpolation methods for evaluating integrals and derivatives with high precision.

The Fourier transform on this grid is a hybrid of the DCT along the z -direction and the DHT along the r -direction. We use the `mk1_fft` Python package to implement the DCT³ with parallel computing. A parallelised implementation of the DHT was written by directly implementing the recipe from [121] that is also presented in Appendix G, and using the `numba` Python package to implement parallel vector and matrix operations.

The application of the BdG formalism that is anticipated in Subsection 6.1.6 will require the application of higher-order Hankel Transforms, to accommodate for the angular dependence of the excitation wave functions.

6.1.4 Imaginary Time Propagation

In general, a direct evaluation of the propagator for a quantum system with the Hamiltonian \hat{H}

$$\hat{U}(t) = e^{-i\hat{H}\Delta t} \quad (6.25)$$

³That does not come with a built in DCT function, but one can be readily constructed from `mk1_fft.rfft`

is very computationally costly due to the fact that \hat{H} consists of components that do not commute - namely $\hat{T} = -\frac{1}{2}\nabla^2$ and $\hat{V} = V(\mathbf{r}) + g_s |\psi|^2 + \hat{H}_{\text{dip}}[\psi]$, and also because the explicit evaluation of \hat{T} in the position basis is challenging. Nevertheless, it turns out that the ansatz:

$$\hat{U}_{\text{split}} = e^{-\frac{i\hat{V}\Delta t}{2}} e^{-i\hat{T}\Delta t} e^{-\frac{i\hat{V}\Delta t}{2}} \quad (6.26)$$

approximates the full propagator \hat{U} with an error that is only third-order in Δt .

The advantage of this method is that the $e^{-i\hat{T}\Delta t}$ term can be evaluated in the inverse (momentum) space, which allows for a significant code speed-up. The recipe for applying this operator to a given state is:

$$e^{-i\hat{T}\Delta t} |\psi\rangle = \mathcal{F}^{-1} \left\{ e^{-i\Delta t \frac{k^2}{2}} \mathcal{F} \{ |\psi\rangle \} \right\}. \quad (6.27)$$

6.1.5 Preconditioned Conjugate Gradient Method

The conjugate gradients method [114] is similar to the steepest descent minimisation, only it does not necessarily follow the gradient during each step. Instead, additional information about the energy landscape is drawn from the Hamiltonian operator to construct a set of directions that would efficiently lead towards the minimum when applied consecutively. It is motivated by the problem of minimising a quadratic functional.

This method is laid out in detail in references [115–117]. Every step in the procedure starts by calculating the residual vector of the Hamiltonian eigenvalue problem in the Hilbert space:

$$|r_n\rangle = \hat{H}[\psi_n] |\psi_n\rangle - \langle \psi_n | \hat{H}[\psi_n] | \psi_n \rangle |\psi_n\rangle. \quad (6.28)$$

Next, the descent direction is calculated using the formula:

$$|d_n\rangle = -\hat{P}|r_n\rangle - \beta_n |p_{n-1}\rangle \quad (6.29)$$

where the β_n is the projection factor that maintains the conjugacy requirement. There is a number of recipes for defining it, and the most common one, called the Polak-Ribière formula, is used here:

$$\beta_n = \max(0, \beta_n^{PR}), \quad (6.30)$$

$$\beta_n^{PR} = \frac{(\langle r_n | - \langle r_{n-1} |) \hat{P} | r_n \rangle}{\langle r_{n-1} | \hat{P} | r_{n-1} \rangle}. \quad (6.31)$$

Finally, one needs to assure that the descent direction is orthogonal to the current state:

$$|p_n\rangle = |d_n\rangle - \langle \psi_n | d_n \rangle | \psi_n \rangle . \quad (6.32)$$

Now, as the descent direction is determined, the minimum of the energy functional along that direction needs to be found. Practically we do that by writing the new wave function as:

$$| \psi_{n+1}^{\text{trial}}(\theta) \rangle = \cos \theta | \psi_n \rangle + \frac{\sin \theta}{\|p_n\|} | p_n \rangle . \quad (6.33)$$

Note that the norm of the new function is automatically equal to unity when written in this form. The energy functional is now minimised w.r.t. θ and this generates the wave function in the next step:

$$\theta_n = \operatorname{argmin}_{\theta} \left\{ E \left[\psi_{n+1}^{\text{trial}}(\theta) \right] \right\} , \quad (6.34)$$

$$| \psi_{n+1} \rangle = | \psi_{n+1}^{\text{trial}}(\theta_n) \rangle . \quad (6.35)$$

The above algorithm will work fine without the preconditioner, i.e. with only $\hat{P} = \hat{I}$. On the other hand, the references suggest using it, as it unleashes the full potential of the method. The first suggestion, presented in references [115–117] and also used in the particular case of finding the ground state of the dipolar gas in [122, 119], is the preconditioner based on the kinetic energy operator, that is diagonal in the momentum space basis:

$$\hat{P}_T = \left(\alpha[\psi_n] - \frac{\nabla^2}{2} \right)^{-1} \quad (6.36)$$

where the number α is evaluated using the current iteration of the wave function via the equation:

$$\alpha[\psi_n] = \langle \psi_n | \hat{H}[\psi_n] | \psi_n \rangle . \quad (6.37)$$

This preconditioner reportedly becomes inefficient for large spatial size of the system or strong interactions. Consequentially, the papers [115–117] define a preconditioner based on the potential and interaction energies, that is diagonal in the position space basis:

$$\hat{P}_V = \left(\alpha[\psi_n] + V + \hat{H}_{\text{int}}[\psi_n] + \hat{H}_{\text{dip}}[\psi_n] \right)^{-1} \quad (6.38)$$

employing the same definition of α . The papers also point out that it is not useful to apply \hat{P}_V on its own, as its performance deteriorates for high-resolution grids, but rather in a combination

together with \hat{P}_T . This leads to three possibilities:

$$\hat{P}_{VT} = \hat{P}_V \hat{P}_T, \quad (6.39)$$

$$\hat{P}_{TV} = \hat{P}_T \hat{P}_V \quad (6.40)$$

and finally, the symmetrised version:

$$\hat{P}_S = \hat{P}_V^{\frac{1}{2}} \hat{P}_T \hat{P}_V^{\frac{1}{2}}. \quad (6.41)$$

The final option should theoretically be a universally good choice according to the reference papers.

6.1.6 Angular Roton Instability

As laid out in [122, 119], ground state clouds that assume concave, ‘red blood cell’ shaped density distributions, are prone to angular roton instabilities. This is manifested through the softening of one of the angular excitations, pushing its energy below the energy of the unperturbed condensate, seeding the instability. A direct consequence is that the energy landscape minimisation techniques that do not account for the angular degree of freedom will overestimate the stability boundary in these cases. Hence, all these candidate ground states need to be vetted using the BdG approach, to assure they are indeed stable. In this picture, starting from the candidate ground state obtained from energy minimisation, Ψ_0 , here assumed real, a trial excited state wave function is constructed following the same approach as in Subsection 1.3.2:

$$\Psi(\mathbf{r}, t) = [\Psi_0(\mathbf{r}) + \delta\Psi(\mathbf{r}, t)] e^{-i\mu t} \quad (6.42)$$

where μ is the chemical potential of the unperturbed system, and takes the form:

$$\begin{aligned} \mu[\Psi_0] = \int \left[\frac{1}{2} |\nabla\Psi_0(\mathbf{r})|^2 + V(\mathbf{r})|\Psi_0(\mathbf{r})|^2 + g_s |\Psi_0(\mathbf{r})|^4 \right. \\ \left. + D \int V_{dd}(\mathbf{r} - \mathbf{r}') |\Psi_0(\mathbf{r}')|^2 |\Psi_0(\mathbf{r})|^2 d^3\mathbf{r}' \right] d^3\mathbf{r}. \end{aligned} \quad (6.43)$$

The perturbation to the wave function is constrained to the form:

$$\delta\Psi(\mathbf{r}, t) = \lambda [u(\mathbf{r})e^{-i\omega t} + v^*(\mathbf{r})e^{i\omega t}] \quad (6.44)$$

when looking for a solution, and $\lambda \ll 1$ is assumed⁴. The above ansatz can be trialled in the time-dependent dGPE (Equation 6.7), leading to the following set of equations when expanded up to first order in λ and with terms collected according to frequency components:

$$(H_0 - \mu + C + 2X)(H_0 - \mu + C)f = \omega^2 f . \quad (6.45)$$

$$(H_0 - \mu + C)(H_0 - \mu + C + 2X)g = \omega^2 g \quad (6.46)$$

where $f = u + v$ and $g = v - u$. The two interaction operators C and X take the form:

$$C\phi(\mathbf{r}) = g_s |\Psi_0(\mathbf{r})|^2 \phi(\mathbf{r}) + D \int_V V_{\text{dd}}(\mathbf{r} - \mathbf{r}') |\Psi_0(\mathbf{r}')|^2 d^3 \mathbf{r}' \phi(\mathbf{r}) , \quad (6.47)$$

$$X\phi(\mathbf{r}) = g_s |\Psi_0(\mathbf{r})|^2 \phi(\mathbf{r}) + D \int_V V_{\text{dd}}(\mathbf{r} - \mathbf{r}') \Psi_0(\mathbf{r}') \phi(\mathbf{r}') d^3 \mathbf{r}' \Psi_0(\mathbf{r}) . \quad (6.48)$$

The angular roton instability is established if the Equations 6.45 and 6.46 yield negative eigenvalues as the solutions for ω^2 , implying imaginary values for ω . This analysis can be performed in the cylindrical coordinate system, but trial functions corresponding to different phase windings must be employed individually [122].

6.2 Results Analysis

The goal of this numerical investigation is to get a better understanding of the effect of the trap geometry onto the shape and stability of the condensate ground state. We first look at the case of a purely dipolar gas, with the contact interaction strength kept at zero, and we consider trapping in a general power law potential (Equation 6.9). Three representative values of the box exponent, $p = 2, 6$ and 20 are used in the initial analysis, representing harmonic trapping, and box potentials of intermediate (soft-wall) and high steepness (hard-wall), respectively. We also vary the strength of dipolar interactions D and the trap aspect ratio γ , and employ the preconditioned conjugate gradient method [114–117] to find the ground state wave functions and energies for each combination of parameters.

The results outlined below only deal with the stability to radial rotons and all candidate ground state wave functions with biconcave shape⁵ need to be further vetted for angular roton instability. Additionally, the numerical methods need to be thoroughly checked for robustness in the limit of large p and γ . Still, the data obtained so far reveals interesting trends that are likely to persist despite future improvements to the simulation code. This data

⁴Also, the normalisation rule enforced for u and v is $\int d^3 \mathbf{r} [u^2 - v^2] = 1$

⁵i.e. having area density that does not monotonically decrease from $r = 0$ outward.

hints that the stability boundaries of all power-law traps for $\gamma \rightarrow \infty$ generally converge to the same level as the infinite harmonically trapped planar condensate [108], at least if only the angular rotons are considered. At the same time, the higher power-laws seem to always develop concave profiles close to the stability boundary, which might eventually lower the actual boundary when the angular rotons are counted in. This would imply that it is the trap wall that seeds the instability. Additionally, it appears that box traps with soft walls ($p \sim 6$) generally produce the most uniform clouds at intermediate aspect ratios in the presence of strong dipolar interactions. Therefore, it is clear that the steepness of the confining potential determines whether the stability and excitation properties are dominated by the bulk density of the gas (as it is the case for the flattened homogeneous gas [108]) or, instead, the effects from the edges.

6.2.1 Stability Against Collapse

Given the anisotropic nature of the DDI force that makes it inevitably attractive for some atoms, a cloud of dipolar atoms trapped in any trap will eventually become unstable with increasing strength of DDI. In this investigation, we constrain the system configuration to a spin polarised, purely dipolar ($g_s = 0$) gas, trapped in the ‘pancake’ trap, as defined in Equation 6.9. Working in dimensionless units (see Subsection 6.1.1 for conventions), such system is fully described by three parameters - D , γ and p . The case of cylindrically symmetric harmonic trap (equivalent to setting $p = 2$) is already well explored [122, 119]. Our goal is to extend this analysis to higher values of p , which is the regime relevant for our experiment. The discussion here is limited to the stability against radial rotons, i.e. excitations that do not have axial dependence. For clouds with fully convex density distribution, it is the radial roton modes that seed the instability, and results obtained here in those cases may be taken as complete. However, as we will see, the steeper power-law potentials very often produce concave clouds, and this is taken into account before drawing any conclusions.

In each run of the simulation, we fix γ and p , and find the ground state of the non-interacting gas. Then, we continue by incrementing the dipolar interaction strength parameter, D , starting a binary search algorithm for the stability boundary. In practice, we do the search in terms of the parameter ν as defined in Equation 6.12, which then yields D .

The stability boundaries for the three different trap geometries used ($p = 2, 6$ and 20) are shown in Figure 6.1. In each case the traps with a small aspect ratio $\gamma \lesssim 10$ reach the point of collapse for comparatively low values of ν , with the stability abruptly increasing at intermediate to high aspect ratios. In the limit of $\gamma \rightarrow \infty$ all three power laws seem to converge to $\nu \approx 5.5$, which coincides with the prediction for an infinite dipolar gas confined harmonically in one direction only, yielding $\nu_{\text{crit}}^{\infty} \approx 5.5$ [108].

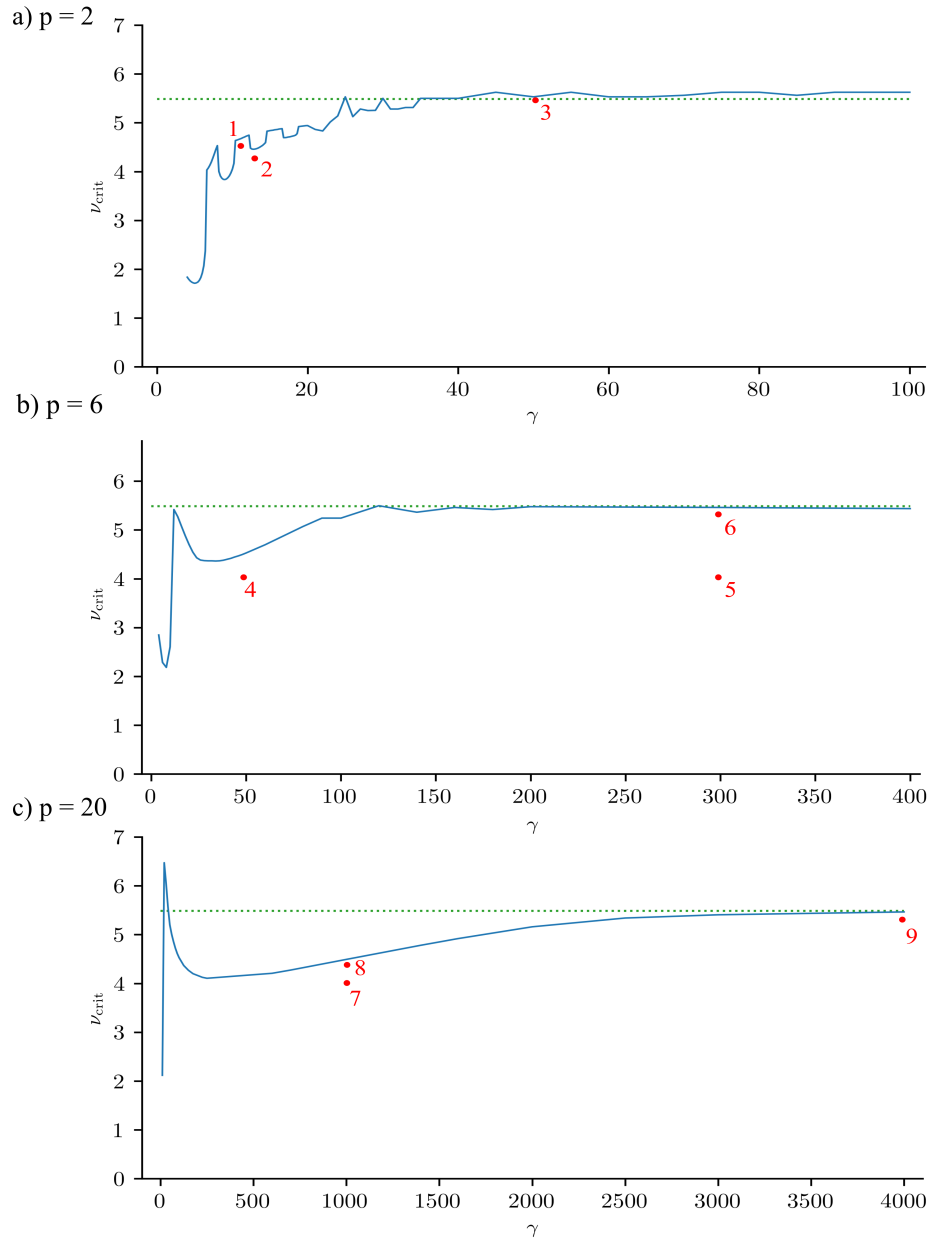


Fig. 6.1 Stability Boundary in the Box Trap - a) Harmonic trapping case ($p = 2$) exhibiting the stability boundary that converges to the ‘infinite cloud’ limit by $\gamma \sim 40$. Most of the stable solutions are convex, apart from some isolated regions near the stability boundary at low values of γ (the upward facing ‘teeth’ in the line at $\gamma = 7 - 20$). Only these convex regions are prone to the angular roton instability and the boundary is expected to be lower there⁶; b-c) Box potentials with soft walls ($p = 6$) and hard walls ($p = 20$), respectively. In both cases, after the initial rise in the stability boundary at low trap aspect ratios, a region of reduced stability follows and eventually converges to a constant value. In all three cases the stability boundary converges to $v_{\text{crit}}^{\infty} \approx 5.5$ [108] for $\gamma \rightarrow \infty$. The numbered red points label the parameters corresponding to the cases shown in Figures 6.2 to 6.4.

The results for the $p = 2$ (Figure 6.1a) case replicate the data from the existing publications on the stability in harmonic traps [122], [119], showing the distinct regions at $\gamma = 7, 11, 15 \dots$ where the cloud assumes the concave, ‘red blood cell’-like shape close to the stability boundary (see Figure 6.2a with $\gamma = 11$ as opposed to Figure 6.2c showing the case of $\gamma = 13$). Further increasing γ seems to suppress the appearance of concave regions, which suggests that the stability should not be affected by the angular roton instability, and the stability boundary truly tends towards the v_{crit}^∞ .

In the case of the box potential, both the soft wall $p = 6$ and the hard wall $p = 20$ (Figure 6.1b-c, respectively) trapping geometries show some common trends. The predicted stability boundary exhibits a spike at intermediate values of γ , followed by a broad dip to lower values, before converging to v_{crit}^∞ . Unlike the harmonic case, the density distributions in the large γ seem to be necessarily concave, implying that the true boundary might be somewhat lower, as a consequence of angular rotons. Whether this shift will be finite or would diminish in the $\gamma \rightarrow \infty$ limit remains an open question that we aim to investigate. Interestingly, the distributions resulting from near-critical clouds in the ‘stability-dip’ region ($\gamma = 20 - 100$ for $p = 6$ and $\gamma = 50 - 250$ for $p = 20$) are characterised by a sharp density spike near the trap wall, implying that the actual boundary will be significantly lowered there.

6.2.2 Measure of Homogeneity

When working with oblate dipolar condensates in box traps, we are interested in establishing a measure of homogeneity of the resulting density distribution. The quantity of interest for us is the area density, as we only implement box confinement in the xy -plane, with the third direction being harmonic:

$$n_{2D}(r) = \int n(\mathbf{r}) dz = \int |\psi(\mathbf{r})|^2 dz. \quad (6.49)$$

In a perfectly uniform cloud, each atom is surrounded by a gas of same local density. As the distribution is made more and more inhomogeneous, this local density as seen by individual atoms takes an increasingly wider range of values across the cloud. Therefore, the information about homogeneity can be best extracted from the probability distribution, $P_H(n_{2D})$, of locating an atom with a local surrounding density of n_{2D} , which is analytically defined as:

$$\frac{dP_H(n'_{2D})}{dn_{2D}} = \frac{n'_{2D} \int_{|n_{2D}(r) - n'_{2D}| < dn} d^2r}{\int n_{2D}(r) d^2r}. \quad (6.50)$$

⁶In fact, first results from our (not yet properly tested) implementation of the Bogoliubov-de-Gennes method (Subsection 6.1.6) indeed suggest that the ultimate critical boundary is lower in these regions, with the values in almost exact agreement with the data from [119, 122].

In practice, this evaluation is done numerically by sampling the area density at a uniformly distributed set of points in the xy -plane, binning the samples by density $N_b(n_i)$ at a range of values $\{n_i\}$ and finally creating a histogram with weights equal to the bin density value assigned to each bin:

$$P_H^{\text{hist}}(n_i) = \frac{n_i N_b(n_i)}{\sum_j n_j N_b(n_j)} . \quad (6.51)$$

This histogram is a discretised version of $P_H(n_{2D})$, and can be used to extract key characteristics about the distribution, such the local density averaged over atoms:

$$n_{\text{mean}} = \sum_i P_H^{\text{hist}}(n_i) n_i \quad (6.52)$$

or the variance of the local density across all the atoms:

$$n_{\text{var}} = \sqrt{\sum_i P_H^{\text{hist}}(n_i) n_i^2 - n_{\text{mean}}^2} . \quad (6.53)$$

Alternatively, these quantities can be evaluated directly from the area density as:

$$n_{\text{mean}} = \frac{\int n_{2D}^2 d^2 r}{\int n_{2D}(r) d^2 r} \quad (6.54)$$

and

$$n_{\text{var}} = \sqrt{\frac{\int n_{2D}^3 d^2 r}{\int n_{2D}(r) d^2 r} - n_{\text{mean}}^2} . \quad (6.55)$$

This allows us to define a simple homogeneity parameter that quantifies the uniformity of the area density of the cloud:

$$H = 1 - \frac{n_{\text{var}}}{n_{\text{mean}}} \quad (6.56)$$

that takes values between 0 and 1, reaching the maximum for a perfectly homogeneous cloud.

A gas with repulsive contact interactions trapped in an optical box trap would reach maximum uniformity for large values of the box exponent p , provided that the Thomas-Fermi approximation applies. In a purely dipolar gas the situation is different, as the anisotropic nature of the DDI leads to depletion of atomic density in the middle of the trap and accumulation of material towards the walls, in the case when the interactions are strong. We observe from the simulation that the most uniform distributions at a given interaction strength are actually obtained for intermediate values of p .

Three examples of density distributions of a harmonically trapped dipolar gas are shown in Figure 6.2. An example of the peculiar ‘red blood cell’ distribution is given in Figure 6.2a,

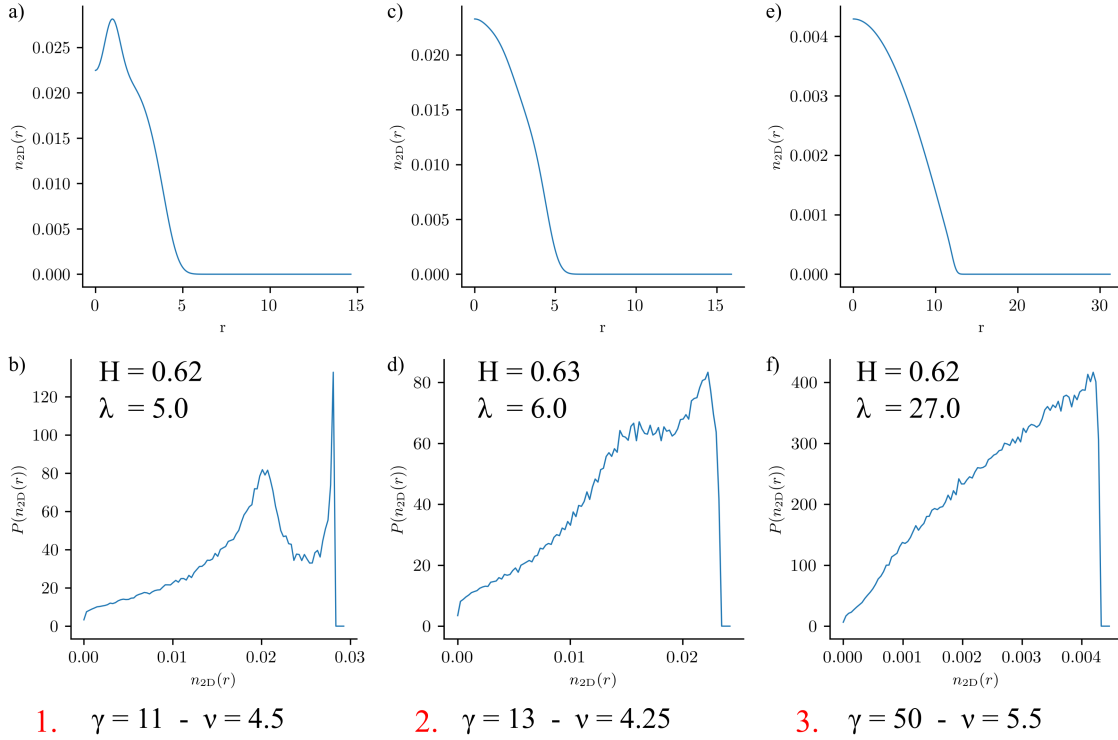


Fig. 6.2 **Area Density Distributions for $p = 2$** - Radial profiles of area density (n_{2D}) and probability distributions of weighted local density for harmonic trapping: a-b) $\gamma = 11$ near stability boundary, showing the ‘red blood cell’ density profile ; c-d) $\gamma = 13$ near stability boundary, but outside the ‘red blood cell’ region, resulting in a convex cloud; e-f) $\gamma = 50$ just below the stability boundary, demonstrating that the distribution remains convex all the way towards the critical point. b), d) and f) also show the values of the homogeneity parameter (Equation 6.56) and the aspect ratio of the density distribution (ratio of second moments along principal directions). The numbers shown in red refer to labels in Figure 6.1.

while the remaining two distributions correspond to convex condensates. In all cases, the homogeneity parameter takes a similar value of $H \approx 0.62$.

Our investigation focuses on the higher power-law potentials, in the context of creating uniform density distributions. We plot some interesting examples of the resulting density distributions for the case of a soft-walled trap ($p = 6$) in Figure 6.3 and that of a hard-walled trap ($p = 20$) in Figure 6.4. Comparing the large γ cases from subplots e) and f) in both figures, we conclude that a hard wall trap will eventually lead to a more uniform cloud, but this will only be the case in the very oblate case, $\lambda \gg 1$ (where λ is the density aspect ratio, defined as the ratio of second moments of the density along principal directions). Interestingly, intermediate values of the density aspect ratio, $\lambda \sim 10 - 20$, which are experimentally very relevant, will fall into the ‘stability dip’ region for the hard-walled trap, while in the case of the soft-walled trap, these same values of λ will be obtained for values of γ above the ‘dip’

region. This has potentially very significant implications for designing the box-trap in the experiment. Firstly, if we compare the density distributions with $\lambda \approx 17$, obtained near the stability boundary at $\gamma = 1000$ in the hard-walled trap (Figure 6.4c-d) with its counterpart⁷ from the soft-walled trap at $\gamma = 300$ (Figure 6.4e-f), we see that the softer trap leads to a more homogeneous distribution ($H = 0.8$ as opposed to $H = 0.75$) while keeping the distribution very close to true-concave. While this discussion is only preliminary, primarily because it is necessary to determine to what extent the angular rotons change or add to the story, it nevertheless calls for further investigation because of its relevance to setting up the box trap in the experiment.

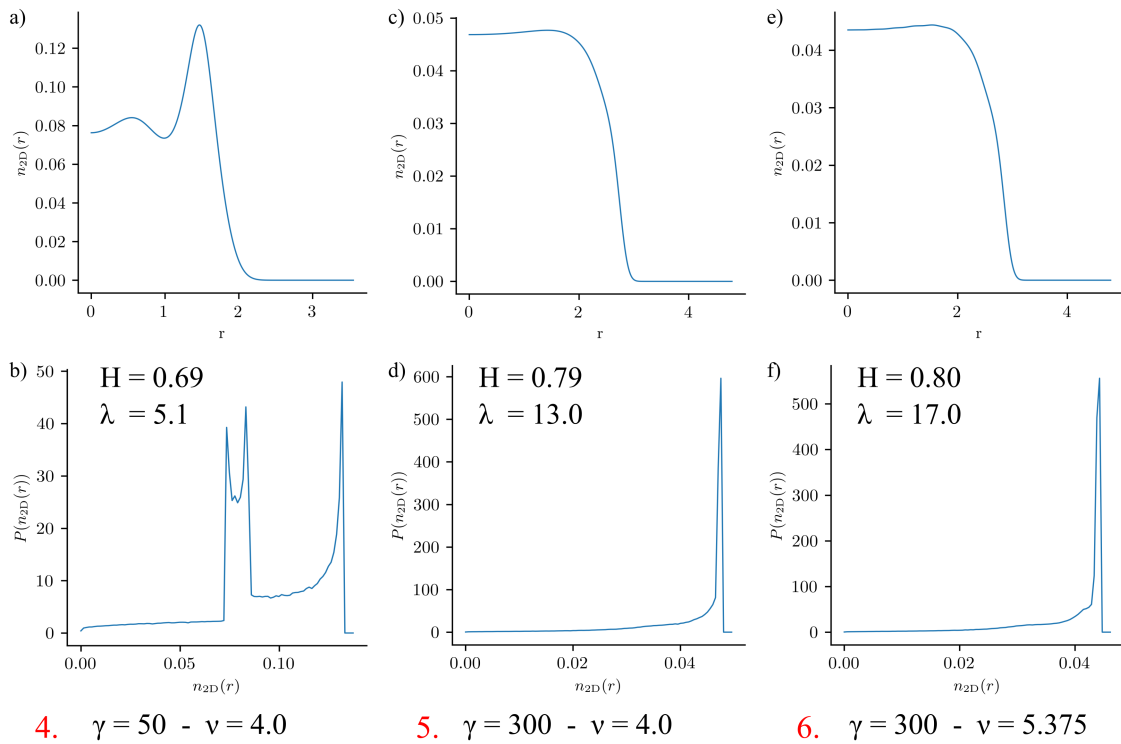


Fig. 6.3 Area Density Distributions for $p = 6$ - Radial profiles of area density (n_{2D}) and probability distributions of weighted local density for a soft-wall box trap: a-b) $\gamma = 50$ as an example of a reduced stability region for $\gamma \lesssim 100$ showing significant build-up of density around the edge of the trap ; c-f) $\gamma = 300$ near and just below the stability boundary, shown here for comparison with a hard-wall trap yielding the same aspect ratio of $\lambda \sim 17$ (Figure 6.4a-d), hinting that for intermediate aspect ratios, softer box traps might yield more homogeneous clouds near the stability boundary. b), d) and f) also show the values of the homogeneity parameter (Equation 6.56) and the aspect ratio of the density distribution (ratio of second moments along principal directions). The numbers shown in red refer to labels in Figure 6.1.

⁷Note that the ν values of the examples used were also selected to be approximately at the same distance from the stability boundary.

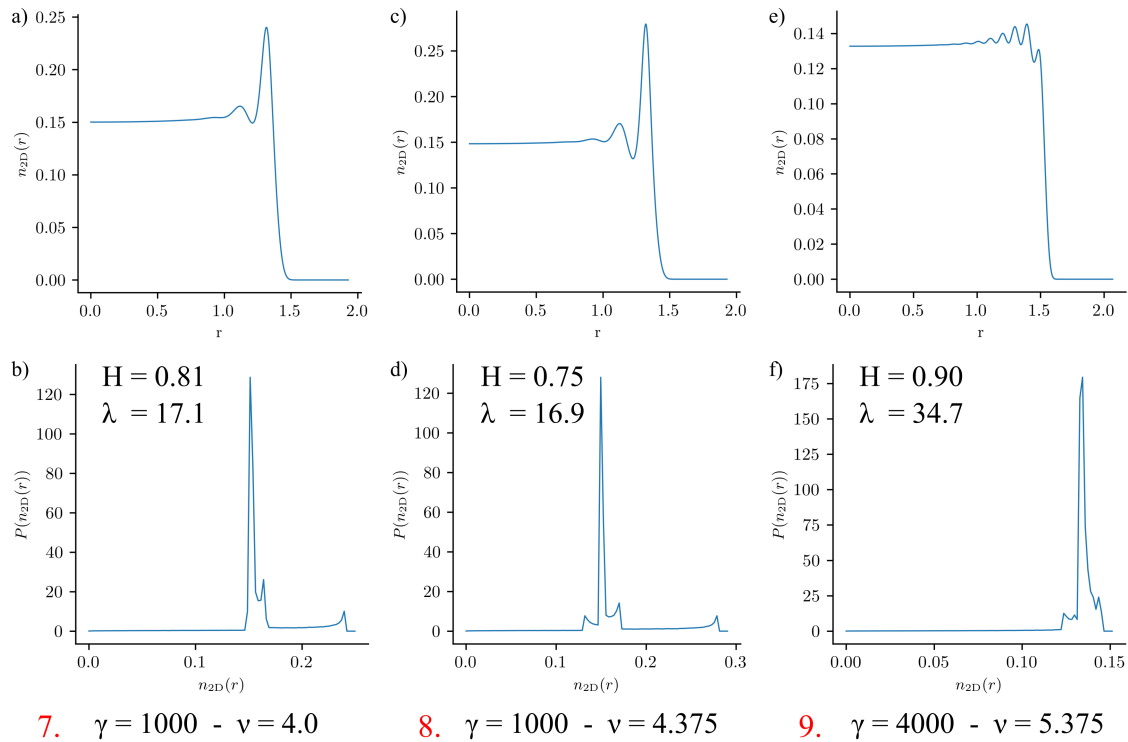


Fig. 6.4 Area Density Distributions for $p = 20$ - Radial profiles of area density (n_{2D}) and probability distributions of weighted local density for a hard-wall box trap: a-d) $\gamma = 1000$ near stability boundary, used for comparison with a soft-wall box trap distributions with the same aspect ratio (see Figure 6.3c-f); e-f) $\gamma = 4000$ close to the stability boundary, showing that for higher aspect ratios, steeper traps still produce uniform clouds without excessive build-up of atoms at near the wall. b), d) and f) also show the values of the homogeneity parameter (Equation 6.56) and the aspect ratio of the density distribution (ratio of second moments along principal directions). The numbers shown in red refer to labels in Figure 6.1.

Chapter 7

Conclusion and Outlook

7.1 Conclusion

This thesis addressed the design and building of an experimental platform for investigating many-body physics in quantum systems with dipole-dipole interactions. The described setup is centred around the optical box trap, that will provide uniform confinement and enable the creation of a flattened homogeneous dipolar gas of erbium.

I reported on the progress in the experimental effort, including building and commissioning a vacuum chamber with UHV pressure levels, loading a narrow-line erbium MOT from an atomic beam using a Zeeman slower and subsequently reaching temperatures of $10\mu\text{K}$ with up to 10^8 atoms. Installation and testing of a system for optical trapping and transport employing focus tunable lenses is also outlined, along with the design and prototyping of the systems for the optical box trap and Bragg spectroscopy. The cooling and trapping procedures in the sequence up to the MOT have shown satisfactory operation and the subsequent transfer into the optical dipole trap reached the desired efficiency of at least 20%. However, problems were encountered with the optical trapping and transport setup where I presented the details of the diagnostics and troubleshooting, along with plans for overcoming these issues. Lastly, I gave an overview of preliminary results from a separate effort resorting to numerical simulations for investigating the relations between trapping geometry and stability of dipolar condensates.

With all these developments, once we reach the stage where the atoms can be evaporatively cooled to BEC and transported to the glass cell, we will implement the optical box potential and the Bragg spectroscopy setup, aiming to address the first scientific projects on this apparatus. We then aim to harness this platform to probe exotic roton physics, out-of-equilibrium systems, phase transition dynamics and superfluidity. In addition, an expansion of the experiment that is introducing potassium will give us access to simulating

impurity physics models such as Bose polarons [66] or open systems with non-Markovian decoherence [67, 68].

7.2 Completing the Experimental Platform

Most of the effort in the period to follow will be directed towards the optical setup for trapping and transport of atoms. In order to battle the problems caused by aberrations and thermally induced distortion in the tunable lenses, we plan to investigate if any modifications to the setup might improve the behaviour. Options being considered are sacrificing some beam waist tunability for tighter confinement, exploring options for better heat management and heat-sinking in the tunable lens mounts [92] and implementing drift compensation to the lens driver. In combination with that, we plan to temporarily build a fixed-lens system to perform evaporation to BEC in the MOT chamber, as a benchmark for any potential improvements to the tunable lens system to be weighed against. If the final outcome turns out to be negative, we will be ready to switch to a different technology, most likely the Moiré lenses [94]. In parallel with the troubleshooting of the ODT and transport, we will install the new laser locking setup for the 583 nm laser based on a ULE optical cavity. This should bring further improvements to the stability and temperature limit of the MOT, and in combination with some maintenance on the Zeeman slower and transversal cooling stages, it should also amount to faster and more efficient loading of the trap.

The optical box setup and Bragg spectroscopy setup prototypes have been designed and successfully tested. With a working blueprint of the optical setup and the design of the magnetic field coils in progress, the region around the science cell will be soon populated with optics. As a result, we expect to be able to implement the optical box soon after a working transport stage is achieved.

In parallel with the progress in the main, erbium branch of the experiment, the potassium setup has been designed and building is in progress. The optical systems for locking the two cooling lasers and controlling the light frequencies are being actively set up, and the vacuum chamber housing the 2D potassium MOT is approaching the point when it will be connected to the main vacuum chamber and pumped down to vacuum.

7.3 Future Projects

7.3.1 Probing the Roton Physics

The existence of a roton minimum in the excitation spectrum of a trapped dipolar gas has been demonstrated experimentally in various system geometries. By tuning the depth of the roton feature via the s -wave scattering length and Feshbach resonances, it was shown how it affects stability of the gas, and how it can be exploited to push the system through a transition into a supersolid state of matter. The shape of the excitation spectrum also has implications for the superfluid critical velocity, v_c . In the absence of vortex excitations, it can be estimated through the Landau criterion, that sets the critical velocity to be equal to the (minimal) slope of the straight line in the $\omega(k)$ graph, passing through the origin and being tangent to the excitation spectrum (Figure 7.1a).

Working with an erbium BEC trapped in the optical box from our platform, we plan to independently measure the critical velocity using a stirring method [123] (Figure 7.1b) and also deduce it from the excitation spectrum via the Landau criterion. The excitation spectrum will be measured using the Bragg spectroscopy technique [101, 102, 36], presented in Section 5.5, while the stirring method can also be implemented using the same optical setup by projecting the appropriate dynamical pattern onto the DMD. This will allow us to compare the two results for critical velocity, and quantify the role of the vortex-like excitations in the spectrum.

7.3.2 Phase Transition Dynamics with Long Range Interactions

The transition from a thermal gas to a BEC is a second order phase transition, meaning that the order parameter evolves continuously while the system is crossing the transition temperature T_c and it always exhibits symmetry breaking. In this particular example, the order parameter is the condensate wave function, Ψ_0 , and the symmetry being broken is the $SU(1)$ symmetry of its phase. In the adiabatic limit, when the transition is crossed infinitely slowly, the entire condensate will assume a state with a unique phase. In contrast to that, if the transition is traversed at a finite rate, domains with different order parameter values will appear, as a consequence of the limited range over which the correlations can spread through the system before being frozen out. This mechanism is described by the Kibble-Zurek (KZ) theory, first developed for cosmological systems [110], and later expanded to a more general scope [111]. Ultracold atom platforms proved to be well equipped for exploring this experimentally, due to the broad ability of tuning system parameters and readily accessible critical phenomena, with the BEC transition being the most important and widely employed.

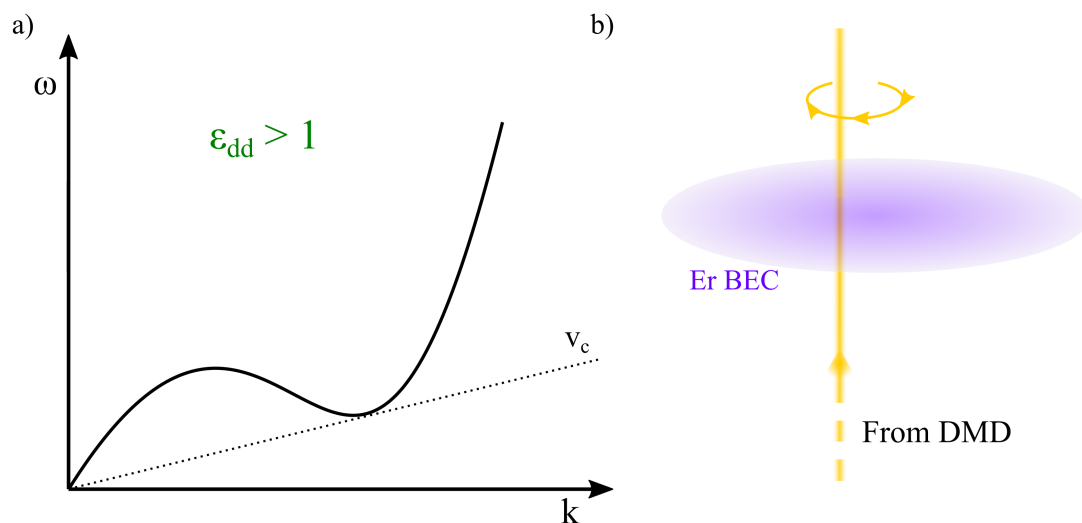


Fig. 7.1 **Superfluid Critical Velocity** - a) The excitation spectrum of a strongly dipolar BEC, exhibiting a roton minimum. According to the Landau criterion, the critical velocity for superfluidity is determined as the slope of the line extending from the origin and tangent to the spectrum from below. This model does not take into account vortex excitations; b) The stirring method for measuring the superfluid velocity, where a dynamic potential generated using a DMD will be used to perturb the trapped gas. If the stirring is performed below the superfluid critical velocity, no excitations should be detected.

Given that this transition is sensitive to density, it is clear that systems with homogeneous density give a crucial advantage in these efforts [23, 124, 125], as all parts of the system traverse the phase transition at the same instance.

The KZ mechanism is based on the universal scaling behaviour of system parameters in the vicinity of the critical point, which predict that the correlation length of the system obeys a power law scaling in temperature (here represented via a dimensionless quantity $\varepsilon = \frac{T-T_c}{T_c}$):

$$\xi \propto |\varepsilon|^{-\nu}. \quad (7.1)$$

Similar scaling relations can be set up for the heat capacity, order parameter magnitude, susceptibility and other parameters, each with its own scaling exponent. It has been shown that these exponents are insensitive to microscopic properties of the system, but rather that they are determined by the dimensionality and symmetries of the system and the order parameter. This led to the establishment of a finite set of universality classes, represented by different collections of scaling exponent values [126]. The BEC transition in Bose gases falls under the XY-Model, together with the superfluid transition in liquid ^4He .

All of the above scaling relations represent static, equilibrium properties of the system. The description of these systems can be expanded with dynamic scaling relations, which

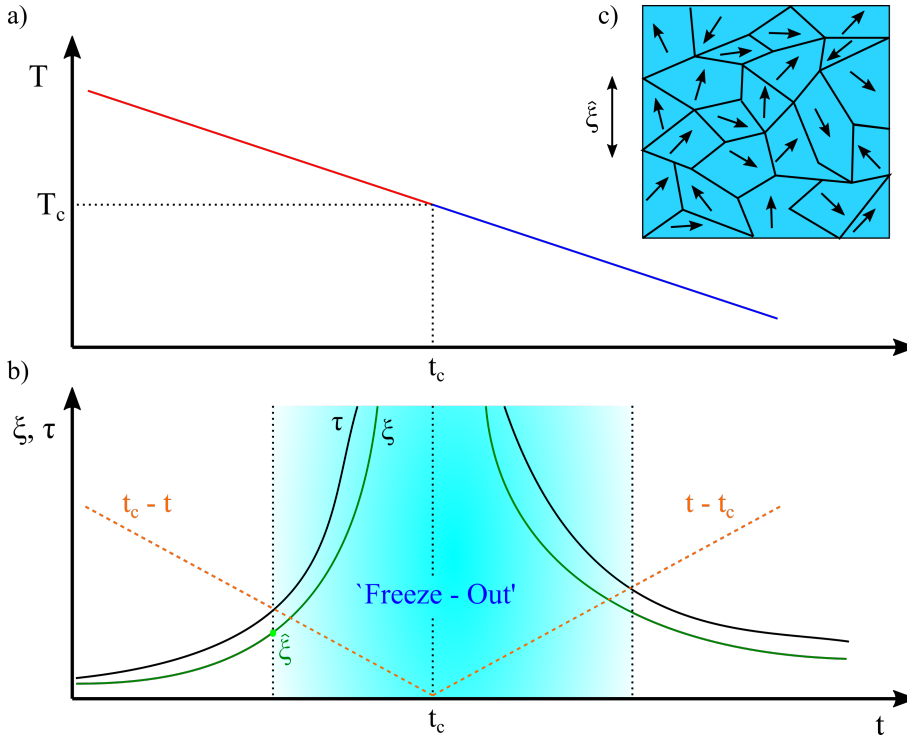


Fig. 7.2 **Kibble-Zurek Theory** - a) Linear temperature ramp inducing a second order phase transition. b) The divergence of the correlation length and the relaxation time in the proximity of the critical point, leading to the freezing out of correlations once the relaxation time becomes longer than the time remaining to the transition crossing. This results in the correlations developing only up to the range quantified by the freeze-out correlation length ξ^z , which is manifested in c) that depicts grains of uniform order parameter of average size $\sim \xi^z$. This figure is inspired by the explanation from [19] and the figure therein.

allows for non-adiabatic scenarios to be addressed. In the context of KZ theory, the scaling of the typical relaxation time of the system is particularly important. This is the timescale that governs how quickly the correlations in the system will adjust to accommodate the new equilibrium value of ξ following a change in temperature. This relaxation timescale scaling is represented by the dynamic exponent z :

$$\tau \propto \xi^z \propto |\epsilon|^{-\nu z} \quad (7.2)$$

which is categorised by a different set of dynamic universality classes, with the F-Model being the relevant class for the BEC transition [127]. These two scaling relations can be used to predict resulting domain size from a finite rate quench within KZ theory. If the quench is assumed to be linear, $\epsilon = \frac{t_c - t}{\tau_Q}$, with τ_Q representing the characteristic quench timescale, then at some point in the ramp, the relaxation time, of the system will exceed the time remaining until the transition is crossed (see Figure 7.2 for a pictorial description). This moment in time

is referred to as the freeze-out time, as it represents the point after which the correlations are no longer able to be communicated across the whole system. It is defined via the relation $t_c - \hat{t} = \tau(\hat{t})$, yielding the characteristic frozen-out correlation length, $\hat{\xi} = \xi(\hat{t})$ with the scaling predicted by KZ theory:

$$\hat{\xi} \propto \tau_Q^{\frac{v}{1+ vz}}. \quad (7.3)$$

Since the transition point is reached without developing correlations at ranges larger than $\hat{\xi}$, it is expected that the resulting domain size will be well described by this length scale, and will obey the scaling with the linear quench rate from Equation 7.3. Experiments have confirmed the agreement with the F-Model prediction ($v = 0.67$ and $z = \frac{3}{2}$) yielding $\frac{v}{1+ vz} = 0.33$ for the KZ scaling factor [23, 24].

Exploring phase transition dynamics in systems with dipolar interactions is attractive and interesting for multiple reasons. Firstly, the long range nature of the dipole-dipole force may alter the mechanism of correlation propagation through the system. This may result in a different set of scaling exponents, or just affect the multiplicative constants in the relations, but in both cases it is a subject worth exploring. In the same context, the effects of the long range force on the coarsening dynamics could also be measurable. Additionally, temperature quenches are not the only tool for inducing phase transitions in quantum gases. The strength of contact interactions can also be ramped via the Feshbach resonances, and unlike evaporative cooling, these are technically reversible. Given that there is a possibility of traversing the BEC transition critical point by quenching interactions, provided by the dependence of T_c on interaction strengths, this leaves an option for examining the reversibility of the transition and presence of any hysteretic artefacts that might be left after crossing the transition multiple times. Finally, another transition that can be addressed by an interaction quench is the supersolid transition seeded by the roton instability [40–42]. Being a quantum phase transition, this could probe into the quantum limit of the KZ theory.

7.3.3 Dual-Species Experiments with Potassium

With the addition of potassium atoms to the platform, making it a dual-species experiment, we lay the grounds for exploring impurity physics in bosonic systems in the presence of dipole-dipole interactions. One route that we might take with the experiments is investigating Bose polarons, that can be made anisotropic by the dipole-dipole force [66]. The rich spectrum of Feshbach resonances in ultracold erbium [29, 57] gives us large freedom in tuning the scattering properties of Er-Er collisions, and due to the anisotropic electronic configuration of erbium that is responsible for that fact, it is also reasonable to expect similar abundance of Feshbach resonances for Er-K scattering. When this is combined with the

long-range and anisotropic nature of the dipolar force, we should be left with an advanced ability of tuning the dispersion relations of the polarons.

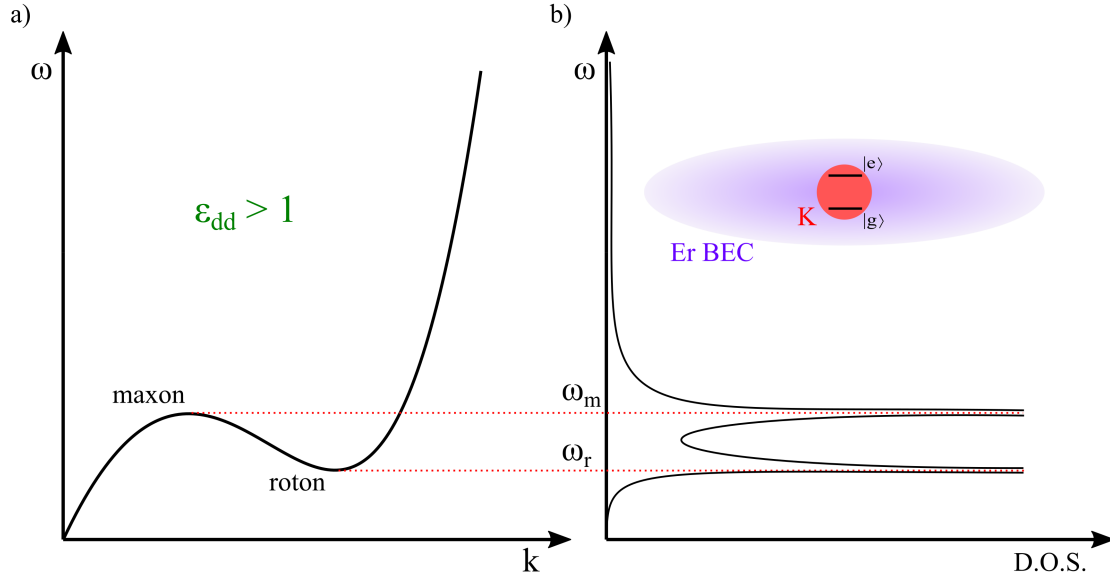


Fig. 7.3 **Non-Markovian Qubit Decoherence** - a) The roton spectrum of a strongly dipolar gas with the roton and maxon features that correspond to a locally flat dispersion relation. This causes the density of states of the dipolar BEC to peak at the energies associated with the roton and the maxon, which has profound consequences if the condensate serves as a thermodynamic reservoir into which a qubit is immersed. The frequencies ω_m and ω_r will dominate the evolution of this open system, possibly rendering the decoherence of the qubit non-Markovian.

The tunability of the excitation spectrum of the erbium BEC makes it a promising candidate for a controllable quantum reservoir in some open quantum system models. As the spectrum softening, exhibited in the creation of the roton minimum and the accompanying maxon feature, leads to very high density of states at the roton and maxon frequencies, ω_m and ω_r , such reservoir might lead to non-Markovian decoherence in a system coupled to it. In a model introduced in [67, 68], the information flow from a single-atom qubit immersed in a dipolar condensate can be controlled by tuning the parameters of the reservoir. In the presence of the roton feature, the decoherence evolution will be dominated by the two frequencies corresponding to the roton and the maxon, leading to non-Markovian behaviour and the possibility of information flow back from the reservoir into the system.

Appendix A

Pumping System Design

The purpose of this section is to provide details on the design considerations for our vacuum chamber from the point of view of vacuum pumping and reaching desired pressures in the UHV range (below 10^{-10} mbar). This includes managing molecular flow conductances, pumping speeds and accounting for sources of the background gas, such as leaks, outgassing and permeation.

A.1 Molecular Flow Regime

At very low pressures, when the mean free path is much larger than the typical linear geometric size of the chamber, gases are in the so called molecular flow regime. The mean free path is defined as:

$$\langle l \rangle = (n\sigma)^{-1} \quad (\text{A.1})$$

where n is the number density of the gas σ is the scattering cross section. For gases expected to be present in the chamber ($\text{N}_2, \text{H}_2, \text{He}, \text{CO}_2 \dots$) the scattering cross sections are $\sim 0.1 - 1.0 \text{ nm}^2$ [128]. This means that at room temperature and pressures below 10^{-6} mbar the mean free path of gas particles will be $> 1 \text{ m}$, which is large compared to vacuum chamber dimensions. Hence, the molecular flow regime can be assumed. The situation with atomic vapours is a little bit more complicated, as data on scattering cross sections is not as readily available. From the information in [128] the scattering cross section of mercury can be deduced to be 1.0 nm^2 , so it is probably reasonable to assume that both erbium and potassium have their scattering cross sections on this scale.

In the molecular flow regime, it is possible to establish an equivalence between systems with gaseous flow and electrical circuits¹:

$$\begin{aligned} \text{Pressure } (P) &\longleftrightarrow \text{Voltage} \\ \text{Molecular Conductance / Pumping Speed } (C / S) &\longleftrightarrow \text{Electrical Conductivity} \\ \text{Molecular Throughput } (Q) &\longleftrightarrow \text{Electrical Current} \\ \text{Volume } (V) &\longleftrightarrow \text{Capacitance} \\ \text{Molecular Quantity } (q = pV) &\longleftrightarrow \text{Charge} \end{aligned}$$

The molecular throughput is defined as $Q = p\dot{V}$, i.e. as pressure multiplied by the volumetric flow rate. For ideal gases it is proportional to the number flow rate, where the constant of proportionality is $k_B T$. The molecular conductivity of a chamber section is then defined as:

$$C = \frac{Q}{\Delta p} \quad (\text{A.2})$$

where Δp is the pressure difference across the section, and Q is the molecular throughput through that section. The conductance has units of $\frac{[\text{Volume}]}{[\text{Time}]}$. In complex vacuum systems, involving chamber sections connected in parallel or in series, the effective conductance can be calculated using the formulas:

$$C_{\text{par}} = C_1 + C_2, \quad (\text{A.3})$$

$$C_{\text{ser}} = (C_1^{-1} + C_2^{-1})^{-1}. \quad (\text{A.4})$$

These formulas assume that the initial conditions for the atoms entering all chamber sections correspond to those of a large reservoir. Care must be taken when applying these formulas to real chambers, as the quality of approximation might vary. Some useful formulas for conductivities of relevant structures [71]:

- **Aperture:**

$$C_{\text{ap}} = \sqrt{\frac{k_B T}{2\pi M}} A = C_0 A \quad (\text{A.5})$$

where A is the surface area of the aperture, and M is the molecular mass. Using this result, the conductivities of many pipe systems can be expressed using the transmission probability, α :

$$C_{\text{sys}} = \alpha C_0 A. \quad (\text{A.6})$$

¹Note that only molecular flow quantities are represented using symbols in this appendix, to avoid ambiguity with the electrical ones, e.g. volume vs. voltage.

- **Straight pipe section:**

A good approximation for α through a tube of diameter D and length L is:

$$\alpha = \frac{1}{1 + \frac{3L}{4D}} \quad (\text{A.7})$$

leading to the overall conductivity of :

$$C_{\text{pipe}} = \sqrt{\frac{\pi k_B T}{18M} \frac{D^3}{L} \frac{1}{1 + \frac{4D}{3L}}} \quad (\text{A.8})$$

- **Elbow:**

A reasonably good approximation for α that matches the experimental results [129] well is

$$\alpha = \frac{1}{1 + \frac{3}{8} \left(\frac{L_1}{D} + \frac{L_2}{D} + \frac{L_1 L_2}{(L_1 + L_2) D} \right)} \quad (\text{A.9})$$

where L_1 and L_2 are the lengths of the two branches of the elbow.

- **Tee:**

An approximation applied in this case is using the series conductivity of the two straight branches for the straight section, and the conductivity of the elbow reduced by the conductivity of one of the straight branches for the orthogonal section.

In this picture, the vacuum pumps are modelled as connections to the electrical ground, i.e. zero pressure, through a conductance equal to the pumping speed of the pumps. Following the same logic, the analogy with electrical circuits can be extended to the kinetics of the pumping process, as the volume V of the given chamber section is effectively its capacitance. Being equivalent to that of an RC -circuit, the pumping time-constant for a chamber section can be written as:

$$t_{\text{pump}} = \frac{V}{C_{\text{tot}}} \quad (\text{A.10})$$

where C_{tot} is the total pumping capacity² from the section in question provided by pumps.

A.2 Gas Sources

The limiting factor on the equilibrium pressure in pumped vacuum systems are sources that replenish the background gas. In our case the three dominant contributors are leaks at the

²i.e. conductance to the pump drain point / conductivity to the grounding point.

flange connections, outgassing from surfaces and gas permeation through the chamber walls and windows. In our simulation, these are modelled in the following way:

- **Leaks:** In our apparatus, all the flange connections are made using *Con Flat* (CF) flanges. Different manufacturers give varying specifications for leak rates of a properly sealed flange, but based on a range of sources, a good estimate seems to be 10^{-11} mbar L s⁻¹ per flange connection. This total rate is then distributed among components present in air according to partial pressures.
- **Outgassing:** Stainless steel contains significant amounts of dissolved hydrogen left over by the manufacturing process, which diffuses through the bulk material and outgasses into the vacuum chamber. According to [71], for clean but not thermally treated 304L or 316LN stainless steel, the outgassing rate of hydrogen is typically $10^{-9} - 10^{-8}$ mbar L s⁻¹ cm⁻². In order to achieve UHV pressure levels, the chamber needs to be baked out until the outgassing drops to levels of $10^{-12} - 10^{-13}$ mbar L s⁻¹ cm⁻², according to the same source. We will use the value of 10^{-12} mbar L s⁻¹ cm⁻² in the calculations and also as a goal for the bakeout procedure.
- **Permeation:** According to the literature, permeation of hydrogen through stainless steel is a significant contributor only at very high temperatures [130]. At room temperature, it is only necessary to account for helium permeation through glass windows. The rate used, for glass of thickness d is $3.8 \cdot 10^{-13}$ mbar L s⁻¹ cm⁻² $\left(\frac{d}{1 \text{ mm}}\right)^{-1}$, derived from the model and data given in [131] and assuming He abundance in air of $5 \cdot 10^{-5}$.

Note that, even after the bakeout, in a typical chamber with exposed steel area of 1000 cm² and 10 flange connections, hydrogen outgassing contribution to the total gas source rate is two orders of magnitude larger than that of the flange connection leaks (also refer to Table A.1 for number specific to our system). This highlights the importance of performing an adequate bakeout for reaching UHV pressure levels.

A.3 Calculations for Our Experiment

Our vacuum chamber can be represented as a collection of ten regions with known conductances between them (Figure 2.2). Basing the model on the assumptions about background gas sources laid out above, we also calculated all the source terms, which are given in Table A.1. The pumping speeds for the appropriate set of gases are available from the pumps' specification sheets, and are reported in Table A.2. This allows us to set up an equivalent

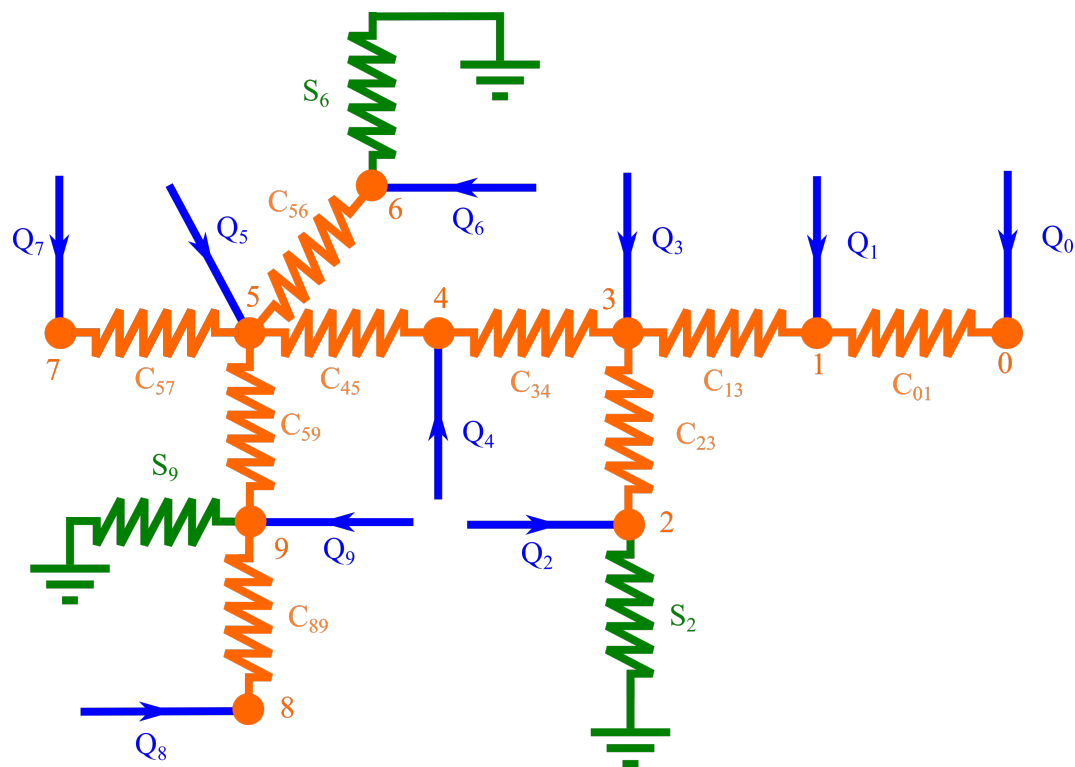


Fig. A.1 Equivalent circuit of the pumping system

electrical circuit, with known resistances and current source terms. The layout of such circuit for our final design of the system is shown in Figure A.1.

This circuit can be straightforwardly solved for voltages at nodes, employing Kirchhoff's circuit laws, and we are particularly interested in pressures in the science cell (region 8), MOT chamber (region 5) and the HV section (region 4). Using the values for system parameters from the Tables A.1, A.2 and A.3, we obtain the pressures of 1.1×10^{-11} mbar, 3.0×10^{-11} mbar and 3.3×10^{-11} mbar in these three regions of the vacuum chamber respectively³. Given that we haven't accounted for any extra outgassing from the oven, due to the general uncertainty how to model that, we check the behaviour of the predictions for these pressures upon increasing the outgassing rate in the oven region. We conclude that with the existing differential pumping tube, an increase of the oven outgassing rate by two orders of magnitude, only yields a 10% increase in the science cell pressure, while going another order of magnitude higher increases it by 50%.

Another interesting test that we have performed using this model is to check how the science cell pressure would behave if there was no extra pump between it and the MOT

³This also implies pressure in the 10–7 mbar range prior to the bake, which agrees well with observations at that point (see Figure 2.12, noting that the UHV turbo pump is only providing $< 10 \text{ L s}^{-1}$ of pumping speed, explaining a higher gauge reading).

Term	Viewports	Flanges	Exposed Area		Sources				
			Steel [cm ²]	Glass [cm ²]	N ₂	O ₂	Ar	H ₂	He
	16CF + 35CF				[10 ⁻¹¹ mbar L s ⁻¹]				
Q_0	0 + 0	2	480	0	1.56	0.42	0.02	48	0
Q_1	0 + 4	5	480	38	3.90	1.05	0.05	48	0.57
Q_2	0 + 3	2	250	29	1.56	0.42	0.02	25	0.44
Q_3	0 + 0	5	160	0	3.90	1.05	0.05	16	0
Q_4	0 + 0	1	70	0	0.78	0.21	0.01	7.0	0
Q_5	4 + 5	18	900	56	14.0	3.78	0.18	90	0.84
Q_6	0 + 1	3	400	9.6	2.34	0.63	0.03	40	0.15
Q_7	0 + 1	9	500	9.6	7.02	1.89	0.09	50	0.15
Q_8	0 + 0	1	10	140	0.78	0.21	0.01	1.0	2.1
Q_9	0 + 0	2	70	0	1.56	0.42	0.02	7.0	0

Table A.1 Source gas influx rates used in the calculations

Term	Model	Pumping Rates [L s ⁻¹]				
		N ₂	O ₂	Ar	H ₂	He
S_2	NexTorr D-100	40	100	6	100	6
S_6	NexTorr D-300	100	300	6	300	6
S_9	NexTorr D-100	40	100	6	100	6

Table A.2 Pumping speeds used in the calculations

Section	C_{01}	C_{13}	C_{23}	C_{34}	C_{45}	C_{56}	C_{57}	C_{59}	C_{89}
Conductance [L s ⁻¹]	5.93	61.8	34.9	61.8	0.113	28.4	2.29	4.17	5.00

Table A.3 Chamber Conductances for N₂ Molecules

chamber. This is an important question as the absence of that pump would allow for a shorter optical transport length between the two chambers. The model predicts a fivefold increase in pressure if the chamber was constructed without that pump in place.

Finally, we calculated the predictions on the pressure differential between the HV and UHV sections for different diameters of the ZS tube. Comparing the case of the model oven

outgassing increased by 3 orders of magnitude, we observe that the science cell and MOT chamber pressures would increase by similar factors of approximately 2 and 3 if the ZS tube had the diameter of 10mm and 12mm respectively. Note that the results from Subsection 2.1.2 suggest that these same increments of the ZS tube diameter will lead up to only a 50% increase in the atomic flux from the oven reaching the chamber.

A.4 Bakeout Process

Diffusion of hydrogen through bulk stainless steel is a thermally activated process, hence the material can be depleted of hydrogen by pumping at elevated temperatures. Typical bakeout procedures of vacuum chambers in ultracold atom experiments involve temperatures of up to 200 °C and last for a number of days. In some cases, certain components limit the bakeout temperature at a lower value, and then a judgement needs to be made on how much the baking should be prolonged to achieve the desired pressure levels. An estimate can be made if we look at the total gas quantity removed from the bulk material, which according to [132, 133] scales as:

$$A \propto (Dt)^{\frac{1}{2}} q \quad (\text{A.11})$$

where D is the diffusion rate, which in the case of hydrogen in steel takes the form:

$$D = D_0 e^{-\frac{E_{\text{diff}}}{k_B T}} \quad (\text{A.12})$$

and for austenitic steels (304L, 316L, 316LN etc.) the constants take the form $D_0 = 5.8 \times 10^{-3} \frac{\text{cm}^2}{\text{s}}$ and $E_{\text{diff}} = 0.558 \text{ eV}$ [134]. As the quantity of hydrogen removed from the bulk metal will directly feed into the post-bakeout outgassing rate, this provides us with the means of scaling the duration and temperature of different bakeout processes for comparison purposes. Basically, a bakeout for time t_1 at temperature T_1 should be equivalent to a bakeout for time t_2 at temperature T_2 if:

$$\frac{t_1}{t_2} = e^{-\frac{E_{\text{diff}}}{k_B} \left(\frac{1}{T_2} - \frac{1}{T_1} \right)} \quad (\text{A.13})$$

In the case of stainless steel this would mean that baking for t at 200 °C is equivalent to baking for $5.0 \times t$ at 150 °C or for $39 \times t$ at 100 °C, clearly showing the large advantage of using maximum practically possible temperature.

Appendix B

Computer Simulation of the Atomic Beam

In order to better understand the process of cooling and slowing of the atomic beam from the effusion cell oven, and to aid the design considerations for the laser cooling optics and the vacuum system, I wrote a Monte-Carlo computer simulation of the atomic beam dynamics¹. The simulation describes the beam from its nascence in the effusion cell to the end of the path at the MOT chamber, implementing transversal cooling and Zeeman slowing along the way. The beam is represented in the simulation by a sample of atoms, with initial parameters generated from appropriate distribution functions, that are propagated through the system one-by one.

B.1 Effusion Cell

Erbium used in our experiment is dispensed from a high temperature oven. As shown in the figure, the oven consists of two chambers fitted with apertures. Solid erbium material is placed into the first chamber, the *effusion cell*, which is equipped with a set of heaters and is typically kept at temperatures between 1000 °C and 1200 °C during normal operation. At these temperatures the vapour pressure of erbium in the cell is significant, and atoms effuse through the tubular aperture into the second chamber of the oven - the *hot lip*. This part of the oven has separate heaters, and it's usually maintained at a slightly elevated temperature compared to the effusion cell, to avoid condensation of erbium on the second aperture, which is at the same time the output port of the oven.

¹Code is written in Matlab

The vapour pressure in the effusion cell can be estimated using the Antoine equation [57, 69]:

$$p_{\text{vap}}(T_{\text{ec}}) = 10^{A - \frac{B}{C + T_{\text{ec}}}} \text{ mbar} \quad (\text{B.1})$$

where the empirical constants for erbium are $A_{Er} = 7.103(4)$, $B_{Er} = 12170(20)$ K and $C_{Er} = -173(2)$ K. The atoms from the erbium saturated cell effuse towards the hot lip section through a tubular aperture of diameter $D_1 = 3$ mm and length $L_1 = 30$ mm. The distribution of the flux of the atoms at the entry to the circular aperture can be calculated as:

$$\frac{d\Phi}{dv d\theta d\phi} = \left(\frac{m}{2\pi k_B T_{\text{ec}}} \right)^{\frac{3}{2}} 4\pi v^2 e^{-\frac{mv^2}{2k_B T_{\text{ec}}}} \frac{nv \sin \theta \cos \theta}{4\pi} \quad (\text{B.2})$$

In the simulation, a representative sample of atoms that enter the tubular aperture is generated from the following distribution functions (employing a random variable drawn from the uniform distribution over the unit interval², x_{rand}):

$$v = \sqrt{-\frac{2k_B T_{\text{ec}}}{m} \left(1 + \mathcal{W} \left(\frac{x_{\text{rand}}^{(1)} - 1}{e} \right) \right)}, \quad (\text{B.3})$$

$$\theta = \sin^{-1} \left(\sqrt{x_{\text{rand}}^{(2)}} \right), \quad (\text{B.4})$$

$$\phi = 2\pi x_{\text{rand}}^{(3)} \quad (\text{B.5})$$

and the spatial position where the atom enters the aperture is chosen randomly using a uniform distribution over the aperture. In the equations above, $\mathcal{W}(z)$ represents the principal branch of the Lambert W function. The atoms are then propagated along the tube, rethermalising them every time they hit the tube wall. The re-thermalisation process implies assigning the atom with a new velocity generated from a Maxwell-Boltzmann distribution at temperature T_{hl} and new direction of motion selected randomly. In order to check the validity of this model, the proportion of the atoms that pass through the tube is compared with a known formula for the transmission probability of a tube in the molecular flow regime:

$$\alpha = \frac{1}{1 + \frac{3L}{4D}}. \quad (\text{B.6})$$

For the 30 mm long tubular aperture with a 3 mm diameter, this equation yields $\alpha = 0.117$ and the simulation reported the value of 0.132 showing good agreement.

²The superscripts in equations are there to clarify that an independent random variable is generated for each of the parameters.

In order to normalize the results of the simulation, the total rate of effusion into the tube is estimated by integrating the formula from above:

$$R_{\text{ec}} = \sqrt{\frac{\pi}{2k_B T_{\text{ec}} m}} P_{\text{vap}}(T_{\text{ec}}) \frac{D_1^2}{4}. \quad (\text{B.7})$$

The atoms that make it through the first aperture are propagated further along the oven, through the hot lip section. The atoms that exit the oven through the second aperture are saved in a sample file, whereas the ones that hit the walls of the hot lip are rethermalised and then an appropriate proportion of them is added to the sample accounting for the atoms that effuse directly from the hot lip.

B.2 Transversal Cooling

In the transversal cooling stage, two pairs of counter-propagating beams are directed onto the atomic beam from transversal directions. In the simulation, the atoms are propagated through the TC region in finite time increments, counting the number of scattered photons from each of the beams during every step, based on the instantaneous position and velocity of the atoms. The scattering rate from each beam is estimated using Equation F.3 for each beam ($i \in \{1, 2, 3, 4\}$) individually:

$$R_{\text{scatt}}^{(i)} = \frac{\Gamma}{2} \frac{s_i}{1 + \sum_{i=1}^4 s_i + \frac{4\delta^2}{\Gamma^2}} \quad (\text{B.8})$$

where Γ is the transition line width, k is the wave number of the laser light, $\delta = \delta_0 + kv_i$ is the effective detuning accounting for the base laser detuning δ_0 and the Doppler shift, and s_i are the saturation parameters of the beams. Once the scattering rates are established, the appropriate momentum adjustments, including the shot and spontaneous emission noise contributions (see Equations F.4 and F.5), are then applied to the atoms. Note that the saturation parameters s_i are spatially varying, accounting for the Gaussian profiles of the cooling beams. As the maximum optical powers used in the experiment limit the individual saturation parameters to $s_i \lesssim 1$, the approximation of using the total saturation parameter in the denominator in Equation B.8 is still justified [135], but it should be expected that the effect of cooling will be somewhat overestimated.

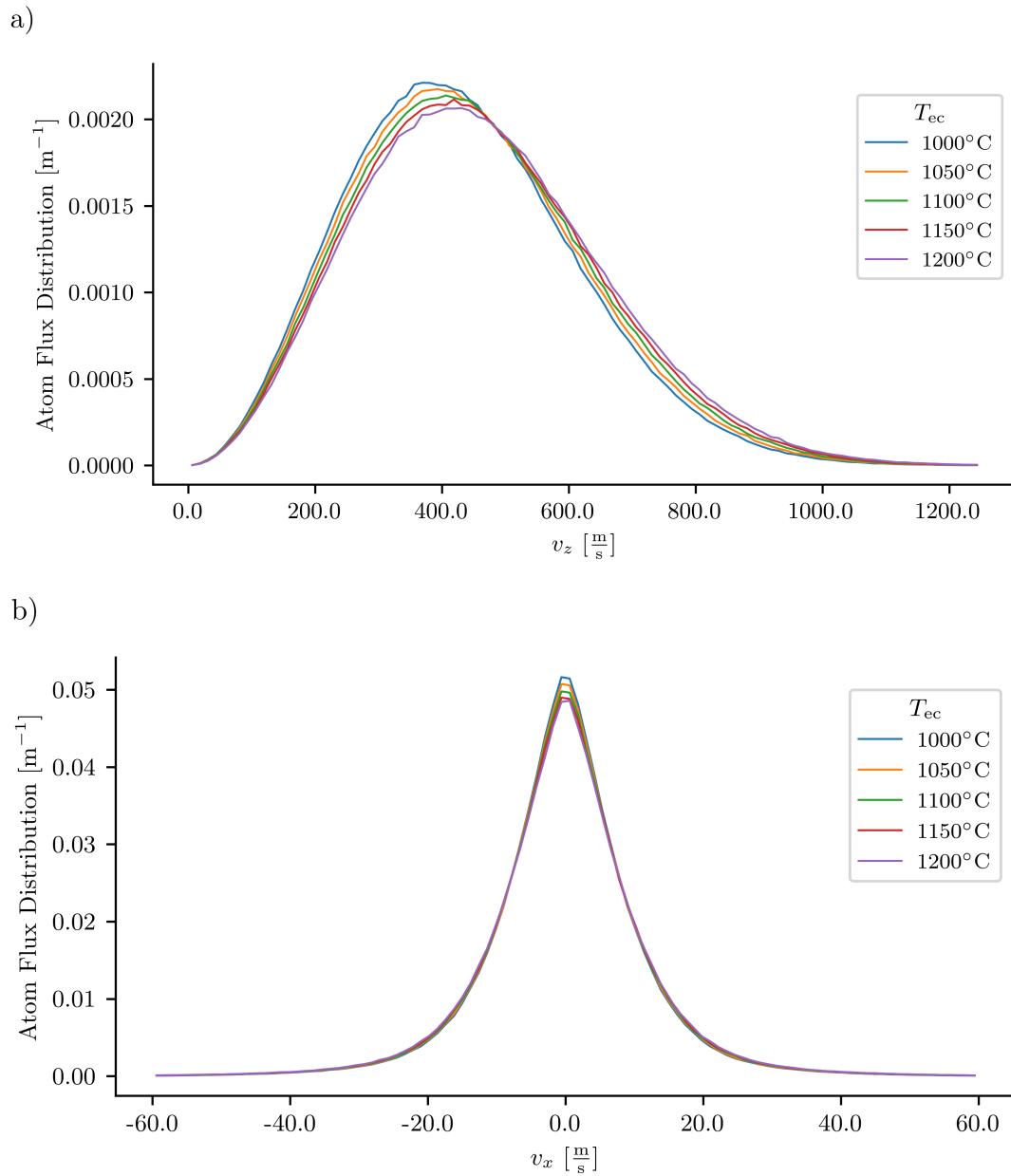


Fig. B.1 Simulated Velocity Distributions -

B.3 Zeeman Slower

The Zeeman slower is also implemented in the simulation and it is treated in much the same way as transversal cooling, only here the scattering rate can be directly calculated based on the light intensity and the effective detuning (that contains the actual laser detuning, along with the Doppler and Zeeman shifts) without resorting to approximations. The magnetic

field profile in the Zeeman slower is calculated prior to propagating atoms, based on the coil geometry and specified currents, using the Biot-Savart law.

However, as this part of the simulation had not been not fully developed and tested by the time we had to make final decisions about the geometry of the chamber and ZS coils, we instead resorted to simpler, 1D simulations of the slower for the purposes of the design.

Appendix C

Atomic Beam Fluorescence Measurements

Since our experiment sources the atoms from a beam emerging from an oven, having an insight into the velocity and spatial profile of the beam is crucial for optimising the early laser cooling stages - the Zeeman slower and the transversal cooling. For this purpose, we have set up a set of beams, that are derived from the MOT beams through a minor temporary adjustment:

- **"Bottom beam"** - Vertical, upward propagating beam derived from the bottom MOT beam by implementing a 8.2 mm diameter iris. This beam may be used to measure the transversal velocity distribution of atoms.
- **"Top beam"** - Beam tilted by 3° in the vertical plane into the stream of atoms, derived from the top MOT beam by implementing a tilt and introducing the same iris as above. This beam is utilised for probing the longitudinal velocity distribution in the MOT chamber, with lower resolution over an extended range.
- **"Side beam"** - Beam derived from one of the horizontal beam by again introducing the 8.2 mm diameter iris. This beam has the same purpose as the Top beam, but due to its tilt of 57° it probes a narrower band of velocities with a higher resolution.

The total photon scattering rate coming from a laser beam overlapped with the atomic beam can be expressed as:

$$R(\delta) = \int \int dv_{\perp} dv_{\parallel} N(v_{\perp}, v_{\parallel}) R_0(v_{\perp}, \delta) \quad (\text{C.1})$$

where $N(v_{\perp}, v_{\parallel})$ represents the number of atoms in the interaction region belonging to the velocity class $(v_{\perp}, v_{\parallel})$ and it can be linked to the velocity distribution of the flux in the atomic beam using:

$$F(v_{\perp}, v_{\parallel}) = \frac{v_{\parallel} N(v_{\perp}, v_{\parallel})}{L_{\text{int}}} \quad (\text{C.2})$$

with L_{int} being the length of the interaction region along the propagation direction, whereas

$$R_0(v_{\perp}, \delta) = \frac{\Gamma}{2} \frac{s}{1 + s + \frac{4(\delta - kv_{\perp})^2}{\Gamma^2}} \quad (\text{C.3})$$

is the single-atom scattering rate [74], given the laser detuning δ and transversal velocity v_{\perp} (along the direction of the laser beam).

C.1 Transversal Probing

C.1.1 Calibration

In the case where the laser beam is orthogonally incident on the stream of atoms, then v_{\parallel} represents the longitudinal velocity of the atomic beam, and v_{\perp} is the transversal velocity. Then, we may use the numerical simulation of the oven atomic beam to model the flux distribution $F(v_{\perp}, v_{\parallel})$ by sampling the atoms that reach the MOT chamber and then empirically constructing a distribution that well matches the sample. Taking the data series for $T_{\text{ec}} = 1100$ °C, which contains $\sim 4.3 \times 10^4$ atom samples that reach the MOT chamber, we first fit the longitudinal velocity distribution with the ansatz¹ $f_{\parallel}(v_{\parallel}) = f_0 v_{\parallel}^2 \exp(-Av_{\parallel}^2)$ yielding $A = 6.3 \times 10^{-6} (\frac{m}{s})^{-2}$. From there, the full flux distribution can be represented using the Bayes theorem:

$$F(v_{\perp}, v_{\parallel}) = 4\pi F_0 \left(\frac{A}{\pi}\right)^{\frac{3}{2}} v_{\parallel}^2 \exp(-Av_{\parallel}^2) F(v_{\perp} | v_{\parallel}). \quad (\text{C.4})$$

Here, $F(v_{\perp} | v_{\parallel})$ represents the conditional probability distribution of v_{\perp} given v_{\parallel} . By taking samples from narrow ($100 \frac{m}{s}$ wide) intervals over the longitudinal velocity and using the fitting ansatz of

$$F(v_{\perp} | v_{\parallel}) = a_1 \exp\left(-\frac{v_{\perp}^4}{2b_1^4}\right) + a_2 \exp\left(-\frac{v_{\perp}^2}{2b_2^2}\right) \quad (\text{C.5})$$

¹Chosen as the best fit for the data among several tried functions of the general form $f_{\parallel}(v_{\parallel}; m, n) = f_0 v_{\parallel}^m \exp(-Av_{\parallel}^n)$

we converge to the empirical form of the conditional probability that describes the simulation data well:

$$F(v_{\perp}|v_{\parallel}) = \frac{\left(1 - e^{-\left(\frac{v_{\parallel}}{v_0}\right)^{\frac{3}{2}}}\right) e^{-\frac{v_{\perp}^4}{2(B_1+C_1v_{\parallel})^4}} + e^{-\left(\frac{v_{\parallel}}{v_0}\right)^{\frac{3}{2}}} e^{-\frac{v_{\perp}^2}{2(B_2+C_2v_{\parallel})^2}}}{\left(1 - e^{-\left(\frac{v_{\parallel}}{v_0}\right)^{\frac{3}{2}}}\right) \sqrt[4]{\frac{(B_1+C_1v_{\parallel})^4}{8}} \Gamma\left(\frac{1}{4}\right) + e^{-\left(\frac{v_{\parallel}}{v_0}\right)^{\frac{3}{2}}} \sqrt{2\pi(B_2+C_2v_{\parallel})^2}} \quad (\text{C.6})$$

with the fit parameters being $B_1 = 0.093 \frac{\text{m}}{\text{s}}$, $C_1 = 0.00345$, $B_2 = 0.054 \frac{\text{m}}{\text{s}}$ and $C_2 = 0.00260$. Despite the cumbersome final form of the expression for the scattering rate, given Γ and s , it can be numerically integrated, first along v_{\parallel} and then along v_{\perp} to give a prediction for the fluorescence signal. By comparing the peak height of the measured signal with the peak height of the unit flux obtained using this method, the total flux in the beam, F_0 can be estimated.

C.1.2 Flux Measurements

The "Bottom" beam, that is incident to the atomic beam at right angle was used to measure the flux in the MOT chamber. The summary of two sets of measurements that are presented in this thesis is given in the Table C.1. A CMOS camera that was employed in these measurements has a conversion constant of $C_{\text{camera}} = 0.36 \frac{\text{counts}}{\text{photon}}$ in the settings configuration that was used².

Data Set	19/10/2020	12/04/2019
Isotope	^{166}Er	^{166}Er
t_{exp} [ms]	990	900
Solid Angle, Ω [sr]	2.1×10^{-3}	2.1×10^{-3}
$s = \frac{I}{I_{\text{sat}}}$	1.5 ± 0.5	20 ± 5
$C_{\text{flux}} \left[\frac{\text{counts}}{\text{atoms/s}} \right]$	$(1.0 \pm 0.3) \times 10^{-3}$	$(3.2 \pm 0.8) \times 10^{-3}$
Signal at 1 100°C [counts]	8.2×10^6	4.0×10^7
Flux at 1 100°C [atoms / s]	$(4.5 \pm 2.6) \times 10^{10}$	$(1.1 \pm 0.6) \times 10^{11}$
Signal width (pred.) [MHz]	1.5	1.6
Signal width (meas.) [MHz]	2.0	2.2

Table C.1 Flux Measurements

²Thorlabs DCC3260M, with 12-bit binning and digital gain level set to 55/100

C.2 Angled Probing

If the laser beam is instead tilted by an angle θ into the atomic beam, then it can be used to probe the longitudinal velocity distribution of the atoms. Sticking to the nomenclature where the longitudinal and transversal atomic velocities are labelled v_{\parallel} and v_{\perp} , the component along the propagation direction of the laser can be expressed as:

$$v_{\theta} = v_{\parallel} \sin \theta - v_{\perp} \cos \theta. \quad (\text{C.7})$$

A full quantitative analysis similar to above can be developed in this case as well by writing $v_{\perp} = \frac{v_{\parallel} \sin \theta - v_{\theta}}{\cos \theta}$, but a heuristic approach can be very informative as well. Since v_{\perp} has a symmetric probability distribution centred around zero, for a given laser detuning δ , there will exist a resonant longitudinal velocity that is dominantly probed by the laser, given by:

$$v_{\parallel} = \frac{\delta}{k \sin \theta}. \quad (\text{C.8})$$

Also, recalling Equation C.2, the flux of any given velocity group will be roughly proportional to $v_{\parallel}(\delta)S(\delta)$, where $S(\delta)$ is the total fluorescence signal measured at laser detuning δ . The resolution of this measurement will be limited by the spread in transversal velocities (provided that a narrow-line transition is used for probing), and this effect can be quantified using the observations from the transversal probing measurements. The observed signal width of $\Delta_{\perp} \sim 2\pi \times 2$ MHz is indicative of the spread in transversal velocities, which can then be estimated as $\Delta v_{\perp} = \frac{\Delta_{\perp}}{k} = 1.2 \frac{\text{m}}{\text{s}}$, where k is the wave number of the laser light³. For an angled probe scenario, this spread will couple into the resolution as:

$$\Delta v_{\theta} = \Delta v_{\perp} \cot \theta \quad (\text{C.9})$$

yielding a resolution of $\Delta v_{\theta, \text{Top}} \sim 30 \frac{\text{m}}{\text{s}}$ for the ‘Top’ beam probing and $\Delta v_{\theta, \text{Top}} \sim 1 \frac{\text{m}}{\text{s}}$ for the ‘Side’ beam probing.

Knowing the velocity resolution, a conversion between the measured fluorescence signal and flux velocity distribution can be established as:

$$S(\delta) = F(v_{\parallel}(\delta)) \Delta v_{\theta} \frac{L_{\text{int}}}{v_{\parallel}(\delta)} t_{\text{exp}} \frac{\Gamma_s}{2(1+s)} C_{\text{camera}} \Omega \quad (\text{C.10})$$

³All of the flux measurements presented here are performed using 583 nm light.

Appendix D

Vacuum Cleaning, Assembly and Bakeout Procedures

In this appendix I give an overview of the steps and procedures related to the vacuum chamber assembly that we adhered to. These are based on instructions from the technical literature [71], doctoral and master's theses of students involving vacuum chamber construction [136, 137], component instruction manuals and experience of our colleagues. Some steps involved a degree of improvisation, necessary to adjust the process to the specifics of our design or resulting from the circumstances.

D.1 Preparation

In order to minimise the amount of dust present during assembly, the area around the optical table was isolated using plastic dust sheets. As the laboratory had been vacant for a long time prior to the start of our project, and hence was very dusty, we decided to go with the safe option of having a clean and isolated area for assembly. The inside of this space was wiped and dusted both before and after installation of the plastic sheets. Any tools or components to be used inside this area, that haven't already arrived in clean packaging were also wiped with a dust cloth or alcohol wipes at this stage.

We proceeded to prepare all the components and accessories to be used during this process. Here, I offer a checklist of required items along with any relevant comments:

- **Copper Gaskets:** Our chamber contains three different sizes of CF flanges, and we also used the softer, fully annealed copper gaskets for viewports, as opposed to the regular, OFHC, gaskets for all other connections. Furthermore, some components required wide-bore gaskets (e.g. the erbium oven could only fit through 38 mm ID

CF35 gaskets). As gaskets often come in unlabelled packaging, they were all sorted in clearly marked plastic containers.

- **Flange Fasteners:** It is important to prepare a sufficient number of bolts, washers and nuts, making sure that appropriate lengths of bolts are used depending on the flange thickness and tapping depth. We also used fasteners made out of 316L stainless steel that has a lower magnetic permeability compared to the standard type 304L, and these were clearly labelled and stored separately.
- **In-vacuum Screws:** If screws are required for fixing components under vacuum, vented screws should be used, and these should be cleaned together with the rest of the vacuum components.
- **Gasket Clamps:** Having a set of these clamps proves useful when dealing with rotatable or upright mounted flanges.
- **Cleaning Solvents:** We used acetone, methanol and isopropyl alcohol for cleaning all of our chamber components, together with distilled water that was used for occasional rough cleaning of metal components and tools. It is acceptable to use technical grade (95%) acetone, as it is only used as a first cleaning step. With isopropyl and methanol we decided to use reagent grade (99%) solvents. It is also helpful to prepare an appropriate number of wash bottles, beakers, funnels and solvent waste containers.
- **Lint Free Wipes:** It is essential to use lint-free wipes that are also solvent resistant when cleaning the chamber components. We used polyester wipes.
- **Wrenches and Drivers:** It is often required to have duplicate, same size spanner wrenches for nut and hex-head bolt connections, so these should be prepared as well. Also, vacuum valves are often operated with spanner wrenches and an appropriate size should be sourced.
- **Aluminium Foil:** Use of thicker, heavy duty grade foil is recommended.
- **Leak Sealant:** Should be used only as a last resort when no further tightening is possible and trying new gaskets is not an option. If applied before the bakeout, temperature ratings should be checked first.
- **Miscellaneous Tools:** This is usually determined by the specific steps in the assembly, but it should be noted that any tools that come into contact with in-vacuum components should be thoroughly cleaned and degreased (e.g. we used wire-cutters to cut the

erbium material into small pieces, a ball-driver for the in-vacuum screws and tweezers for cleaning the internal surfaces of components with solvent soaked cloth).

- **Desk Lamp:** Good lighting is essential for examining components and spotting any possible defects (e.g. damaged CF knife-edges).
- **Alignment and Levelling Tools:** This can include rulers, measuring tape, spirit levels as well as any pre-assembled height references or tape for marking positions on the table.
- **Temporary Supports:** Any complicated assembly should be done by multiple people, but it is a good practice to also use temporary support constructions, especially when installing heavy or bulky components. We used a construction consisting of wires suspended between two optics posts with a cushioning material on top to support the Zeeman Slower tube with the magnetic coil when it was being installed between the two sections of the chamber.
- **Component Trays:** The assembly process involves a lot of loose, small items.

D.2 Cleaning

The cleaning of the vacuum components was performed immediately prior to assembly. Despite the fact that the majority of the components are generally shipped clean by the manufacturers, it is a good practice to clean them at this stage. The standard procedure we used is outlined as follows:

- Metal parts were washed with acetone and rinsed with isopropyl alcohol.
- All components that could fit into the ultrasonic bath¹ were treated with ultrasound for 15 minutes in acetone at room temperature, and then rinsed with isopropyl alcohol.
- Viewports were treated in a similar way, but with methanol rather than acetone, as it is less aggressive towards AR coatings.
- Immediately before mounting, flanges being connected and the gasket used were wiped with methanol² using a lint free tissue.

¹Langford Sonomatic 375 ultrasound bath

²acetone should not be used with copper gaskets [138]

Some components required more thorough cleaning, mostly because they were either made or altered in the machine workshop. These were treated with up to three extra rounds in the ultrasonic bath. All parts were first left exposed in air to dry, and then wrapped in aluminium foil to await installation. Viewports were additionally protected with lint free cloth over the coated glass. We refrained from cleaning the vacuum valves with large quantities of solvents, as we were worried about trapping some liquid in their complex construction. Instead, we have just wiped the vacuum surfaces with solvent soaked lint-free cloth. Finally, the glass science cell was only rinsed with optics grade methanol (99.9% purity and from a recently opened bottle) to remove dust particles that were observed on the glass inside the cell.

D.3 Assembly

The first parts of the chamber to be assembled were the ones mounted directly on the supporting posts. Once the MOT chamber was placed on the fixed posts, we proceeded with adjusting the height of the remaining sections to level the chamber evenly. Once the Zeeman slower tube was installed, connecting the two sections of the chamber, we adjusted the fine alignment across the long dimension of the chamber and then securely clamped all the posts to the table. Next, all the simple components were installed, including remaining valves, crosses and viewports, leaving the vacuum pumps and the effusion cell oven for the end. This was primarily done to avoid exposing the pump getter material to moisture for a prolonged amount of time. The effusion cell oven was carefully assembled and loaded with 8 g of erbium.

In the assembly process, we used the regular, OFHC, copper gaskets for all flanges, with the exception of viewports where fully annealed copper gaskets were used. This is a common and recommended practice as the softer, fully annealed gaskets prevent the viewport flanges to be overly stressed, which can cause damage to the glass-to-metal seals. When establishing CF connections, the flanges were first finger-tightened, with the gasket being held in place with clamps (if required), and then the bolts were uniformly tightened, going around the flange in the periodic star-pattern (shown in Figure D.1). When tightening, care was taken to apply the same torque to all bolts, and also, twisting of no more than a quarter of a turn was applied in any single instance. The target flange-to-flange gap width depends on the depths of the grooves housing the knife-edges, but in general it usually lay in the 1 – 2 mm range. The two flange surfaces should not establish contact in any scenario, and if this happens, the connection should be redone with a new gasket.

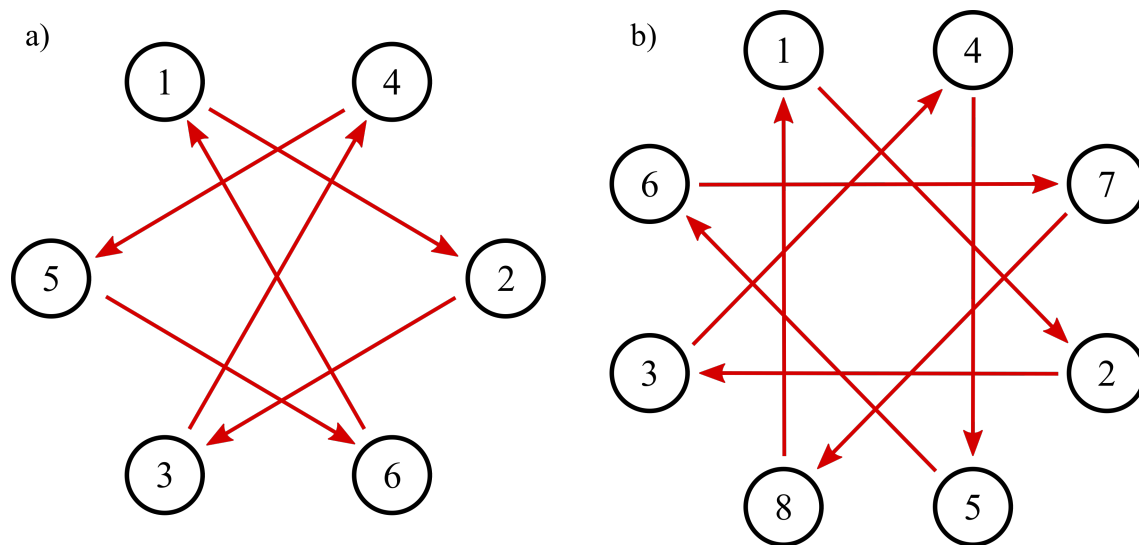


Fig. D.1 **Star Pattern for Tightening Flange Bolts** - a) 6-bolt configuration for CF16 and CF35 flanges b) 8-bolt configuration for CF63 flanges

In parallel with the vacuum system assembly, we had to build and install the magnetic field compensation cage coils, as they had to be positioned in place before the chamber was fully connected due to topological constraints. Furthermore, the ZS coils were also wound on the vacuum tube prior to installation.

D.4 Bakeout

In the preparation for the bakeout, we first removed all the detachable components that are not compatible with high temperatures. This included the RGA controller body and the plastic actuator the HV to UHV section gate valve, and only in the first bakeout, the magnet assemblies on the vacuum pump. We then consulted the specifications of all the remaining components for the maximum temperature ratings, and decided to bake at 180°C, to leave some headroom as the lowest among the temperature limits was 200°C. Then we proceeded with installing the bakeout equipment, following this sequence of steps:

- The clamps securing the HV section of the chamber to the optical breadboard were loosened, to allow for the chamber and its mounts to accommodate thermal expansion and contraction along the Zeeman slower tube³ resulting from the changing temper-

³Not loosening all the clamps was a mistake as the thermal stresses along the deceptively short chamber section between the MOT chamber and the ZS mirror region actually opened a leak during the first bakeout run

ature. Note that all posts carrying the chamber were mounted on ceramic, thermally insulating pedestal bases⁴.

- An aluminium tube was mounted around the glass science cell to act as a heat shield, protecting the glass and the glass-to-metal seal from temperature gradients and abrupt changes.
- The entirety of the chamber was wrapped in aluminium foil, taking special care that there is no direct contact between the foil and the coated glass surfaces of viewports. Where necessary, the foil was secured with Kapton tape.
- A total of sixteen thermocouple sensors were attached to the chamber, making sure that a good thermal contact is established. These were distributed such that sensitive areas (Science cell, MOT chamber) have multiple sensors.
- Twelve electric heater tapes were evenly distributed across the chamber, avoiding overlaps as much as possible. Where overlapping the heater tapes was inevitable due to the geometry of the chamber, thermally insulating material was used as a buffer between tapes.
- The whole setup was insulated with a thick layer of fibre glass material, using heat resistant strings and copper wire for securing it. This was then followed with a layer of aluminium foil to keep the fibre glass debris contained during baking.

⁴Thorlabs RS05PC/M

Appendix E

Computer Control and Data Acquisition

E.1 Control System Architecture

The control and synchronisation of the experiment is mainly realised through a set of National Instruments cards with analog and digital output channels. The system currently employs two analogue¹ and one digital output card², providing in total of 32 digital and 40 analogue independently controllable outputs. The cards are mounted in an appropriate NI chassis³, that will also allow for additional cards to be installed to satisfy the needs of the expansion to a dual species experiment with potassium. From the software side, the experimental sequences are generated and sent to the hardware by the Cicero Word Generator [139]. The system also employs an FPGA chip⁴ that provides the variable time-base clock signal for the NI cards, exploiting the functionality offered by Cicero which greatly increases the maximum sequence length or complexity by reducing the redundancy of the data fed into the cards' buffer.

E.2 Imaging

We implemented both absorption and fluorescence imaging at the MOT chamber. The former was used to record atomic density distributions of clouds from the MOT or the ODT, whereas the fluorescence imaging can be used for probing the flux and the velocity distribution of the atomic beam, in addition to the imaging of the aforementioned clouds. We use a CMOS

¹NI PXIe-6733 - 8 Channel, 16-bit Analog Output Card and NI PXIe 6738 - 32 Channel, 16-bit Analog Output Card

²NI PXIe-6536 - 32 Channel Digital Output Card

³NI PXIe-1082 8-Slot PXI Express Chassis

⁴XEM6001 from Opal Kelly. Cicero Word Generator is originally designed to work with the XEM3001 model, and a minor code modification was necessary.

camera⁵ with a 1936×1216 pixel array for both types of imaging. The camera is triggered by a TTL signal from our digital control card, and the acquisition and storage of images into the database is synchronised from the Cicero Word generator program. This included another minor modification of the Cicero Word Generator program, performed by my colleague Lucas Hofer. More details about the data acquisition and storage in our experiment can be found in [140].

E.2.1 Absorption Imaging

Our absorption imaging system consists of a collimated beam with waist radius of 12 mm and circular polarisation. It is launched into the chamber from an optical fibre, through a plano-convex 150 mm lens and a quarter-wave plate. Upon exiting the chamber, the beam is projected onto the camera with a pair of plano-convex 150 mm lenses in confocal configuration, yielding unit magnification.

This technique measures the optical density of the atomic cloud along the imaging direction, and each measurements requires three images to be taken. First, the image with the light incident on the atoms is taken (I_a), followed by a reference image (I_p) of the probe beam, without any absorption, and finally, a shot without the laser light is performed, yielding the background image (I_b). The optical density of the atomic cloud is then evaluated as:

$$OD = \ln \left(\frac{I_p - I_b}{I_a - I_b} \right) \quad (\text{E.1})$$

The optical density is related to the number density of the atoms through the optical cross section σ , and assuming the z -axis for the imaging direction, one can write:

$$n(x, y) = \frac{1}{\sigma} OD(x, y) \quad (\text{E.2})$$

The optical scattering cross-section of a two-level system is generally given by:

$$\sigma = \left(\frac{3\lambda^2}{2\pi} \right) \frac{1}{1 + s + \frac{4\delta^2}{\Gamma^2}} \quad (\text{E.3})$$

but as we use resonant light with $s \sim 0.1$, we can safely assume $\sigma = \sigma_0 = \left(\frac{3\lambda^2}{2\pi} \right)$.

⁵Thorlabs DCC3260M

E.2.2 Fluorescence Imaging

Fluorescence imaging is performed by collecting the photons scattered by the atomic cloud or beam, and directing them on the camera. We typically use a 2 lens system which produces a focused image of the region of interest on the camera sensor. The magnification can be extracted from the lens system geometry, and we have used various values ranging from $\frac{1}{4}$ to 1 depending on the purpose.

This imaging technique determines the number of atoms present by estimating the total photon scattering rate based on the light intensity that reaches the camera. The first step in the calibration process is determining the solid angle Ω , centred on the atoms, over which the imaging optical system collects photons. Then, it is necessary to know the conversion constant between camera pixel counts and the number of incident photons, C_{cam} . It generally depends on the quantum efficiency of the camera and sensor gain and binning settings. Knowing these, along with the imaging exposure time, t_{exp} , one can calculate the total scattering rate corresponding to each pixel of the image $I(x, y)$:

$$R_{\text{tot}} = \frac{4\pi C_{\text{cam}} I(x, y)}{\Omega t_{\text{exp}}} \quad (\text{E.4})$$

E.3 Publication : Atom Cloud Detection and Segmentation Using a Deep NN

I present the publication titled "Atom Cloud Detection and Segmentation Using a Deep Neural Network" published in the journal Machine Learning: Science and Technology where I am listed as the second author. This effort was spearheaded by my colleague Lucas Hofer, and my contribution to this work involved building, calibration and operation of the experimental apparatus which provided the dataset for the study, minor contributions to writing and editing of the manuscript and involvement in responding to referee comments. The preprint version is given below.

Atom Cloud Detection and Segmentation Using a Deep Neural Network

Lucas R. Hofer¹, Milan Krstajić^{1,2}, Péter Juhász¹, Anna L. Marchant¹‡ and Robert P. Smith¹

¹ Clarendon Laboratory, University of Oxford, Parks Road, Oxford OX1 3PU, United Kingdom

² Cavendish Laboratory, University of Cambridge, J. J. Thomson Avenue, Cambridge CB3 0HE, United Kingdom

E-mail: robert.smith@physics.ox.ac.uk

Abstract. We use a deep neural network to detect and place region-of-interest boxes around ultracold atom clouds in absorption and fluorescence images—with the ability to identify and bound multiple clouds within a single image. The neural network also outputs segmentation masks that identify the size, shape and orientation of each cloud from which we extract the clouds’ Gaussian parameters. This allows 2D Gaussian fits to be reliably seeded thereby enabling fully automatic image processing. The method developed performs significantly better than a more conventional method based on a standardized image analysis library (Scikit-image) both for identifying regions-of-interest and extracting Gaussian parameters.

Keywords: ultracold quantum matter, machine learning, deep neural networks, Bayesian optimization, object detection, instance segmentation, image processing

1. Introduction

Deep neural networks have revolutionized data analysis and led to automation of tasks that previously required human supervision. Image analysis has particularly benefited through the use of convolutional neural networks (CNNs) [1] and their derivatives which have allowed for image classification [2, 3], object detection [4, 5] and instance segmentation [6]. Although many of these neural networks (NNs) were developed for tasks such as facial recognition by social media networks [7, 8], they have also been used to identify laser modes [9], classify phases in condensed-matter systems [10, 11], reduce measurement errors for trapped-ion qubits [12] and process images from cold atom experiments [13, 14, 15]. In this work, we use an instance segmentation NN (see

‡ Current address: RAL Space, Science and Technology Facilities Council, Rutherford Appleton Laboratory, Harwell, Didcot, Oxfordshire, OX11 0QX, UK

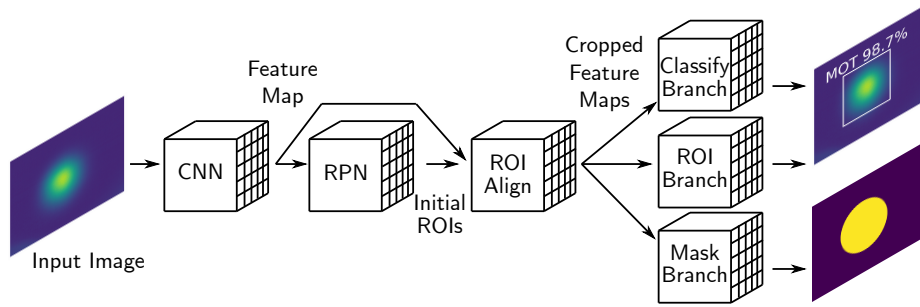


Figure 1. Overview of the neural network (NN). An experimental image is initially fed into a convolutional neural network (CNN) which produces a ‘feature map’ of the image. The region-proposal network (RPN) uses this feature map to generate regions-of-interest (ROI) where atom clouds are likely contained. In the ROI alignment stage, the CNN’s feature map is cropped and resized for each cloud’s ROI before being fed into three parallel branches. The first branch (ROI) generates refined ROIs, whereas the second branch (class) classifies the type of atom cloud in the ROI. Finally, the third branch (mask) generates a segmentation mask corresponding to the $1/e^2$ contour of the atom cloud.

Fig. 1) to analyze experimental images containing atom clouds in magneto-optical traps (MOTs) and optical dipole traps (ODTs).

Neural networks consist of an input layer and an output layer with a number of intermediate hidden layers which are connected to one another via ‘weights’. Rather than employing hard-coded algorithms, NNs learn to emulate data they encounter through training cycles, in which data is iteratively passed through the NN and the output compared to the ‘ground truth’. The difference between the two is then used to update the weights between the NN’s layers, thereby improving its accuracy. When employing supervised training, this requires a dataset which includes both input data and their associated ground truth values. For object detection NNs, these ground truth values are rectangular bounding boxes for each object, as well as labels classifying the object types in the bounding boxes. Instance segmentation NNs build upon object detection NNs by also requiring pixel-to-pixel segmentation masks in which image pixels comprising the object have mask values of one, whereas all other pixels have mask values of zero.

Our dataset consists of images of cold atom clouds in a MOT [16] and an ODT [17] (see Fig. 2a–c). Atom clouds in these traps form approximately Gaussian density distributions [18]. Fitting a cloud allows the parameters describing the distribution (Gaussian parameters) to be extracted and used to ascertain information such as the cloud’s size and density. Furthermore, by using time-of-flight measurements [19] the temperature of the atoms can be determined.

A region-of-interest (ROI) [20] centered on the atom cloud is used during fitting as objects in the image other than the atom cloud can cause an inaccurate fit (e.g. an atom cloud in another trap or extraneous noise). Additionally, decreasing the fit area can significantly decrease the fit time when using two-dimensional fitting. Manually

determining the ROI is time-consuming when analyzing a large number of images and an algorithmic procedure is often employed, such as taking the ‘center of mass’ and then iteratively expanding the ROI around this point until the fractional enclosed ‘power’ exceeds some threshold. Another method involves performing connected component analysis on a binarized version of the image and then measuring the resulting regions using common image processing libraries [21]. However, if the image is noisy (e.g. contains fringing), the proposed ROIs will be inaccurate for these types of methods (Sec. 6).

Here we propose a deep neural network based approach to ROI determination in which a NN finds the ROI for each atom cloud in an image (see Fig. 1). Furthermore, the NN differentiates between clouds (classification) in a MOT and those in an ODT and also outputs a segmentation mask for each cloud from which Gaussian parameters are directly extracted. The classification feature is particularly useful when the cloud type is not *a priori* known from the experimental sequence (e.g. images containing both MOT and ODT clouds during the ODT loading). Although features such as the position or aspect ratio can be used for classification with additional manual or experimental input, the NN needs the image alone (beyond training on an appropriate dataset) to determine cloud types and so is easily adaptable to other cold atom experiments with different numbers of clouds or cloud types.

The rest of the article is arranged as follows: Sec. 2 describes the experimental dataset used for NN training and validation, Sec. 3 describes the training process, Sec. 4 discusses Bayesian optimization [22, 23] of the NN’s hyperparameters [23] and Sec. 5 examines how the Gaussian parameters are calculated from the segmentation mask. In Sec. 6 we compare our proposed NN method to a more conventional method of determining both ROIs and Gaussian parameters.

2. Experiment and Dataset

To produce the ultracold atom clouds, erbium atoms are initially trapped and cooled to $\sim 20 \mu\text{K}$ in a narrow-line MOT [24] before being loaded into an ODT formed from a 30 W, 1030 nm laser beam focused down to a $\sim 40 \mu\text{m}$ waist (see Fig. 2). Optimization of the trap loading involves maximizing the atom number while minimizing the cloud temperature. The atom number is found by fitting the atom cloud in either a fluorescence or absorption image[§] with a two-dimensional (2D) Gaussian (see Eq. 1) and then integrating under the curve. The cloud temperature can be determined from how the cloud width evolves during time-of-flight expansion.

The experimental dataset consists of 260 fluorescence and absorption images (1936×1216 pixels) along with their ROIs, labels and segmentation masks. Of these, 130 images contain clouds released from the MOT with no ODT present (see Fig. 2b)

[§] Experimental images shown in the paper are processed from 2–3 raw images. Fluorescence images require both an image with atoms and a background image without atoms. Absorption images additionally require a probe image in which the probe beam is turned on, but no atoms are present.

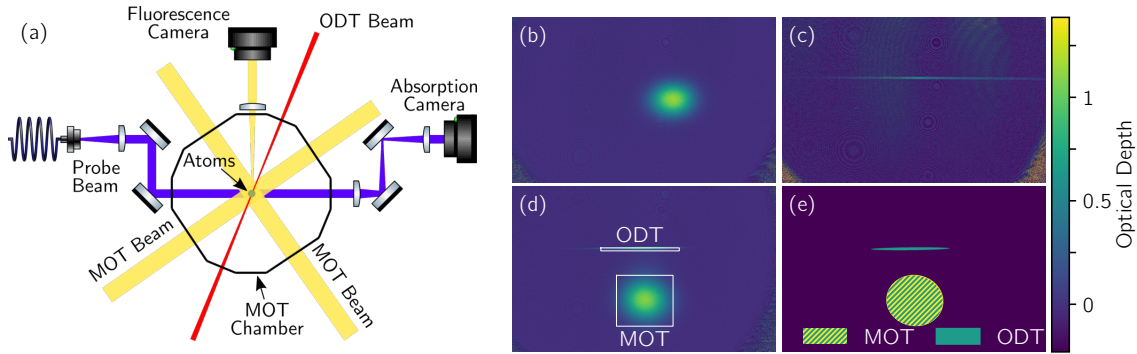


Figure 2. Construction of labelled experimental dataset. (a) Experimental setup. The MOT is formed from six 583 nm laser beams in conjunction with a quadrupole magnetic field. Atoms trapped in the MOT can be loaded into an ODT formed from a single 1030 nm laser beam. The fluorescence camera captures the light scattered by the atoms from the MOT beams. During absorption imaging, a 401 nm probe beam passes through the atom cloud which absorbs a portion of the light creating a shadow imaged by the camera. (b) Image of an atom cloud released from the MOT. (c) Image of an atom cloud released from the ODT. The optical depth is multiplied by six to increase ODT visibility. (d) Image with both MOT and ODT atom clouds. Each cloud is labelled and a region-of-interest (ROI) box is drawn around it (white lines). (e) Segmentation masks for the MOT (hatched yellow) and ODT (solid green) clouds in (d).

and 130 images contain either just atoms released from the ODT (see Fig. 2c) or images where atoms released from the ODT and the MOT are both present (see Fig. 2d). We manually label the atom clouds in the images as ‘MOT’ or ‘ODT’ and draw a ROI box at the clouds’ edges which we define as the $1/e^2$ radii along the x and y axes (see Fig. 2d). This definition prevents the ROI boxes from overlapping when the MOT and ODT are both present; however, the ROI boxes are also easily expandable when analysis requires the wings of the distribution.

The manually drawn ROIs were expanded by a factor of two—excepting where the expanded ROIs would overlap—and the atom clouds inside fit with a 2D Gaussian

$$I(x, y) = I_b + I_0 e^{-2 \left(\frac{[(x-x_0) \cos \theta + (y-y_0) \sin \theta]^2}{w_x^2} + \frac{[(y-y_0) \cos \theta - (x-x_0) \sin \theta]^2}{w_y^2} \right)}, \quad (1)$$

where $I(x, y)$ is the image intensity, I_b is the background intensity, I_0 is the peak intensity, x_0 and y_0 are the center coordinates, w_x and w_y are the $1/e^2$ radii along the major and minor axes and θ is the angular orientation of the distribution. To increase the accuracy of the ROIs used for training, the fit parameters were used to calculate the $1/e^2$ radii along the image axes [9] (previously estimated by eye) and the ROI boxes redrawn using these values. The process of fitting and redrawing the ROI boxes from the fit parameters was then completed a second time with subsequent iterations neglected due to an insignificant increase in accuracy.

A segmentation mask was generated for each atom cloud (see Fig. 2e) with the mask borders placed at the $1/e^2$ contour of the cloud—calculated from the final fit

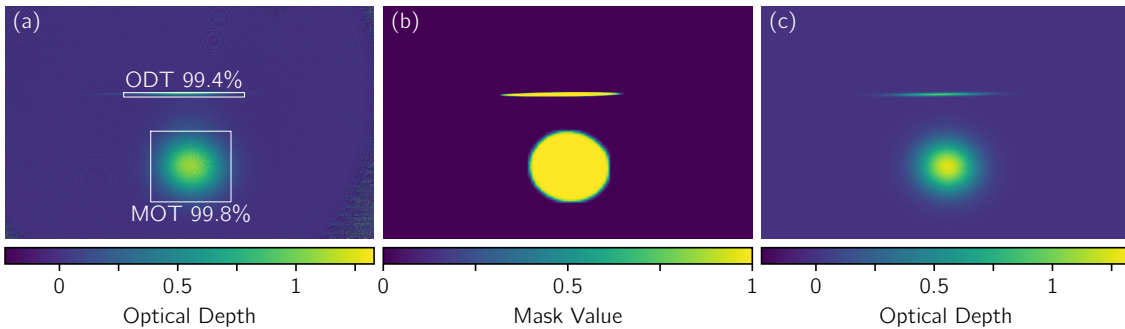


Figure 3. Neural network output. (a) Sample image from the validation dataset with the regions-of-interest (solid white lines), labels and confidence scores predicted by the NN. (b) The segmentation masks returned by the NN for (a) which, due to the internal structure of the NN, have values between zero and unity. (c) Reconstruction of (a) using Eq. 1 and the extracted 2D Gaussian parameters from (b).

parameters; pixels within the $1/e^2$ contour were set to one, whereas pixels outside were set to zero. Finally, the dataset was randomly split into a training dataset with 200 images and a validation dataset with 60 images.

3. Neural Network and Training

We use the neural network Mask R-CNN [25] to detect and bound the atom clouds, as well as to provide segmentation masks for each cloud (see Fig. 3a–b). The NN (see Fig. 1) begins with the experimental image being fed into a convolutional neural network base (CNN, ResNet-50 [26]). The CNN’s outputted feature map [27] is then passed into a region-proposal network (RPN) which generates ROIs where objects are likely located. Next, these ROIs are cropped from the CNN’s feature map in a ROI alignment stage and resized to uniform dimensions. The cropped feature maps are then fed into three parallel branches. The first applies a classifier to determine the object type and give the confidence of its prediction—which is helpful in determining whether to use the ROI in post-NN analysis. The second branch gives a more accurate ROI box prediction (see Fig. 3a) and finally the third outputs a segmentation mask for the object inside the ROI (see Fig. 3b). Since all three branches share the same base, computation speed is significantly increased [28] for both training and evaluation.

During training, the NN output is compared to the ground truth (i.e. the expected output from the training dataset) via a loss function; the loss is then back-propagated [29] through the NN to adjust the weights between layers and refine the NN model (see Fig. 4a). The loss function for the RPN stage is L1 loss [30], for the ROI branch it is Smooth L1 loss [31], the classifier uses categorical cross entropy loss [32] and lastly the mask branch utilizes binary cross entropy loss [33]. Although the loss can be separately back-propagated for each branch, a simpler approach is taken here in which the losses are summed together and then back-propagated to update the weights of the NN [25].

An epoch denotes a single cycle of training in which every image in the training dataset is passed through the NN, the loss calculated and the model weights updated. Increasing the number of training epochs can increase the NN’s final accuracy so long as the NN does not overfit on the training data. However, due to finite computational resources, we restrict the training of an individual NN to fifteen epochs—determined to be sufficient, see below—and instead use Bayesian optimization (BO) to increase the accuracy of the final trained model (see Sec. 4).

Five hyperparameters, which tune the learning process, are set before the NN’s training phase. The first is the *learning rate* which determines the size of the step the NN takes during stochastic gradient descent [34]. If the learning rate is too low, the NN will take too long to converge to the minimum of the loss function, whereas if the learning rate is too high, the NN will not be able to descend to the minimum, but will oscillate around it or diverge. Since larger learning rates are useful at the beginning of training and smaller learning rates are useful towards the end, a learning rate scheduler [35] is employed which decreases the learning rate by some scalar (*decay*, the second hyperparameter) after a fixed number of epochs (*step size*, the third hyperparameter). The fourth hyperparameter is the *momentum* which prevents the NN from getting stuck in a local minimum during training [36]. The last hyperparameter is the *batch size*—the number of images simultaneously passed through the NN—and, unlike the other hyperparameters which are tuned with BO, is fixed to four for all NNs.

The accuracy of the NN is evaluated (see Fig. 4b) using the COCO evaluation metric which entails calculating the intersection-over-union [37],

$$\text{IoU} = \frac{\text{area}(\text{ROI}_p \cap \text{ROI}_{\text{gt}})}{\text{area}(\text{ROI}_p \cup \text{ROI}_{\text{gt}})}, \quad (2)$$

where ROI_p is the ROI prediction from the NN and ROI_{gt} is the ground truth ROI. Values below a predetermined IoU threshold (e.g. $\text{IoU} = 0.5$) are considered a false prediction—mislabelling the object class within the ROI is also a false prediction—, whereas values above are considered a true prediction. A precision recall-curve [38] is then constructed and integrated to give the average precision (AP) for the given threshold (e.g. AP_{50} for the $\text{IoU} = 0.5$ threshold). Finally, the AP is calculated for ten IoU thresholds (0.50–0.95 with a step size of 0.05) and averaged to give the mean average precision (mAP)—which is the metric generally reported for object detection. The mask AP values and mAP can be similarly calculated [39].

The NNs are trained in a Google Colab notebook [40] utilizing a GPU backend and implemented in PyTorch [41] using the pre-built Mask-RCNN model in the Torchvision package. Rather than training the NN from scratch, the model weights are loaded from a network pre-trained on the COCO train2017 dataset [42]—which significantly reduces the time required to train the network and increases the model’s final accuracy [43]. Additionally, this transfer learning, complemented by data augmentation (in which images are randomly flipped horizontally during training), allows us to use a relatively small training dataset. After each training epoch, the updated NN is evaluated on the validation dataset which yields the mAP for both the object detection and the

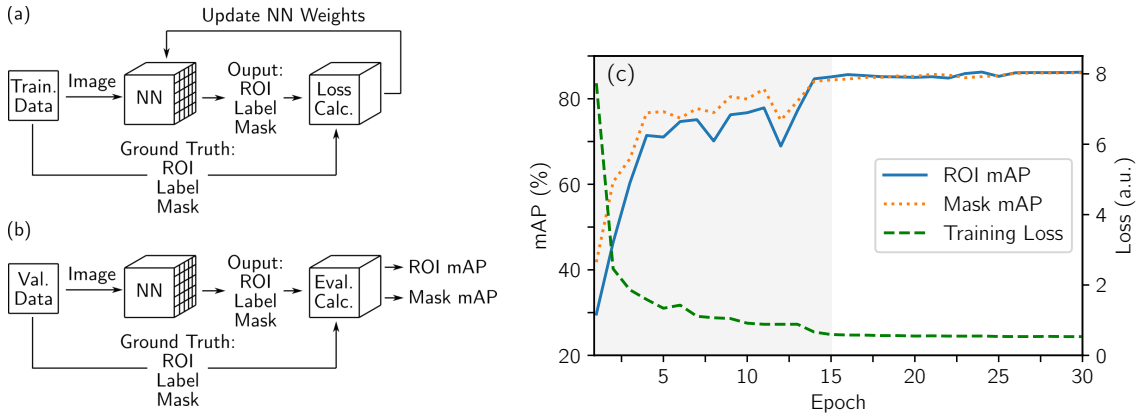


Figure 4. Training and validating the neural network. (a) During training of the NN, images from the training dataset are fed into the NN which outputs the regions-of-interest, labels and masks. These outputs are compared to the ground truth values and the loss calculated. The loss is then back-propagated through the NN and used to update the weights between the NN’s layers. (b) When evaluating the NN, the validation dataset is used in a process similar to (a); however, the mean average precision (mAP) for both the object detection branch (ROI) and segmentation mask branch are calculated rather than the loss. (c) The mAP of the ROI branch (solid line), the mAP of the segmentation mask branch (dotted line) and the training loss (dashed line) as a function of the training epoch for the NN trained with the best set of hyperparameters (see Table 1). The shaded region represents the number of epochs used during Bayesian optimization.

segmentation mask branches. These two values are averaged together to give the accuracy of the training epoch (average mAP) and the epoch with the highest average mAP determines the overall accuracy of the NN model. After using BO to determine the hyperparameters which give the highest accuracy, we retrain the NN with these parameters for 30 epochs (see Fig. 4c) and verify that the NN’s accuracy becomes asymptotic at the 15 epoch mark—with no overfitting seen thereafter.

4. Bayesian Optimization of Hyperparameters

The accuracy of the trained NN is sensitive to the hyperparameters used during training. In the past, the hyperparameters were tuned through grid search, random search [44] or by hand; however, in recent years, Bayesian optimization (BO) has been successfully employed to find the best set of hyperparameters [23, 45]. BO is particularly useful when trying to find the minimum (or maximum) of a function which is noisy and expensive to evaluate—such as NN training—thereby making a grid search of the parameter space impractical [22].

Bayesian optimization takes the function value (cost) at previously evaluated points and uses a Gaussian process to model the cost as a function of the parameter space [46]. The model also determines the confidence of its predictions in a given region of the

parameter space: perfect certainty at evaluated points, low uncertainty near evaluated points and high uncertainty far from evaluated points. The BO loop then determines where to evaluate the function next by weighing the benefits of evaluating the function near the model’s predicted minimum (or maximum) or evaluating the function in an unexplored region of the parameter space [47].

When optimizing our NN training with BO, the average mAP of the NN is evaluated as a function of the hyperparameter space which consists of the learning rate, momentum, and the learning rate scheduler step size and decay (see Table 1). As a warm start, the NN is initially trained and evaluated at five quasi-randomly (Sobol generated [48]) distributed points (see black squares in Fig. 5a–f). Further evaluation points (red circles in Fig. 5a–f) are iteratively determined by the BO loop. The Ax Python package is used for the BO loop as it provides a high level interface to the BoTorch [49] BO package.

With an increasing number of BO evaluation trials the best achieved average mAP rises and converges (see Fig. 5g). The best set of hyperparameters (see Table 1) gives a mAP of 86.3% for the object detection branch—locating 88 of the 89 clouds—and a mAP of 85.8% for the mask branch. These mAP values are higher than those for similar NNs trained on the COCO validation dataset [25, 50] which is likely due to our NN only needing to classify two object types rather than the eighty in the COCO validation dataset [37], as well as the relatively simple features of the MOT and ODT clouds. The NN also performs well for clouds with a low signal-to-noise ratio (SNR) which we define as the cloud’s peak amplitude divided by the standard deviation of the image’s background intensity; the validation dataset’s noisiest cloud has an SNR of only 2.1 but returns an ROI IoU score of 0.86.

5. Gaussian Parameter Analysis

We can extract the parameters characterizing the cloud’s 2D Gaussian distribution (see Eq. 1) directly from the NN’s segmentation mask output (see Fig. 6a). Taking the 1st moments of the mask yields the center coordinates $\{x_0, y_0\}$ of the atom cloud, whereas the $1/e^2$ radii $\{w_x, w_y\}$ and the angular orientation θ can be determined by calculating the 2nd moments [51] of the mask. The background intensity I_b is calculated by generating a histogram of the experimental image’s pixel values (where there is

Parameters	Lower Bound	Upper Bound	Log Scale	Best Value
Learning Rate	0.0001	0.009	Yes	0.0033
Momentum	0.7	0.92	No	0.86
LRS Step Size	3	15	No	13
LRS Decay	0.001	1	Yes	0.049

Table 1. The hyperparameter search space used during Bayesian optimization along with the hyperparameter values used to train the NN to the highest average mAP (see Figs. 4a and 5).

no cloud) and then taking the peak position (see Fig. 6c). The amplitude of the 2D Gaussian I_0 is calculated by summing the image's intensity inside the $1/e^2$ contour to find the power (P) and then applying

$$I_0 = \frac{2}{(1 - e^{-2})} \left(\frac{P}{\pi w_x w_y} - I_b \right). \quad (3)$$

This method of extracting clouds' Gaussian parameters directly from the segmentation mask was applied to the validation dataset (see Fig. 3c) and the results compared to the Gaussian parameters extracted via a 2D fit of the experimental image (see Fig. 7, blue bars). Apart from θ , we normalized the differences to obtain a relative error. The cloud center $\{x_0, y_0\}$ and the cloud radii $\{w_x, w_y\}$ were divided by the fitted radii, whereas

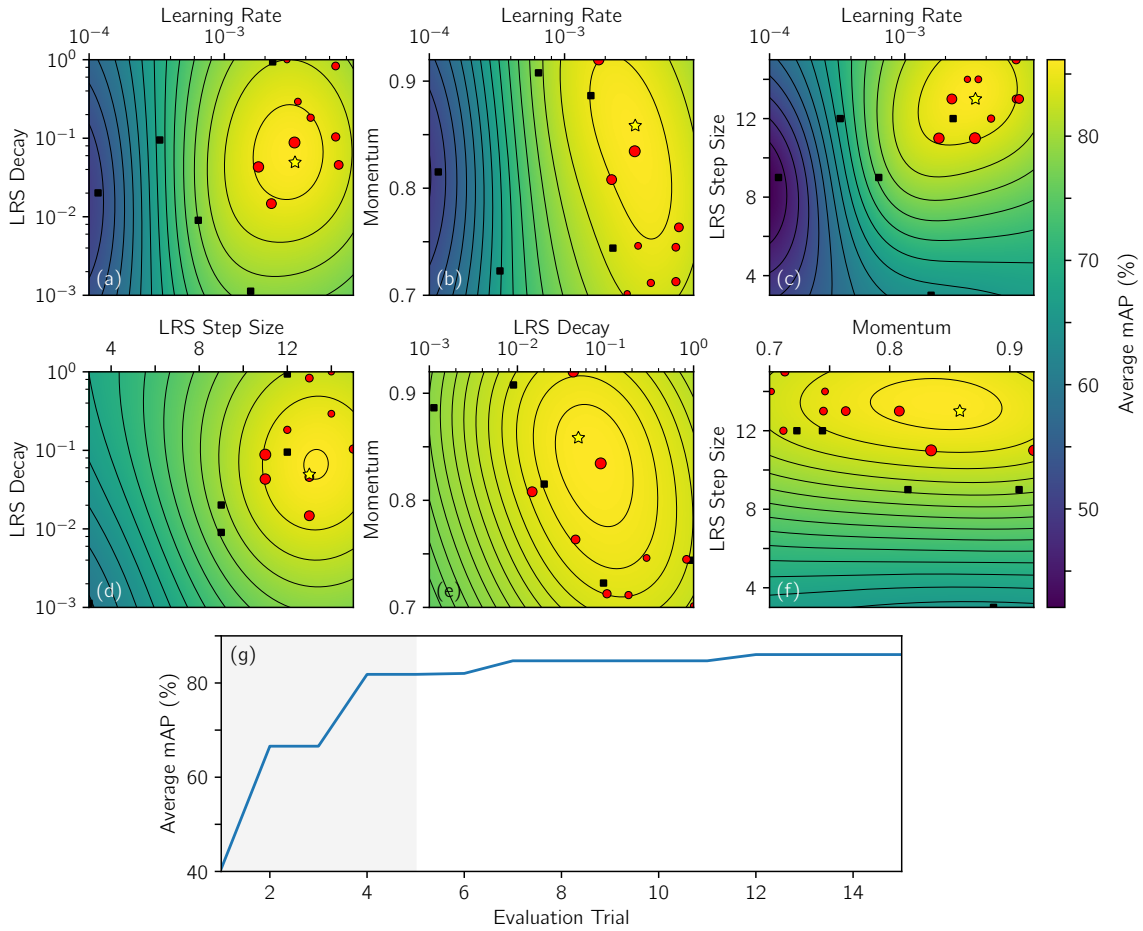


Figure 5. Bayesian optimization of hyperparameters. (a)–(f) The average mAP of the NN predicted by the Bayesian optimization (BO) model as a function of the hyperparameters. The plots are 2D slices through the 4D parameter space taken at the best position (yellow star) for those parameters not displayed. The NN is initially trained and evaluated at five quasi-random hyperparameter positions (black squares) after which the BO loop iteratively determines the evaluation points (red dots, size increases with trial). (g) The best achieved average mAP as a function of the evaluation trial; the quasi-random trial region is shaded in grey.

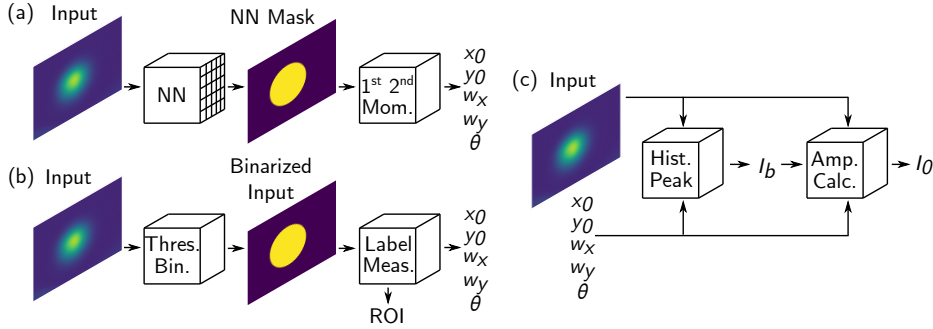


Figure 6. Extraction of Gaussian parameters. (a) NN extraction of the parameters is performed by first inputting the experimental image into the NN which returns a segmentation mask for each atom cloud. Applying the first and second moments (mom.) directly to the segmentation mask yields the center coordinates of the atom cloud $\{x_0, y_0\}$, its $1/e^2$ radii $\{w_x, w_y\}$ and its angular orientation θ . (b) For conventional extraction the experimental image is binarized using a thresholding method (Thres. Bin.) and the binarized image regions labelled and measured (Label Meas.) using Scikit-image’s regionprops function to yield the ROI as well as $\{x_0, y_0, w_x, w_y, \theta\}$. (c) Extracting the intensity parameters. The intensity offset I_b is determined by taking the intensity level corresponding to the peak of a histogram of the experimental image pixel values (hist. peak). The peak intensity I_0 is then calculated (see Eq. 3) using the power inside the $1/e^2$ contour and the previously extracted parameters $\{x_0, y_0, w_x, w_y, \theta, I_b\}$.

the peak amplitude I_0 and the background intensity I_b were both divided by the fitted peak amplitude.

The Gaussian parameters extracted from the NN’s segmentation mask can either be used directly or as seed parameters for a conventional 2D fit—increasing the likelihood of fit convergence and reducing the fitting time. Without a seed, the fit time for a full image (1936×1216 pixels) is approximately 15 seconds on an Intel Xeon 2.2 GHz processor core. For the validation dataset, this is reduced to an average of 3 seconds when using the ROIs proposed by the NN—expanded by a factor of two except where the expanded ROIs would overlap—, which substantially increases the fit speed despite the NN’s processing time of 0.17 seconds per image using a Nvidia Tesla V100 GPU. Extracting the Gaussian parameters takes an average of 0.18 seconds, but results in an average fit speed up of 2 seconds per region when used as a seed. Thus, our method of determining ROIs and seed parameters using a NN offers a significant speedup in conjunction with fitting.

6. Comparison with Conventional Analysis

For comparison with the NN, a conventional method is used to find the ROIs and Gaussian parameters of the clouds (see Fig. 6b). We utilize standard methods based on Python’s Scikit-image (Skimage) package [21] to pre-process the images, determine ROIs for the clouds, and extract the Gaussian parameters.

During pre-processing, a histogram is taken of the image’s pixel intensities. As the cloud areas are much smaller than that of the overall image an approximately Gaussian peak corresponding to the image’s background level and noise is seen. The mean μ and standard deviation σ of a Gaussian fit to this peak are used to define a threshold value $I_{\text{thresh}} = \mu + 3\sigma$ [52] and the image is binarized by setting pixels with $I > I_{\text{thresh}}$ to one and the remainder to zero.

After pre-processing, connected component analysis [53] is applied to the binarized image which groups pixels of the same value together into ‘regions’ (e.g. an atomic cloud). These regions are fed into Skimage’s regionprops method which returns both the ROI coordinates and the geometric parameters $\{x_0, y_0, w_x, w_y, \theta\}$ for each region. ROIs with an area $> \frac{1}{2}$ or $< \frac{1}{800}$ the image size (i.e. much larger or smaller than the size

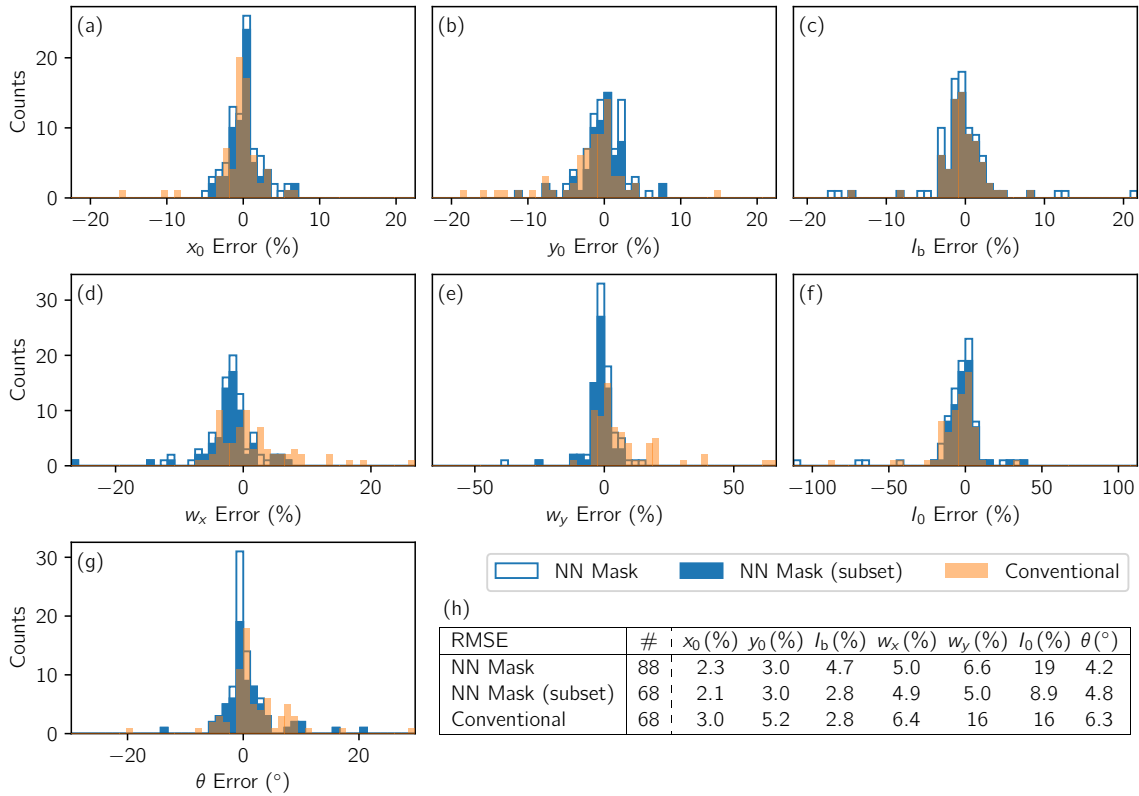


Figure 7. Gaussian parameter errors. (a)–(g) Histograms of the extracted Gaussian parameter errors—calculated by comparison to the 2D fit values—for the atom clouds in the validation dataset. Both the relative errors for the neural network segmentation mask method (subset, filled blue) and the conventional method (orange) are shown for the 68 clouds which the conventional method locates. The relative errors for all 88 clouds the NN method locates are also shown (outlined blue). Cloud center coordinates $\{x_0, y_0\}$ and cloud radii $\{w_x, w_y\}$ are normalized by the fitted cloud radii. The peak amplitude and the background intensity $\{I_0, I_b\}$ are both normalized by the fitted peak amplitude. (h) The root-mean-square error (RMSE) of the Gaussian parameters and the number of clouds analyzed (#).

of the clouds under measurement) are removed and the two largest remaining ROIs—if there are more than one—are taken as the MOT and ODT ROIs since smaller regions generally coincide with remaining high noise regions.

Applying this method to the validation set locates 68 of the 89 clouds with an IoU $> 50\%$; this is significantly worse than the NN which locates 88 of the 89 clouds. The mAP is also calculated, but since the conventional method does not differentiate between MOT and ODT clouds, all the validation dataset regions are relabelled as ‘cloud’. Even with this simplification, an mAP of only 11.1% is achieved—much lower than the NN’s object detection mAP of 86.3% . On closer inspection, the conventional method fails on images with low signal-to-noise ratios (SNR) such as images with significant fringing.

To determine the Gaussian parameters of the 68 successfully bounded clouds we apply a numerical scaling factor (to account for our thresholding method [51]) to the $\{w_x, w_y\}$ returned from regionprops and then generate a binary mask from the resulting $\{x_0, y_0, w_x, w_y, \theta\}$ which is used to find the cloud’s background intensity I_b and amplitude I_0 (see Fig. 6c) as in Sec. 5. The parameters are normalized and compared to those from the 2D fit (see Fig. 7, orange bars). Since the conventional method only recognizes a subset of the clouds, we quantitatively compare against the NN segmentation method for the same cloud subset (shown as filled blue bars in Fig. 7); a direct comparison of the root mean squared errors is shown in Fig. 7h.

When considering both object detection and Gaussian parameter extraction, the NN method significantly outperforms the conventional method. Additionally, the conventional method’s efficacy depends on the SNR of the data, whereas the NN is more robust against high noise levels and fringing since it learns higher level features of the atom clouds. Furthermore, the conventional method requires manual determination of the best pre-processing procedures and therefore potentially needs further tuning for new data; however, when faced with new data the NN simply needs to be retrained with more labelled data, thus making it effective in a laboratory setting.

7. Conclusion

An instance segmentation neural network (Mask R-CNN) was trained to identify ultracold atom clouds in magneto-optical traps and optical dipole traps. The neural network (NN) generates both a region-of-interest (ROI) and a segmentation mask for each cloud—corresponding to the cloud’s $1/e^2$ radii—with a mean average precision of 86.3% and 85.8% on the ROI and the segmentation mask branches, respectively. We show that the Gaussian parameters describing the atom clouds’ distributions can also be extracted directly from the segmentation masks. Both ROI determination and Gaussian parameter extraction via the NN are significantly more accurate than a conventional method based on Python’s Scikit-image library.

With an appropriate training dataset these techniques could be applied to ultracold atom clouds in other traps such as optical lattices [54, 55] and box potentials [56]; they

are also directly applicable to laser beam profiling and other machine vision applications which require analysis of one or more 2D Gaussian distributions.

In the future a custom NN could be created by adding a branch after the ROI alignment stage which would output the cloud parameters directly. This would enable the characterization of non-Gaussian density profiles, useful, for example, in the detection, identification and parameterization of the bimodal clouds seen when a Bose–Einstein condensate [57, 58] is present.

Acknowledgements and Funding

We thank Elliot Bentine, Shu Ishida and Jirka Kučera for helpful discussions and comments on the manuscript. This work was supported by EPSRC Grant No. EP/P009565/1, the John Fell Oxford University Press (OUP) Research Fund and the Royal Society. M.K. acknowledges funding from Trinity College, University of Cambridge.

Data Availability Statement

The data that support the findings of this study are openly available at <https://doi.org/10.5287/bodleian:Y56kydgmj>.

Disclosures

The authors declare no conflicts of interest.

References

- [1] Lecun Y, Bottou L, Bengio Y and Haffner P 1998 *Proceedings of the IEEE* **86** 2278–2324 URL <https://doi.org/10.1109/5.726791>
- [2] Krizhevsky A, Sutskever I and Hinton G E 2012 *Advances in Neural Information Processing Systems* 1097–1105 URL <https://doi.org/10.1145/3065386>
- [3] Simonyan K and Zisserman A 2015 (*Preprint* 1409.1556) URL <https://arxiv.org/abs/1409.1556>
- [4] Girshick R, Donahue J, Darrell T and Malik J 2014 *IEEE Conference on Computer Vision and Pattern Recognition* 580–587 URL <https://doi.org/10.1109/CVPR.2014.81>
- [5] Redmon J, Divvala S, Girshick R and Farhadi A 2016 *IEEE Conference on Computer Vision and Pattern Recognition* 779–788 URL <https://doi.org/10.1109/CVPR.2016.91>
- [6] Long J, Shelhamer E and Darrell T 2015 *IEEE Conference on Computer Vision and Pattern Recognition* 3431–3440
- [7] Taigman Y, Yang M, Ranzato M and Wolf L 2014 *IEEE Conference on Computer Vision and Pattern Recognition* 1701–1708 URL <https://doi.org/10.1109/CVPR.2014.220>
- [8] Schroff F, Kalenichenko D and Philbin J 2015 *IEEE Conference on Computer Vision and Pattern Recognition* 815–823 URL <https://doi.org/10.1109/CVPR.2015.7298682>
- [9] Hofer L R, Jones L W, Goedert J L and Dragone R V 2019 *Journal of the Optical Society of America A* **36** 936–943 URL <https://doi.org/10.1364/JOSAA.36.000936>

- [10] Ch'Ng K, Carrasquilla J, Melko R G and Khatami E 2017 *Physical Review X* **7** 031038 URL <https://doi.org/10.1103/PhysRevX.7.031038>
- [11] Carrasquilla J and Melko R G 2017 *Nature Physics* **13** 431–434 URL <https://doi.org/10.1038/nphys4035>
- [12] Seif A, Landsman K A, Linke N M, Figgatt C, Monroe C and Hafezi M 2018 *Journal of Physics B: Atomic, Molecular and Optical Physics* **51** 174006 URL <https://doi.org/10.1088/1361-6455/aad62b>
- [13] Picard L R, Mark M J, Ferlaino F and van Bijnen R 2019 *Measurement Science and Technology* **31** 025201 URL <https://doi.org/10.1088/1361-6501/ab44d8>
- [14] Ness G, Vainbaum A, Shkedrov C, Florshaim Y and Sagi Y 2020 *Physical Review Applied* **14**(1) 014011 URL <https://doi.org/10.1103/PhysRevApplied.14.014011>
- [15] Miles C, Bohrdt A, Wu R, Chiu C, Xu M, Ji G, Greiner M, Weinberger K Q, Demler E and Kim E A 2020 (*Preprint* 2011.03474) URL <https://arxiv.org/abs/2011.03474>
- [16] Raab E, Prentiss M, Cable A, Chu S and Pritchard D E 1987 *Physical Review Letters* **59** 2631 URL <https://doi.org/10.1103/PhysRevLett.59.2631>
- [17] Chu S, Bjorkholm J, Ashkin A and Cable A 1986 *Physical Review Letters* **57** 314 URL <https://doi.org/10.1103/PhysRevLett.57.314>
- [18] Pethick C J and Smith H 2008 *Bose–Einstein condensation in dilute gases* (Cambridge University Press)
- [19] Lett P D, Watts R N, Westbrook C I, Phillips W D, Gould P L and Metcalf H J 1988 *Physical Review Letters* **61** 169 URL <https://doi.org/10.1103/PhysRevLett.61.169>
- [20] Muessel W, Strobel H, Joos M, Nicklas E, Stroescu I, Tomkovič J, Hume D B and Oberthaler M K 2013 *Applied Physics B* **113** 69–73 URL <https://doi.org/10.1007/s00340-013-5553-8>
- [21] van der Walt S, Schönberger J L, Nunez-Iglesias J, Boulogne F, Warner J D, Yager N, Gouillart E, Yu T and the scikit-image contributors 2014 *PeerJ* **2** e453 ISSN 2167-8359 URL <https://doi.org/10.7717/peerj.453>
- [22] Shahriari B, Swersky K, Wang Z, Adams R P and de Freitas N 2016 *Proceedings of the IEEE* **104** 148–175 URL <https://doi.org/10.1109/JPROC.2015.2494218>
- [23] Snoek J, Larochelle H and Adams R P 2012 *Advances in Neural Information Processing Systems* **25** 2951–2959 URL <https://proceedings.neurips.cc/paper/2012/file/05311655a15b75fab86956663e1819cd-Paper.pdf>
- [24] Frisch A, Aikawa K, Mark M, Rietzler A, Schindler J, Zupanič E, Grimm R and Ferlaino F 2012 *Physical Review A* **85** 051401 URL <https://doi.org/10.1103/PhysRevA.85.051401>
- [25] He K, Gkioxari G, Dollár P and Girshick R 2017 *IEEE International Conference on Computer Vision* 2980–2988 URL <https://doi.org/10.1109/ICCV.2017.322>
- [26] He K, Zhang X, Ren S and Sun J 2016 *IEEE Conference on Computer Vision and Pattern Recognition* 770–778 URL <https://doi.org/10.1109/CVPR.2016.90>
- [27] Zeiler M D and Fergus R 2014 *Computer Vision – ECCV* 818–833 URL <https://doi.org/10.1007/978-3-319-10590-1>
- [28] Ren S, He K, Girshick R and Sun J 2015 *Advances in Neural Information Processing Systems* **28** 91–99 URL <https://proceedings.neurips.cc/paper/2015/file/14bfa6bb14875e45bba028a21ed38046-Paper.pdf>
- [29] Hecht-Nielsen 1989 *International 1989 Joint Conference on Neural Networks* 593–605 vol.1 URL <http://doi.org/10.1109/IJCNN.1989.118638>
- [30] Zhao H, Gallo O, Frosio I and Kautz J 2017 *IEEE Transactions on Computational Imaging* **3** 47–57 URL <https://doi.org/10.1109/TCI.2016.2644865>
- [31] Feng Z, Kittler J, Awais M, Huber P and Wu X 2018 *IEEE Conference on Computer Vision and Pattern Recognition* 2235–2245
- [32] Goodfellow I, Bengio Y and Courville A 2016 *Deep Learning* (MIT Press) URL <http://deeplearningbook.org>
- [33] Keren G, Sabato S and Schuller B 2018 *IEEE International Conference on Data Mining* 227–236

- URL <https://doi.org/10.1109/ICDM.2018.00038>
- [34] Bottou L 1999 *On-line Learning and Stochastic Approximations* (Cambridge University Press) p 9–42 URL <https://doi.org/10.1017/CB09780511569920.003>
- [35] Jastrzebski S, Kenton Z, Arpit D, Ballas N, Fischer A, Bengio Y and Storkey A 2018 (*Preprint 1711.04623*) URL <https://arxiv.org/abs/1711.04623>
- [36] Bengio Y 2012 *Practical Recommendations for Gradient-Based Training of Deep Architectures* (Springer Berlin Heidelberg) pp 437–478 ISBN 978-3-642-35289-8 URL https://doi.org/10.1007/978-3-642-35289-8_26
- [37] Everingham M, Van Gool L, Williams C K, Winn J and Zisserman A 2010 *International Journal of Computer Vision* **88** 303–338 URL <https://doi.org/10.1007/s11263-009-0275-4>
- [38] Boyd K, Eng K H and Page C D 2013 *Joint European Conference on Machine Learning and Knowledge Discovery in Databases* 451–466 URL <http://doi.org/10.1007/978-3-642-40994-3>
- [39] Cordts M, Omran M, Ramos S, Rehfeld T, Enzweiler M, Benenson R, Franke U, Roth S and Schiele B 2016 *IEEE Conference on Computer Vision and Pattern Recognition* 3213–3223 URL <https://doi.org/10.1109/CVPR.2016.350>
- [40] Bisong E 2019 *Google Colaboratory* (Springer) pp 59–64 URL <https://link.springer.com/book/10.1007/978-1-4842-4470-8>
- [41] Paszke A, Gross S, Chintala S, Chanan G, Yang E, DeVito Z, Lin Z, Desmaison A, Antiga L and Lerer A 2017 *31st Conference on Neural Information Processing Systems* URL <https://openreview.net/forum?id=BJJsrmfCZ>
- [42] Lin T Y, Maire M, Belongie S, Hays J, Perona P, Ramanan D, Dollár P and Zitnick C L 2014 *Computer Vision – ECCV* 740–755 URL <https://doi.org/10.1007/978-3-319-10602-1>
- [43] Yosinski J, Clune J, Bengio Y and Lipson H 2014 *Advances in Neural Information Processing Systems* **27** 3320–3328 URL <https://proceedings.neurips.cc/paper/2014/file/375c71349b295f8e2dcdca9206f20a06-Paper.pdf>
- [44] Bergstra J and Bengio Y 2012 *The Journal of Machine Learning Research* **13** 281–305 URL <https://dl.acm.org/doi/abs/10.5555/2188385.2188395>
- [45] Eggenberger K, Feurer M, Hutter F, Bergstra J, Snoek J, Hoos H and Leyton-Brown K 2013 *NIPS Workshop on Bayesian Optimization in Theory and Practice* **10** 3 URL <https://www.cs.ubc.ca/~hoos/Publ/EggEtA113.pdf>
- [46] Frazier P I 2018 (*Preprint 1807.02811*) URL <https://arxiv.org/abs/1807.02811>
- [47] Brochu E, Cora V M and de Freitas N 2010 (*Preprint 1012.2599*) URL <https://arxiv.org/abs/1012.2599>
- [48] Sobol’ I M 1967 *Zhurnal Vychislitel’noi Matematiki i Matematicheskoi Fiziki* **7** 784–802 URL <http://mi.mathnet.ru/eng/zvmmf7334>
- [49] Balandat M, Karrer B, Jiang D R, Daulton S, Letham B, Wilson A G and Bakshy E 2020 (*Preprint 1910.06403*) URL <https://arxiv.org/abs/1910.06403>
- [50] Redmon J and Farhadi A 2018 (*Preprint 1804.02767*) URL <https://arxiv.org/abs/1804.02767>
- [51] Hofer L R, Dragone R V and MacGregor A D 2017 *Optical Engineering* **56** 043110 URL <https://doi.org/10.1117/1.OE.56.4.043110>
- [52] ISO 11146-3 Lasers and laser-related equipment. Test methods for laser beam widths, divergence angles and beam propagation ratios. 2004. International Organization for Standardization Geneva, Switzerland URL <https://www.iso.org/standard/33627.html>
- [53] Fiorio C and Gustedt J 1996 *Theoretical Computer Science* **154** 165–181 URL [https://doi.org/10.1016/0304-3975\(94\)00262-2](https://doi.org/10.1016/0304-3975(94)00262-2)
- [54] Bloch I 2005 *Nature Physics* **1** 23–30 URL <https://doi.org/10.1038/nphys138>
- [55] Viebahn K, Sbroscia M, Carter E, Yu J C and Schneider U 2019 *Physical Review Letters* **122** 110404 URL <https://doi.org/10.1103/PhysRevLett.122.110404>
- [56] Gaunt A L, Schmidutz T F, Gotlibovych I, Smith R P and Hadzibabic Z 2013 *Physical Review Letters* **110** URL <https://doi.org/10.1103/PhysRevLett.110.200406>

- [57] Anderson M H, Ensher J R, Matthews M R, Wieman C E and Cornell E A 1995 *Science* **269** 198–201 URL <https://doi.org/10.1126/science.269.5221.198>
- [58] Davis K B, Mewes M O, Andrews M R, van Druten N J, Durfee D S, Kurn D and Ketterle W 1995 *Physical Review Letters* **75** 3969 URL <https://doi.org/10.1103/PhysRevLett.75.3969>

Appendix F

Laser Cooling

When an atom finds itself in a (near-)resonant light field and is excited by absorbing a photon, a momentum unit of $\hbar k$, where $k = \frac{2\pi}{\lambda}$ is the wave number of the light, is transferred to it in the direction of the incoming photon. If the subsequent de-excitation happens via spontaneous emission, the emitted photon carries away another unit of momentum, $\hbar k$, but this time in a random direction. The net effect of a large number of such events is that each one will on average transfer a recoil momentum unit of $\hbar k$ to the atom in the direction of the incident light. The randomised force originating from the spontaneous emission events will additionally lead to diffusive motion in momentum space, and has to be considered in the context of limits on the lowest achievable temperatures using these methods.

This scattering force, for an atom with a resonant transition of line width Γ , at wavelength λ (with $k = \frac{2\pi}{\lambda}$, again), takes the form [74]:

$$F_{\text{scatt}} = \frac{\hbar k \Gamma}{2} \frac{s}{1 + s + \frac{4\delta^2}{\Gamma^2}} \quad (\text{F.1})$$

where δ is the detuning of light w.r.t. to the resonance and $\frac{I}{I_{\text{sat}}}$ is the ratio of the light intensity and the saturation intensity of the transition, defined as $I_{\text{sat}} = \frac{2\pi^2 \hbar \Gamma c}{3\lambda^3}$.

What renders the light scattering force useful for cooling applications is its dependence on velocity via the Doppler effect, and in most cases magnetic field, through the Zeeman effect. In both cases the dependence comes in through detuning, which then generally takes the form $\delta = \delta_0 - kv + \frac{\mu B}{\hbar}$ where δ_0 represents the bare detuning of the light w.r.t. to the resonant frequency, μ is the transition magnetic moment and B is the magnetic field magnitude.

In the simplest scenario, where a pair of counter-propagating beams is incident onto the atoms, the effective detuning is different for the two beams, namely $\delta_{\pm} = \delta_0 \pm kv$. Then, provided that $\delta_0 < 0$, the combined scattering force will always be directed against the atom's

velocity, bringing about slowing. For small velocities, ($kv \ll \delta$), the scattering force has the form of a viscous force (the multi-beam saturation parameter s' is introduced below):

$$F_{\text{scatt}} = -\alpha v = \frac{8\hbar k^2 s \delta_0}{\Gamma \left(1 + s' + \frac{4\delta_0^2}{\Gamma^2}\right)^2} v. \quad (\text{F.2})$$

In order to provide cooling in multiple spatial directions, pairs of counter-propagating beams can be superimposed. The scattering force in this configuration is more difficult to calculate, as the different beams all contribute to saturating the transition. An approximation valid in the weakly to intermediately saturated limit, that is frequently employed, is to substitute the single beam saturation parameter s in the denominator with the combined saturation parameter s' that accounts for the total light intensity from all beams [135]:

$$F_{\text{scatt}} = \frac{\hbar k \Gamma}{2} \frac{s}{1 + s' + \frac{4\delta^2}{\Gamma^2}}. \quad (\text{F.3})$$

The fluctuations in the scattering force originate from the randomly directed spontaneous emission events, as well as the shot noise in the incident beam. The contribution of the former can be quantified by viewing its effect as a random walk in momentum space with step length equal to the recoil momentum $\hbar k$, leading to the increase in mean-square velocity after N_{scatt} events of

$$\Delta \langle p_i^2 \rangle_{\text{spont.}} = \frac{N_{\text{scatt}}}{3} \hbar^2 k^2 \quad (\text{F.4})$$

along each axis[74]. The contribution from the shot noise has the same 'random-walk' nature, but this time only along the direction of the incident beam:

$$\Delta \langle p_x^2 \rangle_{\text{shot}} = N_{\text{scatt}} \hbar^2 k^2. \quad (\text{F.5})$$

Regardless of the beam geometry, the diffusive motion in momentum space will be governed by diffusion coefficients D_i that are proportional to the scattering rate and account for the geometry of the cooling beams:

$$\frac{1}{2} \frac{d \langle p_i^2 \rangle}{dt} = D_i - \frac{\alpha_i}{m} \langle p_i^2 \rangle. \quad (\text{F.6})$$

In a system with a viscous-type velocity damping (e.g. Equation F.2), the equilibrium temperature reached can be estimated as:

$$T_{\text{eq}} = \frac{D}{k_B \alpha} \quad (\text{F.7})$$

where α and D represent averages of the velocity damping coefficients and diffusion coefficients along individual axes. In the case of three orthogonal pairs of cooling beams (3D molasses), the minimum achievable temperature, called the Doppler temperature, is:

$$T_D = \frac{\hbar\Gamma}{2k_B} \quad (\text{F.8})$$

and is reached for $\delta_0 = -\frac{\Gamma}{2}$ and $s, s' \ll 1$. For the two optical transitions in erbium that we use for laser cooling in our experiment, the Doppler temperature values are $T_{D,583 \text{ nm}} = 4.6 \mu\text{K}$ and $T_{D,401 \text{ nm}} = 712 \mu\text{K}$

Appendix G

Integral and Discrete Transforms for the Numerical Simulation

G.1 Continuous Fourier and Hankel Transforms

For the 1D Fourier transform (FT) in Cartesian coordinates we use the definition:

$$\tilde{f}(k) = \mathcal{F}\{f\} = \int f(x) e^{-ikx} dx \quad (\text{G.1})$$

and its inverse then takes the form:

$$f(x) = \mathcal{F}^{-1}\{\tilde{f}\} = \frac{1}{2\pi} \int \tilde{f}(k) e^{ikx} dx . \quad (\text{G.2})$$

This formalism extends straightforwardly to the 2D and 3D cases, with the normalisation prefactor in the inverse transform being raised to the appropriate power.

If working in cylindrical coordinate, the Hankel transform (HT) comes useful as it is adapted for that geometry. The HT of order $m \in \mathcal{Z}$ is defined as:

$$\tilde{f}(k) = \mathcal{H}_m\{f\} = \int f(r) J_m(kr) r dr \quad (\text{G.3})$$

and its inverse is:

$$f(r) = \mathcal{H}_m^{-1}\{\tilde{f}\} = \int \tilde{f}(k) J_m(kr) k dk \quad (\text{G.4})$$

In the special case of $m = 0$, the Hankel transform is equivalent to a 2D Fourier transform of a function with radial symmetry, i.e. $f(x, y) = f(r)$ where $r = \sqrt{x^2 + y^2}$. In fact, this relation

can be extended to all integer values of m if a function of the form $f(r)e^{im\phi}$ is considered:

$$\mathcal{F}_{2D}\{f(r)e^{im\phi}\} = 2\pi i^{-m} e^{im\phi_k} \mathcal{H}_m\{f\} \quad (\text{G.5})$$

demonstrating one of the aspects that motivate the usage of this transform.

G.2 Discrete Transforms

G.2.1 Discrete Fourier Transform

To do numerical simulations, we use the discrete equivalents of these and here it is important to establish connections to the continuous transforms. In the case of the FT, the discrete version (DFT) is defined as:

$$\tilde{f}_l = \mathcal{D}\mathcal{F}\mathcal{T}\{f\} = \sum_{m=0}^{N-1} f_m e^{-2\pi i \frac{ml}{N}} \quad (\text{G.6})$$

and the inverse discrete transform is:

$$f_m = \mathcal{T}\mathcal{D}\mathcal{F}\mathcal{T}\{\tilde{f}\} = \frac{1}{N} \sum_{l=0}^{N-1} \tilde{f}_l e^{2\pi i \frac{ml}{N}}. \quad (\text{G.7})$$

If a function $f(x)$ sampled at N regularly distributed points such that $f_m = f(x_m)$ for:

$$x_m = -\frac{L}{2} + \frac{mL}{N} \quad \text{for } m \in \{0, \dots, N-1, \} \quad (\text{G.8})$$

then, as long as $\tilde{f}(k)$ is band limited within $|k| \leq \frac{\pi N}{L}$, the DFT from Equation G.6 samples the FT of $f(x)$ at spatial frequencies:

$$k_l = \begin{cases} \frac{2\pi}{L_x} l & \text{for } 0 \leq l < \frac{N_x}{2} \\ \frac{2\pi}{L_x} (l - N_x) & \text{for } \frac{N_x}{2} \leq l \leq N_x - 1 \end{cases} \quad (\text{G.9})$$

which results in the following relation between the DFT and the FT:

$$\tilde{f}(k_l) = \frac{L}{N} e^{i \frac{k_l L}{2}} \mathcal{D}\mathcal{F}\mathcal{T}\{f\}_l \quad (\text{G.10})$$

A recipe for developing a well behaved interpolation function for the purpose of calculating derivatives can be found in [141].

G.2.2 Discrete Cosine Transform

The discrete cosine transform (DCT) is a derivative of DFT that can be applied to data with appropriate parity and periodicity. There are multiple types of DCT, and here we use DCT-I, that is defined as:

$$\tilde{f}_l = \text{DCT}\{f\} = f_0 + (-1)^l f_{N-1} + 2 \sum_{m=1}^{N-2} f_m \cos\left(\frac{\pi ml}{N-1}\right) \quad (\text{G.11})$$

and the inverse discrete transform is:

$$f_m = \text{IDCT}\{\tilde{f}\} = \frac{1}{N-1} \left(\tilde{f}_0 + (-1)^m \tilde{f}_{N-1} + 2 \sum_{l=1}^{N-2} \tilde{f}_l \cos\left(\frac{\pi ml}{N-1}\right) \right) \quad (\text{G.12})$$

One option for the sampling points is:

$$x_m = -L + \frac{mL}{N-1} \quad \text{for } m \in \{0, \dots, N-1, \} \quad (\text{G.13})$$

This transform is applicable to periodic functions that are even around x_0 and $x_N - 1$. It can be derived from an equivalent DFT applied to an extended even function g_m defined on a grid of length $2N - 2$ such that:

$$g_m = f_m \quad \text{for } m \in \{0, \dots, N-1\} \quad (\text{G.14})$$

$$g_m = g_{2N-2-m} \quad \text{for } m \in \{N, \dots, 2N-3\} \quad (\text{G.15})$$

Since the DCT is derived directly from the extended grid DFT, the associated spatial frequencies are also borrowed from it (remembering that the DFT sampling range is also doubled):

$$k_l = \frac{\pi}{L} l \quad (\text{G.16})$$

Finally, the relation to the continuous FT is:

$$\tilde{f}(k_l) = \frac{L}{N-1} e^{ik_l L} \text{DCT}\{f\}_l \quad (\text{G.17})$$

G.2.3 Discrete Hankel Transform

An efficient numerical approach to perform the Hankel transform on discrete data, that relies on the Dini series expansion, is laid out in [121]. The first step in the procedure for a grid of

N_r points extending over $[0, b]$ is evaluating the quantity S that is defined as:

$$S = 2|J_0^{-1}(\alpha_\kappa)| \sqrt{1 + \sum_{n=1}^{N-1} J_0^{-2}(\alpha_n) J_0^2\left(\frac{\alpha_\kappa \alpha_n}{J_N}\right)} \quad (\text{G.18})$$

where J_m and α_m are the m -th zeros of $J_0(r)$ and $J'_0(r)$ respectively and $\kappa = \text{Int}(\frac{N+1}{4})$. Then, the grid points can be defined as:

$$r_n = \frac{\alpha_n b}{S} \quad (\text{G.19})$$

and also introducing the size of the inverse space grid to be $\beta = \frac{S}{b}$, a similar expression stands for the spatial frequencies:

$$k_m = \frac{\alpha_m}{b} = \frac{\alpha_m \beta}{S}. \quad (\text{G.20})$$

Once these have been defined, the procedure for performing the DHT may be stated:

$$\tilde{f}(k_m) = \frac{|J_0(\alpha_m)| b^{N-1}}{\beta} \sum_{n=0}^{N-1} C_{mn} f(r_n) |J_0^{-1}(\alpha_n)| \quad (\text{G.21})$$

$$f(r_n) = \frac{|J_0(\alpha_n)| \beta^{N-1}}{b} \sum_{m=0}^{N-1} C_{nm} \tilde{f}(k_m) |J_0^{-1}(\alpha_m)| \quad (\text{G.22})$$

where C_{nm} are the elements of the transform matrix

$$C_{nm} = \frac{2}{S} |J_0^{-1}(\alpha_n)| |J_0^{-1}(\alpha_m)| J_0\left(\frac{\alpha_n \alpha_m}{S}\right). \quad (\text{G.23})$$

The results obtained this way correspond directly to the function $f(r)$ and its HT $\tilde{f}(k)$ evaluated on the grid.

We can define analytic interpolation function for any function based on this transform. Essentially, when spatial samples of the function $f(r_n)$ are supplied the following interpolation is assumed by the HT:

$$f(r) = \frac{2}{b^2} \sum_{m=0}^{N-1} \tilde{f}(k_m) J_0^{-2}(\alpha_m) J_0(k_m r) \quad (\text{G.24})$$

where α_m and k_m are the same as defined above, and the interpolation is defined over the domain $[0, b]$. Similarly, given the spatial samples we can also do the interpolation of the

Hankel transform of the function:

$$f(k) = \frac{2}{\beta^2} \sum_{n=0}^{N-1} f(r_n) J_0^{-2}(\alpha_n) J_0(kr_n) \quad (\text{G.25})$$

These interpolation can be exploited for evaluations of integrals, where one can write:

$$\int_0^b 2\pi f(r) r dr = \frac{2}{b^2} \sum_{m=0}^{N-1} \tilde{f}(k_m) J_0^{-2}(\alpha_m) \int_0^b 2\pi J_0(k_m r) r dr \quad (\text{G.26})$$

and these Bessel function integrals can now be performed analytically:

$$\int_0^b 2\pi J_0(k_m r) r dr = \begin{cases} \pi b^2 & \text{for } k_m = 0 \\ \frac{2\pi b}{k_m} J_1(bk_m) = 0 & \text{otherwise} \end{cases} \quad (\text{G.27})$$

In some cases, for example when calculating dot products, we would also need integrals of products of two functions:

$$\int_0^b 2\pi f(r) g(r) r dr = \frac{4}{b^4} \sum_{m=0}^{N-1} \sum_{n=0}^{N-1} \tilde{f}(k_m) \tilde{g}(k_n) J_0^{-2}(\alpha_m) J_0^{-2}(\alpha_n) \int_0^b 2\pi J_0(k_m r) J_0(k_n r) r dr \quad (\text{G.28})$$

the integral here can also be done analytically:

$$\int_0^b 2\pi J_0(k_m r) J_0(k_n r) r dr = \pi b^2 J_0^2(\alpha_m) \delta_{mn} \quad (\text{G.29})$$

where δ_{mn} represents the Kronecker delta.

References

- [1] S. Chu, L. Hollberg, J. E. Bjorkholm, A. Cable, and A. Ashkin. Three-dimensional viscous confinement and cooling of atoms by resonance radiation pressure. *Phys. Rev. Lett.*, 55:48–51, (1985).
- [2] M. H. Anderson, J. R. Ensher, M. R. Matthews, C. E. Wieman, and E. A. Cornell. Observation of Bose-Einstein condensation in a dilute atomic vapor. *Science*, 269:198–201, (1995).
- [3] K. B. Davis, M. O. Mewes, M. R. Andrews, N. J. van Druten, D. S. Durfee, D. M. Kurn, and W. Ketterle. Bose-Einstein condensation in a gas of sodium atoms. *Phys. Rev. Lett.*, 75:3969–3973, (1995).
- [4] C. C. Bradley, C. A. Sackett, J. J. Tollett, and R. G. Hulet. Evidence of Bose-Einstein condensation in an atomic gas with attractive interactions. *Phys. Rev. Lett.*, 75:1687–1690, (1995).
- [5] B. DeMarco and D. S. Jin. Onset of Fermi degeneracy in a trapped atomic gas. *Science*, 285:1703–1706, (1999).
- [6] S. Inouye, M. R. Andrews, J. Stenger, H. J. Miesner, D. M. Stamper-Kurn, and W. Ketterle. Observation of Feshbach resonances in a Bose-Einstein condensate. *Nature*, 392:151–154, (1998).
- [7] Ph. Courteille, R. S. Freeland, D. J. Heinzen, F. A. van Abeelen, and B. J. Verhaar. Observation of a Feshbach resonance in cold atom scattering. *Phys. Rev. Lett.*, 81:69–72, (1998).
- [8] M. R. Andrews, C. G. Townsend, H.-J. Miesner, D. S. Durfee, D. M. Kurn, and W. Ketterle. Observation of interference between two Bose condensates. *Science*, 275:637–641, (1997).
- [9] I. Bloch, T. W. Hänsch, and T. Esslinger. Measurement of the spatial coherence of a trapped Bose gas at the phase transition. *Nature*, 403:166–170, (2000).
- [10] M. Greiner, C. A. Regal, and D. S. Jin. Emergence of a molecular Bose-Einstein condensate from a Fermi gas. *Nature*, 426:537–540, (2003).
- [11] M. W. Zwierlein, C. A. Stan, C. H. Schunck, S. M. F. Raupach, S. Gupta, Z. Hadzibabic, and W. Ketterle. Observation of Bose-Einstein condensation of molecules. *Phys. Rev. Lett.*, 91:250401, (2003).

- [12] S. Jochim, M. Bartenstein, A. Altmeyer, G. Hendl, S. Riedl, C. Chin, J. Hecker Denschlag, and R. Grimm. Bose-Einstein condensation of molecules. *Science*, 302:2101–2103, (2003).
- [13] M. R. Matthews, B. P. Anderson, P. C. Haljan, D. S. Hall, C. E. Wieman, and E. A. Cornell. Vortices in a Bose-Einstein condensate. *Phys. Rev. Lett.*, 83:2498–2501, (1999).
- [14] K. W. Madison, F. Chevy, W. Wohlleben, and J. Dalibard. Vortex formation in a stirred Bose-Einstein condensate. *Phys. Rev. Lett.*, 84:806–809, (2000).
- [15] J. R. Abo-Shaeer, C. Raman, J. M. Vogels, and W. Ketterle. Observation of vortex lattices in Bose-Einstein condensates. *Science*, 292:476–479, (2001).
- [16] M. Greiner, O. Mandel, T. Esslinger, T. W. Hansch, and I. Bloch. Quantum phase transition from a superfluid to a Mott insulator in a gas of ultracold atoms. *Nature*, 415:39–44, (2002).
- [17] T. Langen, R. Geiger, and J. Schmiedmayer. Ultracold atoms out of equilibrium. *Annual Review of Condensed Matter Physics*, 6:201–217, (2015).
- [18] M. Lewenstein, A. Sanpera, V. Ahufinger, B. Damski, A. Sen(De), and U. Sen. Ultracold atomic gases in optical lattices: mimicking condensed matter physics and beyond. *Advances in Physics*, 56:243–379, (2007).
- [19] J. Beugnon and N. Navon. Exploring the Kibble–Zurek mechanism with homogeneous Bose gases. *Journal of Physics B: Atomic, Molecular and Optical Physics*, 50:022002, (2017).
- [20] X. Zhang and J. Ye. Precision measurement and frequency metrology with ultracold atoms. *National Science Review*, 3:189–200, (2016).
- [21] I. Bloch. Quantum coherence and entanglement with ultracold atoms in optical lattices. *Nature*, 453:1016–1022, (2008).
- [22] A. L. Gaunt, T. F. Schmidutz, I. Gotlibovych, R. P. Smith, and Z. Hadzibabic. Bose-Einstein condensation of atoms in a uniform potential. *Phys. Rev. Lett.*, 110:200406, (2013).
- [23] N. Navon, A. L. Gaunt, R. P. Smith, and Z. Hadzibabic. Critical dynamics of spontaneous symmetry breaking in a homogeneous Bose gas. *Science*, 347:167–170, (2015).
- [24] N. Navon, A. L. Gaunt, R. P. Smith, and Z. Hadzibabic. Emergence of a turbulent cascade in a quantum gas. *Nature*, 539:72–75, (2016).
- [25] B. Paredes, A. Widera, V. Murg, O. Mandel, S. Fölling, I. Cirac, G. Shlyapnikov, T. Hänsch, and I. Bloch. Tonks–Girardeau gas of ultracold atoms in an optical lattice. *Nature*, 429:277–281, (2004).
- [26] T. Kinoshita, T. Wenger, and D. S. Weiss. Observation of a one-dimensional Tonks–Girardeau gas. *Science*, 305:1125–1128, (2004).

- [27] Z. Hadzibabic, P. Krüger, M. Cheneau, B. Battelier, and J. Dalibard. Berezinskii–Kosterlitz–Thouless crossover in a trapped atomic gas. *Nature*, 441:1118–1121, (2006).
- [28] A. Griesmaier, J. Werner, S. Hensler, J. Stuhler, and T. Pfau. Bose-Einstein condensation of chromium. *Phys. Rev. Lett.*, 94:160401, (2005).
- [29] K. Aikawa, A. Frisch, M. Mark, S. Baier, A. Rietzler, R. Grimm, and F. Ferlaino. Bose-Einstein condensation of erbium. *Phys. Rev. Lett.*, 108:210401, (2012).
- [30] M. Lu, N. Q. Burdick, S. H. Youn, and B. L. Lev. Strongly dipolar Bose-Einstein condensate of dysprosium. *Phys. Rev. Lett.*, 107:190401, (2011).
- [31] T. Lahaye, T. Koch, B. Fröhlich, M. Fattori, J. Metz, A. Griesmaier, S. Giovanazzi, and T. Pfau. Strong dipolar effects in a quantum ferrofluid. *Nature*, 448:672–675, (2007).
- [32] T. Lahaye, J. Metz, B. Fröhlich, T. Koch, M. Meister, A. Griesmaier, T. Pfau, H. Saito, Y. Kawaguchi, and M. Ueda. *d*-wave collapse and explosion of a dipolar Bose-Einstein condensate. *Phys. Rev. Lett.*, 101:080401, (2008).
- [33] T. Koch, T. Lahaye, J. Metz, B. Fröhlich, A. Griesmaier, and T. Pfau. Stabilization of a purely dipolar quantum gas against collapse. *Nature Physics*, 4:218–222, (2008).
- [34] T. Maier, I. Ferrier-Barbut, H. Kadau, M. Schmitt, M. Wenzel, C. Wink, T. Pfau, K. Jachymski, and P. S. Julienne. Broad universal Feshbach resonances in the chaotic spectrum of dysprosium atoms. *Phys. Rev. A*, 92:060702, (2015).
- [35] L. Chomaz, R. M. W. van Bijnen, D. Petter, G. Faraoni, S. Baier, J. H. Becher, M. J. Mark, F. Wächtler, L. Santos, and F. Ferlaino. Observation of roton mode population in a dipolar quantum gas. *Nature Physics*, 14:442–446, (2018).
- [36] D. Petter, G. Natale, R. M. W. van Bijnen, A. Patscheider, M. J. Mark, L. Chomaz, and F. Ferlaino. Probing the roton excitation spectrum of a stable dipolar Bose gas. *Phys. Rev. Lett.*, 122:183401, (2019).
- [37] L. Landau. Theory of the superfluidity of helium ii. *Phys. Rev.*, 60:356–358, (1941).
- [38] H. Kadau, M. Schmitt, M. Wenzel, C. Wink, T. Maier, I. Ferrier-Barbut, and T. Pfau. Observing the Rosensweig instability of a quantum ferrofluid. *Nature*, 530:194–197, (2016).
- [39] I. Ferrier-Barbut, H. Kadau, M. Schmitt, M. Wenzel, and T. Pfau. Observation of quantum droplets in a strongly dipolar Bose gas. *Phys. Rev. Lett.*, 116:215301, (2016).
- [40] G. Natale, R. M. W. van Bijnen, A. Patscheider, D. Petter, M. J. Mark, L. Chomaz, and F. Ferlaino. Excitation spectrum of a trapped dipolar supersolid and its experimental evidence. *Phys. Rev. Lett.*, 123:050402, (2019).
- [41] F. Böttcher, J.-N. Schmidt, M. Wenzel, J. Hertkorn, M. Guo, T. Langen, and T. Pfau. Transient supersolid properties in an array of dipolar quantum droplets. *Phys. Rev. X*, 9:011051, (2019).

- [42] J. Hertkorn, F. Böttcher, M. Guo, J. N. Schmidt, T. Langen, H. P. Büchler, and T. Pfau. Fate of the amplitude mode in a trapped dipolar supersolid. *Phys. Rev. Lett.*, 123:193002, (2019).
- [43] I. Ferrier-Barbut, H. Kadau, M. Schmitt, M. Wenzel, and T. Pfau. Observation of quantum droplets in a strongly dipolar Bose gas. *Phys. Rev. Lett.*, 116:215301, (2016).
- [44] G. A. Phelps. *A dipolar quantum gas microscope*. PhD thesis, Harvard University, (2019).
- [45] W. Lunden, L. Du, M. Cantara, P. Barral, A. O. Jamison, and W. Ketterle. Enhancing the capture velocity of a dy magneto-optical trap with two-stage slowing. *Phys. Rev. A*, 101:063403, (2020).
- [46] J. Ulitzsch, D. Babik, R. Roell, and M. Weitz. Bose-Einstein condensation of erbium atoms in a quasidelectrostatic optical dipole trap. *Phys. Rev. A*, 95:043614, (2017).
- [47] D. Dreon, L. A. Sidorenkov, C. Bouazza, W. Mainault, J. Dalibard, and S. Nascimbene. Optical cooling and trapping of highly magnetic atoms: the benefits of a spontaneous spin polarization. *Journal of Physics B: Atomic, Molecular and Optical Physics*, 50:065005, (2017).
- [48] E. Lucioni, G. Masella, A. Fregosi, C. Gabbanini, S. Gozzini, A. Fioretti, L. Del Bino, J. Catani, G. Modugno, and M. Inguscio. A new setup for experiments with ultracold dysprosium atoms. *The European Physical Journal Special Topics*, 226:2775–2780, (2017).
- [49] B. Seo, P. Chen, Z. Chen, W. Yuan, M. Huang, S. Du, and G.-B. Jo. Efficient production of a narrow-line erbium magneto-optical trap with two-stage slowing. *Phys. Rev. A*, 102:013319, (2020).
- [50] J. L. Bohn, A. M. Rey, and J. Ye. Cold molecules: Progress in quantum engineering of chemistry and quantum matter. *Science*, 357:1002–1010, (2017).
- [51] K.-K. Ni, S. Ospelkaus, M. H. G. de Miranda, A. Pe’er, B. Neyenhuis, J. J. Zirbel, S. Kotochigova, P. S. Julienne, D. S. Jin, and J. Ye. A high phase-space-density gas of polar molecules. *Science*, 322:231–235, (2008).
- [52] T. Vogt, M. Viteau, J. Zhao, A. Chotia, D. Comparat, and P. Pillet. Dipole blockade at Förster resonances in high resolution laser excitation of Rydberg states of cesium atoms. *Phys. Rev. Lett.*, 97:083003, (2006).
- [53] R. Blatt and C. F. Roos. Quantum simulations with trapped ions. *Nature Physics*, 8:277–284, (2012).
- [54] C.G. Mosander. Xxx. on the new metals, lanthanum and didymium, which are associated with cerium; and on erbium and terbium, new metals associated with yttria. *The London, Edinburgh, and Dublin Philosophical Magazine and Journal of Science*, 23:241–254, (1843).

- [55] A. Kramida, Yu. Ralchenko, J. Reader, and NIST ASD Team. NIST Atomic Spectra Database (ver. 5.8), [Online]. Available: <https://physics.nist.gov/asd> [2021, May 26]. National Institute of Standards and Technology, Gaithersburg, MD., (2020).
- [56] Martin, W. C. and Zalubas, R. and Hagan, L. *Atomic Energy Levels – The Rare-Earth Elements*. Nat. Bur. Stand., U.S., (1978).
- [57] A. Frisch. *Dipolar Quantum Gases of Erbium*. PhD thesis, University of Innsbruck, (2014).
- [58] B. Odom, D. Hanneke, B. D’Urso, and G. Gabrielse. New measurement of the electron magnetic moment using a one-electron quantum cyclotron. *Phys. Rev. Lett.*, 97:030801, (2006).
- [59] I. Bloch, Jean D., and W. Zwerger. Many-body physics with ultracold gases. *Rev. Mod. Phys.*, 80:885–964, (2008).
- [60] C. Pethick and H. Smith. *Bose-Einstein condensation in dilute gases*. Cambridge University Press, (2002).
- [61] S. Kotochigova. Controlling interactions between highly magnetic atoms with Feshbach resonances. *Reports on Progress in Physics*, 77:093901, (2014).
- [62] T. Maier. *Interactions in a Quantum Gas of Dysprosium Atoms*. PhD thesis, University of Stuttgart, (2015).
- [63] L.P. Pitaevskiĭ and S. Stringari. *Bose-Einstein Condensation and Superfluidity*. International series of monographs on physics. Oxford University Press, (2016).
- [64] N Bogoliubov. On the theory of superfluidity. *J. Phys*, 11(1):23, (1947).
- [65] L. Santos, G. V. Shlyapnikov, and M. Lewenstein. Roton-maxon spectrum and stability of trapped dipolar Bose-Einstein condensates. *Phys. Rev. Lett.*, 90:250403, (2003).
- [66] B. Kain and H. Y. Ling. Polarons in a dipolar condensate. *Phys. Rev. A*, 89:023612, (2014).
- [67] B. Bylicka, D. Chruściński, and S. Maniscalco. Non-markovianity and reservoir memory of quantum channels: a quantum information theory perspective. *Scientific Reports*, 4(1):5720, 2014.
- [68] J.-B. Yuan, H.-J. Xing, L.-M. Kuang, and S. Yi. Quantum non-Markovian reservoirs of atomic condensates engineered via dipolar interactions. *Phys. Rev. A*, 95:033610, (2017).
- [69] C. Yaws. *The Yaws Handbook of Vapor Pressure: Antoine Coefficients*. Elsevier Science, (2015).
- [70] N. B. Vilas. Laser cooling of erbium. Master’s thesis, University of Cambridge, (2018).

- [71] A. Chambers, R. Fitch, and B. Halliday. *Basic Vacuum Technology*. CRC Press, (1998).
- [72] G. Camy, Ch.J. Bordé, and M. Ducloy. Heterodyne saturation spectroscopy through frequency modulation of the saturating beam. *Optics Communications*, 41:325–330, (1982).
- [73] J. H. Shirley. Modulation transfer processes in optical heterodyne saturation spectroscopy. *Opt. Lett.*, 7:537–539, (1982).
- [74] C. J Foot. *Atomic physics*. Oxford master series in atomic, optical, and laser physics. Oxford University Press, Oxford, (2007).
- [75] G. Lindblad. On the generators of quantum dynamical semigroups. *Communications in Mathematical Physics*, 48:119–130, (1976).
- [76] V. Gorini, A. Kossakowski, and E. C. G. Sudarshan. Completely positive dynamical semigroups of n-level systems. *Journal of Mathematical Physics*, 17:821–825, (1976).
- [77] M. Ducloy and D. Bloch. Theory of degenerate four-wave mixing in resonant Doppler-broadened systems - I. Angular dependence of intensity and lineshape of phase-conjugate emission. *Journal de Physique*, 42:711–721, (1981).
- [78] M. Ducloy and D. Bloch. Theory of degenerate four-wave mixing in resonant Doppler-broadened media. - II. Doppler-free heterodyne spectroscopy via collinear four-wave mixing in two- and three-level systems. *Journal de Physique*, 43:57–65, (1982).
- [79] R. K. Raj, D. Bloch, J. J. Snyder, G. Camy, and M. Ducloy. High-frequency optically heterodyned saturation spectroscopy via resonant degenerate four-wave mixing. *Phys. Rev. Lett.*, 44:1251–1254, (1980).
- [80] D. J. McCarron, S. A. King, and S. L. Cornish. Modulation transfer spectroscopy in atomic rubidium. *Measurement Science and Technology*, 19:105601, (2008).
- [81] L. Neuhaus, R. Metzdorff, S. Chua, T. Jacqmin, T. Briant, A. Heidmann, P.-F. Cohadon, and S. Deléglise. Pyrpl (python red pitaya lockbox) — an open-source software package for fpga-controlled quantum optics experiments. In *2017 Conference on Lasers and Electro-Optics Europe European Quantum Electronics Conference (CLEO/Europe-EQEC)*, pages 1–1, (2017).
- [82] B. Plotkin-Swing, A. Wirth, D. Gochner, T. Rahman, K. E. McAlpine, and S. Gupta. Crossed-beam slowing to enhance narrow-line ytterbium magneto-optic traps. *Review of Scientific Instruments*, 91:093201, (2020).
- [83] T. H. Loftus, T. Ido, M. M. Boyd, A. D. Ludlow, and J. Ye. Narrow line cooling and momentum-space crystals. *Phys. Rev. A*, 70:063413, (2004).
- [84] I Manai, A Molineri, C Fréjaille, C Duval, P Bataille, R Journet, F Wiotte, B. Laburthe-Tolra, E Maréchal, M. Cheneau, and M. Robert-De-Saint-Vincent. Shelving spectroscopy of the strontium intercombination line. *Journal of Physics B: Atomic, Molecular and Optical Physics*, 53:085005, (2020).

- [85] T. Maier, H. Kadau, M. Schmitt, A. Griesmaier, and T. Pfau. Narrow-line magneto-optical trap for dysprosium atoms. *Opt. Lett.*, 39(11):3138–3141, (2014).
- [86] J. E. Bjorkholm. Collision-limited lifetimes of atom traps. *Phys. Rev. A*, 38:1599–1600, (1988).
- [87] T. Arpornthip, C. A. Sackett, and K. J. Hughes. Vacuum-pressure measurement using a magneto-optical trap. *Phys. Rev. A*, 85:033420, (2012).
- [88] M. Lepers, J.-F. Wyart, and O. Dulieu. Anisotropic optical trapping of ultracold erbium atoms. *Phys. Rev. A*, 89:022505, (2014).
- [89] J. H. Becher, S. Baier, K. Aikawa, M. Lepers, J.-F. Wyart, O. Dulieu, and F. Ferlaino. Anisotropic polarizability of erbium atoms. *Phys. Rev. A*, 97:012509, (2018).
- [90] J. Léonard, M. Lee, A. Morales, T. M Karg, T. Esslinger, and T. Donner. Optical transport and manipulation of an ultracold atomic cloud using focus-tunable lenses. *New Journal of Physics*, 16:093028, (2014).
- [91] P. Juhász. Optical trapping and transport of ultracold erbium atoms. DPhil Transfer of Status Report, University of Oxford, (2019).
- [92] D. Bloch. Optical transport of ultracold atoms. Pre-Doctoral Research Year report, ENS Paris-Saclay, (2020).
- [93] T. L. Gustavson, A. P. Chikkatur, A. E. Leanhardt, A. Görlitz, S. Gupta, D. E. Pritchard, and W. Ketterle. Transport of Bose-Einstein condensates with optical tweezers. *Phys. Rev. Lett.*, 88:020401, (2001).
- [94] G. Unnikrishnan, C. Beulenkamp, D. Zhang, K. P. ZamarSKI, M. Landini, and H.-C. Nägerl. Long distance optical transport of ultracold atoms: A compact setup using a Moiré lens. *arXiv*, page 2103.02387, (2021).
- [95] A. L. Gaunt. *Degenerate Bose Gases: Tuning Interactions & Geometry*. PhD thesis, University of Cambridge, (2014).
- [96] G. Clausen. Generation of Bragg spectroscopy potentials with a DMD. Master’s thesis, ETH Zürich and University of Oxford, (2020).
- [97] R. W. Floyd and L. Steinberg. An adaptive algorithm for spatial grey scale. *Proceedings of the Society of Information Display*, 17:75–77, (1976).
- [98] W. Alt. An objective lens for efficient fluorescence detection of single atoms. *Optik*, 113:142–144, (2002).
- [99] M. Krstajić. Arbitrary dynamical potentials for ultracold atoms. Master’s thesis, University of Cambridge, (2014).
- [100] A. Norden. Bragg spectroscopy setup for probing ultracold erbium atoms. Master’s thesis, University of Oxford, (2020).

- [101] J. Stenger, S. Inouye, A. P. Chikkatur, D. M. Stamper-Kurn, D. E. Pritchard, and W. Ketterle. Bragg spectroscopy of a Bose-Einstein condensate. *Phys. Rev. Lett.*, 82:4569–4573, (1999).
- [102] D. M. Stamper-Kurn, A. P. Chikkatur, A. Görlitz, S. Inouye, S. Gupta, D. E. Pritchard, and W. Ketterle. Excitation of phonons in a Bose-Einstein condensate by light scattering. *Phys. Rev. Lett.*, 83:2876–2879, (1999).
- [103] J. Steinhauer, R. Ozeri, N. Katz, and N. Davidson. Excitation spectrum of a Bose-Einstein condensate. *Phys. Rev. Lett.*, 88:120407, (2002).
- [104] I. Gotlibovych, T. F. Schmidutz, A. L. Gaunt, N. Navon, R. P. Smith, and Z. Hadzibabic. Observing properties of an interacting homogeneous Bose-Einstein condensate: Heisenberg-limited momentum spread, interaction energy, and free-expansion dynamics. *Phys. Rev. A*, 89:061604, (2014).
- [105] L.-C. Ha, L. W. Clark, C. V. Parker, B. M. Anderson, and C. Chin. Roton-maxon excitation spectrum of Bose condensates in a shaken optical lattice. *Phys. Rev. Lett.*, 114:055301, (2015).
- [106] P. Zupancic, P. M. Preiss, R. Ma, A. Lukin, M. E. Tai, M. Rispoli, R. Islam, and M. Greiner. Ultra-precise holographic beam shaping for microscopic quantum control. *Opt. Express*, 24:13881–13893, (2016).
- [107] K. Góral and L. Santos. Ground state and elementary excitations of single and binary Bose-Einstein condensates of trapped dipolar gases. *Phys. Rev. A*, 66:023613, (2002).
- [108] D. Baillie and P. B. Blakie. A general theory of flattened dipolar condensates. *New Journal of Physics*, 17:033028, (2015).
- [109] H.-Y. Lu, H. Lu, J.-N. Zhang, R.-Z. Qiu, H. Pu, and S. Yi. Spatial density oscillations in trapped dipolar condensates. *Phys. Rev. A*, 82:023622, (2010).
- [110] T. W. B. Kibble. Topology of cosmic domains and strings. *Journal of Physics A: Mathematical and General*, 9(8):1387–1398, (1976).
- [111] W. H. Zurek. Cosmological experiments in superfluid helium? *Nature*, 317:505–508, (1985).
- [112] M. D. Feit, J. A. Fleck, and A. Steiger. Solution of the Schrödinger equation by a spectral method. *Journal of Computational Physics*, 47:412–433, (1982).
- [113] T. Bland. *Elementary and topological excitations in ultracold dipolar Bose gases*. PhD thesis, Newcastle University, (2018).
- [114] W. H. Press, S. A. Teukolsky, W. T. Vetterling, and B. P. Flannery. *Numerical Recipes 3rd Edition: The Art of Scientific Computing*. Cambridge University Press, USA, 3 edition, (2007).
- [115] J. Gaidamour, Q. Tang, and X. Antoine. BEC2HPC: a HPC spectral solver for nonlinear Schrödinger and Gross-Pitaevskii equations. Stationary states computation. working paper or preprint, (2020).

- [116] X. Antoine, A. Levitt, and Q. Tang. Efficient spectral computation of the stationary states of rotating Bose-Einstein condensates by the preconditioned nonlinear conjugate gradient method. *Journal of Computational Physics*, 343:92–109, (2017).
- [117] X. Antoine, Q. Tang, and Y. Zhang. A Preconditioned Conjugated Gradient Method for Computing Ground States of Rotating Dipolar Bose-Einstein Condensates via Kernel Truncation Method for Dipole-Dipole Interaction Evaluation. *Communications in Computational Physics*, 24:966–988, (2018).
- [118] R. Lehoucq and J. Scott. An evaluation of software for computing eigenvalues of sparse nonsymmetric matrices preprint mcs-p54. (1996).
- [119] S. Ronen, D. C. E. Bortolotti, and J. L. Bohn. Radial and angular rotons in trapped dipolar gases. *Phys. Rev. Lett.*, 98:030406, (2007).
- [120] H.-Y. Lu, H. Lu, J.-N. Zhang, R.-Z. Qiu, H. Pu, and S. Yi. Spatial density oscillations in trapped dipolar condensates. *Phys. Rev. A*, 82:023622, (2010).
- [121] Y. Kai-Ming, W. Shuang-Chun, C. Lie-Zun, W. You-Wen, and H. Yong-Hua. A quasi-discrete Hankel transform for nonlinear beam propagation. *Chinese Physics B*, 18:3893–3899, (2009).
- [122] S. Ronen, D. C. E. Bortolotti, and J. L. Bohn. Bogoliubov modes of a dipolar condensate in a cylindrical trap. *Physical Review A*, 74, (2006).
- [123] C. Raman, M. Köhl, R. Onofrio, D. S. Durfee, C. E. Kuklewicz, Z. Hadzibabic, and W. Ketterle. Evidence for a critical velocity in a Bose-Einstein condensed gas. *Phys. Rev. Lett.*, 83:2502–2505, (1999).
- [124] L. Corman, L. Chomaz, T. Bienaimé, R. Desbuquois, C. Weitenberg, S. Nascimbène, J. Dalibard, and J. Beugnon. Quench-induced supercurrents in an annular Bose gas. *Phys. Rev. Lett.*, 113:135302, (2014).
- [125] L. Chomaz, L. Corman, T. Bienaimé, R. Desbuquois, C. Weitenberg, S. Nascimbène, J. Beugnon, and J. Dalibard. Emergence of coherence via transverse condensation in a uniform quasi-two-dimensional Bose gas. *Nature Communications*, 6:6162, (2015).
- [126] P. M. Chaikin and T. C. Lubensky. *Principles of Condensed Matter Physics*. Cambridge University Press, Cambridge, (1995).
- [127] P. C. Hohenberg and B. I. Halperin. Theory of dynamic critical phenomena. *Rev. Mod. Phys.*, 49:435–479, (1977).
- [128] K. Jousten. *Wutz Handbuch Vakuumtechnik: Theorie und Praxis; 10th ed.* Vieweg, Wiesbaden, (2010).
- [129] X. Tingwei and W. Kaiping. The relation between the conductance of an elbow and the angle between the tubes. *Vacuum*, 32:655–659, (1982).
- [130] J. K. Gorman and W. R. Nardella. Hydrogen permeation through metals. *Vacuum*, 12:19–24, (1962).

-
- [131] W. Kohl. *Handbook of Materials and Techniques for Vacuum Devices*. AVS Classics in Vacuum Science and Technology. American Inst. of Physics, (1997).
- [132] J. M. Lafferty. *Foundations of Vacuum Science and Technology*. Wiley, (1998).
- [133] J. F. O’Hanlon. *A User’s Guide to Vacuum Technology*. John Wiley and Sons, Ltd, (2003).
- [134] V. Baglin. Vacuum Systems - Lecture 2. CERN Joint Universities Accelerator School, (2017).
- [135] P. D. Lett, W. D. Phillips, S. L. Rolston, C. E. Tanner, R. N. Watts, and C. I. Westbrook. Optical molasses. *J. Opt. Soc. Am. B*, 6:2084–2107, (1989).
- [136] A. Suleymanzade. Ultracold atoms experiment for trapping ^{39}K in an optical box trap. Master’s thesis, University of Cambridge, (2014).
- [137] K. M. Birnbaum. *Cavity QED with Multilevel Atoms*. PhD thesis, California Institute of Technology, (2005).
- [138] S. V. Kagwade, C. R. Clayton, D. Chidambaram, and G. P. Halada. Photochemical breakdown of acetone on copper. *Electrochimica Acta*, 46:2337–2342, (2001).
- [139] A. Keshet and W. Ketterle. A distributed, graphical user interface based, computer control system for atomic physics experiments. *Review of Scientific Instruments*, 84:015105, (2013).
- [140] L. Hofer. Design and construction of a dual erbium-potassium experiment. DPhil Transfer of Status Report, University of Oxford, (2019).
- [141] S. G. Johnson. Notes on FFT-based differentiation. (2011).